DENSITY FUNCTIONAL TIGHT-BINDING AND CLUSTER EXPANSION STUDIES OF LITHIATED/SODIATED SILICON ANODES FOR HIGH-ENERGY-DENSITY BATTERIES

by

Katlego William Phoshoko

THESIS

Submitted in fulfilment of the requirements for the degree of

DOCTOR OF PHILOSOPHY (PhD)

in

PHYSICS

in the

FACULTY OF SCIENCE AND AGRICULTURE

(School of Physical and Mineral Sciences)

at the

UNIVERSITY OF LIMPOPO

South Africa

SUPERVISOR: Prof. P.E. Ngoepe

2020

DEDICATION

I dedicate this thesis

To

My wife Lethabo,

Sons Benhail and Gabriel,

Daughters Abigail and Ivannah

Brother Abram

And

Mother Presida.

DECLARATION

I declare that this thesis hereby submitted to the University of Limpopo, for the degree of Doctor of Philosophy in Physics has not previously been submitted by me for a degree at this or any other university; that it is my work in design and in execution, and that all material contained herein has been duly acknowledged.

Phoshoko K.W. (Mr.)	2020
Surname, Initials, Title	**Date**

ACKNOWLEDGEMENTS

This thesis and work entailed herein could have not been completed without God gracing me with life and the opportunity to advance my knowledge, together with the support and contributions I received from the following persons:

I thank my wife Lethabo Phoshoko, for her immense patience, encouragement and wholehearted support; my mother Presida Phoshoko for having faith in my capacity; my father-in-law, Esrom Mogano, for his continual motivation; my family and friends at large for their strengthening support; I want to pass a special thanks to my supervisor Professor Phuti Ngoepe for his guidance, support and for providing resources required to conduct the research work; a special thank you to Kenneth Kgatwane, Professor Rapela Maphanga, Doctor Cliffton Masedi and Kemeridge Malatji for all their academic contributions, kindness, and earnest assistance; I want to thank all colleagues and friends at Materials Modelling Centre for their willingness to actively advice on areas I needed assistance with; I as well want to thank the National Cyber Infrastructure System: Center for High-Performance Computing (NICIS-CHPC) for computing resources, the National Research Foundation (NRF) and the University of Limpopo for the financial support provided.

ABSTRACT

This work presents a computational modelling workflow that uniquely combines several techniques, proposed as a means for studying and designing high-energy-density electrodes for the next-generation of rechargeable batteries within the era of the fourth industrial revolution (4IR).

The Self-Consistent Charge Density Functional-based Tight Binding (SCC-DFTB) parameterisation scheme for the Li-Si and Na-Si systems is presented. By using the Li-Si system, a procedure for developing the Slater-Koster based potentials is shown. Using lessons learned from the Li-Si framework, the parameterisation of the Na-Si is reported. The Li-Si SCC-DFTB parameter set has been developed to handle environments that consist of Si-Si, Li-Si and Li-Li interactions; and the Na-Si SCC-DFTB parameter set is developed for Na-Na, Na-Si, and Si-Si interactions. Validations and applications of the developed sets are illustrated and discussed.

By calculating equilibrium lattice constants, the Li-Si set is shown to be compatible with various phases in the crystalline Li-Si system. The results were generally within a margin of less than 8% difference, with some values such as that of the cubic $Li_{22}Si_5$ being in agreement with experiments to within 1%. The volume expansion of Si as a function of Li insertion was successfully modelled via the Li-Si SCC-DFTB parameter set. It was shown that Si gradually expands in volume from 53.6% for the LiSi phase composed of 50 *atm %* Li, to 261.57% for $Li_{15}Si_4$ with 78.95 *atm* % Li, and eventually shoots over 300% for the $Li_{22}Si_5$ phase with the expansion at 316.45%, which agrees with experiments.

Furthermore, the ability of the Li-Si SCC-DFTB parameter set to model the mechanical properties of Si is evaluated by calculating the mechanical properties of pristine cubic Si. The parameter set was able to produce the mechanical properties of Si, which agree with experiments to within 6%. The SCC-DFTB parameter set was then used to model the volume expansion of amorphous silicon (*a*-Si) as a result of lithiation within concentrations ranging from 33 – 50 *atm* % Li. Consistent with experiments, the *a*-Si was found to marginally expand in a linear form with increase in Li content. *a*-Si was observed to exhibit a lower expansion compared to *c*-Si. Additionally, the structural stability of the amorphous Li-Si alloys was examined, and observations agree with experiments.

The Na-Si SCC-DFTB parameter set produced equilibrium lattice parameters that agree with experiments to within 4% for reference structures, and the transferability was tested on three Na-Si clathrate compounds (*i.e.* the *Pm-3n* Na_8Si_{46}, the *Cmcm* $NaSi_6$ and *Fd-3m* $Na_{24}Si_{136}$).

By employing the approach used when lithiating Si, the sodiation of crystalline silicon (*c*-Si) was modelled. It was predicted that *c*-Si expands by over 400% at 77 *atm*% Na and shoots above 500% for concentrations exceeding 80 *atm*% of Na. By comparing how *c*-Si expands as a result of lithiation to the expansion consequent to sodiation for concentrations ranging from 66.6 – 81.4 *atm*%, *c*-Si is shown to be unsuitable for Na-ion batteries. As a test, the ability of the developed Na-Si SCC-DFTB parameter set to handle large and complex geometries was shown by modelling the expansion of *a*-Si at 33 *atm*% Na. It was deduced that *a*-Si would be more preferable for Na-ion batteries since at 33 *atm*% Na, *a*-Si expanded a lot less than when *c*-Si was used. Using the Li-Si and the Na-Si SCC-DFTB parameter sets, it was noted that amorphisation appears to lower the magnitude by which Si expands, therefore agreeing with experiments in that amorphous structures are reported to exhibit a buffering effect towards volume expansion.

The material space for the Li-Si alloy system is explored through crystal structure predictions conducted via a machine learning powered cluster expansion (CE). Using the FCC and BCC – based parent lattice in the grid search, 12 thermodynamically stable Li-Si alloys were predicted by the genetic algorithm. Viz. the trigonal Li_4Si (*R-3m*), tetragonal Li_4Si (*I4/m*), tetragonal Li_3Si (*I4/mmm*), cubic Li_3Si (*Fm-3m*), monoclinic Li_2Si_3 (*C2/m*), trigonal Li_2Si (*P-3m1*), tetragonal LiSi (*P4/mmm*), trigonal $LiSi_2$ (*P-2m1*), monoclinic $LiSi_3$ (*P2/m*), cubic $LiSi_3$ (*Pm-3m*), tetragonal $LiSi_4$ (*I4/m*) and monoclinic $LiSi_4$ (*C2/m*).

The structural stabilities of the predicted Li-Si alloys are further studied. With focus on pressure, the thermodynamic conditions under which the Li-rich phase, Li_4Si (*R-3m*), would be stable are tested. Li_4Si (*R-3m*) was subjected to pressures during geometry optimization and found to globally maintain its structural stability within the range 0 – 25GPa. Hence, Li_4Si was predicted to be a low pressure phase. In studying the PDOS, the Li_4Si (*I4/m*) was noted to be more stable around 40GPa and

45GPa, which is consistent with the prediction made from other works, wherein intelligence-based techniques were used.

A test for exploring the Na-Si material space was done using insights acquired from the Li-Si framework. Three thermodynamically stable Na-Si (*i.e*. the *I4/mmm* Na_3Si, *P4/nmm* NaSi and *Immm* $NaSi_2$) were predicted. Using the Na-Si SCC-DFTB parameter set, a correlation of the total DOS in the vicinity of the Fermi level (E_f) with the structural stability of the three Na-Si alloys is done. NaSi (*P4/nmm*) was shown to be unstable at 0GPa, $NaSi_2$ (*Immm*) is found to be stable, and the Na-rich Na_3Si exhibited metastability. The stability of Na_3Si was seen to improve when external pressure ranging from 2.5 – 25GPa was applied; hence, suggesting Na_3Si (*I4/mmm*) to be a high-pressure phase. Furthermore, expanding on the groundwork laid from the Li-Si and Na-Si CE, the Mg-Si system was tested to illustrate that the approach can be used to rapidly screen for new materials. The ground-state crystal structure search predicted 4 thermodynamically stable Mg-Si alloys. *Viz*. Mg_3Si (*Pm-3m*), MgSi (*P4/mmm*), $MgSi_2$ (*Immm*) and $MgSi_3$ (*Pmmm*).

Lastly, to highlight the power of combining various computational techniques to advance material discovery and design, a framework linking SCC-DFTB and CE is illustrated. Candidate electrode materials with nano-architectural features were simulated by designing nanospheres comprised of more than 500 atoms, using the predicted Li-Si and Na-Si crystal structures. The stability of the nanospheres was examined using SCC-DFTB parameters developed herein. The workflow presented in this work paves the way for rapid material discovery, which is sought for in the era of the fourth industrial revolution.

LIST OF ABBREVIATIONS

4IR	Fourth Industrial Revolution
ABNR	Adjusted basis set Newton-Raphson
AI	Artificial intelligence
a-Si	Amorphous Silicon
BNNT	Boron nitride nanotube
BYLYP	Becke, Lee, Yang and Parr
CE	Cluster expansion
CMC	Carboxy methyl cellulose
c-Si	Crystalline Silicon
CV	Cross-validation
DFT	Density functional theory
DL	Deep learning
DN	double-numerical
ECI	Effective cluster interaction
DNN	Deep neural network
DOD	Depth of discharge
DOS	Density of states
EV	Electric vehicle
GA	Genetic algorithm
GGA	Generalized gradient approximation
GPR	Gaussian process regression
GZ	Gaussian double-zeta
HEV	Hybrid electric vehicle
HPC	High-performance computing
IoT	Internet of things
KS-DFT	Kohn-Sham density functional theory
LAMMPS	Large-scale Atomic/Molecular Massively Parallel Simulator

LCAO	Linear combination of atomic orbital
LCN	Local charge neutrality
LDA	Local Density approximation
LDOS	Local density of states
LIB	Li-ion battery
MC	Monte carlo
MD	Molecular dynamics
ML	Machine learning
MM	Molecular modelling
MMC	Materials Modelling Centre
NIB	Na-ion battery
NICIS-CHPC	National Cyber Infrastructure System: Center for High-Performance Computing
NRF	National Research Foundation
PBC	Periodic boundary conditions
PBE	Perdew, Burke, and Ernzerhof
PDA	Portable digital assistants
PDOS	Partial density of states
PDVF	Polyvinylidine fluoride
PHEV	Plug-in hybrid electric vehicle
PW91	Perdew-Wang from 1991
RDF	Radial distribution function
SCC	Self-consistent charge
SCC-DFTB	Self-consistent charge density functional tight-binding
SCF	Self-consistency field
SCTB	Self-consitent tight-binding
SE	Schrödinger equation
SEI	Solid-electrolyte interface

S-K	Slater-Koster
SOC	State of charge
TB	Tight-binding
UNCLE	Universal cluster expansion
VR	Virtual reality

LIST OF SYMBOLS

ρ	Charge density
E	Energy
$T[\rho]$	Kinetic energy of a system of non-interacting particles of density ρ
$U[\rho]$	Classical electrostatic energy due to Coulombic interactions
E_{XC}	Exchange-correlation energy
$V(r)$	External potential
$V_{eff}(r)$	Effective potential
ψ_i	Wave function of electronic state i
ϵ_i	Kohn-Sham eigenvalue
V_H	Hartree potential of the electrons
V_{XC}	Exchange-correlation potential
E_{band}	Band energy
E_{rep}	Repulsive energy
U_{ij}	Repulsive pair energy terms
$H^0_{\mu\upsilon}$	Hamiltonian matrix elements
c^i_μ, c^i_υ	Wave function expansion coefficients
Δq_α , Δq_β	Charge fluctuation terms associated with atoms α and β respectively
$R_{\alpha\beta}$	Distance between atoms α and β,
U_α , U_β	Hubbard parameters for atoms α and β
E_f	Fermi level
ΔH_f	Heats of formation
F	Applied force
A	Cross-sectional area
ΔL	Change in length

L_0	Initial length
Y	Young's modulus
V_0	Equilibrium volume
C_{ij}	Elastic constants
ε	Strain
E_0	Energy of a crystal prior deformation
$O(\varepsilon^3)$	Terms of the order ε^3 or greater
B	Bulk modulus
G	Shear modulus
ϑ	Poisson's ratio
ϕ	Anisotropic factor
E_{kin}	Kinetic energy
E_{pot}	Potential energy
$\boldsymbol{v}$	*Velocities*
U(*r*)	Potential energy function
t	Time
$\vec{x}(t)$	Position at time t
$\vec{v}(t)$	Velocity at time t
$\vec{a}(t)$	Acceleration at time *t*
$\langle K_E \rangle$	Average kinetic energy
T	Thermodynamic temperature
m	Mass
p_i	Momentum
k_B	Boltzmann constant
N_f	Number of degrees of freedom of a system
$T_{instant}$	Instantaneous kinetic temperature
$\overline{\Pi}_F$	Correlation function for each class of symmetry-equivalent figures *F*

D_F	Number of figures of class *F* per site
S_{cv}	Fitness cross-validation score
r_0	Wave function confinement radius
n_0	Density confinement radius
ΔV	Change in volume
V_f	Final volume
V_i	Reference initial volume
$E_{DFT}(\vec{\sigma})$	DFT total energy of the structure $\vec{\sigma}$
$n_i(\vec{\sigma})$	Number of atoms of atomic species i contained in $\vec{\sigma}$
E_{DFT}^{i}	DFT total energy of the pure phase of atomic species i

TABLE OF CONTENTS

LIST OF FIGURES

LIST OF TABLES

Chapter 1 **Introduction and Background**

1.1 Overview

The world is becoming ‘smarter’, technology is rapidly evolving and in the process, various sorts of portable electronic devices that aim to conveniently improve people’s lives are continually produced. These devices include smartphones, camcorders, portable digital assistants (PDAs), digital navigators, portable computers, smartwatches and virtual reality (VR) headsets. The roles they play are desirable; nonetheless, they remain coupled with the ever-increasing demand for portable energy. To meet the portable energy demand, research based on the development of rechargeable lithium-ion (Li-ion) batteries is being conducted since they have been identified to serve as good sources of portable energy [1].

In addition to the massive presence of portable devices, there is a progressive increase in oil and fuel costs as well as the need to reduce air pollution. This observation is inspiring research interest towards the development of non-traditional motor vehicles such as hybrid electric vehicles (HEVs), electric vehicles (EVs), as well as plug-in hybrid electric vehicles (PHEVs) [2]. The good performance of Li-ion batteries in portable electric devices makes them the potential candidate for serving as the electrical energy source in the new vehicle designs. However, existing Li-ion technologies are reported to be inadequate for meeting the high charge-discharge rate capability requirements found in these vehicles [3].

Since the demand for high-performance batteries exceeds capabilities of current Li-ion technologies, electrode materials with superior properties, low production costs and sustainable performance must be developed. In this work, a combination of various techniques is used to formulate a computer simulation workflow that could be used to deliver value that is relevant for finding energy storage solutions within the era of the fourth industrial revolution (4IR) [4 – 6]. The workflow is used to study models based on the lithium-silicon (Li-Si) system. These lithium silicide models are used to simulate the properties of active materials in high energy density battery electrodes. The Li-Si systems serve as negative electrode materials in Li-ion batteries. The focus will be on their electronic, structural and thermal properties.

Insights generated from the Li-Si systems are used to probe into other metal alloys such as those in the Na-Si system.

1.2 Structural Aspects for the Li-Si and Na-Si systems

This section presents the structural aspects of the models used in this work as depicted by figures 1-1 and 1-2 for the Li-Si and Na-Si systems respectively.

1.2.1 Structural properties of Li-Si systems used in the development and validation of Li-Si SCC-DFTB parameters

The binary phase diagram as reported by Okamoto [7] presents four crystalline lithium-silicon systems which are given as the face-centered cubic $Li_{22}Si_5$, orthorhombic $Li_{13}Si_4$, rhombohedral Li_7Si_3 and orthorhombic $Li_{12}Si_7$.

LiSi

Lithium monosilicide, LiSi, a silicide with a crystal structure that belongs to the space group *I41/a*, had often been excluded from the reporting of binary compounds already known in the Li-Si system. It was shown by Evers *et al* [8] in the first successful synthesis of LiSi that this compound remains stable to 470^{o}C, beyond which it decomposes to $Li_{12}Si_7$ + Si. Stearns *et al* [9] later reported a successful synthesis in which the formation of LiSi was achieved in good yields at pressures of 1 – 2.5 GPa, at temperatures between 500^{o}C and 700^{o}C. The crystalline structure of LiSi has a tetragonal geometry with its lattice parameters as ***a***=9.354 Å and ***c***=5.746 Å. LiSi was found not to be isostructural with other alkali monosilicides. It is comprised of a 3-dimensional network of 3-coordinated Si anions. The Si-Si bond forms puckered 8-membered rings that are linked together into interpenetrating sheets. The Si sheets have cavities that consist of Li^+ ions arranged in groupings that appear tetrahedral in geometry.

$Li_{21}Si_5$ and $Li_{22}Si_5$

The most lithium-rich phase is the $Li_{21}Si_5$ and is often reported as $Li_{22}Si_5$ in literature [10]. The $Li_{21}Si_5$ unit cell contains 16 cluster M_{26} formed by 4 + 4 + 6 + 12 atoms which belong to an inner tetrahedron, an outer tetrahedron, an octahedron and a cube-octahedron respectively [11]. $Li_{21}Si_5$ has a cubic crystal structure, a space group of *F-43m* and a lattice constant of 18.71 Å [12]. The primitive cell of $Li_{22}Si_5$ with a space group *F23m* consists of 16 coordinates of lithium and 4 coordinates of silicon. The $Li_{22}Si_5$ system has a lattice constant of 18.75 Å. This system is

commonly associated with a high energy density that is desirable for application in rechargeable lithium-ion batteries.

$Li_{13}Si_4$

As published by Frank *et al* [13], the orthorhombic crystal system of $Li_{13}Si_4$ with the space group *Pbam* contains only two different layers of atoms in the *ab* plane. One layer is constituted of silicon dimers and the other single silicon atoms. These layers are surrounded by 12 lithium atoms. The lattice parameters in this crystalline system are ***a***=7.99 Å, ***b***=15.21 Å and ***c***=4.43 Å.

$Li_{12}Si_7$

The $Li_{12}Si_7$ system with space group *Pnma*, being the lowest-lithium containing binary phase, has a crystal structure described by 5-membered Si_5. The silicon rings are charge compensated by six lithium atoms existing in a form of staggered Li_5 rings with an extra Li in the center (Li_6Si_5 unit). The system also has intertwined chains of Si_4 stars $Si(Si)_3$ that are Y-shaped in a plane, which is charge compensated by a cloud of 12 lithium ions around them ($Li_{12}Si_4$ unit). The lattice parameters for $Li_{12}Si_7$ are ***a***=8.60 Å, ***b***=19.77 Å, and ***c***=14.34 Å [14] .

Li_7Si_3

The Li_7Si_3 with space group classification *P3212* is the only phase known to have some of its sites with partial occupancy. All Si atoms in Li_7Si_3 are members of six dumbells. The crystalline Li_7Si_3 structure has a hexagonal symmetry with its lattice parameters as ***a***=7.629 Å and ***c***=18.009 Å [15].

$Li_{15}Si_4$

These lithium silicides generally exist as high-temperature phases in ranges within 400 – 500 ^{0}C. However, upon electrochemical lithiation at room temperature, silicon undergoes a crystalline to amorphous transition and then recrystallises to form a metastable phase $Li_{15}Si_4$ [16]. The $Li_{15}Si_4$ crystalline system has the space group of *I-43d* and is formed by a series of unit figures in which six Li atoms surround a Si atom with two Li-Si bond lengths of 2.62 Å and 2.72 Å. $Li_{15}Si_4$ has a cubic geometry with a lattice constant of 10.685 Å [17].

For this study, we shall consider seven lithium silicides whose structural representations are presented in Figure 1-1.

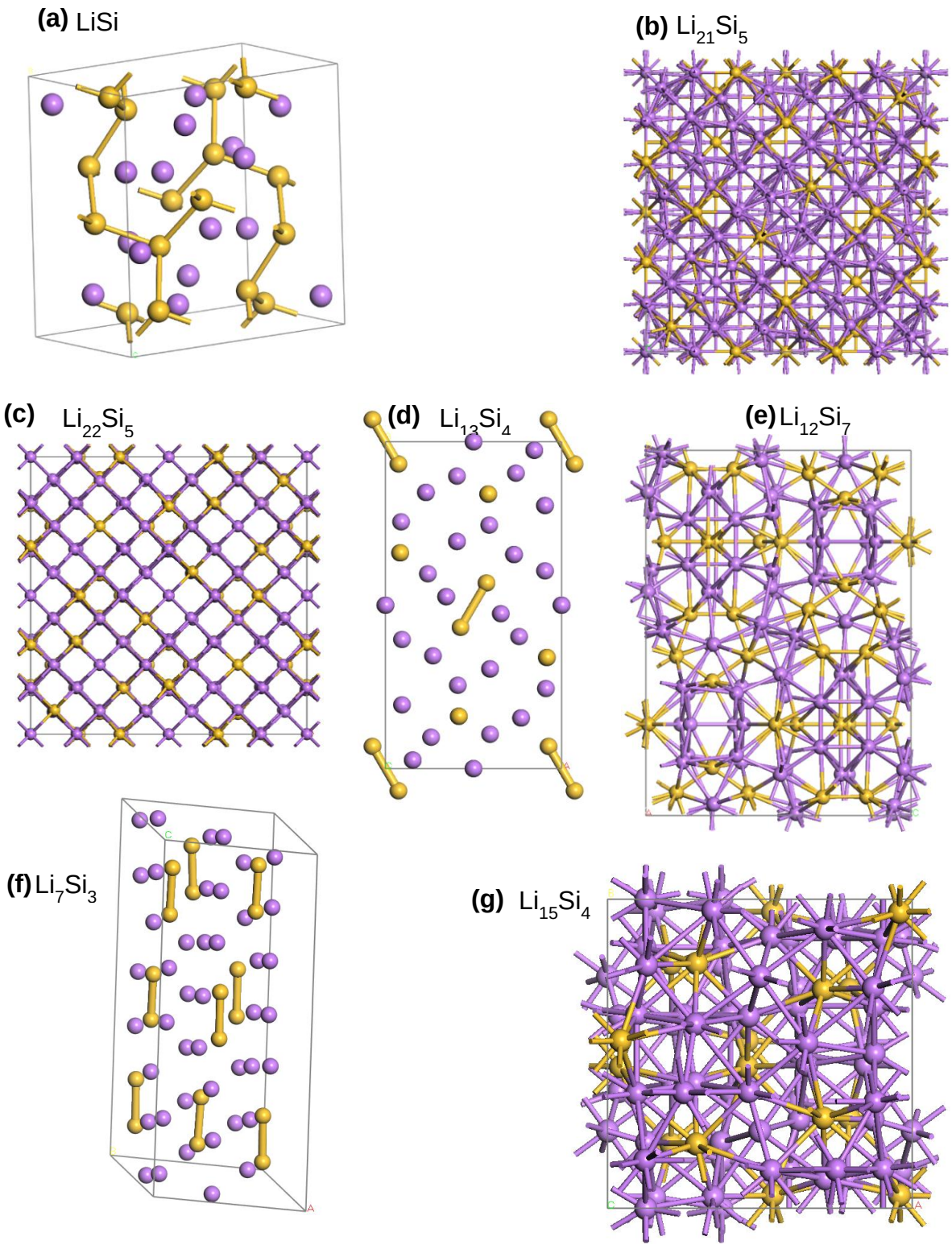

Figure 1-1. The structural illustration of binary phases present in the Li-Si system: (a) LiSi (*I41/a*), (b) $Li_{21}Si_5$ (*F-43m*), (c) $Li_{22}Si_5$ (*F23*), (d) $Li_{13}Si_4$ (*Pbam*), (e) $Li_{12}Si_7$ (*Pnma*), (f) Li_7Si_3 (*P3212*) and (g) $Li_{15}Si_4$ (*I-43D*). The lithium and silicon atoms are shown in purple and yellow colours respectively.

1.2.2 Structural properties of Na-Si systems used in the development and validation of Na-Si SCC-DFTB parameters

Na and Si

The Na system has body-centred cubic crystal structure whereas the Si has a face-centred cubic crystal structure. These systems belong to the *Im-3m* and *Fd-3m* space groups respectively. The reference experimental lattice parameter of Na is 4.29 Å [18] whereas that of Si is 5.43 Å [19]. The primary cells of the Na and Si systems consist of 2 and 8 atoms respectively.

NaSi

NaSi has a monoclinic crystal structure with lattice parameters ***a*** = 12.19 Å, ***b*** = 6.55.87 Å and ***c*** = 11.18 Å. NaSi belongs to the *C2/c* space group [20]. The lattice angles are such that γ = α = 64^0, whereas β = 119^0. This lithium-silicon system is characterised by isolated Si_4^{4-} tetrahedral that are surrounded by Na^+ ions [21].

$NaSi_6$

The $NaSi_6$ has an orthorhombic crystal structure and lattice parameters ***a*** = 4.106 Å, ***b*** = 10.563 Å and ***c*** = 12.243 Å, and belongs to the *cmcm* space group. $NaSi_6$ is a clathrate compound that is comprised of Si tunnels that are intercalated with Na atoms in the a-axis [22].

Na_3Si_{17}

The sodium-silicon clathrate Na_3Si_{17} commonly known as $Na_{24}Si_{136}$ has a cubic crystal structure belonging to the *Fd-3m* space group, and a lattice parameter of the value 14.716 Å. This compound in comprised of 16 smaller and 8 larger cages. The smaller cages are formed by 12 pentagonal faces whilst the larger cages are formed by 12 pentagonal and 4 hexagonal faces [23].

Na_4Si_{23}

Na_4Si_{23} also known as Na_8Si_{46}, has a cubic crystal structure that belongs to the *Pm-3n* space group, and has a lattice parameter of the value 10.2 Å. This clathrate compound is characterised by 2 smaller cages formed by 12 pentagonal faces and 6 larger cages formed by 12 pentagonal and 2 hexagonal faces. The primary unit cell consists of 46 Si atoms [24].

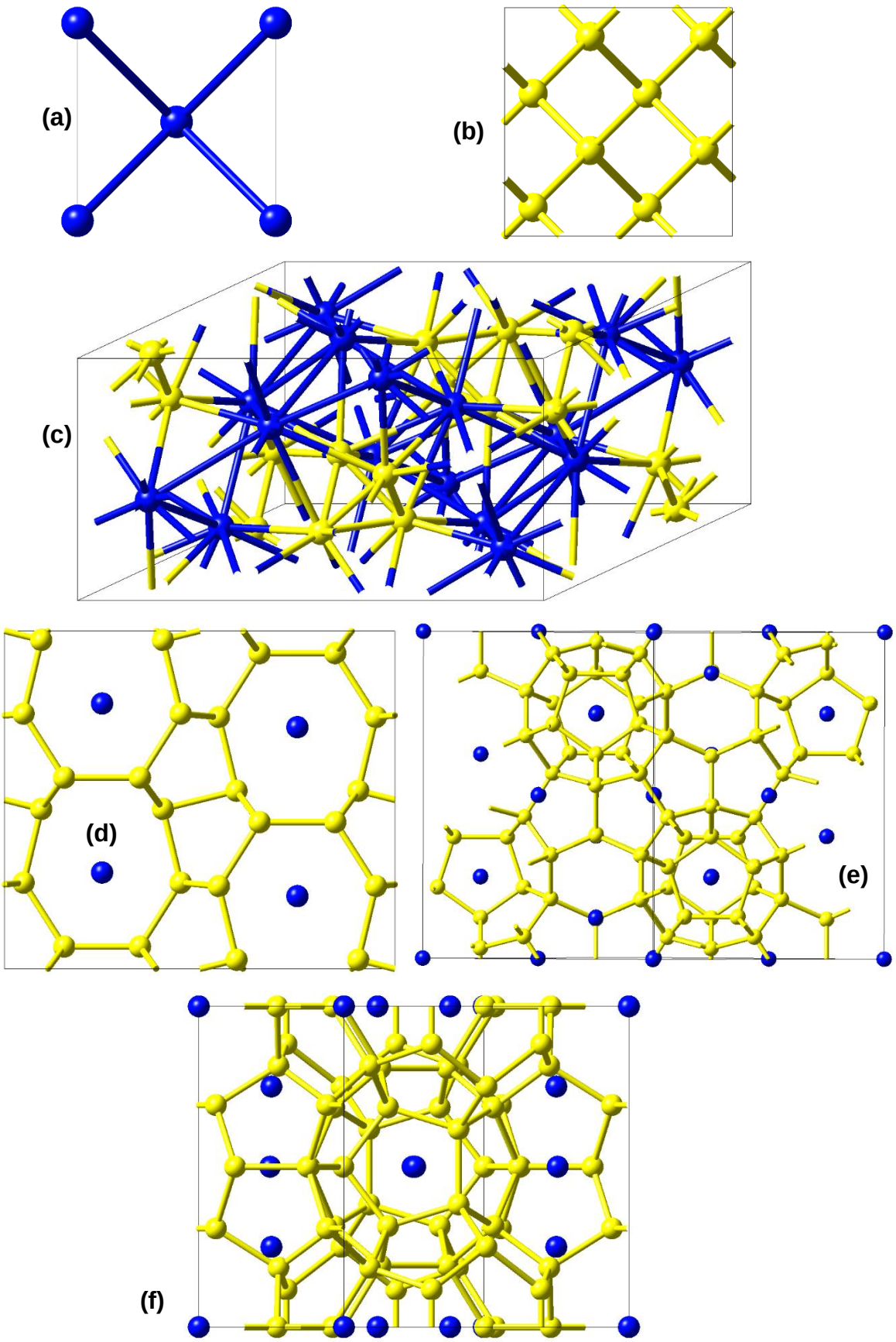

Figure 1-2. A structural presentation of the systems used in the development of Na-Si SCC-DFTB parameters. (a) Na (*Im-3m*), (b) Si (*Fd-3m*), (c) NaSi (*C2/c*), (d) $NaSi_6$ (*cmcm*), (e) Na_3Si_{17}, and (f) Na_4Si_{23} (*Pm-3n*).

1.3 Computational Modelling and Materials Research

The arena of scientific investigation presents two well-known approaches, namely the theoretical and the experimental approach. Many phenomena have been successfully studied using techniques offered by these approaches. Over the years, a third approach known as computational modelling has emerged. Computational modelling employs computer resources wherein systems are modelled or simulated in reference to their physical forms using computer programs [25]. This approach does not seek to eliminate the importance of the former two approaches, but aims to complement efforts towards efficacy. The approach combines insights and fundamental knowledge from theory, whilst making use of experimental determinations as validation.

Owing to the rapid growth in computational power [26], materials research is advancing in the ability to investigate a wider range of material systems. This makes it possible for predicting structures and material properties; as well as explaining phenomena that are not so facile through experimental techniques.

The ambit of scientific techniques available within materials research is quite broad [27]. This is because materials can be modelled as per requirement, usually by relative size. Material sizes can vary from small scales such as at the level of the width of a hair strand measured in nanometres, to larger scales such as in rocks with surface areas that span over meters.

Within computational modelling, material structures are often characterized by signatures presented by their electronic or atomic behaviour. This quality allows research approaches to spread over an array of disciplines ranging from Physics through but not limited to Engineering [28].

The levels of investigations are usually classified as being electronic, classical, microstructural or continuum in nature. The extent of applicability can be illustrated hierarchically as shown in Figure 1-3; the choice of which technique to apply is usually motivated by the aim of the investigation.

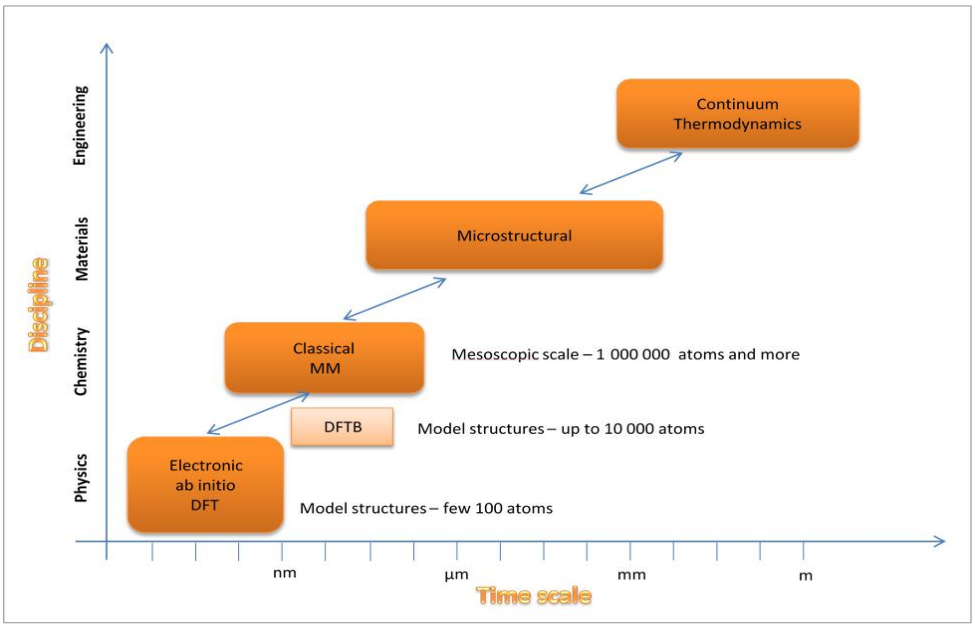

Figure 1-3. Schematic presentation of the hierarchies of modelling in materials research

The density functional theory (DFT) based technique is commonly applied in physics and is usually limited to simulations of electronic and structural properties for systems consisting of a few 100 atoms. Beyond which, classical techniques such as molecular modelling (MM), become more suitable for the larger systems, whose structures may consist of up to 1 000 000 atoms or possibly more. In some instances, the electronic and physical behaviour of large systems can simultaneously be important for consideration; however, for these techniques, it is either very difficult, computationally expensive or even impossible to predict one property without a compromise of the other.

Density functional-based tight-binding (DFTB) has emerged as an approach that is equipped with the flexibility of investigating electronic behaviour and structural aspects of large systems, which may contain up to 10 thousands of atoms. DFTB inherits the accuracy of DFT in predicting electronic properties, whilst exhibiting the ability to handle large systems usually studied through classical techniques [29]. This technique makes it possible to examine structural, electronic and thermal properties of large systems with minimised computational cost, and minimised number of required fitting parameters. The DFTB approach is employed in this work by studying candidate negative electrode materials. Its ability to bridge the gap between DFT and MM based techniques is demonstrated.

1.4 The 4th Industrial Revolution (4IR)

The human civilization experienced transformations that revolutionized how people live, work and play. It was in wake of the 19th century that societies saw the emergence of a new form of economic structuring that was driven by industrialization. The shift from an agricultural to an industrial economy constituted what was is referred to as the 1st industrial revolution. In that era, heat energy was used as the core that made mechanization of production to be possible. As such, the 1st industrial revolution is characterized by mechanical steam engines [4].

Towards the end of the 19th century, new forms of energy such as oil, gas and electricity took stage. The discovery of these forms of energy led to the development of telephonic systems, cars and airplanes; these characterized what is referred to as the 2nd industrial revolution. Later around mid of the 20th century, the 3rd revolution occurred. It was in the 3rd industrial revolution that success in nuclear energy led to the rise of electronics and computers [5].

Presently societies are experiencing the 4th industrial revolution (4IR) also referred to as 'industry 4.0'. This revolution is characterized by developments that integrate the internet, cyber-physical systems and intelligent automation [6]. Themes of the 4IR include but not limited to: the internet of things (IoT), big data, artificial intelligence (AI), data analytics, cloud computing, augmented reality, supercomputing, and simulations.

Research in the 4IR has led to trends that integrate disciplines. Computer scientists, engineers, computational materials scientists are now using similar technologies for research. I.e. Simulations are now making use of machine learning, deep learning, supercomputing, which are largely thought of as computer science topics.

Today, even non-scientists are large consumers of IoT and machine learning. People are using smartwatches, smartphones, smart cars, virtual reality headsets, home automation systems, *etc*. Interestingly, many of our day-to-day activities make use of machine learning. This includes image processing and recognition, speech recognition technology, fraud detection, insurance policy administration, credit scoring, email filters, web searches and weather prediction to cite a few. The successful application of machine learning in these areas suggests that many more developments are yet to be witnessed.

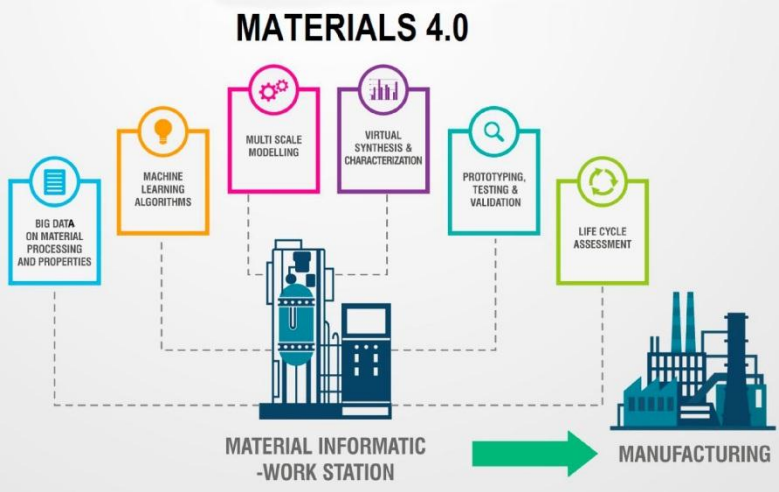

Figure 1-4. The concept of 'Materials 4.0' [30]

Jose et *al* [30] proposed what they call 'Materials 4.0', depicted by Figure 1-4 in which the primary resource is data. Analogous to industry revolutions, in their work they also presented the evolution of materials research. This shows that in the era of 4IR, some level of familiarity with topics such as supercomputing, artificial intelligence, machine learning, deep learning can be quite useful for researchers in computational materials science.

1.5 Supercomputing

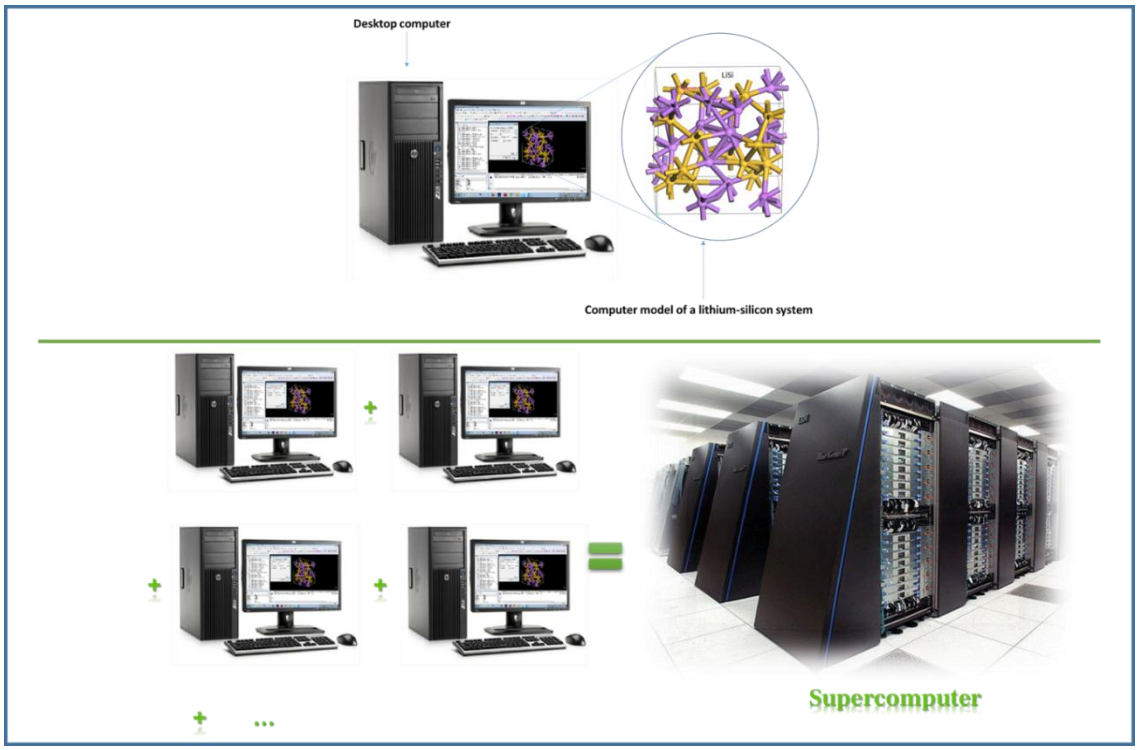

Figure 1-5. A simplified schematic presentation of the concept of a supercomputer: a computer with high-level performance and computing capacity compared to a general-purpose desktop computer or laptop.

The mention of a supercomputer to many people often gives the idea of a hypothetic computer similar to a desktop computer, but perhaps with a very large physical design. Although the thinking is size is not entirely wrong, supercomputers are not fictional but are physically existent. In essence, as suggested by Figure 1-5, a supercomputer can be thought of as an aggregated system of computing units (hardware and software) that are configured to operate as one. As such, a supercomputer refers to a computer with high-level performance and computing capacity compared to a general-purpose desktop computer or laptop. Supercomputing, therefore, refers to the use of supercomputers to process very large data or complex systems to address problems or explore opportunities and predict solutions in a fast and accurate manner [31]. A standard computer usually cannot be able to achieve the capacities of a supercomputer unless when coupled to other computers.

The term ‘supercomputing’ is commonly used interchangeably to ‘high-performance computing’ (HPC). HPC has been used across many domains; from physics, bioinformatics, medicine, security, space science, engineering, and economics, *etc*. HPC as a field encompasses technology, methodologies and applications that are usually associated with high computing capabilities. A detailed discussion on the field of HPC can be quite expansive [32]; therefore with respect to the scope of the work entailed herein, it is not presented. As a tool, HPC enables inquiry into new paths of research and it provides avenues to the development of new techniques and design methods. Within the theme of energy storage, processes of designing new materials usually entail iterative synthesis and characterisation techniques applied to a broad range of materials. The procedures are traditionally carried out in a laboratory and can take a long time before large scale manufacturing can be effected, as many trials are usually required. HPC puts into perspective a new dimension in that it allows the discovery processes to be carried out in what can be referred to as a ‘virtual laboratory’ [33]. In this ‘virtual laboratory’ computer simulations are used to model materials properties and reactions. HPC heavily relies on parallel programs (*i.e.* programs that can spread a computational problem over a cluster of computers and simultaneously solve it) that scale to compute solutions. Many models, databases and algorithms have in turn been developed and are found in domains including computational materials science, artificial intelligence, machine

learning and deep learning. These advancements make it possible for the 'virtual laboratory' to span various material length-scales, thus accelerating the design and discovery of new materials as well [34].

1.6 Artificial Intelligence, Machine Learning, and Deep Learning

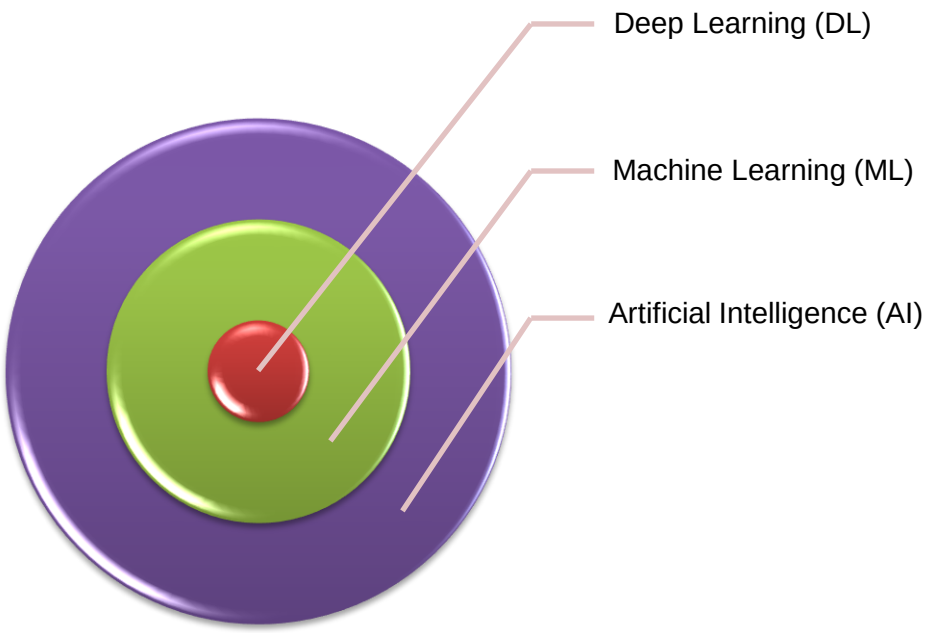

Figure 1-6. Schematic illustration of the relationship between artificial intelligence, machine learning, and deep learning.

To briefly discuss the relationship between artificial intelligence (AI), machine learning (ML) and deep learning (DL) as well as how it relates to the work herein, we perhaps should begin with basic definitions.

AI can be defined as the branch of computer science that is concerned with the automation of intelligent behaviour. As such, it is a field of study that is focused on using a computer to do tasks that require human-level intelligence. As shown in Figure 1-6, it consists of subdomains including machine learning and deep learning. It has been around since the '50s but was limited in practical applications.

On one hand, ML as a subdomain of AI, is primarily an approach to AI that makes use of statistical techniques to build a model from observed data. It generally relies on human-defined classifiers or "feature extractors" that can be as basic as a linear regression. ML gives computers the ability to learn without being explicitly programmed.

DL, on the other hand, can be regarded as a subdomain of ML. DL is an ML technique that automates the construction of feature extractors using large amounts of data to train complex “deep neural networks”, which are electrically analogous to the biological nervous systems. Deep neural networks (DNNs) are capable of attaining human-level correctness for numerous tasks, but require enormous computational resources to train. It is necessary to note that deep learning is more useful for large problems using a tremendous amount of parameter sets. The deep learning approach is to teach the computer rules for performing the task directly from data. This is done by simply providing a DNN with thousands of examples and thus training it how to perform a given task.

In this work, ML is employed; therefore we expand a bit more on the background in ML.

The basic concept of Machine Learning is to use example data or experience to solve a given problem. According to Mitchell [35], a formal expression of machine learning can be stated as follows: “A computer program is said to learn from experience E with respect to some class tasks T and performance measure P, if its performance at tasks in T, as measured by P, improves with experience E.”

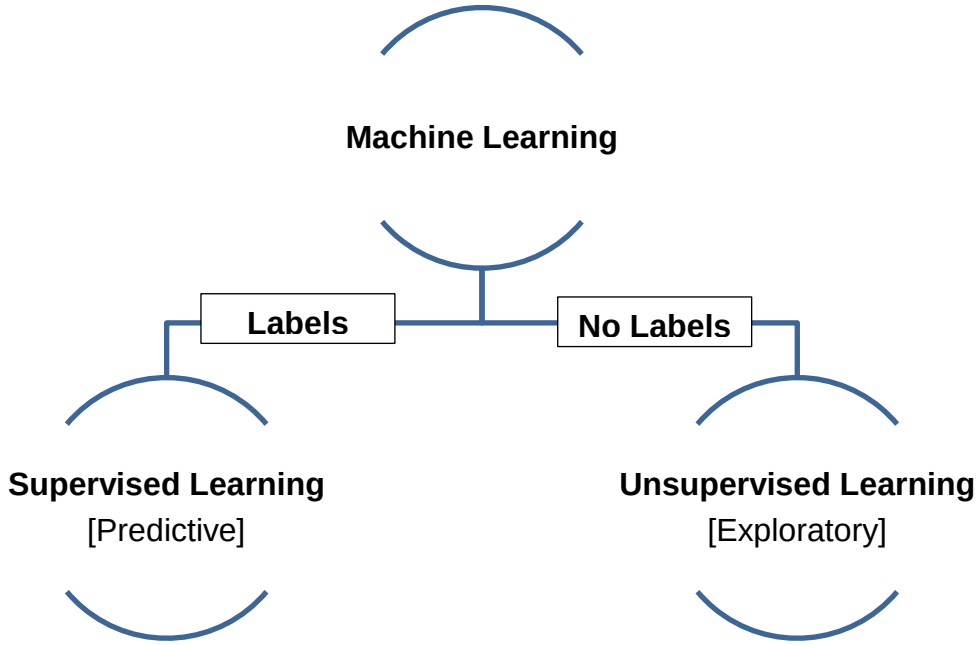

Figure 1-7. Illustration of two main categories of machine learning.

As depicted in Figure 1-7, ML can be broadly classified into two main categories: (i) supervised learning and (ii) unsupervised learning. Supervised learning makes use

of labels and can be regarded as a predictive technique. It deals with the mapping between inputs and output using correct values to “train” a model. Supervised learning is used when aiming to predict unknown answers from known answers. In supervised learning, data is divided into two parts: the data used to “teach” the system (data set), and the data used to evaluate the accuracy (test set) of the computer algorithms.

Unsupervised learning does not require labels and is regarded as an exploratory technique. It is used when you want to find unknown answers, mostly groupings obtained directly from data. In unsupervised learning, there is no single way to evaluate the accuracy of what you learn.

It should be noted that machine learning is not a single discipline approach, but spans a collection of areas including but not limited to information theory, computer science, neuroscience, statistics and physics. In this work, the supervised form of machine learning is used through genetic algorithms embedded in the cluster expansion technique to predict stable Li-Si, Na-Si and Mg-Si alloys.

1.7 The Convergence of Machine Learning and Computational Materials Science

The developments and design of new materials have been largely driven by experiments. In designing these materials, experiments generally involve measurements of microstructures, property analysis, and synthesis processes, which have high requirements with regard to equipment, experimental environment and the expertise of the researchers. This, therefore, translates to a long journey before new materials can be deployed. However, computer simulations employing already well-established theories together with the growing power of computing capacities help guide experiments and in turn reduce costs as well as time for finding new materials [36].

In the pursuit to find new materials solutions, the exploration for high-performance materials is impossible without probing through vast compositions and enormous structure space, because there is a lot of data that is consequently involved. As a result, structure prediction based on composition is one of the key challenges in materials science. However, ML has been proposed as an alternative to deal with

this limitation, and recently it has sparked a strong interest for application in computational materials science [36 – 39].

One of the qualities of interest in the application of ML is its ability to produce accurate results in a fairly short space of time. There have been several reports in which successful models and frameworks have been proposed for application in materials science.

Examples include the work by Möller *et al* [40] in which ML was used for compositional optimization to identify chemical compositions that exhibit good magnetic properties whilst consisting of few rare-earth elements. Jung *et al* [41] demonstrated an interesting use of an ML technique, Gaussian process regression (GPR), to establish accurate structure-property linkages across a microstructure database composed of synthetic microstructures in excess of 1100 by only evaluating a small fraction of the entire microstructure database. Cecen *et al* [42] illustrated the use of convolutional neural networks in the design and exploration of 3-D microstructure analytics and the extraction of robust structure-property linkages. Wen *et al* [43] proposed a property-oriented materials design strategy that combines ML with design of experiments and feedback from experiments to search for high-entropy alloys that exhibit large hardness. Using the Li_xSi alloy as a case study, Artrith *et al* [44] presented an approach for calculating *ab-initio* phase diagrams of amorphous materials through a sampling technique powered by machine learning.

The growth in successful frameworks, models, algorithms and pipelined techniques, shows that the convergence of machine learning with computational materials science promises to unblock new design strategies and accelerate the development as well as the deployment of high-performance materials. Hence, the use of techniques such as cluster expansion, which employ machine-learning-based algorithms can positively aid efforts directed toward discovering new electrode materials as well.

1.8 Cluster Expansion

Cluster expansion (CE) is an approximate computational method that was proposed by Mayer *et al* [45] around 1941, which expresses the partition function as power series expansion. In computational materials science, cluster expansion is often applied to pipeline models of calculations by serving as a joint that combines first-principle (DFT) calculations with Monte Carlo (MC) simulations, to predict materials properties [46]. CE combines quantum mechanics and statistical physics based on electronic structure density functional theory, which can independently establish the range, type and chemical character of interaction energies. CE also unblocks the pathway to huge parameter space studies such as ground state searches and microstructural systems comprised of millions of atoms. It makes it possible to treat materials with sizes that range from a few atoms up to millions without compromising the accuracy of current DFT calculations, and when combined with MC simulations, it permits research aiming at addressing problems associated to alloy formation, phase stabilities, and geometric structure to be conducted without the need for empirical input data, whilst giving access to accurate quantitative comparison with experimental data [47]. Cluster expansion employs one of the algorithms in machine learning, the genetic algorithm to conduct crystal structure predictions.

In this work, artificial intelligence through machine learning embedded within cluster expansion, is employed to search for stable configurations necessary for the alloying of Li-Si. The initial basis is to sample a concentration regime that produces stable Li-Si alloys, which are validated against other known phases as proposed by experiments or intelligence-based predictive simulation techniques. Then, additional sampling involving Na-Si and Mg-Si is done to use CE as a tool to predict and identify stable alloy compositions of these systems. The outcome helps experiments to probe into new areas and help advance the design of new energy storage materials alternative to existing Li-based technologies.

1.9 Literature Review

Since the successful Li-ion battery development introduced by Sony in the 1990s [48], a significant amount of research has been focused on the electrochemical performance and design of advanced electrode materials for rechargeable Li-ion batteries [49]. Several factors affect battery performance; hence, the ability to model and study batteries using computers becomes an important tool that could be employed amongst efforts aimed at improving their performance. The factors include electrode material synthesis mechanisms, battery cell design, packaging strategies, cycle life, state of charge (SOC) effects, depth of discharge (DOD) effects, rate of recharging and temperature [50 – 52]. Amongst these factors, temperature is one of the major factors that significantly affect battery life span and voltage control. It has been illustrated that higher temperatures dramatically affect electrode materials [53]. As a result, the capacity of a battery becomes lower when the surrounding temperature is very low. The other crucial factor towards battery performance is the electrochemistry of materials used (*viz*. electrochemistry of cathode and anode active materials, electrolytes, binder, collectors, *etc*.) [54]. The electrochemistry prompts scrutiny into what research has yielded and reported in the available literature.

1.9.1 Negative electrode materials

A Li-ion battery generally uses a carbonaceous compound such as graphite, coke, pyrolytic carbon, graphene, carbon nanotubes, *etc.*, as the active material in the anode [55]. The primary motivation for the choice of carbonaceous materials is usually their low cost and low operational voltage. The carbonaceous anode is commonly coupled with a high voltage cathode, such as $LiCoO_2$, to obtain a battery that operates in the 4 V plateau. During lithium intercalation in the graphitisable carbons, anodes reversibly undergo stages corresponding to progressive intercalation within discrete graphene layers, to reach the formation of LiC_6, with a maximum theoretical capacity of 372 $mAhg^{-1}$ [56].

The drawback with the graphitic anode is that it has low energy density, safety issues related to lithium deposition and a significant irreversible capacity loss after one cycle [57]. To resolve the safety issues commonly associated with graphite anodes, the spinel $Li_4Ti_5O_{12}$ system has been identified amongst candidate anode materials considered for application in high power batteries for HEVs [58]. One of its

most important properties is that its lattice parameters are almost unchanged when lithium ions are inserted/de-inserted. However, $Li_4Ti_5O_{12}$ also suffers from poor rate capability due to low electronic conductivity.

Alloy anode materials such as $Li_{22}Si_5$, with high theoretical capacity, long cycle life, better safety, and low cost, have been considered as the most promising alternatives. The central challenge for the employment of such anodes is their deleterious volume expansion (~300%) during lithiation and delithiation [59]. Because of the expansion in volume, the electrodes suffer cracking and crumbling, and consequently lose inter-particle contact, resulting in capacity fade [60].

1.9.2 Strategies adopted for improving electrode performance

Several strategies that attempt to improve the cycling stability, rate capability, and energy storage capacity of electrode materials, are continually developed. Part of the motive to the developments is to reduce the associated detrimental effects. Some of the strategies are discussed as follows:

1.9.2.1 Microstructured electrodes

Charge-discharge processes occurring in batteries involve electronic and ionic flow as well as their spatial relationships to conductivity in multiple phases and interfacial contact potential. Stress distributions arising as a result of concentration-induced strains and resistive heating significantly affect battery performance [61]. These processes essentially depend on the structure, size, and spatial distribution of electrolyte and active material phases. Furthermore, modelling the galvanostatic cycling of rechargeable battery provides valuable insight into optimising the performance of electric-based applications. Thus, an analysis that simultaneously resolves the microstructural details includes the non-linearities and history from successive charge-discharge cycles can be quite useful for improving cell design [62]. It is, therefore, believed that the incorporation of microstructure into battery models can provide design criteria for improved battery performance [63].

1.9.2.2 Nanostructured electrodes

Materials in the nanoscale are commonly linked to impressive mechanical, electrical and optical properties. As a result of confining the dimensions, and overall behaviours of nanostructured materials, combinations of bulk and surface properties have been successfully exhibited [64]. The application of nanostructured electrode

materials has significantly improved the Li-ion intercalation capability, such as cyclic stability, storage capacity, and interaction rates [65]. Nanostructured electrodes meet the liquid/solid interface reaction characteristic of Li-ion intercalation, large surface area and short Li-ion diffusion path requirements in battery material. Consequently, they are regarded to be highly favourable as intercalation hosts instead of bulk electrodes consisting of micrometer-sized particles. Nonetheless, it is noteworthy that nano-sized particles may portray disadvantages such as high costs for manufacturing and exhibit handling difficulties. The large surface areas in nanostructures has also been reported to increase the side-reactions and solid-electrolyte interface (SEI) formation, which may result with poor cycling-life, self-discharge and a shortened calendar life [60].

1.9.2.3 Porous structured materials

The design of porous structured materials with porosity that is sufficient to accommodate the large volume expansion arising during charge-discharge processes is also a promising strategy [66]. Porous materials have several advantages for use in Li-ion battery electrodes. These include the provision of (i) a porous surface area, which provides a large contact area between the active material and the electrolyte; (ii) a continuous network, that is expected to improve electrical conductivity; (iii) abundant pores which can aid in buffering the large volume changes attributed to disintegration of the structure; and (iv) suitable microporous structures that may block the re-aggregation of very fine particles. Consequently, such materials can show enhanced cycling performance, improvement of reversible capacity, and elevated rate capability.

1.9.2.4 Carbon-based composites

Owing to their high electronic conductivity, and the rich functional surface chemistry, carbon-based materials are regarded as a key component of electrodes. Great research attention has also been devoted to the development of electrodes with advanced architectures using nanostructured carbon materials (*e.g.* carbon nanotubes and nanofibres, *etc.*), in contrast to the conventional carbon materials based on graphite, shiny carbon, and carbon black [67]. Wang and Kumta [68] reported the use of nanocomposites comprised of Si, C and single-walled carbon nanotubes as anode materials for Li-ion batteries, which showed cycling stability of ~900 $mAhg^{-1}$. Nevertheless, the beneficial effects of adding carbon and/or coating

with carbon have been widely recorded in several studies [69 – 73]. The coating Si particles with carbon, was understood to suppress the SEI layer formations [74]. In addition, it has also been proposed that coating with carbon exerts compressive stress on the active particles, which acts as a buffering mechanism against particle volume expansion during Li insertion, and thus restrict the pulverisation of the particles [75].

1.9.2.5 Multiphase composites

The primary motivation for using composite materials is that the host matrix could be used to cushion the huge volume change of the dispersed active particles so that the integrity of the electrode and the electronic contact between the active particle and conductive phase can be sustained [76]. Consequently, the host matrix must permit rapid electron and Li-ion transportation, and also uphold the microstructural stability of the entire electrode. The host matrix aids the reduction of mechanical stress in the electrode by decreasing the active particle aggregation during cycling [77]. It has been widely recounted that the increased amounts of host phases enhance the cycling stability of the anode but reduce specific capacity [78]. To circumvent this problem, the host matrix must possess good electronic and ionic conductivities, as well as suitable mechanical strength. That is to say, the matrix must have the capacity to tolerate high stress with a huge elastic deformation when the active particles expand during lithiation.

1.9.2.6 Selecting appropriate binder and electrolyte systems

The choice of binder and electrolyte is also crucial in mitigating the problem of the enormous capacity fade noted with cycling for Sn, Si, and transition metal oxide anode materials. The binder commonly used for graphite and alloy anodes is polyvinylidene fluoride (PVDF), which is a thermoplastic material with poor elastomeric properties. The poor elastomeric property of PVDF makes it reasonable to expect that an alternative elastomeric binder may have a better ability to accommodate the large volume change of alloy particles than PVDF. However, the idea was contested by the observation that the stiff and brittle polymer, known as sodium carboxymethyl cellulose (Na-CMC) binder was even more effective in improving the capacity retention of Si anode than the PVDF [79]. CMC binder can also improve the cycling performance of iron-based materials [80]. It was suggested that the CMC binder may act as a surface modifier that promotes the formation of a

stable SEI passive layer, while the extended conformation of CMC in solution leads to a more homogeneous dispersion and networking of the conductive carbon and active particles [81]. Thus, selecting an appropriate binder system, electrolyte together with an organic solvent, conducting salt and additives, can improve the electrode performance and enhance its cyclability.

1.9.2.7 Controlling particle size and operating voltage

The use of smaller particle size has been reported to decrease the electronic and ionic transport distance, and reduces the stress or strain induced by inhomogeneous Li diffusion [82]. The high density of grain boundaries in nanocomposites also provides a fast diffusion path for Li-ions and acts as additional Li storage sites [68].

As for the operating voltage, alloyed anodes have been observed to demonstrate better cycling life when cycled within a constrained voltage range as compared to the full voltage range. Jung *et al.* [83] illustrated an improved cycle life of an amorphous Si anode from 20 to 400 cycles by altering the lower cutoff voltage from 0.0 to 0.2 V. Obrovac and Christensen [84] suggested that a lithiated amorphous Si is suddenly transformed into crystalline $Li_{15}Si_4$ below 50 mV, resulting in high internal stress and capacity fade. Shu *et al.* [85] studied various over-discharge behaviours of $LiFePO_4$, $LiNiO_2$, and $LiMn_2O_4$ down to 1.0 and 0.0 V, and found that $LiFePO_4$ and $LiMn_2O_4$ cathode materials illustrate higher structural stability than that of $LiNiO_2$ in 1.0 – 4.3 V. All the three cathode materials experienced solid-state amorphisation when they were cycled between 0.0 and 4.3 V. Such studies, therefore, suggest that cycling stability can be improved by limiting either the lower or upper cutoff voltage, which in essence reduces the amount by which volume changes, the aggregation tendency of the particle, and the degree of structural change. However, the limitation of voltage control is that it may reduce electrode capacity.

1.9.2.8 Using thin films and amorphous alloys

Thin-film anodes are commonly prepared by magnetron sputtering or physical vapor deposition, and most thin-films prepared to date are amorphous [86]. Takamura *et al.* [87] reported that an amorphous Si thin film vacuum deposited 50 nm thick on a Ni foil, showed a high specific capacity of over 2000 $mAhg^{-1}$ and better cyclability of over 1000 cycles at a charge rate of 12 C. The good capacity retention of thin-film anodes was ascribed to the strong adhesion of active material to the conductive

support. However, the cycle life was reduced drastically, when the film increased in thickness.

1.9.3 The need for alternative battery technology

1.9.3.1 Na-ion battery technology as a potential alternative

The availability of Li resources and the rising costs of producing Li is a growing concern. This prompts consideration into an alternative material for application in energy storage systems [88; 89]. As such, Na has received attention amongst the alternative of Li-based battery technology. Na batteries were originally researched parallel to Li batteries around the late 1970 - 1980s [90]. However, the success in Li batteries outnumbered those of Na batteries. As such the Na batteries have not been extensively studied.

1.9.3.2 Studies about candidate electrode materials for the Na-ion batteries

Although Na-ion batteries (NIBs) may exhibit similar storage mechanisms as Li-ion batteries (LIBs), certain electrode materials commonly used in LIBs such as graphite-based anodes cannot be used for the NIBs. Thus, appropriate anode materials with high performance are still required to promote the further development of NIBs. Lan *et al.* [91] used first-principles techniques to study the layered molybdenum dinitride (MoN_2) as a candidate anode for the NIBs. Their results predicted that a formula unit of the MoN_2 layer could accommodate 4 Na atoms and yield specific capacity of 864 $mAhg^{-1}$. As such, indicating this material as having potential for use in high-performance NIBs.

The interest in the development of sodium-ion battery technology has been reignited and few considerations have been presented in literature. Cue *et al* [92] reviewed the rational design of candidate anode materials for the Na-ion batteries. In their work a broad comparison was presented, of which the widely studied electrode materials were driven mainly from their lithium equivalents. Some materials known to possess limited electrochemical performance in Li-ion batteries were shown to exhibit better performance NIBs. For example, $Na_3V_2(PO_4)_3$ outperformed the $LiFePO_4$ as a cathode in NIBs. Their study predicted that NIBs can be greatly improved through investigating phosphorous and its alloys, Sn and Sb-oxides/sulphides as the choice of anode materials for the NIB.

Nejati *et al.* [93] conducted a DFT study that looked into the possibility of using nanostructured electrodes for the Na-ion batteries. Their focus was on the adsorption of Na and Na^+ on boron nitride nanotubes (BNNTs) composed of different diameters as well as boron nitride nanosheets. Their results suggested that BN nanosheets would be more appropriate than the BNNT for application in NIBs.

Edison *et al.* [94] studied the electrochemical performance of pristine $FeSn_2$ and $FeSn_2$-carbonaceous composites as candidate negative electrodes for the Na-ion batteries. They reported the composite to exhibit superior performance over the pristine $FeSn_2$.

1.9.3.3 The potential use of Si as an anode for the Na-ion batteries and effort for promoting the commercialisation of NIBs.

The energy density in the lithiated Si incites interest in exploring the use of Si as an anode material in Na-ion batteries. The DFT study by Jung *et al.* [95] showed that although crystalline Si is generally considered inappropriate for Na-ion batteries compared to other alloy type anode materials, the amorphous Si phase owing to its performance, may be the competitive candidate among the Na-ion battery anodes. The study reported that when Si is in amorphous state, it can host 0.76 Na atoms per Si atom. This composition corresponded to a specific capacity of $725 mAhg^{-1}$. Furthermore, the volume expansion of the amorphous $Na_{0.76}Si$ phase was found to be 114%.

Lim *et al.* [96] presented an experimental study that looked into the preparation of amorphous silicon as well as its electrochemical sodiation properties. Their findings suggested that the mechanical fusion of Si-Sn would yield the highest sodiation capacity of amorphous Si. The compositional/structural optimisation of the *a*-Si-Sn composite is still required.

Studies on the compositional effects of electrodes are necessary as well. Aladinli *et al.* [97] illustrated that optimising compositional electrode effects could improve the cyclic performance of a dual-ion battery. Furthermore, they indicated that more electrolyte and additive research remains necessary to restrain the irreversible losses to make the Na-based dual-ion cells feasible.

1.9.3.4 The approach used in this study

It is evident that several strategies aimed at improving the battery electrode performance are being employed; nevertheless, more insight is still needed to address many of the existing battery issues. In this work, computer simulations are used to study, design and model high energy density electrode materials for rechargeable batteries. Semi-empirical models will be developed using a density functional based tight-binding simulation code (*i.e.* DFTB+). Slater-Koster [98] (S-K) potentials of the Li-Si and Na-Si systems will be used to reproduce known structural details of these systems. Structural details of modelled systems would represent properties directly linked to the real materials. By fitting experimental data to models, validations will be made, and then an attempt to describe and explain some of the phenomena in experimental work will be made. Using the derived potentials, the electronic and thermal properties of the respective electrode materials will be studied. Cluster expansion is used to computationally screen for novel and stable alloy compositions for the Li-Si, Na-Si systems, and in turn guide the design of new high-performance electrodes that can be considered for the next generation of rechargeable batteries.

1.10 Research Problem

1.10.1 Problem statement

Lithium-ion batteries are considered to be good portable energy storage devices, but the existing commercially applicable technologies are associated with performance and production limitations. Current Li-ion batteries are designed based on the use of the end compound LiC_6 as the active material in the negative electrode [99]. Due to a low theoretical maximum capacity (372 $mAhg^{-1}$), this compound consequently makes them less viable for high energy applications such as in EVs. Alternative anode materials to the LiC_6 are therefore needed. Amongst the anode materials for rechargeable Li-ion batteries, Si has emerged as an attractive candidate due to its highest theoretical capacity (4200 $mAhg^{-1}$) corresponding to a fully lithiated state $Li_{4.4}Si$ [100]. The capacity of this alloy anode is about 10 times that of LiC_6. However, coupled with this attractiveness are cyclability issues, an irreversible capacity loss, and a deleterious volume expansion leading to capacity fade [101; 102].

1.10.2 Rationale

There is a great demand for high-performance electrode materials which can be employed in the next generation of Li-ion batteries. The success in developing high-performance electrode materials would not only improve life by introducing convenient electronic devices and vehicles, but would also help in reducing air pollution and oil costs. The use of portable energy sources in electronic devices as well as in high power applications such as electric vehicles is directly linked to battery lifetime and cyclability performance. Therefore, long-lasting batteries with good performance are needed.

The causes of capacity fade with cycling in the Si-based systems as potential Li-ion battery electrodes have not been completely resolved as yet. The prevalent techniques commonly used to study these materials are based on experimental work. It is widely known that experimental investigations customarily require lengthy durations of time. However, computing power and the range of techniques available to study the most complex systems has increased. Since computer simulations provide ways for studying materials over relatively shorter periods, and also provide tools for determining material properties that could not be readily obtained, they, therefore, can be used to complement experimental work.

The use of computer simulations in this work will allow studies, observations, and correlations of concepts which may aid in developing insights towards resolving the capacity fade problem of the Li-Si electrode materials. The focus of this study is to calculate the electronic, structural, and thermal properties of these electrode materials. However, great effort will be spent on the derivation of SCC-DFTB parameters that can handle the Li-Si interaction pair, because they are currently non-existent. The DFTB approach makes it possible to determine both quantum mechanical properties, as well as the molecular and mechanical properties of large systems. Using DFTB, the computer simulation of such systems can be done with a minimum computational cost and a minimum number of fitting parameters. DFTB can exhibit a high degree of transferability and universality for both ground-state and excited-state properties. Moreover, it operates with the same accuracy as well as efficiency for organic molecules, solids, clusters, insulators, semiconductors, metals, as well as biomolecular systems. Thus, SCC-DFTB becomes ideal for use in this

study as it can accommodate a range of Li-Si alloys with different sizes and architectures. The calculations done herein can be used to report the electrical conductivity, structural qualities and the temperature dependencies exiting in Li-Si based electrodes. The knowledge produced from the study is also intended to contribute towards the improvement of the performance in prospective high energy density electrodes for rechargeable batteries.

1.11 Purpose of the Study

1.11.1 Aim

To formulate a computer simulation workflow that could be used to study and design high-energy-density electrode materials earmarked for the next generation of batteries within the era of the fourth industrial revolution (4IR).

1.11.2 Objectives

The objectives of this study will be to:

i. perform structural optimisations of bulk Li-Si systems,
ii. derive SCC-DFTB parameters for the Li-Si system,
iii. calculate structural properties such as lattice parameters and bond length to validate the developed semi-empirical models using available experimental data,
iv. use the derived SCC-DFTB parameters to study the electronic and molecular dynamics properties of Li-Si systems.
v. calculate mechanical properties of Si using SCC-DFTB
vi. derive SCC-DFTB parameters for the Na-Si system
vii. perform machine-learning-powered crystal structure predictions of stable M-Si alloys (M = Li, Na)
viii. evaluate the electronic stability of predicted structures using SCC-DFTB
ix. develop a computational framework for generating amorphous M-Si alloys
x. demonstrate the ability of SCC-DFTB to compute the electronic properties of large systems
xi. demonstrate the path for modelling electrodes of nano-architectural design

1.12 Outline of the Study

Chapter 1: A general overview of the study is presented and aspects integral to the advancement of high energy electrodes for rechargeable Li-ion batteries are reviewed. The section also highlights the intentions of the study entailed herein.

Chapter 2: The theoretical techniques and methodologies employed in the study are introduced and background information is provided.

Chapter 3: This section reports the development of self-consistent density functional tight-binding (SCC-DFTB) potentials for the Li-Si and Na-Si systems. The accuracy of the potentials is illustrated through evaluations of structural details of Li, Si, Na, NaSi and LiSi systems.

Chapter 4: To demonstrate the validity and application of the obtained parameter sets, molecular dynamics results are presented using the derived potentials. Also, a preliminary assessment of the lithiation of a bulk silicon system in comparison to observations recorded from experiments as reported in literature is presented through the use of potentials derived in this work. Furthermore, the ability of the SCC-DFTB parameters to calculate the electronic and mechanical properties of Si are assessed.

A framework for amorphizing silicon is presented. The developed set of Li-Si SCC-parameters is employed on lithiated amorphous silicon. This is done to demonstrate the technique's ability to handle large complex systems. The change in volume of amorphous Si as a function of Li inserted, is explored using the SCC-DFTB approach. The electronic properties of the lithiated amorphous systems are shown.

The development of SCC-DFTB parameters for the Na-Si system is presented. The parameters are validated against DFT reference details as well as available experimental details. A graphical presentation of the sodiation of crystalline and amorphous silicon is illustrated.

Chapter 5: Reports of crystal structure predictions using cluster expansion on the M-Si (M= Li, Na, Mg) systems are given. The stabilities of predicted binary structures are further examined using the SCC-DFTB by calculating the partial density of states for these structures. The effect of pressure on the state of stability for predicted structures is tested. To demonstrate the power of combining various computational

techniques to advance material discovery and design, a framework that links DFTB and cluster expansion is shown by exploring the nano-architectural design of new active material using predicted binary alloys.

Chapter 6: The details of the work entailed herein are summarised and recommendations for future work are made.

Chapter 2 **Methodology**

The 4IR necessitates digital transformations in many sectors including research and development. This means rethinking and improving the traditional approaches used in research techniques/methods. Computational modelling as one of the available means for intelligently advancing material discovery, development and manufacturing is used in this work. In the 4IR era, it is helpful to harness the strength of various technologies to address issues in areas such as energy storage. This chapter presents various computational theories and techniques used to study and design electrode materials that can be applied in rechargeable batteries.

2.1 Computational Details

Density functional theory and density functional tight-binding (DFTB) theory will be employed to study the electronic and structural properties of electrode systems. The theories are based on Kohn-Sham equations and their second-order expansions relative to energy representations [103]. The simulation codes, DFTB+ [104], DMol^3 which are implemented in the BIOVIA Materials Studio® software package [105] employ these theories. A machine-learning-powered crystal structure prediction of stable binary alloys is performed using the MedeA-UNCLE package [106].

2.2 Density Functional Theory

Density functional theory is one of the successful and popular quantum mechanical modelling approaches used in physics and chemistry to investigate primarily the ground-state electronic structure of many-body systems [103; 107]. The systems include atoms, molecules and the condensed phases of matter. Developments of DFT have also led to its broad application by calculating several properties such as the binding energy of molecules, the band structure of solids and magnetic properties of alloys. In spite of its flexibility and generality, DFT is based on a rigid conceptual framework composed of two core elements, the Hohenberg-Kohn theorem [108] and the Kohn-Sham equation [103]. Within DFT, the properties of a many-electron system can be determined by using functionals, which in this case refers to the spatially dependent electron density. Density functional theory begins with the Hohenberg-Kohn theorem and then goes on to state that the many-body

system's total energy is presented as functionals of the charge density ρ. The total energy may thus be written as:

$$E = E[\rho]. \tag{2.1}$$

The total energy is decomposed into the following terms:

$$E_t[\rho] = T[\rho] + U[\rho] + E_{XC}[\rho], \tag{2.2}$$

where $T[\rho]$ is the kinetic energy of a system of non-interacting particles of density ρ, $U[\rho]$ is the classical electrostatic energy due to Coulombic interactions, and $E_{XC}[\rho]$ is the exchange-correlation energy, which includes all many-body contributions to the total energy.

Within DFT, the Kohn-Sham equations represent a mapping of the intermingling many-electron system onto a system of non-intermingling electrons that move in an effective potential as a result of all other electrons. Their implementation within DFT codes is comparable to the Schrödinger Equation (SE), and they reorganise the many-body SE into a set of coupled, single-particle equations. The Kohn-Sham equations also isolate the ignorance concerning many-body interactions into the exchange-correlation density functional, $E_{XC}[\rho(r)]$. Instead of solving the complicated real system of electrons interacting within an external potential, $V(r)$, a much simpler but equivalent, fictitious system of non-interacting 'Kohn-Sham particles' in an effective potential, $V_{eff}(r)$ is solved [109].

The Kohn-Sham total-energy functional for a set of doubly occupied electronic states ψ_i, can be minimised by determining the set of wave functions which are given by the self-consistent solutions to the Kohn-Sham equation [103]:

$$\left[\frac{-\hbar^2}{2m}\nabla^2 + V_{ion}(r) + V_H(r) + V_{XC}(r)\right]\psi_i(r) = \epsilon_i\psi_i(r), \tag{2.3}$$

where ψ_i is the wave function of electronic state i, ϵ_i is the Kohn-Sham eigenvalue, and V_H is the Hartree potential of the electrons given by:

$$V_H(r) = e^2\int\frac{\rho(r')}{|r-r'|}d^3r'. \tag{2.4}$$

The exchange-correlation potential, V_{XC}, is given by the functional derivative

$$V_{XC}(r) = \frac{\delta E_{XC}[\rho(r)]}{\delta \rho(r)}. \quad \textbf{(2.5)}$$

Modelling the exchange-correlation energy of many-body systems can be a difficult task and require the use of computational approximations. The two commonly used approximations are the local density approximation (LDA) and the generalized gradient approximation (GGA) and are discussed briefly in the next subsections.

2.2.1 Local density approximation

The local density approximation is a simple approximation which assumes that the density of electrons can be treated locally as that of a uniform electron gas; it uses only the electron density, $\rho(r)$, at a spatial point r to determine the exchange-correlation energy density at that point [110]. Within the local density approximation, the exchange-correlation energy of an electronic system is constructed on the assumption that the exchange-correlation energy per electron at a point r in the electron gas, $E_{XC}[r]$, is equal to the exchange-correlation energy per electron in a homogeneous electron gas that has the same density as the electron of the electron gas at point r [111], so it follows that:

$$E_{XC}[\rho(r)] = \int \varepsilon_{XC}(r)\rho(r)d^3\,r. \quad \textbf{(2.6)}$$

This approximation assumes that the exchange-correlation energy functional is purely local and in principle it ignores the correction to the exchange-correlation energy at a point r due to nearby inhomogeneities in the electron density.

2.2.2 Generalized gradient approximation

The generalized gradient approximation incorporates the gradient of the density, $|\nabla\rho(r)|$, as an independent variable [112]. Thus, the gradient introduces non-locality into the description of exchange and correlation. The GGA still entails some locality however it also takes into account the gradient of the density, the density at the same coordinates as given by:

$$E_{XC}[\rho_\uparrow, \rho_\downarrow] = \int \varepsilon_{XC}(\rho_\uparrow, \rho_\downarrow, \nabla\rho_\uparrow, \nabla\rho_\downarrow)\rho(r)d^3\,r, \quad \textbf{(2.7)}$$

where $\rho(r) = \rho_\uparrow + \rho_\downarrow$ and ρ_σ is the density of electrons with spin σ.

The GGA functionals have advanced in two main orientations, with one sometimes referred to as the parameter-free, where the new parameters are derived from

known expansion coefficients, and other exact theoretical conditions; and the second is empirical, with parameters developed from fits correlated to experimental data or accurately calculated atomic and molecular properties. The GGA functionals most commonly used in physics are Perdew, Burke, and Ernzerhof (PBE) [112] and Perdew-Wang from 1991 (PW91) [113], and are parameter-free. Most GGAs used in chemistry applications, such as Becke, Lee, Yang and Parr (BLYP), are empirical [114; 115].

2.3 Density Functional Based Tight-Binding Theory

The density functional tight-binding (DFTB) method can be viewed as an approximate Kohn-Sham density functional theory (KS-DFT) scheme with a linear combination of atomic orbital (LCAO) representation of the Kohn-Sham orbitals [116]. It includes *ab-initio* DFT concepts; however, it keeps efficiency and flexibility by also using ideas of the semi-empirical tight-binding (TB) method [117]. Unlike purely DFT based calculations which are usually limited to systems of ∼100 atoms, DFTB enables calculations on larger systems with thousands of atoms to be conducted [118]. The DFTB method is primarily based on the second-order Taylor expansion of the Kohn-Sham DFT energy with respect to charge density fluctuations and has been applied over a variety of problems in physics, chemistry, materials science, and biochemistry [119]. After the development of a non-self-consistent zeroth-order approach [120], a self-consistent charge (SCC) extension [121] was formulated with an augmentation to the consideration of spin polarisation [122]. The method was further adapted for calculating optical properties within a time-dependent DFT approach and in combination with the non-equilibrium Green's function technique for the calculation of electron transport properties on the molecular scale [123].

2.3.1 The tight-binding scheme as an atomistic method

As part of the development of the TB scheme into an atomistic method, Chadi [124] proposed that the total energy of an atomistic model system could be written as:

$$E_t = E_{band} + E_{rep}, \quad \textbf{(2.8)}$$

where E_{band} is the band energy, E_{rep} is the repulsive energy. The repulsive energy expressed as a sum of the repulsive pair energy terms, U_{ij},

$$E_{rep} = \sum_{i,j} U_{ij}. \tag{2.9}$$

2.3.2 Self-consistency

The tight-binding technique is ordinarily used in a non-self-consistent manner wherein the Hamiltonian matrix is independent of the distribution of electrons. This, however, does not imply that the electrons are non-interacting, as Fermi exclusion is imposed by the orthogonality of the eigenstates, but the Coulombic interactions are neglected. This approximation may collapse in two circumstances; first, when charge transfer is important, for instance in materials with significant ionic bonding, and secondly when the solutions of the Hamiltonian give rise to spurious charge transfers which should be prevented by Coulombic screening. Three ways of introducing a degree of self-consistency are described in order of their frequency of use as, local charge neutrality (LCN), Hubbard *U*, and self-consistent tight-binding (SCTB), the last of which is discussed as part of *ab initio* tight-binding, below.

To begin, it is necessary to consider how the charge on an atom is defined in the tight-binding model. Writing the eigenstates of the Hamiltonian in terms of the atomic-like basis set,

$$\psi_k = \sum_{i\alpha} c_{i\alpha}^{(k)} \psi_{i\alpha} \tag{2.10}$$

and the number of electrons 'on' atom i can be written as:

$$Q_i = \sum_{k\alpha} \left| c_{i\alpha}^{(k)} \right|^2 f_k \tag{2.11}$$

where f_k is the occupation of eigenstate *k*. The net charge on the atom is then obtained by the disparity between this value and the ionic charge of the atom.

Since a charged particle attracts an opposite charge, it will gather a 'screen' of equal and opposite charge around itself, so that from the outside it appears neutral. Of particular interest is the distance scale over which this occurs, known as the screening length. In metallic materials, this length is shorter than the interatomic spacing, as a result of which no atom can carry any significant charge. This situation

is described in tight-binding by the imposition of LCN. In this scheme, the on-site energies are adjusted site by site by a local offset,

$$H_{i\alpha i\alpha} = H^0_{i\alpha i\alpha} + \delta E_i \qquad \textbf{(2.12)}$$

where δE_i is chosen such that the electron count on atom *i* is equal to the ionic charge [117].

2.3.3 Self-consistent charge density-functional tight-binding

The detailed foundational descriptions of the DFTB method have been well presented in literature and the developments into the self-consistent charge density-functional tight-binding (SCC-DFTB) have been reviewed [121; 125 – 133]. Therefore, only a brief description of the method is presented in this work.

The general expression of the total energy can be written as:

$$E = \sum_{i}^{occ} \langle \psi_i | \hat{H}_0 | \psi_i \rangle + \frac{1}{2} \sum_{\alpha\beta} \gamma_{\alpha\beta}\, \Delta q_\alpha \Delta q_\beta + E_{rep} \qquad \textbf{(2.13)}$$

When a minimal basis set consisting of atomic-orbital-like functions $\eta\mu$ is introduced, and the linear combination of atomic orbitals (LCAO) wave function is $\gamma_i = \sum c^i_\mu \eta_\mu$, the first term in equation (13) becomes

$$\sum_{i}^{occ} \langle \psi_i | \hat{H}_0 | \psi_i \rangle = \sum_{i}^{occ} \sum_{\mu} \sum_{\upsilon} c^i_\mu c^i_\upsilon H^0_{\mu\upsilon} \qquad \textbf{(2.14)}$$

With the Hamiltonian matrix elements being evaluated by employing the minimal basis set of pseudoatomic orbitals, together with a two-center approximation, the total energy function within the SCC-DFTB is therefore given by:

$$E^{SCC-DFTB}_{total} = \sum_{i\mu\upsilon} c^i_\mu c^i_\upsilon H^0_{\mu\upsilon} + \frac{1}{2} \sum_{\alpha\beta} \gamma_{\alpha\beta}\, \Delta q_\alpha \Delta q_\beta + E_{rep} \qquad \textbf{(2.15)}$$

where $H^0_{\mu\upsilon}$ are the Hamiltonian matrix elements, c^i_μ, c^i_υ are the wave function expansion coefficients, Δq_α and Δq_β are the charge fluctuation terms associated with atoms α and β respectively; and E_{rep} accounts for the short-range repulsion terms.

$\gamma_{\alpha\beta}$ is comprised of the long-range pure Coulomb term and an exponentially decaying short-range function S. The $\gamma_{\alpha\beta}$ function is determined by:

$$\gamma_{\alpha\beta} = \frac{1}{R_{\alpha\beta}} - S(U_{\alpha\beta}, U_{\alpha}, U_{\beta}) \quad \textbf{(2.16)}$$

where $R_{\alpha\beta}$ is the distance between atoms α and β, U_{α} and U_{β} are the Hubbard parameters for these atoms respectively.

2.4 Stability in Materials

2.4.1 Electronic stability

2.4.1.1 Density of states

The density of states (DOS) for a given system describes the number of electron (or hole) states per volume at each energy level that are available. The DOS function is useful for determining the energy distributions of carriers and the carrier concentrations within materials. A high DOS at a specific energy level implies that there are many states available for occupation. A DOS of zero, therefore, means no states can be occupied at that particular energy level.

The density of states for a given energy band $n, N_n(E)$ can be defined by the following equation:

$$N_n(E) = \int \frac{d\boldsymbol{k}}{4\pi^3} \delta(E - E_n(\boldsymbol{k})) \quad \textbf{(2.17)}$$

Where $E_n(\boldsymbol{k})$ describes the dispersion of the given band and the integral is determined over the Brillouin zone. The total density of states, $N(E)$, is given by a summation over all energy bands. The integral of $N(E)$ from minus infinity to the Fermi level gives the total number of electrons within a unit cell.

Using the DOS it is possible to characterize solid materials as exhibiting the nature of insulators, metals, semiconductors, *etc*., and can also be used to predict the electronic stability of the systems. DOS allows integration with respect to electron energy to be used, and characteristics such as the energy gap, the width of the valence band, the number as well as the intensity of main features on the DOS are helpful in the qualitative interpretation of experimental spectroscopic data.

Studies on the electronic structure behaviour in materials are as well helpful for understanding alloy formation, phase stabilities as well as other physical properties. As posited by Jones *et al* [134] and as illustrated by Ravindran *et al* [135], the behaviour of the electronic density of states in the vicinity of the Fermi level (E_f) can be related to structural stability. Generally, many ordered intermetallic compounds will exhibit the shape of a deep valley in the electronic density of states around the vicinity of E_f. The deep valley is commonly referred to as a pseudogap. In general, a given phase will be regarded as structurally stable if the E_f falls exactly on pseudogap. Furthermore, a material would exhibit higher stability if (i) the conduction band is narrow, (ii) conduction electron states accumulate in a relatively lower energy region, (iii) the ratio of the width of the occupied part of the DOS to the width of the bonding states region is closer to unity, (iv) for s, p solids, the number of electrons in E_f is lower, (v) and if E_f falls on a locally flat peak of the DOS [135].

The use of partial density of states (PDOS) and local density of states (LDOS) can be instrumental for the analysis of electronic structures. Both the LDOS and PDOS identify which atoms' electronic states contribute to various parts of the energy spectrum. The knowledge of whether the main peaks in the DOS are of s, p or d character is useful. An analysis of a material's DOS can help deduce which atoms aid in the stabilization of a given structure. In this work, electronic densities of states are used to predict the stability of selected structures.

2.4.2 Thermal stability

2.4.2.1 Heats of formation

From a fundamental perspective, heats of formation also known as enthalpy of formation refers to the amount of heat energy that is absorbed or released when one molecule of a compound is formed from its constituents elements, with all substances being in their normal physical state. As a thermal property of materials, the change in heats of formation can be used to predict a given materials' relative thermal stability. A negative value of the heats of formation suggests that the structure or material in question is thermally stable, whereas a positive value suggests that the structure would be unstable. The relative thermal stability in binary alloys can be determined through the following equation [136]:

$$\Delta H_f = E_{A_xB_y} - xE_A - yE_B \quad \textbf{(2.18)}$$

Where E_A, E_B, and $E_{A_xB_y}$ are the total energies of atoms A, B, and binary alloy A_xB_y at equilibrium, and x and y are the atomic concentration of A and B. Heats of formations are calculated in this work using the VASP engine within the UNCLE code used for predicting structures through cluster expansion technique.

2.4.3 Mechanical stability

2.4.3.1 Elasticity

Elasticity is a fundamental property of materials and is crucial in physical, materials, as well as geological sciences. It describes the macroscopic reaction of crystals to external forces and relates it to the strength and hardness of materials. This then makes elastic constants to serve a crucial role in assessing the mechanical stability of crystals [137].

Any material can be deformed when force is applied to it. The theory of elasticity is helpful for studies about mechanical properties in materials. Interpretations in this context are done using properties such as stress, strain, bulk modulus, shear modulus, and Young's modulus, which shall be briefly defined in the following passages.

If a material returns to its original shape after an applied force is removed, it is then said to be elastic. When force is being applied to a material, it is said to be under stress. Therefore in general sense, stress can be obtained by diving the applied force by a given cross-sectional area.

$$Stress = \frac{F}{A} \quad \textbf{(2.19)}$$

A measure of how much force distorts an object or the measure of the distortion of the object is referred to as strain.

Strain is defined as the ratio of change in a given spatial variable to its original value.

E.g. If the variable is length, then strain is given by

$$Strain = \frac{\Delta L}{L_0} \tag{2.20}$$

where ΔL is the change in length and L_0 is the initial length.

Materials may exhibit some level of resistance to compression or tensile stress, and a measure of this resistance is referred to as the materials' bulk modulus. An inversion of the bulk modulus, that is it say, its reciprocal, give what is referred to as a materials measure of compressibility.

When a material is deformed in shape whilst its volume is constant, the measure of respective stiffness can be obtained and is referred to as the shear modulus or modulus of rigidity. The shear modulus is given by the ratio of shear stress to the shear strain.

In materials science Hooke's law, F= kx, where k is the proportionality constant or spring constant, x in length increase, is used in observing the stress-strain relationship of a given material within its elastic limit. From Hooks law, stress is proportional to strain. I.e.

$$\frac{F}{A} = Y \frac{\Delta L}{L_0} \tag{2.21}$$

Where Y is the elastic constant for proportionality for distortion in length and is called Young's modulus. Young modulus defines the stress-strain relationship in a material within its linear elasticity regime of uniaxial deformation.

2.4.3.2 Mechanical stability criterion

Conditions for determining mechanical stability were first proposed by Born [138] in 1940. Recently, Mouhat *et al* [139] presented an updated and detailed discussion of the closed-form necessary and sufficient elastic stability conditions for all crystal classes. Thus only a brief illustration derived from reference [139] is given herein.

The elastic behaviour of a lattice is described by its matrix of second-order elastic constants

$$C_{ij} = \frac{1}{V_0} \frac{\partial^2 E}{\partial \varepsilon_i \partial \varepsilon_j} \tag{2.22}$$

Where E is the energy of the crystal, V_0 is the equilibrium volume, C_{ij} refers to the elastic constants and ε is the strain. The 6 x 6 elastic matrix, (also known as the stiffness matrix) is symmetric and comprised of 21 independent components [139].

When a crystal structure undergoes an arbitrary homogenous deformation as a result of an infinitesimal strain, its energy can be given by the following quadratic equation:

$$\boldsymbol{E} = E_0 + \frac{1}{2} V_0 \sum_{i,j=1}^{6} C_{ij}\varepsilon_i\varepsilon_j + O(\varepsilon^3) \qquad \textbf{(2.23)}$$

where E_0 is the energy of the crystal prior deformation, V_0 is the reference volume, and $\boldsymbol{\varepsilon}$ signifies a strain, and $O(\varepsilon^3)$ denotes terms of the order ε^3 or greater.

In the absence of an external load in the harmonic approximation, a crystal is said to be stable if and only if (i) all its phonon modes have positive frequencies for all wave vectors (for dynamic stability), and (ii) the elastic energy given by equation (2.23) is always positive (**E** > 0, $\forall_{\varepsilon} \neq 0$) for elastic stability.

From Born's work [138], it can be noted that necessary and sufficient stability conditions can be expressed as

(a) the matrix ***C*** is definite positive; (b) all eigenvalues of ***C*** are positive; all the leading principal minors of ***C*** (determinants of its upper-left *k* by *k* submatrix, $1 \leq k \leq 6$) are positive and (d) and arbitrary set of minors of ***C*** are all positive.

The theoretical background of necessary and sufficient conditions for establishing the elastic stability of crystal structures have been discussed elsewhere [139]. Hence, only a terse synopsis is presented in this work.

(i) Cubic crystal system

The cubic crystal system has only three independent constants, C_{11}, C_{12}, and C_{44}.

$$\boldsymbol{C_{cubic}} = \begin{pmatrix} C_{11} & C_{12} & C_{12} & & & \\ \cdot & C_{11} & C_{12} & & & \\ \cdot & \cdot & C_{11} & & & \\ & & & C_{44} & & \\ & & & & C_{44} & \\ & & & & & C_{44} \end{pmatrix} \quad \textbf{(2.24)}$$

(The dots indicate nonzero elements constrained by the symmetric nature of the matrix)

The Born stability criteria for the cubic system are given as:

$$C_{11} - C_{12} > 0, \qquad C_{11} + 2C_{12} > 0, \qquad C_{44} > 0 \quad \textbf{(2.25)}$$

The bulk, shear, Young's moduli as well as Poisson's ratio for the cubic crystal system are given by

$$B = \left(\frac{C_{11} + 2C_{12}}{3}\right), \quad G_V = \left(\frac{C_{11} - C_{12} + 3C_{44}}{5}\right), \quad G_R = \left(\frac{C_{44}(C_{11} - C_{12})}{4C_{44} + 3(C_{11} - C_{12})}\right), \quad \textbf{(2.26)}$$

$$G = G_H = \left(\frac{G_V + G_R}{2}\right), \quad \mathrm{Y} = \left(\frac{9BG}{3G + G}\right), \quad \vartheta = \left(\frac{\mathrm{Y}}{2G - 1}\right), \quad \vartheta = \left(\frac{C_{12}}{C_{11} - C_{12}}\right), \quad \phi = \left(\frac{2C_{44}}{C_{11} - C_{12}}\right) \quad \textbf{(2.27)}$$

where *B* is the bulk modulus, *G* is the shear modulus (with *V, R, H* being the Voigt, Reuss and Hill notation), Y is the young modulus, ϑ is the Poisson's ratio and ϕ is the anisotropic factor.

(ii) Hexagonal and tetragonal crystal systems

The Laue classes of the hexagonal crystal system and the tetragonal (I) class of (Laue class 4/mmm), have the same elastic matrix form given as:

$$\boldsymbol{C_{hexagonal\ /\ tetragonal\ I}} = \begin{pmatrix} C_{11} & C_{12} & C_{13} & & & \\ \cdot & C_{11} & C_{13} & & & \\ \cdot & \cdot & C_{33} & & & \\ & & & C_{44} & & \\ & & & & C_{44} & \\ & & & & & C_{66} \end{pmatrix} \quad \textbf{(2.28)}$$

The crystals of the tetragonal (I) class have six independent elastic constants, while the hexagonal crystal system has only five, due to the additional relation

$$C_{66} = \frac{C_{11} - C_{12}}{2} \quad \textbf{(2.29)}$$

The four necessary and sufficient conditions for elastic stability in the hexagonal and tetragonal (I) are:

$$C_{11} > |C_{12}|,\ 2C_{13}^2 < C_{33}(C_{11} + C_{12}),\ C_{44} > 0,\ C_{66} > 0 \quad \textbf{(2.30)}$$

(where the condition on C_{66} is redundant for the hexagonal case)

Tetragonal II

$$\boldsymbol{C_{tetragonal\ II}} = \begin{pmatrix} C_{11} & C_{12} & C_{13} & & & C_{16} \\ \cdot & C_{11} & C_{13} & & & -C_{16} \\ \cdot & \cdot & C_{33} & & & \\ & & & C_{44} & & \\ & & & & C_{44} & \\ \cdot & \cdot & & & & C_{66} \end{pmatrix} \quad \textbf{(2.31)}$$

The tetragonal (II) class with Laue class 4/m has an extra elastic constant C_{16}, bringing the total of independent C_{ij}'s to seven.

The conditions for tetragonal (II) are similar to those for tetragonal (I) except the condition on C_{66} is replaced by $2C_{16}^2 < C_{66}(C_{11} - C_{12})$. The necessary and sufficient Born stability criteria for the tetragonal (II) class is therefore given by:

$$C_{11} > |C_{12}|, \quad 2C_{13}^2 < C_{33}(C_{11} + C_{12}), \quad C_{44} > 0, \quad 2C_{16}^2 < C_{66}(C_{11} - C_{12}) \quad \textbf{(2.32)}$$

(iii) Rhombohedral crystal system

Crystals in the rhombohedral (I) class (of Laue class $\bar{3}m$)

$$\boldsymbol{C_{rhombohedral\ I}} = \begin{pmatrix} C_{11} & C_{12} & C_{13} & C_{14} & & \\ \cdot & C_{11} & C_{13} & -C_{14} & & \\ \cdot & \cdot & C_{33} & & & \\ \cdot & \cdot & & C_{44} & & \\ & & & & C_{44} & C_{14} \\ & & & & \cdot & C_{66} \end{pmatrix} \tag{2.33}$$

Similar to the hexagonal class,

$$C_{66} = \frac{C_{11} - C_{12}}{2}$$

Therefore, four necessary and sufficient conditions are obtained as:

$$C_{11} > |C_{12}|, \qquad C_{44} > 0, \qquad C_{13}^2 < \frac{1}{2} C_{33}(C_{11} + C_{12}),$$
$$C_{14}^2 < \frac{1}{2} C_{44}(C_{11} - C_{12}) = C_{44} C_{66} \tag{2.34}$$

(iv) Rhombohedral II crystal system

The rhombohedral (II) class has an additional independent elastic constant, i.e. C_{15}.

$$\boldsymbol{C_{rhombohedral\ II}} = \begin{pmatrix} C_{11} & C_{12} & C_{13} & C_{14} & C_{15} & \\ \cdot & C_{11} & C_{13} & -C_{14} & -C_{15} & \\ \cdot & \cdot & C_{33} & & & \\ \cdot & \cdot & & C_{44} & & -C_{15} \\ \cdot & \cdot & & & C_{44} & C_{14} \\ & & & \cdot & \cdot & C_{66} \end{pmatrix} \tag{2.35}$$

The respective necessary and sufficient Born criteria for elastic stability are given by:

$$C_{11} > |C_{12}|, \qquad C_{44} > 0, \qquad C_{13}^2 < \frac{1}{2} C_{33}(C_{11} + C_{12}),$$
$$C_{14}^2 + C_{15}^2 < \frac{1}{2} C_{44}(C_{11} - C_{12}) = C_{44} C_{66} \tag{2.36}$$

(v) Orthorhombic crystal system

The orthorhombic crystal system has lower symmetry, nine independent constants, with no relationships between them:

$$\boldsymbol{C_{orthorhombic}} = \begin{pmatrix} C_{11} & C_{12} & C_{13} & & & \\ \cdot & C_{22} & C_{23} & & & \\ \cdot & \cdot & C_{33} & & & \\ & & & C_{44} & & \\ & & & & C_{55} & \\ & & & & & C_{66} \end{pmatrix} \quad \textbf{(2.37)}$$

The matrix has three trivial eigenvalues, C_{44}, C_{55}, and C_{66}, all of which should be positive. The necessary and sufficient Born criteria the orthorhombic system are:

$$C_{11} > 0, \qquad C_{11}C_{22} > C_{12}^2, \quad \textbf{(2.38)}$$

$$C_{11}C_{22}C_{33} + \ 2C_{12}C_{13}C_{23} - \ C_{11}C_{23}^2 - \ C_{22}C_{13}^2 - \ C_{33}C_{12}^2 > 0, \quad C_{44} > 0, \qquad C_{55} > 0, \qquad C_{66} > 0 \quad \textbf{(2.39)}$$

(vi) Monoclinic and triclinic crystal systems

The monoclinic and triclinic crystal systems have 13 and 21 independent elastic constants respectively. The generic necessary and sufficient criterion is that all eigenvalues of matrix C should be positive.

$$\boldsymbol{C_{monoclinic}} = \begin{pmatrix} C_{11} & C_{12} & C_{13} & & C_{15} & \\ C_{12} & C_{22} & C_{23} & & C_{25} & \\ C_{13} & C_{23} & C_{33} & & C_{35} & \\ & C_{11} & & C_{44} & & C_{46} \\ C_{15} & C_{25} & C_{35} & & C_{55} & \\ & & & C_{46} & & C_{66} \end{pmatrix} \quad \textbf{(2.40)}$$

$$\boldsymbol{C_{triclinic}} = \begin{pmatrix} C_{11} & C_{12} & C_{13} & C_{14} & C_{15} & C_{16} \\ C_{12} & C_{22} & C_{23} & C_{24} & C_{25} & C_{26} \\ C_{13} & C_{23} & C_{33} & C_{34} & C_{35} & C_{36} \\ C_{14} & C_{24} & C_{34} & C_{44} & C_{45} & C_{46} \\ C_{15} & C_{25} & C_{35} & C_{45} & C_{55} & C_{56} \\ C_{16} & C_{26} & C_{36} & C_{46} & C_{56} & C_{66} \end{pmatrix} \quad \textbf{(2.41)}$$

2.5 Molecular Dynamics

The molecular dynamics (MD) method is used in the simulation of kinetic and thermodynamic properties of molecular systems using Newton's equations of motion. By relating forces entailed in Newton's equations of motion to the potential energy of a system, the total energy of the system becomes obtainable from the relation $E = E_{kin} + E_{pot}$ and hence would be conserved. Through the integration of Newton's equations of motion the constant-energy surface of a given system can be investigated. However, most practicable cases occur under conditions wherein the system is exposed to external influences such as a change in heat (temperature) and pressure. Because of these influences, the total energy of the system under study is no longer conserved, hence extended forms of molecular dynamics are required. Several methods are available for controlling temperature and pressure where specific ensembles are selected to calculate the structural, energetic, and dynamic properties of a system. Different ensembles that may be used in MD calculations and included are the NVE, NVT, and NPT ensembles.

2.5.1 Ensembles

2.5.1.1 Microcanonical ensemble

The *microcanonical* (*NVE)* ensemble is one in which a system is isolated from changes in moles (N), volume (V) and energy (E). This ensemble corresponds to an adiabatic process wherein there is exchange of heat energy. A microcanonical molecular dynamics trajectory may be perceived as an exchange of potential and kinetic energy, with a conserved total energy. For a system of N particles with coordinates *r* and velocities $\boldsymbol{\dot{V}}$, the following pair of first-order differential equations may be written in Newton's notation as:

$$F(r) = -\nabla U(r) = M\dot{\boldsymbol{V}} \quad \textbf{(2.42)}$$

$$\mathrm{V}(t) = \dot{r}(t) \quad \textbf{(2.43)}$$

The potential energy function $U(r)$ of the system is a function of the particle coordinates *r*. It is also known as the force field. The equation (2.42) comes from Newton's laws; the force *F* acting on each particle with mass M in the system can be

calculated as the negative gradient of $U(r)$. For every time-step, each particle's position r and velocity $\boldsymbol{v}$ may be integrated with a symplectic method such as Verlet [140]. Given the initial positions (*e.g.* from theoretical knowledge) and velocities (*e.g.* randomised Gaussian), prospective or previous positions and velocities associated with a system can be calculated.

2.5.1.2 Canonical ensemble

For a canonical (NVT) ensemble, the moles (N), volume (V) and temperature (T) are conserved; and the energy of endothermic and exothermic processes is exchanged with a thermostat. Various thermostat methods are available to allow the addition and removal of energy from the boundaries of a molecular dynamics system in a somewhat realistic way, approximating the canonical ensemble. Popular techniques to control temperature include velocity rescaling, the Nosé-Hoover [141] thermostat, Nosé-Hoover chains, the Berendsen [142] thermostat, and Langevin dynamics.

2.5.1.3 Isothermal-Isobaric ensemble

In the isothermal-isobaric ensemble, moles (N), pressure (P) and temperature (T) are conserved. In addition to a thermostat, a barostat is needed. It corresponds most closely to laboratory conditions with a flask that is open to ambient temperature and pressure. NPT is the ensemble of choice when the correct pressure, volume, and densities are important in the simulation. This ensemble can also be used during equilibration to achieve the desired temperature and pressure before changing to the constant-volume or constant-energy ensemble when data collection starts.

2.5.2 Velocities

The velocities are usually computed using the Störmer-Verlet method [140], and although they are not explicitly given in the basic Störmer equation they often are necessary for the calculation of physical quantities such as kinetic energy. In MD kinetic energy and instantaneous temperatures at time *t* cannot be calculated for a given system until positions are known at time *t* + Δ*t*. The commonly used algorithm for MD velocity calculations is the *Velocity Verlet* algorithm. The Basic Verlet algorithm is given by using the equations:

$$\vec{x}(t + \Delta t) = \vec{x}(t) + \vec{v}(t)\Delta t + \frac{\vec{a}(t)\Delta t^2}{2} \quad \textbf{(2.44)}$$

$$\vec{a}(t + \Delta t) = \frac{f(t + \Delta t)}{m} \quad \textbf{(2.45)}$$

$$\vec{v}(t + \Delta t) = \vec{v}(t) + \frac{\vec{a}(t) + \vec{a}(t + \Delta t)}{2}\Delta t \quad \textbf{(2.46)}$$

where $\vec{x}(t)$, $\vec{v}(t)$, and $\vec{a}(t)$, which are respectively the position, velocity, and acceleration at time *t*.

2.5.3 Temperature

Temperature is an important concept in MD studies because it is the state variable that specifies the thermodynamic state of a system. It is a macroscopic quantity that is related to the microscopic description of MD simulations through the kinetic energy, which is calculated from the atomic velocities. A temperature-related phenomenon arises due to the small number of atoms that are used in MD simulations. For macroscopic systems, if the number of atoms is large enough, the statistical temperature can be estimated from the instantaneous temperature, which is obtained by equating the system's kinetic energy as shown by the relation:

$$\langle K_E \rangle = \langle \sum_{i}^{N} \frac{{p_i}^2}{2m} \rangle = \frac{N_f k_B T}{2} \quad \textbf{(2.47)}$$

where the left side of (2.47) is the average kinetic energy of the system, *T* is the thermodynamic temperature, m is the mass, p_i refers to momentum, k_B is the Boltzmann constant and $\mathrm{N_f}$ is the number of degrees of freedom of the system. Instantaneous kinetic temperature is thus defined by the equation:

$$T_{instant} = \frac{2K_E}{N_f k_B} \quad \textbf{(2.48)}$$

2.5.4 Pressure

Pressure is the effect of a force applied to a surface. Pressure also is a thermodynamic variable that can be used in defining a state and is calculated through the use of the virial theorem [81]. Thermodynamic pressure, thermodynamic temperature, volume, and internal virial can be related by the following expression:

$$PV = Nk_B T + \frac{2}{3}\langle W \rangle \quad \textbf{(2.49)}$$

where *W* is defined as

$$W = \frac{1}{2}\sum_{i=1}^{N} r_i \cdot f_i \qquad \textbf{(2.50)}$$

So that the instant pressure is defined by

$$P = \frac{Nk_BT}{V} + \frac{2}{3}\frac{W}{V} \qquad \textbf{(2.51)}$$

2.6 Cluster Expansion

2.6.1 Evolutionary algorithms

An algorithm is a sequential process or a set of instructions that are followed to produce an outcome. Algorithms are typically used to solve problems or a class of calculations. An evolutionary algorithm is a generic, population-based, metaheuristic optimization method. Common to the domain of artificial intelligence (AI), especially in machine learning (ML), evolutionary algorithms can be used to generate approximate solutions to problems in parameter spaces such as in materials science. In the field of materials science, the materials space problem (i.e. estimating how many new materials can be made from elements on the periodic table as a result of using laws of chemical valence and reactivity) is cumbersome. The exploration of a vast materials space by computational methods through evolutionary algorithms rather than experimental means alone can be much faster and more efficient, consequently leading to rapid identification and optimization of novel materials [143]. Evolutionary algorithms stem from biological processes such as selection, reproduction, mutation, and recombination. There are several types of evolutionary techniques including particle swarm optimization, genetic swarm optimization, evolutionary programming, and genetic algorithms. The evolutionary algorithm used in this work is the genetic algorithm (GA).

2.6.2 Genetic algorithms

A genetic algorithm is a metaheuristic search method inspired by Darwinian evolution entailing the performance of crossover, mutation, and selection operations; it progresses through a population of evolving candidates solutions. Schmitt [144] presented a detailed theory of genetic algorithms, thus, a broad background on genetic algorithms is not documented in this work. Bhasin *et al* [145] showcased

the application of genetic algorithms in machine learning. In materials science, genetic algorithms evolve populations of materials toward improved solutions to the problem being investigated and aided by machine learning, they help accelerate the prediction of chemical ordering and material structures [146]. In this work, a genetic algorithm is employed to predict ground-state structures for the Li-Si, Na-Si and Mg-Si systems that could find use as high-energy-density electrode materials for rechargeable batteries.

2.6.3 Overview of the cluster expansion formalism

A detailed illustration of the cluster expansion method can be found elsewhere. In this work, a brief description derived from a review authored by Muller [47] is presented.

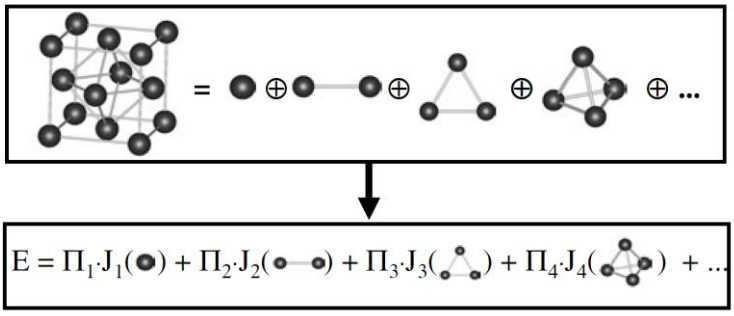

Figure 2-1. The cluster expansion concept. Shown for an FCC lattice, the crystal is decomposed into characteristic figures. The energy of any configuration can be expressed as a linear combination of the characteristic energies J_f of the figures.

The basic idea of the cluster expansion technique was proposed by Sanchez *et al* [147] and is shown as Figure 2.1 wherein for a given underlying lattice, the crystalline structure is decomposed into distinctive figures such as pairs, triangles and so forth. Then, the energy of any configuration σ on this lattice can be distinctively expressed as a linear combination of the characteristic energies J of the individual figure.

To demonstrate this concept in a practical manner, the 'alloy problem' is transformed to an Ising model [148]. Each atom i of an $A_{1-x}B_x$ alloy is assigned to a spin value S_i = -1 if i is an A atom, and to S_i = +1, if i is a B atom.

Then, each configuration's energy can be expressed by an Ising expansion as:

$$E(\sigma) = J_0 + \sum_i J_i S_i(\sigma) + \sum_i J_{ij} S_i(\sigma) S_j + \sum_i J_{ijk} S_i(\sigma) S_j(\sigma) S_k(\sigma) + \cdots \quad \textbf{(2.52)}$$

The first two terms on the right of the equation describe the energy of the random alloy with zero mutual interactions, whereas the third term comprises of all pair interactions, the fourth refers to all three-body interactions, etc. This equation can be compacted by introducing a correlation function $\overline{\Pi}_F$ for each class of symmetry-equivalent figures *F*, and therefore be written as:

$$\overline{\Pi}_F(\sigma) = \frac{1}{ND_F}\sum_f S_{i_1}(\sigma)S_{i_2}(\sigma)\ldots S_{i_m}(\sigma) \qquad \textbf{(2.53)}$$

D_F gives the number of figures of class *F* per site. The index *f* runs over the ND_F figures in class *F* and *m* denotes the number of sites in figure f. Then, equation (2.52) takes a general form and becomes:

$$E(\sigma) = N\sum_F D_F\overline{\Pi}_F(\sigma)J_F \qquad \textbf{(2.54)}$$

where each of the terms in the sum is the product of the local structure $\overline{\Pi}_F$ and an expansion coefficient J_F (which refers to an effective cluster interaction, ECI). D_F is a factor that corresponds to the number of degeneracies of the figure-class *F* that is normalized to the number of sites *N* within the configuration *σ*.

2.6.4 The procedure for conducting ground-state search

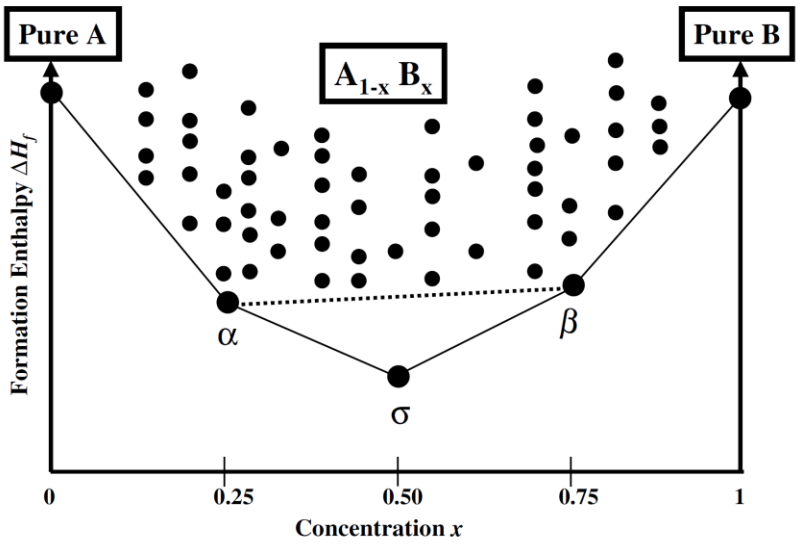

Figure 2-2. The schematic presentation of the ground-state (convex hull) diagram for a binary $A_{1-x}B_x$ alloy. The ground-state line was constructed from 60 energies of relaxed structures (shown as dots) by using equation (2.54). Excluding the pure elemental crystals, the ground state line is formed by three structures α, σ and β for the concentrations x = 0.25, 0.50 and 0.75, respectively. If σ would lie energetically above the dotted tie-line between α and β, a mixture of α and β would be more stable than σ [47].

The ground-state search can be considered an efficient tool for finding structures with crucial structure information for the determination of interactions. Cluster expansion is performed for an initialisation set of approximately 20 DFT energies of arbitrary input structures. The energy of all possible structures is then predicted from the resulting interactions using, for example, 16 atoms per unit cell. After the analysis is not on computational resources, the corresponding CE formation enthalpies, ΔH_f, of all structures are plotted as a function of composition and a ground-state line (convex hull) is constructed. This procedure is schematically shown in Figure 2.2, wherein an individual structure σ contributes only to the ground-state line if the average linear energy between the stable structures at the next highest and lowest concentration is energetically less favourable than the formation enthalpy of σ.

To be more precise, for three structures α, σ and β with x(α) < x(σ) < x(β) which are the lowest in energy for their individual concentrations, the structure σ has to fulfil the condition

$$\Delta H_f(\sigma) < \frac{\mathrm{x}\,(\sigma) - (\beta)}{\mathrm{x}\,(\alpha) - (\beta)}\,\Delta H_f(\alpha) + \frac{\mathrm{x}\,(\sigma) - \mathrm{x}(\beta)}{\mathrm{x}\,(\beta) - \mathrm{x}(\alpha)}\,\Delta H_f(\beta) \qquad \textbf{(2.55)}$$

to be the ground-state at x(σ). If equation (2.55) holds, a mixture of the phases α and β would be higher in energy than structure σ. With the ground-state line constructed, a check for all structures lying on or very close to the line regarding whether they were already considered as input structures for the CE is done. If not, their DFT energy is calculated and added to the input-structure set, while input structures with ΔH_f values far above the ground-state line are removed from the original input structure list. The routine is iterated until the ground-state line becomes stable.

2.6.5 Model fitness criterion using cross validation score

Alongside predictive techniques commonly used in machine learning, is the requirement to provide a criterion for determining accuracy in the fitting, which in turn leads to a model being selected. Model selection can be seen as a particular statistical algorithm selection. Cross-validation (CV) is a popular strategy for algorithm selection. The basic idea behind CV is to divide data once or more, for estimating the risk of each algorithm: part of data (training sample) is used for training each algorithm, and the remaining part (the validation sample) is used for

estimating the risk of the algorithmic. The CV then selects the algorithm with the smallest estimated risk. There several approaches in which cross-validation scores can be employed namely the k-fold cross-validation, leave-one-out validation, leave-p-out, balanced incomplete cross-validation, Monte-Carlo cross-validation, bias-corrected, leave-one-out bootstrap to list a few. A detailed discussion on cross-validation procedures can be found in the paper presented by Arlot *et al* [149]. In this work, the leave-out-out approach of the cross-validation scoring is used to determine how well energies of structures with a given training set compare to each other in a cluster expansion.

2.6.6 The MedeA-UNiversal CLuster Expansion (UNCLE) simulation package

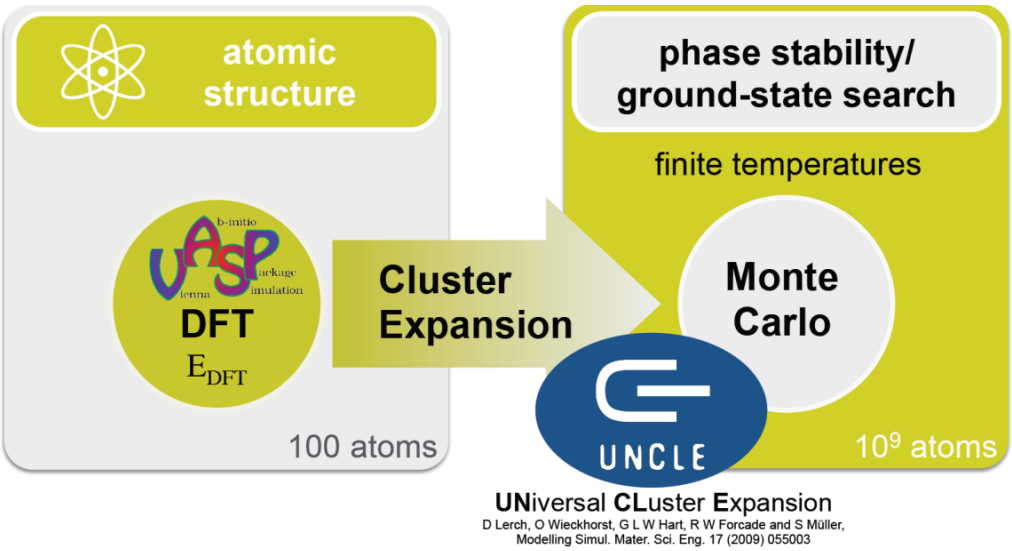

The MedeA-UNCLE package is used in the work herein. According to Lerch *et al*, [106] the package has been developed to reduce the need for user intervention; the method in the package is automated so that human error and judgment can be decreased. Furthermore, the code extends the cluster expansion formalism to cases such as ternary compounds, and surfaces, including adsorption and in equivalent sites [106]. Some aspects entailed in the UNCLE code, which have been derived from Lerch *et al*'s paper [106], are presented in the discussions that follow.

Atomic-level problems in materials science are broadly classified as 'configurational'. Research examinations relating to disorder transitions, solid-state crystalline metallic and semiconductor compounds in their ground state, segregation of defects in alloy interfaces and surfaces cannot be explored directly from DFT methods.

Nonetheless, cluster expansion makes it possible to deduce the physics of atom-atom interactions from a set of DFT, small-unit-cell calculations and then simulate unit cells comprised of millions of atoms (as in Monte Carlo modelling), or explore tens of million variant atomic configurations in different cell shapes.

As already alluded to in the brief presentation of the cluster expansion formalism, the idea of the cluster expansion is to express the energy (or other observable) configurational dependence as a sum over bonds. A particular configuration dealing with the question which atom type is located at each given site, is specified by a vector, σ, each component of which corresponds to one site. The energy is dependent on the configuration, $E(\sigma)$, and can be disintegrated [147] into a sum over bonds in pairs, triplets, and so forth. In the cluster expansion community, the bonds are referred to as *clusters* or *figures*, denoted F in equation (2.54).

2.6.6.1 Definition of lattice and figures

The fields in which cluster expansions are typically applied are the modelling of binary metal alloys that are in bulk phases, surface adsorption, and separation studies; and the fundamental element of such cluster expansion is the underlying parent lattice. In the UNCLE environment, the range goes beyond simple lattices (*i.e.* into what is referred to as mutilattices), which are well applicable to cases where more than one site per unit cell exists. Simply put, the cluster expansion is an expansion over figures (i.e. clusters or bonds within a system) where each figure has an associated expansion coefficient. The following figure illustrates how these figures are extracted as decomposition from a cubic lattice.

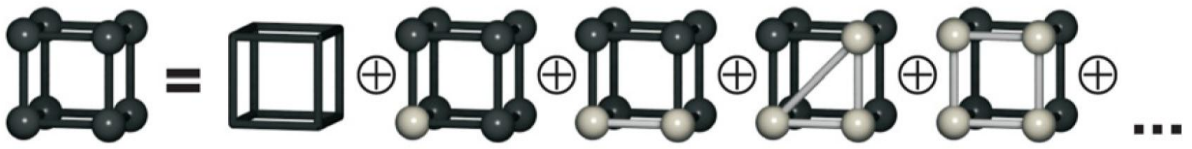

Figure 2-3. A presentation of the decomposition from a cubic lattice into figures that are used in the cluster expansion. The sum has been truncated with regard to the number of vertices as well as possible orientations and shapes of figures with the same number of vertices [106].

2.6.6.2 Checking the input database

The effective cluster interactions, which are the coefficients of the cluster expansion, are determined through fitting in an input database. The database is comprised of a set of atomic configurations whose energy has been determined through DFT techniques. By efficiently facilitating the exchange of structural information between

the fitting routines and the DFT code, the cluster expansion decreases the amount of required user time and effectively reduces the probability of human error. UNCLE's format of structural information has been designed to match that of the DFT code VASP [150; 151] and to adapt to the input of the FLAPW code FLAIR [152; 153]. After the input structures are read in, the input is validated. UNCLE verifies whether all their basis atoms lie on the lattice and whether there are symmetric-equivalent structures within the input list.

2.6.6.3 Choosing the input structures

The way in which atomic configurations are chosen affects the ECIs because the ECIs are derived from them. To avoid biasing the input database, and consequently, the ECIs, the database is systematically increased. Beginning with, a hand-chosen set {σ} of usual suspects, small-unit-cell structures derived from the parent lattice, and some quasi-random structures, the first cluster expansion determined from this set makes predictions. These predictions are then computed via DFT and incorporated into the database. The routine is repeated as presented by Figure 2.4, lets the current cluster expansion select new structures to be add to the database by itself.

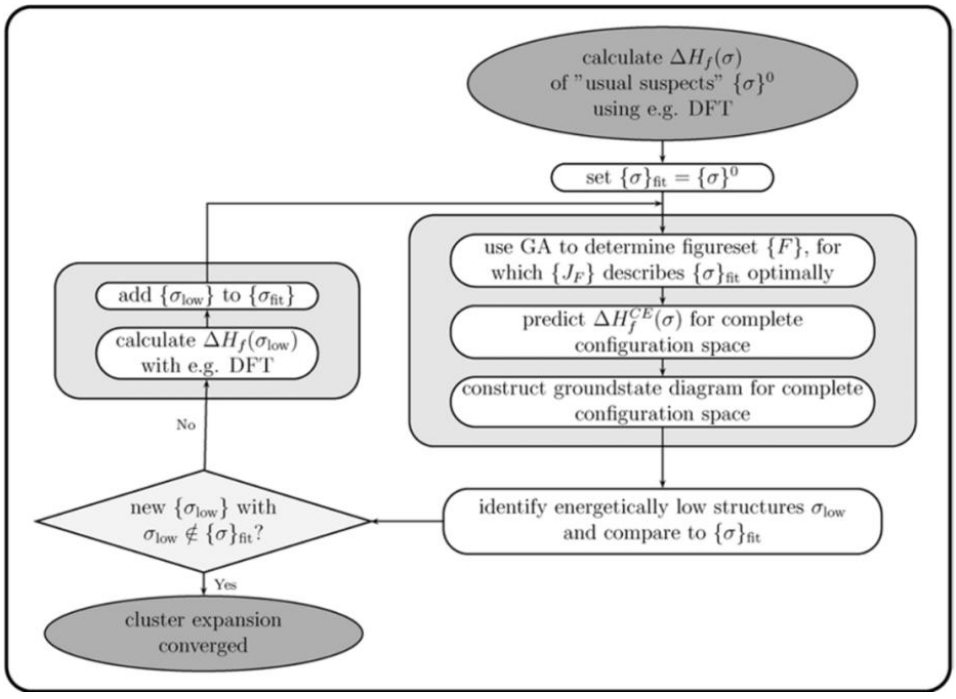

Figure 2-4. The graphic presentation of the self-consistent 'outer loop', which selects the input structures of the cluster expansion [106].

2.6.6.4 The identification of relevant figures

Given that the success of a cluster expansion lies in how figures are widely identified and included with truncation to a comparatively small number of terms without losing the predictive power, an evolutionary approach that is based on a genetic algorithm (GA) has been employed within UNCLE to choose the figures. The validation of figure selections is done through the leave-many-out cross-validation-score technique as a fitness criterion

A schematic presentation of the fitness cross-validation score S_{CV} is shown as follows

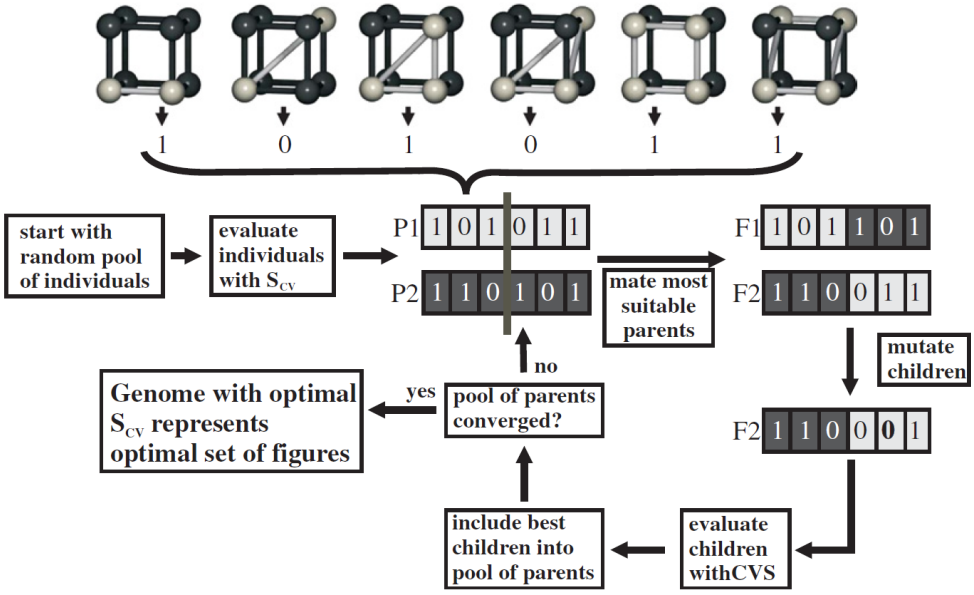

Figure 2-5. A depiction of the genetic algorithm, which aids the safe identification of relevant figures that are required in the cluster expansion-sum [106].

A description of the details of the algorithm implemented within UNCLE has been provided elsewhere [154; 155].

The fitness cross-validation score, Scv, gives the quantification of the predictive power for a given choice of figures and is computed through the following scheme:

(i) N sets$\{\sigma\}^{i}_{prediction}$, ($i \in \{1...N\}$) of n different structures are randomly chosen out of the total pool of input structures.

(ii) For each of the N prediction-sets$\{\sigma\}^{i}_{prediction}$, a cluster expansion based on all input structures except for those contained in $\{\sigma\}^{i}_{prediction}$ is performed. The resulting ECIs are independent from the influence by the energetics of $\{\sigma\}^{i}_{prediction}$.

(iii) The resulting ECIs are ten used to predict the energy of every member of $\{\sigma\}^{i}_{prediction}$ prediction and compare it with the energy calculated by DFT.

(iv) The expectation value of the root-mean-square error for all the predicted structures is thus calculated using the expression:

$$S_{CV} = \sqrt{\frac{1}{N \cdot n}\sum_{N}\sum_{n}|E_{DFT}(\sigma) - E_{CE}(\sigma)|^2} \quad \textbf{(2.56)}$$

2.7 Reliability and Validity

2.7.1 Data collection and analysis

Energy calculations and geometry optimisations of simulation systems were carried out using the DFTB+ code. Pre-optimisations are done using DMol^3 [156] code and the results are then used as input to the DFTB+ program. Suitable algorithms such as smart, steepest descent and conjugate gradient were sampled to fit structures used herein. The Monkhorst-Pack [157] grids for k-point sampling were used to ensure suitable configurations necessary for obtaining optimised structural details such as lattice constants and bond lengths. The parameterisation procedure implemented within the DFTB+ code was used to derive tight-binding Slater-Koster [98] potentials. This code is well designed to accommodate non-periodic and periodic systems. Successful parameterisation would imply that the main properties of reference systems are well reproduced with respect to DFT; thus, to achieve this, adjustments will be made to the confinement radii, suitable basis set, and eigensolvers. Available experimental data will be used to validate input models so that the derived potentials may further be used to study the electronic, mechanical and thermal properties of electrode materials investigated in this work.

The theories to be used in this work have been widely used and significant results have been reported. Moreover, there is an extensive ambit of scientific literature with experimental data that can be used to validate simulation results. Mathematical models implemented in the simulation codes to be employed were founded on

fundamental principles. The codes are well designed to report electronic, structural and thermal properties required in this study. Numerous accurate solutions have been reported on work done using computer simulations. High-performance computing resources are used to perform all the necessary calculations.

Available facilities that are needed to make the study a success include the following: Software such as Materials Studio®, MedeA®, for simulations; Sigma Plot for plotting graphs, and Microsoft Office for further reporting and documentation. Calculations are done on the high-performance computing infrastructure in Materials Modelling Centre (MMC) and at the National Cyber Infrastructure System (NICIS)'s Center for High-Performance Computing (CHPC).

Chapter 3 **Derivation of Slater-Koster Potentials for Li-Si and Na-Si systems**

In this section, the procedure for developing Slater–Koster type of potentials which are based on the DFTB method is discussed. SCC-DFTB parameters are derived using the DFTB+ code as implemented within the BIOVIA Materials Studio simulation software [158]. Fundamentally, the DFTB+ parameterisation procedure refers to the process of creating Slater-Koster files for a chosen set of element pairs with parameters chosen for particular types of target systems. A Slater-Koster file consists of two types of parameters, which are the electronic and the repulsive parameters.

To employ the DFTB method in computational materials science, atomic parameters for materials being investigated are required. In some cases, standard sets of atomic parameters are readily available for use and can be obtained from the DFTB website (http://www.dftb.org/parameters). However, there are cases wherein the published parameter sets are not compatible or applicable to a wide context; as such, a researcher is required to create their Slater-Koster file using the DFTB+ code.

In this work, an SCC-DFTB parameter set for the Li-Si element pair is required to study the Li-Si alloy as a candidate negative electrode for Li-ion batteries. However, such as set in non-existent on the DFTB website and in available literature; therefore, the Li-Si SCC-DFTB parameter set is created in this work. The following discussions entail the aspects considered in the process and the framework used in the development of the potentials is documented.

Furthermore, at the time of writing, a parameter set that contains the Na-Si element pair on the DFTB website is the *matsci* library. However, the Na-Si pair in *matsci* library was developed for zeolites which are sorbate in state; as such, the library is not adapted for solids. Therefore, since the sodiation of silicon in this work is done based on solid states, it is necessary for the Na-Si SCC-DFTB parameter set to be developed in this respect. This section also presents the SCC-DFTB parameterisation of the Na-Si system.

3.1 Pre-Optimisation with the DMol^3 code

3.1.1 Choosing a basis set, a local functional and lowering symmetry

3.1.1.1 Geometry optimisation

When modelling a material computationally, there is usually a need for the modelled structure to be relaxed to a stable geometry with ground-state energy. This is achieved through an iterative routine, wherein the coordinates of atoms in the structure are adjusted so that forces on the atoms are brought to zero. It is through this routine that the geometry of any model in question is optimised.

3.1.1.2 Basis set

To optimise bulk input systems using DMol^3, one needs to select an appropriate basis set. The basis set in this context refers to a mathematical description of the orbitals of a given system. It is required to enable the theoretical approximations to best represent the physical materials. In principle, basis set types can be broadly classified as minimal basis sets; pople basis sets; correlation consistent basis sets; split valence basis sets; double, triple and quadruple zeta basis sets; and plane-wave basis sets.

Within the DMol^3 software implementation, the basis sets are derived numerically. During the iterative optimisation routine, matrix elements are required to solve the self-consistency field (SCF) equations in DFT, which are then used to compute the total energy. DMol^3 employs numerical orbitals for basis functions, and each function corresponds to an atomic orbital.

For variational freedom and to provide larger basis sets, basis functions are doubled and this is referred to as double-numerical (DN) set. The notation is employed analogously to the Gaussian double-zeta (GZ) sets, but with the N primarily used to emphasise the numerical nature of orbitals. In this work, the Double Numerical plus d-functions (DND) and Double Numerical plus polarisation (DNP) basis sets are evaluated, with the intention being to derive semi-empirical potentials that would be able to accurately handle a variety of systems.

3.1.1.3 Local functional

As it is known that modelling the exchange-correlation energy of many-body systems tends to be problematic and requires the use of computational approximations, it makes sense to consider the appropriate functional to be used in the calculations herein. As a test, two commonly used approximations are chosen, the local density approximation and the generalized gradient approximation.

It is worth noting that with exception of the parameterisation task, the DFTB+ implementation generally does not provide the option to make such a choice, but it essentially inherits the local functional used as input in the $DMol^3$. Input systems would all be prepared using the $DMol^3$, thus a comparison on the effects of the LDA and GGA on the systems is necessary.

3.1.1.4 Lowering symmetry during geometry optimisation

The periodicity and symmetry of a material affect how it will be treated during a calculation. These concepts are coupled to the description of properties, relationships which will exist, and translational operations that will be possible. When a model retains a symmetry associated with a given space group, it possesses a set of constraints which affect the duration of a calculation. Sometimes it becomes necessary to convert higher symmetry crystals to P1 symmetry to control the simulation time. The lower P1 symmetry removes all symmetry in a crystal lattice but maintains the periodic relationships, and this simplicity somewhat adjusts the duration to be shorter.

Although a short computational time may be desirable in modelling materials, it is also important to understand how lowering symmetry will affect systems during geometry optimisation.

Table 3-1. Configurations used during the structural relaxation of lithium monosilicide (LiSi) and the calculated results.

System	Space Group	Basis 4.4	Functional	Lattice (Å) a = 9.34 [159] c = 5.76 [159]	Bandgap (eV) 0.057 eV [9]	% Diff
LiSi	P1	DND	LDA-PWC	a = 9.191 c = 5.652	0.027	52.63
LiSi	P1	DND	GGA-PBE	a = 9.355 c = 5.757	0.082	43.86
LiSi	P1	DNP	LDA-PWC	a = 9.178 c = 5.655	0.027	52.63
LiSi	P1	DNP	GGA-PBE	a = 9.347 c = 5.758	0.082	43.86
LiSi	*I41/a*	DND	LDA-PWC	a = 9.191 c = 5.652	-	
LiSi	*I41/a*	DND	GGA-PBE	a = 9.355 c = 5.757	0.054	5.26
LiSi	*I41/a*	DNP	LDA-PWC	a = 9.178 c = 5.655	-	
LiSi	*I41/a*	DNP	GGA-PBE	a = 9.347 c = 5.758	0.054	5.26

Table 3-1 illustrates configurations used when the geometries of lithium monosilicide (LiSi) unit cells were optimised to a relaxed state. The LiSi system has a tetragonal symmetry and belongs to the *I41/a* space group. The experimental value of the lattice parameter ***a*** for LiSi is 9.34 Å, and 5.76 Å for the ***c*** parameter. When the DND basis set was selected, the LDA functional used, and the symmetry lowered to P1, the calculated values of ***a*** and ***c*** were seen to be 9.191 Å and 5.652 Å respectively. These values agree with experiments to within 1.60% and 1.88% for the ***a*** and ***c*** parameters respectively. When the configuration used in relaxing the geometry of LiSi was retained, but with only the symmetry imposed to *I41/a*, the resulting lattice values remained unchanged.

The basis set was then changed to DNP whilst the functional employed remained to be LDA, and the symmetry P1; calculated lattice parameters changed to 9.178 Å for ***a*** and 5.655 Å for ***c*** parameter. The percentage differences for these values are 1.73% and 1.82% respectively. When the configuration was retained for this calculation, but with an imposed symmetry of *I41/a*, like those of the DND basis set, the lattice parameter values did not change.

As illustrated in Table 3-1, the performance of the GGA functional on LiSi was evaluated. What becomes noticeable, is that when the symmetry is lowered to P1, whilst the DND basis set is employed, the values depict a similar trend for the imposed *I41/a* symmetry in comparison to results found when LDA was used. The lattice parameter values are noted to be 9.355 Å and 5.757 Å for ***a*** and ***c*** respectively. The percentage difference for these values is 0.16% for the ***a*** parameter and 0.05% for the ***c*** parameter. When the basis set is changed to DNP, the ***a*** parameter changes to 9.347 Å and ***c*** parameter to 5.758 Å for the P1 symmetry; the differences are 0.07% and 0.35% respectively. For the *I41/a* symmetry, the ***a*** changes to 9.347 Å and the ***c*** parameter changes to 5.758 Å; the percentage difference now becomes 0.07% and 0.35%.

The calculated lattice parameter for the lithium monosilicide is in agreement with available experimental values to within a percentage difference less than 2% despite that the symmetry is lowered to P1. However, what is noticeable is that when the functional is changed to GGA, the values improve to a percentage difference of less than 1%. It is as well evident that the LDA fails to estimate the lithium monosilicide bandgap for both P1 and *I41/a* symmetry regardless of the basis set selected. According to experiments, the bandgap of LiSi is ~0.057 eV for temperatures less than 450K [9]; as depicted in Table 3-1, the calculated bandgap is 0.054 eV which agrees to a 5.26% difference.

What is also noted is that for the lower P1 symmetry, the bandgap is overestimated by 53.63% for the DND basis set, and 43.68% for the DNP basis set. These observations suggest that the suitable basis set and functional for predicting electronic and physical properties of LiSi would be DNP and GGA respectively.

The reference samples necessary for generating potentials that will handle lithiated silicon systems include bulk lithium and silicon. It, therefore, becomes necessary to evaluate how the GGA and DNP treat bulk lithium and bulk silicon systems.

Table 3-2. Configurations used during the structural relaxation of lithium (Li) and the calculated results.

System	Space Group	Basis 4.4	Functional	Lattice(Å) a = 3.51 [160]	% Diff
Li	P1	DND	LDA-PWC	a: 3.164	9.86
Li	P1	DND	GGA-PBE	a: 3.229	8.01
Li	P1	DNP	LDA-PWC	a: 3.164	9.86
Li	P1	DNP	GGA-PBE	a: 3.217	8.35
Li	*Im-3m*	DND	LDA-PWC	a: 3.164	9.86
Li	*Im-3m*	DND	GGA-PBE	a: 3.231	7.95
Li	*Im-3m*	DNP	LDA-PWC	a: 3.164	9.86
Li	*Im-3m*	DNP	GGA-PBE	a: 3.219	8.29

Two symmetries were used in relaxing the geometry of lithium, namely the P1 and the *Im-3m* symmetry. The suitability of the functional and the basis set type was assessed for the bulk lithium system. Table 3-2 reflects that the GGA functional yielded better estimates of the lattice parameter values for lithium. This is asserted by lower percentage differences obtained by comparing the calculated values using GGA and LDA to that reported from experiments. For both P1 and *Im-3m* symmetry, Table 3-2 suggests that the basis set does not affect the lattice values. This observation is brought forth by noting that for P1 the value of ***a***, 3.164 Å, is the same when both DND and DNP are employed using LDA. However, when GGA is employed, the lattice parameter changes for both the DND and DNP basis set. It is evident from the results that a combination of DND basis set and GGA functional would be recommendable for relaxing the bulk lithium system as the percentages differences, 8.01% and 7.95%, are least for both symmetries.

Table 3-3. Configurations used during the structural relaxation of silicon (Si) and the calculated results.

System	Space Group	Basis 4.4	Functional	Lattice(Å) a = 5.43 [19]	% Diff	Bandgap (eV) 1.17 [161]	% Diff
Si	P1	DND	LDA-PWC	a: 5.409	0.39	0.569	51.37
Si	P1	DND	GGA-PBE	a: 5.446	0.29	0.759	35.13
Si	P1	DNP	LDA-PWC	a: 5.409	0.39	0.569	51.37
Si	P1	DNP	GGA-PBE	a: 5.446	0.29	0.759	35.13
Si	*Fd-3m*	DND	LDA-PWC	a: 5.409	0.39	0.683	41.62
Si	*Fd-3m*	DND	GGA-PBE	a: 5.446	0.29	0.913	21.97
Si	*Fd-3m*	DNP	LDA-PWC	a: 5.409	0.39	0.683	41.62
Si	*Fd-3m*	DNP	GGA-PBE	a: 5.446	0.29	0.913	21.97

A comparison of calculated results for the low P1 symmetry and that of the *Fd-3m* symmetry is presented by Table 3-3 in reference to experimental values of the lattice constant ***a***, 5.43 Å, and the indirect bandgap, 1.17 eV at 0K, for silicon. Two functionals LDA and GGA, as well as two basis set types, DND and DNP,

implemented within the DMol^3 simulation code, were employed on the silicon system. Both the bandgap, 0.569 eV, and lattice parameter, 5.409 Å, estimates for the low P1 symmetry remain unchanged when the LDA functional is employed whilst the basis set is varied. Again the bandgap, 0.759 eV, and the lattice parameter, 5.446 Å, do not change for the P1 symmetry when the GGA functional is used whilst the basis set is varied. When considering the calculations conducted on the silicon system of the *Fd-3m* symmetry, it becomes clear that the trend on the P1 symmetry for the LDA and GGA calculations is present as well. Thus, the lattice, 5.409 Å, and bandgap, 0.683 eV, do not vary when LDA is employed whilst the basis set is varied between DND and DNP, and a similar result is noticed when GGA is employed. Table 3-3 suggests that either of the two basis sets, DND and DNP can give good estimates of silicon properties, but it is worth noting that the GGA functional gives better estimates because the lattice values agree with experiments to within a 0.29% difference. Although the bandgap is underestimated for both symmetries, what is noteworthy is that lowering the symmetry further decreases the accuracy. However, it can be generalised that GGA would likely give better bandgap estimates. The least percentage difference of the bandgap underestimate was obtained to be 21.97%; which is somewhat a reasonable compromise as it is well known that traditional DFT underestimates the bandgap in solids. Considering all three reference systems (Li, Si and LiSi), it is noted that for GGA-PBE, there is no significant difference in the choice of basis set between DND and DNP. Having explored the effect of symmetry, functional and basis set on the reference samples, the influence effected by introducing thermal smearing in structural relaxation calculations is now considered.

3.1.2 Thermal smearing

The smearing approach may introduce computational simplicity by improving convergence of the SCF procedure, as is allows orbitals to relax more rapidly. This consequently aids in adjusting the duration a calculation requires to converge; however, the introduction of thermal smearing might affect the accuracy of the energy derivatives. Since it sometimes may be required to smear electrons in orbitals within a given range of the Fermi level, it becomes useful to assess the influence resulting from the use of small and large smearing values.

Table 3-4. The effect of thermal smearing during the structural relaxation of lithium

System	Basis 4.4	Functional	Quality	Smearing (Ha)	Lattice (Å) a=3.51 **[160]**	% Diff
Li	DNP	GGA-PBE	Fine	0.005	3.419	2.59
Li	DNP	GGA-PBE	Fine	0.000	3.390	3.42
				0.010	3.477	0.94
				0.020	**3.494**	**0.46**
				0.030	3.469	1.17
				0.040	3.691	5.16
				0.050	3.870	10.25
Li	DNP	GGA-PBE	Fine	0.035	3.587	2.19
				0.034	3.556	1.31
				0.033	**3.510**	**0.00**
				0.032	3.482	0.80
				0.031	3.477	0.94

Table 3-5. The effect of thermal smearing during the structural relaxation of silicon

System	Basis 4.4	Functional	Quality	Smearing (Ha)	Lattice (Å) a=5.43 [19]	% Diff	Bandgap (eV)	% Diff
Si	DNP	GGA-PBE	Fine	0.005	5.446	0.29	0.913	21.97
Si	DNP	GGA-PBE	Fine	0.000	5.445	0.28	0.913	21.97
				0.010	5.445	0.28	0.916	21.71
				0.020	**5.448**	**0.33**	**0.921**	**21.28**
				0.030	5.460	0.55	0.906	22.56
				0.040	5.482	0.96	0.863	26.24
				0.050	5.531	1.86	0.736	37.09
Si	DNP	GGA-PBE	Fine	0.025	5.452	0.41	0.916	21.37
				0.024	5.451	0.39	0.918	21.54
				0.023	5.450	0.37	0.919	21.54
				0.022	5.449	0.35	0.920	21.37
				0.021	**5.449**	**0.35**	**0.920**	**21.37**

At this point, the effects of the functionals and basis sets on the bulk systems have been shown. Now, Table 3-4 and Table 3-5 present the influence of introducing thermal smearing during the structural relaxation of bulk lithium and silicon systems. Smearing of 0.005 Ha, which is the default value in DMol^3 as implemented in Materials Studio, was used on lithium and silicon systems. The smearing was then varied in increments of 0.01 Ha from 0.000 Ha to 0.050 Ha for both systems.

It is shown in Table 3-4 that the accuracy in predicting the value of the lattice parameter for lithium decreases with the increase of smearing above 0.030 Ha. To sample a bit closer to the smearing value of 0.030 Ha, the smearing was varied in

decrements of 0.001 Ha from 0.035 Ha down to 0.031 Ha. It was deduced that smearing of 0.020 Ha yields a lattice parameter of 3.494 Å, which agrees with experiments to within 0.46%. By varying the smearing around 0.030 Ha it was found that smearing of 0.033 Ha yields a better estimate, 3.510 Å which agrees with experiments to within a difference of 0.00%.

As reflected by results in Table 3-5, silicon can be brought to ground state energy using thermal smearing of values from 0.000 Ha to 0.050 Ha. However, when considering both the lattice and the bandgap, smearing values above 0.020 Ha tend to generally increase the magnitude by which the bandgap is underestimated. In sampling the smearing values around 0.020 Ha, it is noted that when the values were varied in decrements of 0.001 Ha from 0.025 Ha to 0.020 Ha, the smearing with better accuracy was detected to be 0.021 Ha. Nonetheless, 0.020 Ha appears to be better as it corresponds to a lattice parameter of 5.448 Å and a bandgap of 0.921 eV, of which these values agree with experiments to within 0.33% and 21.28% respectively. Once more the 21.28% underestimation of the bandgap can be attributed to the limits of traditional DFT, and would, in essence, require extensions which include the use of hybrid functionals to improve the accuracy.

After noting the influence caused by lowering symmetry, the choice of a suitable functional and basis set, as well as the application of thermal smearing, the reference input models are then transferred to the DFTB+ environment. These insights feed to the configuration required to derive the self-consistent charge density functional tight-binding Slater-Koster potentials.

3.2 Derivation of Slater-Koster Potentials

3.2.1 Target systems, reference samples and data coverage

The DFTB+ code makes it possible for *ab initio* calculations to be performed on large systems, and this quality is desirable for studying complex systems of silicon. It is, however, necessary for a Slater-Koster (S-K) library to be present to use the tasks embedded within the code. One of these tasks is parameterisation, which is used to derive tight-binding potentials, and the details are then stored in the skflib file.

The target is to derive S-K potentials that will handle various lithiated silicon systems. Hence, the samples used as reference are presented below. To successfully

generate potentials, the conformational coverage should first be defined. Each sample structure will introduce specific contributions to the fitting process when element pairs are evaluated.

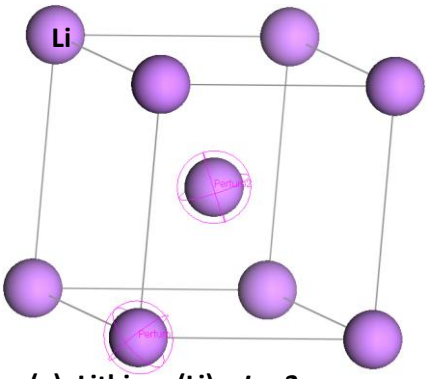

(a) Lithium (Li) – *Im-3m*

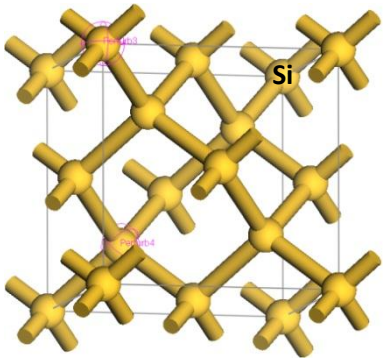

(b) Silicon (Si) – *Fd-3m*

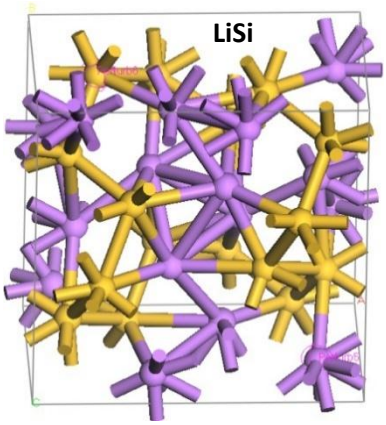

(c) Lithium silicide (LiSi) – *I41/a*

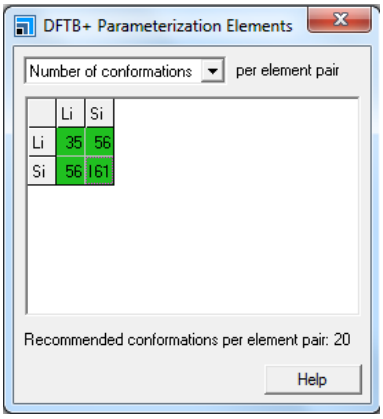

(d) Conformational coverage

Figure 3-1. Reference samples used as input and the conformational coverage required for parameterisation.

The Figure 3-1 depicts the standard unit cells of systems which were used as input for the parameterisation, namely (a) body-centered-cubic lithium belonging to the *Im-3m* space group, (b) a face-centered-cubic silicon belonging the *Fd-3m* space group and (c) a tetragonal lithium monosilicide belonging to the *I41/a* space group. The diagram labelled (d) illustrates the conformational coverage for the element pairs included in the calculation setup. The potentials cover the Si-Si, Li-Li and the Li-Si interactions. The parameterisation was employed within the potential mode, wherein the input systems were scaled and their atoms perturbed. The functional used for parameterisation was set to GGA and the basis set inherited from the DMol^3 settings was DND.

3.3 Preliminary Tests of Derived Slater-Koster Potentials Using DFTB+

Preliminary tests were conducted on the derived Slater-Koster potentials by performing structural relaxation calculations on the Si, Li and LiSi systems using the DFTB+ code. The objective was to assess the initial level of accuracy of the potentials' ability to reproduce known material properties. The calculations were performed according to the following setup: the smart algorithm was employed, 0.02 kcal/mol was used to converge the energy within a maximum of 500 iterations, the electronic integration tolerance was set to a fine quality, the SCF tolerance was set to 1.0×10^{-8}, the maximum SCF iteration was 100 and a thermal smearing of 0.02 Ha was applied. Furthermore, for comparison purposes, the potentials were also evaluated for the LiSi system using the setup described above, but without the application of thermal smearing (*i.e.* 0.00 Ha).

Table 3-6. Optimisation of systems using Slater-Koster potentials derived by using only the LiSi system as parameterisation reference structure.

		Lattice (Å)			Density (g/cm^3)			Bandgap (eV)		
System: Group	**k-mesh**	**Calc.**	**Exp.**	**%diff**	**Calc.**	**Exp.**	**%diff**	**Calc.**	**Exp.**	**%diff**
Li : *Im-3m*	29x29x29	a = 4.025	3.51	14.67	0.354	0.533	33.58			
Si : *Fd-3m*	11x11x11	a = 5.415	5.43	0.28	2.349	2.329	0.86	4.463	1.17	281.45
Li-Si : *I41/a*	11x11x12	a = 9.710	9.34	3.96	1.749	1.852	5.56	0.381	0.057	568.00
		c = 5.643	5.76	2.03						

Table 3-7. Optimisation of systems using Slater-Koster potentials derived by using Li, Si and LiSi systems as parameterisation reference structures.

		Lattice (Å)			Density (g/cm^3)			Bandgap (eV)		
System: Group	**k-mesh**	**Calc.**	**Exp.**	**%diff**	**Calc.**	**Exp.**	**%diff**	**Calc.**	**Exp.**	**%diff**
Li : *Im-3m*	29x29x29	a = 3.527	3.51	0.48	0.525	0.533	1.50			
Si : *Fd-3m*	11x11x11	a = 5.419	5.43	0.20	2.345	2.329	0.69	4.463	1.17	281.45
Li-Si : *I41/a*	11x11x12	a = 10.115	9.34	8.30	1.381	1.852	25.43	0.000	0.057	100
		c = 6.587	5.76	14.36						

Two sets of Slater-Koster potentials were developed using the DFTB+ code. The first set was prepared by using only a standard unit cell of bulk LiSi as the primary input reference system for the parameterisation task. The second was prepared by using a combined set of structures comprised of Li, Si and LiSi as input reference systems. Table 3-6 presents values of the calculated lattice constants, density and bandgap obtained by employing the first set of potentials. Table 3-7 presents the lattice constants, density and bandgap values obtained when the second set was used.

The calculations in both tables were done to converge the systems such that their properties conformed to ground state energy.

Table 3-6 illustrates that the lattice constant for Si has been well reproduced as it agrees with experiments to within a difference of 0.28%. The lattice constant for cubic lithium has been overestimated, for it was found to differ by 14.67%. As for the LiSi system, it was shown that the lattice constants are generally less than 4% different from experiments. The prediction accuracy of the set of potentials used is poor since it would ideally be desirable for all systems consisting of either Li or Si or an alloy of the two, to be well reproduced.

By considering Table 3-7, one notices that the accuracy in predicting the properties of pure Si and Li has been greatly improved. The lithium lattice agrees with experiments to within 0.48%, which is a significant improvement from the 14.67% reflected in Table 3-6. Silicon properties did not vary much when the second set of potentials was employed. The results agree with experiments with a difference of less than 1%. However, the structural properties of LiSi were compromised as it now becomes evident that the ***c*** parameter is overestimated by 14.36% when compared to the known experimental value of 5.76 Å.

Lithium is metallic and therefore has no bandgap, but calculations on silicon and lithium monosilicide are expected to yield bandgaps. The two sets of potentials overestimate the bandgap in silicon by over 200%. The first Slater-Koster potentials estimated a bandgap of 0.381 eV for LiSi, which is a huge deviation of over 500% from the known experimental value ~0.057 eV. The second set of potentials also did no improvement to the estimated LiSi bandgap value. Since thermal smearing of 0.020 Ha was applied for both Table 3-6 and Table 3-7 calculations, a quick look into how omitting the application of thermal smearing would affect the accuracy in predicting properties of the LiSi system became necessary.

Table 3-8. Optimisation of the LiSi system using S-K potentials derived by using only the LiSi.

		Lattice (Å)						
System: Group	**k-mesh**	**Calc.**	**Exp.**	**%diff**	**Density (g/cm^3)**	**%diff**	**Bandgap (eV)**	**%diff**
Li-Si : *I41/a*	11x11x12	a = 9.705 c = 5.658	9.34 5.76	3.91 1.77	1.746	5.72	0.408	615.79

Table 3-9. Optimisation of the LiSi system using Slater-Koster potentials derived by using Li, Si and LiSi.

		Lattice (Å)						
System: Group	**k-mesh**	**Calc.**	**Exp.**	**%diff**	**Density (g/cm^3)**	**%diff**	**Bandgap (eV)**	**%diff**
Li-Si : *I41/a*	11x11x12	a = 11.105	9.34	18.90	1.422	23.22	0.190	233.33
		c = 5.306	5.76	7.88				

The above tables present the results obtained when thermal smearing was omitted from the calculations. A comparison of results in Table 3-6 to those in Table 3-8, depicts a minute variation (of 0.05% and 0.26%) in producing the lattice parameters of LiSi. The differences have changed from 3.96% to 3.91% for ***a***, 2.03% to 1.77% for ***c*** when the first set of Slater-Koster potentials was employed. The bandgap too was even more badly estimated as it was found to be over 600% for the first set of potentials and over 200% for the second set.

Generally, lithium insertion into silicon systems is of interest because the insight gained from studying lithiated silicon would be crucial for high-energy-density battery applications. It thus suggests that using a combination of Si, Li and LiSi systems would be a better option for parameterisation than just using a unit cell of LiSi as the sole input reference sample. Furthermore, the variety of input systems could avail a wider atomic environment, and would, in essence, permit various phases with different *atm.* % of lithium in silicon to be handled with reasonable accuracy by the potentials.

And of course, using a variety of input systems is not the solitary aspect to be considered, because several factors could effectively limit the extent by which derived Slater-Koster potentials can accurately predict material properties. It is sensible to as well infer that since the parameterisation task implemented within the DFTB+ code inherits details of structures prepared and imported from DMol^3, the accuracy of potentials could also be limited by level to which the DMol^3 results agree to experiments.

This prompts for the geometry of Li, Si and LiSi to be well optimised within the DMol^3 environment before transferring the structures to DFTB+. One aspect that was not included in preparing the systems used for generating the potentials evaluated in Table 3-6 to Table 3-9, is using suitable Monkhorst–Pack k-point meshes. Hence,

obtaining suitable k-points for the respective input structures is thus necessary for improving accuracy.

3.4 Adjusting Reference Samples with a Note on K-Point Sampling Using DMol^3

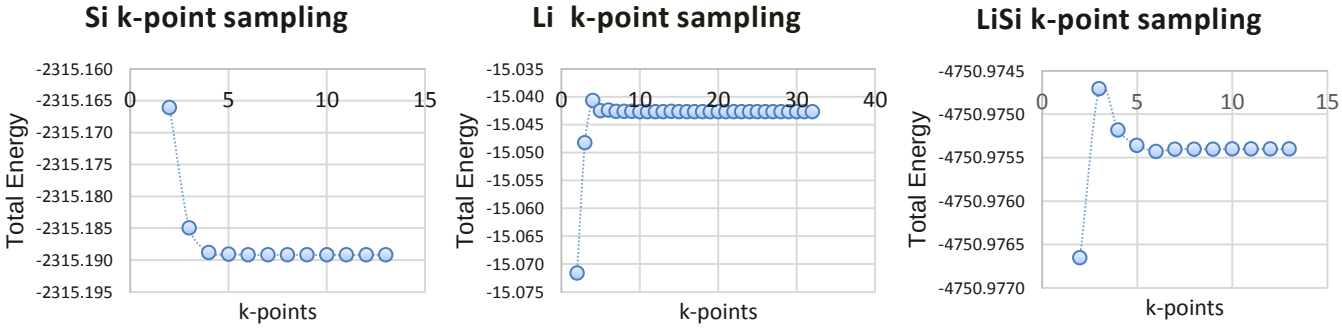

Figure 3-2. k-points convergence plots for lithium, silicon and lithium monosilicide

Table 3-10. Structural properties for Si, Li and Li-Si systems

System	Functional	k-mesh	Lattice (Å)	
			This work	Experiment
Li	GGA-PBE	28x28x28	a = 3.504	3.51 [160]
Si	GGA-PBE	10x10x10	a = 5.472	5.43 [19]
LiSi	GGA-PBE	10x10x11	a = 9.354 c = 5.761	9.34 [159] 5.76 [159]

As shown by Figure 3-2, single-point-energy calculations were conducted in order to converge the k-points for Li, Si and LiSi. Table 3-10 presents the lattice parameters obtained when the noted k-points were applied during the structure relaxation calculations. For the exchange-correlation function, the GGA-PBE functional was adopted and employed for all the three systems. As suggested by the convergence plots, a k-point mesh of 28x28x28 was used for Li, 10x10x10 for Si and 10x10x11 for LiSi.

The calculated lattice constants are 3.504 Å and 5.472 Å, for Li and Si respectively. As for the LiSi system, the values 9.354 Å and 5.761 Å were obtained for ***a*** and ***c*** parameters respectively. All the values presented by Table 3-10 as calculated in this work agree with experiments to within a difference less than 1%. After geometry optimisation calculations are carried out to a point wherein material properties can be reproduced with reasonable accuracy in comparison to experiments, attempts to generate Slater-Koster potentials can then be made.

3.5 Slater-Koster Potentials Refinement

After sample structures have been relaxed to ground-state energy using DMol^3 and their properties agree to available experimental values, the parameter sets could then be generated. However, the parameterisation task as implemented in the Materials Studio simulation package requires that suitable configuration be set up to generate sets with best fits. Various parameters were tested to arrive at the setup with the least fitting error. These parameters include k-point, cut-off radius scaling, covalent (compression) radii and the parameterisation mode. The following tables present the output obtained when varying the parameterisation setup.

As a start, the cut-off scaling and k-points are evaluated using the potential mode of parameterisation.

Table 3-11. Parameterisation fits obtained by using potential mode, a variation of k-points and number of cut-off steps, a minimum cut-off factor of 1.3 and a maximum cut-off factor of 1.6.

k-points	Basis	Functional	Cut-off Steps	Fit	Cut-off factor	Covalent Radii1 Li, Si	Polynomial Degree	Total Error
Li: 8x8x8 **LiSi:** 3x3x4 **Si:** 6x6x6	DND	PBE	16	16	1.600	2.00	9	1.006
8x8x8	DND	PBE	16	10	1.480	2.00	10	0.192
9x9x9	DND	PBE	16	16	1.600	2.00	10	0.388
10x10x10	DND	PBE	16	11	1.500	2.00	10	0.275
11x11x11	DND	PBE	16	2	1.320	2.00	10	0.563
29x29x29	DND	PBE	16	6	1.400	2.00	10	190.900
10x10x10	DND	PBE	32	31	1.600	2.00	10	0.144
Li: 8x8x8 **LiSi:** 3x3x4 **Si:** 6x6x6	DND	PBE	32	32	1.600	2.00	9	0.651
29x29x29	DND	PBE	32	4	1.329	2.00	10	194.400
Li: 8x8x8 **LiSi:** 3x3x4 **Si:** 6x6x6	DND	PBE	32	22	1.503	2.00	10	0.264

The parameterisation task generated several libraries containing many fits, and the best in each set was selected. Table 3-11 presents configurations used for each of these best-fit runs and their corresponding total error. As notated in the table above, three sample structures, lithium, lithium monosilicide and silicon were used as input to the parameterisation process. The DND basis set and the GGA-PBE functional were applied in relaxing all the sample structures using DMol^3, and this setting was

as a result adapted into the DFTB+ environment. The cut-off steps, which specify the number of conformations to be generated by the parameterisation, were set to a maximum of 16, and other runs were set to 32 steps for comparison.

To evaluate if using a fine k-point mesh would automatically reduce the total error in fits, the k-point sets were varied. For some of the fits, the quality of the integration accuracy was set to a k-point separation distance of 0.04/Å and applied to individual sample structures. This corresponded to an 8x8x8 k-point mesh for Li, 6x6x6 for Si, 3x3x4 for LiSi. On the other hand, a single mesh was applied across all structures during parameterisation. Thus, 8x8x8 was applied to all structures, 9x9x9, 10x10x10, 11x11x11 and 29x29x29 in a similar manner.

Although it could be assumed that a finer mesh provided by a large k-point set would bring improvement to the accuracy in calculations, it is noticeable from results in Table 3-11 that the 29x29x29 k-point mesh yielded the highest error, 194.900, whereas the 10x10x10 yielded the least error with the value 0.114. The difference suggests that using a larger number of k-points will not necessarily reduce the error present within parameter sets during fitting. This result also corresponds to the 31st fit, which could mean that using a higher number of cut-off steps could aid in sampling enough conformations and hopefully arriving at a fit with even lower error.

At times when the quality of fits obtained is not satisfactory, it becomes helpful to proceed by further refining the parameter sets using the density mode of parameterisation.

Table 3-12. Parameterisation fits obtained by using density mode, a variation of k-points and number of cut-off steps, a minimum cut-off factor of 1.3 and a maximum cut-off factor of 1.6.

k-points	Basis	Functional	Cut-off Steps	Fit	Cut-off factor	Covalent Radii1 Li, Si	Covalent Radii 2 Li, Si	Polynomial Degree	Total Error
Li: 8x8x8 **LiSi:** 3x3x4 **Si:** 6x6x6	DND	PBE	16	12	1.520	2.00	6	10	0.833
10x10x10	DND	PBE	16	16	1.600	2.00	6	9	0.878
29x29x29	DND	PBE	16	3	1.340	2.00	6	10	210.800

Table 3-12 presents the best fits obtained when the density mode of parameterisation was employed. The cut-off number of steps was set to 16 to note

the effect of using additional compression radii. The fit obtained by applying a k-point separation of 0.04 yielded better results corresponding to a total error of 0.833, compared to the 29x29x29 mesh with a total error of 210.800. This fit is however poor compared to that presented in Table 3-11. This observation suggests that compression radii should be varied to improve the fitting quality.

Before the density mode can be further used in an attempt to refinine parameter sets, it is better to vary the first compression radii within the potential mode. It would be when the mode fails to improve the accuracy of fits, that the additional compression radii are varied using the density mode of parameterisation.

Table 3-13. Parameterisation fits obtained by using potential mode, a variation of k-points, number of cut-off steps and covalent radii1, basis: DND, functional: PBE, min cut-off factor: 1.1, max cut-off factor: 1.8

k-points	Cut-off Steps	Fit	Cut-off factor	Covalent Radii1:Li	Covalent Radii1:Si	Polynomial Degree	Total Error
8x8x8	16	8	1.427	2.51	2.19	10	0.242
8x8x8	32	15	1.416	2.51	2.19	10	0.257
10x10x10	16	8	1.427	2.51	2.19	10	0.208
10x10x10	32	31	1.800	2.51	2.19	10	0.585
18x18x18	16	16	1.800	2.51	2.19	9	0.261
18x18x18	32	4	1.168	2.51	2.19	10	0.243
29x29x29	16	16	1.800	2.51	2.19	10	156.700
29x29x29	32	28	1.710	2.51	2.19	10	156.000

The scaling factor was lowered to a minimum of 1.1 and the maximum increased to 1.8. The covalent radii were set to correspond to the experimental value of the covalent radii in Si and Li. The radii were set to 2.51 Bohr and 2.19 Bohr for Li and Si respectively. The cut-off steps were varied between a maximum of 16 and 32. The resulting fits with least error in generated sets are presented by Table 3-13. The fit with the lowest error was found to correspond to a configuration that applies a k-point set of 10x10x10 and cut-off steps of 16 conformations. The 8th conformation in the configuration yielded a total error of 0.208. This observation indicates that one may have to alternate between varying the radii, k-points, and cut-off steps a bit further.

Table 3-14. Parameterisation fits obtained by using density mode, a variation of k-points, number of cut-off steps and covalent radii1 & 2, basis: DND, functional: PBE, min cut-off factor: 1.1, max cut-off factor: 1.8

k-points	Cut-off Steps	Fit	Cut-off factor	Covalent Radii1:Li	Covalent Radii1:Si	Covalent Radii2:Li	Covalent Radii2:Si	Polynomial Degree	Total Err
8x8x8	16	6	1.333	2.51	2.19	6	6	10	0.143
8x8x8	32	11	1.326	2.51	2.19	6	6	10	0.120
10x10x10	16	6	1.333	2.51	2.19	6	6	10	0.199
10x10x10	32	12	1.348	2.51	2.19	6	6	10	0.136
18x18x18	16	12	1.613	2.51	2.19	6	6	10	0.172
18x18x18	32	18	1.484	2.51	2.19	6	6	10	0.126
29x29x29	16	16	1.800	2.51	2.19	6	6	10	156.400
29x29x29	32	32	1.800	2.51	2.19	6	6	10	153.900

Table 3-14 presents fits obtained by applying a combination of varying k-points, cut-off scaling factor, cut-off steps and introducing additional compression radii through the density mode of parameterisation. This approach yielded the best fit result even better than the one presented in Table 3-11. Part of the guide in selecting the compression radii was the experimental covalent radii of Li and Si, which are 2.51 Bohr and 2.19 Bohr respectively. The total error was reduced from 0.144 to 0.120. This improvement posits that using a wide range of scaling factor, a larger number of k-points and a higher number of cut-off steps will not primarily be the magic trick toward yielding least error during fitting; but, varying the compression radii may impose a greater impact to the accuracy of the generated parameter sets.

Table 3-15. Parameterisation fits obtained by using potential mode, a variation of Li covalent radii1 (1.5 – 6.5), basis: DND, functional: PBE, min cut-off factor: 1.1, max cut-off factor: 1.8

k-points	Cut-off Steps	Fit	Cut-off factor	Covalent Radii1:Li	Covalent Radii1:Si	Polynomial Degree	Total Error
18x18x18	32	16	1.439	1.50	2.00	10	0.631
18x18x18	32	16	1.439	2.00	2.00	10	0.245
18x18x18	32	6	1.213	2.50	2.00	10	0.247
18x18x18	32	5	1.190	3.00	2.00	10	0.233
18x18x18	32	32	1.800	3.50	2.00	9	0.179
18x18x18	32	32	1.800	4.00	2.00	9	0.356
18x18x18	32	32	1.800	4.50	2.00	9	0.128
18x18x18	32	27	1.687	5.00	2.00	9	0.389
18x18x18	32	17	1.461	5.50	2.00	10	0.481
18x18x18	32	19	1.506	6.00	2.00	10	0.599
18x18x18	32	17	1.461	6.50	2.00	10	0.578

As presented by Table 3-15, the k-points and cut-off steps were fixed at 18x18x18 and 32 respectively. The compression radius of silicon was kept at 2.00 Bohr whilst that of Li was systematically increased from 1.5 to 6.50 Bohr. The best fit was found to correspond to compression radii of 4.5 Bohr for Li. These results illustrate that when varying the compression radius of Li, keeping the values to a minimum of around 2.0 Bohr and a maximum of 4.5 Bohr could aid in ensuring that the fitting accuracy is improved.

Table 3-16. Parameterisation fits obtained by using potential mode, a variation of Si covalent radii1 (1.5 – 6.5), Li covalent radii1 (2.0) basis: DND, functional: PBE, min cut-off factor: 1.1, max cut-off factor: 1.8

k-points	Cut-off Steps	Fit	Cut-off factor	Covalent Radii1:Li	Covalent Radii1:Si	Polynomial Degree	Total Error
18x18x18	32	27	1.687	2.00	1.50	9	0.206
18x18x18	32	16	1.439	2.00	2.00	10	0.245
18x18x18	32	17	1.461	2.00	2.50	10	0.213
18x18x18	32	26	1.665	2.00	3.00	9	0.216
18x18x18	32	27	1.687	2.00	3.50	9	0.129
18x18x18	32	27	1.687	2.00	4.00	9	0.221
18x18x18	32	30	1.755	2.00	4.50	9	0.103
18x18x18	32	17	1.461	2.00	5.00	10	0.314
18x18x18	32	17	1.461	2.00	5.50	10	0.146
18x18x18	32	27	1.687	2.00	6.00	9	0.214
18x18x18	32	31	1.777	2.00	6.50	9	0.154

To evaluate the applicable range for varying the compression radius in Si, the radii of Li was kept at 2.00 Bohr whilst that of Si was systematically varied from 1.5 to 6.5 Bohr. This variation yielded a conformation with a total fitting error of 0.103 corresponding to the 30^{th} fit. This result is an improvement compared to those presented from Tables 3-11 through to 3-15. Although this is the smallest total error in Table 3-16, it appears it may be possible to achieve conformations with smaller errors beyond a radius of 4.5 Bohr for Si. At this point, it is safe to say that the range is wider than that of Li.

With the insight presented by Tables 3-11 to 3-16, it makes sense to check if the result in Table 3-16 can be further improved using a smaller number of k-points since the error of 0.103 was achieved using 18x18x18.

Table 3-17. Parameterisation fits obtained by using potential mode, a variation of Li covalent radii1 (2.1 – 2.9), Si covalent radii1 (1.8), basis: DND, functional: PBE, min cut-off factor: 1.1, max cut-off factor: 1.8

k-points	Cut-off Steps	Fit	Cut-off factor	Covalent Radii1 - Li	Covalent Radii1 - Si	Polynomial Degree	Total Error
Fine	32	32	1.800	2.10	1.80	9	0.125
Fine	32	28	1.710	2.20	1.80	9	0.162
Fine	32	23	1.597	2.30	1.80	10	0.210
Fine	32	31	1.777	2.40	1.80	10	0.184
Fine	32	31	1.777	2.50	1.80	10	0.199
Fine	32	32	1.800	2.60	1.80	9	0.109
Fine	32	32	1.800	2.70	1.80	9	0.145
Fine	32	30	1.755	2.80	1.80	10	0.189
Fine	32	32	1.800	2.90	1.80	9	0.126

The results presented by Table 3-17 are based on parameterisation done using the fine integration quality, a k-point scheme corresponding to a 6x6x6 grid. Aside from k-points, in this set of fits, two other parameters were kept unchanged. Thus, the cut-off steps were fixed at 32 and the compression radii of Si was set to 1.8 Bohr. The parameterisation was then done by systematically varying the radii of Li in increments of 0.1 Bohr from 2.10 up to 2.90 Bohr. The 32nd fit in the sets was noted to be of the least error corresponding to the total error of 0.109. A comparison of this result to the one presented in Table 3-16, with a total error of 0.103, indicates that parameterisation accuracy may not largely depend on the use of a large number of k-points.

Table 3-18. Parameterisation fits obtained by using potential mode, a variation of Li covalent radii1 (2.1 – 2.9), Si Covalent radii1 (1.9) basis: DND, functional: PBE, min cut-off factor: 1.1, max cut-off factor: 1.8

k-points	Cut-off Steps	Fit	Cut-off factor	Covalent Radii1 - Li	Covalent Radii1 - Si	Polynomial Degree	Total Error
Fine	32	32	1.800	2.10	1.90	10	0.200
Fine	32	32	1.800	2.20	1.90	9	0.202
Fine	32	31	1.777	2.30	1.90	10	0.260
Fine	32	32	1.800	2.40	1.90	9	0.124
Fine	32	32	1.800	2.50	1.90	9	0.051
Fine	32	32	1.800	2.60	1.90	9	0.146
Fine	32	17	1.461	2.70	1.90	10	0.297
Fine	32	17	1.461	2.80	1.90	10	0.189
Fine	32	32	1.800	2.90	1.90	9	0.455

At this point, is has been shown in Table 3.16 that concerning the Li-Si system, it is not necessary to employ a large number of k-points during the parameterisation process. As such, Table 3-18 substantiates this observation in that a better result with a fit yielding a total error of 0.051 is presented. This result was obtained by using a k-point scheme of 6x6x6, fixing the cut-off number of steps to 32 and the compression radii of silicon to 1.9 Bohr, whilst systemically increasing the radii of Li from 2.10 to 2.9 Bohrs. Tables 3-13 through to 3-18 present a strategy that focuses primarily on yielding a fit with the least total fitting error within the potential mode of parameterisation. This approach implies that only the wave function confinement radii are put to perspective. To note the accuracy further, it becomes necessary to evaluate a selected range of the S-K libraries on known geometric and electronic properties present in the reference systems; and if need be, the density mode of parameterisation can then be applied.

3.6 Selection of Slater-Koster Library From Refined Sets of Potentials

Table 3-19. Validation of various sets of Slater-Koster potentials using structural details of LiSi; k-points used during parameterisation: 18x18x18, fitting mode: potential mode

SK-Library	System	Smearing	a	%diff	b	%diff	c	%diff
LiSi-P-18-CS-32-rd-Li-2.51-Si-2.19	LiSi	0.00	9.149	-2.15	9.149	-2.15	5.755	-0.09
	LiSi	0.02	9.150	-2.13	9.150	-2.13	5.752	-0.13
LiSi-P-18-CS-32-rd-Li-1.5-Si-2.0	LiSi	0.00	9.225	-1.34	9.225	-1.34	5.651	-1.9
	LiSi	0.02	9.224	-1.34	9.224	-1.34	5.649	-1.93
LiSi-P-18-CS-32-rd-Li-2.5-Si-2.0	LiSi	0.00	9.186	-1.75	9.186	-1.75	5.768	0.13
	LiSi	0.02	9.187	-1.74	9.187	-1.74	5.765	0.08
LiSi-P-18-CS-32-rd-Li-3.0-Si-2.0	LiSi	0.00	9.113	-2.53	9.113	-2.53	5.810	0.87
	LiSi	0.02	9.117	-2.49	9.117	-2.49	5.807	0.82
LiSi-P-18-CS-32-rd-Li-6.5-Si-2.0	LiSi	0.00	9.456	1.13	9.456	1.13	5.903	2.48
	LiSi	0.02	9.456	1.13	9.456	1.13	5.902	2.46

Table 3-20. Validations using the bandgap of Si, lattice parameter values of Si and Li

SK-Library	Smearing	Si Bandgap	%diff	Si (a)	%diff	Li (a)	%diff
LiSi-P-18-CS-32-rad-Li-2.51-Si-2.19	0.00	5.071	-333.4	5.318	-2.06	3.506	-0.13
	0.02	5.071	-333.4	5.318	-2.06	3.506	-0.13
LiSi-P-18-CS-32-rd-Li-1.5-Si-2.0	0.00	4.846	-314.2	5.220	-3.87	3.718	5.94
	0.02	4.605	-293.6	5.338	-1.70	3.718	5.93
LiSi-P-18-CS-32-rd-Li-2.5-Si-2.0	0.00	4.678	-299.8	5.301	-2.38	3.584	2.12

In some instances, it is possible that a specific S-K library though with the least fitting error, may not always be the most accurate one in predicting known properties of materials. As such, this necessitates further validation using parameters such as lattice constants, electronic bandgap, bond lengths, *etc*. Table 3-19 presents a list of selected S-K libraries generated by parameterising within the potential mode, using a grid of 18x18x18 k-points, 32 cut-off number of steps, and various confinement radii.

The geometries of the bulk tetrahedral LiSi systems were relaxed by interchanging between omitting and applying large thermal smearing of 0.02 Ha, to note the impact smearing introduces. This was also to assess if smearing is a requisite to converge these systems. The first row in Table 3-19 presents a library generated by setting the wave function confinement radii of cubic Li and cubic Si, to 2.51 Bohr and 2.19 Bohr respectively. From the second row, the table indicates libraries generated by varying the wave function confinement radius of Li in increments of 0.5 Bohr from 1.5 to 6.5 Bohr, whilst keeping that of Si fixed at 2.00 Bohr. The calculated lattice parameters ***a***, ***b*** and ***c*** for the LiSi system were generally underestimated or overestimated to within a difference of 2.6% in comparison to experiments. A focus on how the S-K libraries estimate the bandgap in Si shows that the potentials perform inaccurately as they underestimate the value by over 290% as illustrated by Table 3-20. In addition, Table 3-20, shows that the first set reproduces the lattice constant of Li to within less than 0.2% but underestimates the lattice constant of Si by 2.06% in comparison to experiments. As the confinement radii of Li are varied, it is shown that resulting potentials begin to generally overestimate the lattice parameter of Si whilst underestimating that of Li to within 4% and 6% respectively. These observations suggest that the density mode of parameterisation may be invoked to see if the accuracy of the generated potentials could be improved. However, since it was noted that using a large number of k-points during parameterisation is not always going to yield higher accuracy, it is worthwhile to check how the S-K libraries generated by using a smaller number of k-points perform.

Table 3-21. Validation of various sets of Slater-Koster potentials using structural details of LiSi; k-points used during parameterisation: quality set to fine, fitting mode: potential mode

SK-Library	System	Smearing	a	%diff	b	%diff	c	%diff
LiSi-P_Fine-CS-32-rd-Li-2.1-Si-1.9	LiSi	**0.00**	**9.516**	**1.78**	**9.516**	**1.78**	**5.873**	**1.96**
LiSi-P_Fine-CS-32-rd-Li-2.1-Si-2.1	LiSi	0.00	9.596	2.64	9.596	2.64	5.690	-1.21
LiSi-P_Fine-CS-32-rd-Li-2.7-Si-2.1	LiSi	0.00	9.576	2.42	9.576	2.42	5.920	2.77
	LiSi	0.02	9.575	2.40	9.575	2.40	5.920	2.78
LiSi-P_Fine-CS-32-rd-Li-2.9-Si-2.1	LiSi	**0.00**	**9.533**	**1.95**	**9.533**	**1.95**	**5.738**	**-0.39**
	LiSi	**0.02**	**9.536**	**1.99**	**9.536**	**1.99**	**5.732**	**-0.49**
LiSi-P_Fine-CS-32-rd-Li-2.1-Si-2.2	LiSi	0.00	9.393	0.46	9.393	0.46	5.990	3.99
	LiSi	0.02	9.395	0.48	9.395	0.48	5.986	3.92
LiSi-P_Fine-CS-32-rd-Li-2.7-Si-2.2	LiSi	0.00	9.453	1.10	9.453	1.10	5.885	2.17
	LiSi	0.02	9.459	1.16	9.459	1.16	5.877	2.02
LiSi-P_Fine-CS-32-rd-Li-2.1-Si-2.3	LiSi	0.02	9.361	0.11	9.361	0.11	5.988	3.96
LiSi-P_Fine-CS-32-rd-Li-2.7-Si-2.3	LiSi	0.00	9.381	0.33	9.381	0.33	5.947	3.24
	LiSi	0.02	9.387	0.40	9.387	0.40	5.939	3.11
LiSi-P_Fine-CS-32-rd-Li-2.9-Si-2.3	LiSi	0.00	9.403	0.57	9.403	0.57	5.921	2.79
	LiSi	0.02	9.411	0.66	9.411	0.66	5.912	2.64

Table 3-21 presents a selection of S-K libraries generated by using the potential mode of parameterisation, with the integration quality set to fine, which corresponds to a smaller number of k-points. The cut-off number of fitting steps was kept at 32, whilst the wave function confinement radii was varied systematically by 0.1 Bohr from 2.1 to 2.9 Bohr for Li, and from 1.9 Bohr to 2.3 Bohr for Si. Once again, thermal smearing of 0.02Ha was introduced during the geometry optimisation of the LiSi systems, and in other cases, the smearing was set to 0.00 Ha. By considering how the values of the lattice parameters in Table 3-21 generally change when smearing is applied, it becomes apparent that the ***a*** parameter tends to increase whilst **c** becomes reduced, both by a small margin. As the wave function confinement radius of Si is increased, it seems the average measure by which the calculated ***c*** parameter in the LiSi system differs from experiments value of ***c*** increases to about 2-3%. A look at the S-K libraries in the first and the fourth row of Table 3-21 together with corresponding results, indicates that there might be room for improvement if the wave function confinement radii of Li is kept or varied around 2.1 Bohr, whilst that of Si is fixed or varied around 1.9 Bohr.

Table 3-22. Validation of various sets of Slater-Koster potentials using structural details of LiSi; k-points used during parameterisation: quality set to fine, fitting mode: density mode

SK-Library	System	Smearing	a	%diff	b	%diff	c	%diff
LiSi-D_Fine-CS-32-rd-Li-2.1-Si-1.9_4.2-3.8	LiSi	**0.00**	**9.295**	-0.58	**9.295**	-0.58	**5.648**	**-1.94**
	LiSi	**0.02**	**9.296**	-0.58	**9.296**	-0.58	**5.646**	**-1.98**
LiSi-D_Fine-CS-32-rd-Li-2.1-Si-1.9_4.1-3.7	LiSi	0.00	9.211	-1.49	9.211	-1.49	5.655	-1.83
	LiSi	0.02	9.208	-1.51	9.208	-1.51	5.653	-1.85
LiSi-D_Fine-CS-32-rd-Li-2.15-Si-1.95_4.3-3.9	LiSi	**0.00**	**9.311**	**-0.42**	**9.311**	**-0.42**	**5.667**	**-1.61**
	LiSi	**0.02**	**9.312**	**-0.41**	**9.312**	**-0.41**	**5.665**	**-1.66**
LiSi-D_Fine-CS-32-rd-Li-2.15-Si-1.95_4.35-3.95	LiSi	0.00	9.219	-1.40	9.219	-1.40	5.712	-0.83
	LiSi	0.02	9.220	-1.39	9.220	-1.39	5.710	-0.87
LiSi-D_Fine-CS-32-rd-Li-2.1-Si-1.9_4.15-3.750	LiSi	0.00	9.185	-1.76	9.185	-1.76	5.679	-1.41
	LiSi	0.02	9.184	-1.77	9.184	-1.77	5.677	-1.44
LiSi-D_Fine-CS-32-rd-Li-2.1-Si-1.9_4.15-3.752	LiSi	0.00	9.533	1.96	9.533	1.96	5.621	-2.42
	LiSi	0.02	9.530	1.93	9.530	1.93	5.620	-2.43
LiSi-D_Fine-CS-32-rd-Li-2.1-Si-1.9_4.15-3.755	LiSi	0.00	9.228	-1.30	9.228	-1.30	5.668	-1.59
	LiSi	0.02	9.227	-1.32	9.227	-1.32	5.667	-1.61
LiSi-D_Fine-CS-32-rd-Li-2.1-Si-1.9_4.151-3.75	LiSi	**0.00**	**9.321**	-0.31	**9.321**	-0.31	**5.638**	**-2.12**
	LiSi	**0.02**	**9.321**	-0.31	**9.321**	-0.31	**5.636**	**-2.15**

Table 3-23. Validations using the bandgap of Si, lattice parameter value of Si and Li

SK-Library	Smearing	Si Bandgap	%diff	Si (a)	%diff	Li (a)	%diff
LiSi-D_Fine-CS-32-rd-Li-2.1-Si-1.9_4.2-3.8	0.00	**2.442**	108.7	**5.449**	0.34	**3.721**	**6.02**
	0.02	**2.418**	106.7	**5.452**	0.40	**3.721**	**6.02**
LiSi-D_Fine-CS-32-rd-Li-2.1-Si-1.9_4.151-3.75	0.00	**2.301**	96.67	**5.460**	0.55	**3.721**	**6.00**
	0.02	**2.277**	94.62	**5.463**	0.61	**3.721**	**6.00**

The observations made in Table 3-21 about fixing or varying the wave function confinement radii of Li and Si around 2.1 and 1.9 Bohr respectively were noted. As such, Table 3-22 presents a selection of S-K libraries that made use of this aspect. The libraries were generated by parameterising within the density mode, the cut-off number of fitting steps was kept at 32, the integration quality was set to a fine k-point mesh, then the density confinement radii was varied around 4.1 Bohr for Li, and around 3.7 Bohr for Si. As presented by Table 3-22, the calculated lattice parameter results for the LiSi system have generally been brought to a difference of less than 3% in comparison to experiments. The set of results in the 1st, 3rd and last rows of Table 3-22 are found to be closest to experimental values. It thus becomes necessary to evaluate how the SCC-DFTB parameter sets corresponding to the first and the last row results of Table 3-22 perform on bulk Li and Si. Table 3-23 presents

the quality by which these parameter sets can estimate the lattice constant for a cubic Si and Li systems, as well as the bandgap of Si. It is quite evident that the lattice parameter of Li is overestimated by 6% for both sets. The bandgap is extremely overestimated by over 90%. Despite the questionable result of the lattice parameter of Li and the bandgap of Si, the lattice parameter in Si is however found to be in excellent agreement with the experimental value of 5.43 Å, with a percentage difference of less than 0.7%.

Table 3-24. Validation of various sets of Slater-Koster potentials using structural details of LiSi; k-points used during parameterisation with quality set to fine using density mode

SK-Library	System	Smearing	a	%diff	b	%diff	c	%diff
LiSi-D_Fine-CS-32-rd-Li-2.1-Si-1.9_4.153-3.75	LiSi	0.00	9.156	-2.07	9.156	-2.07	5.726	-0.58
LiSi-D_Fine-CS-32-rd-Li-2.1-Si-1.9_4.155-3.75	LiSi	0.02	9.487	1.46	9.487	1.46	5.610	-2.61
LiSi-D_Fine-CS-32-rd-Li-2.1-Si-1.9_4.156-3.75	LiSi	0.02	9.180	-1.81	9.180	-1.81	5.682	-1.36
LiSi-D_Fine-CS-32-rd-Li-2.1-Si-1.9_4.158-3.75	LiSi	0.02	9.487	1.46	9.487	1.46	5.602	-2.75
LiSi-D_Fine-CS-32-rd-Li-2.1-Si-1.9_4.152-3.752	LiSi	0.02	9.295	-0.58	9.295	-0.58	5.591	-2.94
LiSi-D_Fine-CS-32-rd-Li-2.1-Si-1.9_4.157-3.757	LiSi	**0.00**	**9.295**	-0.59	**9.295**	-0.59	**5.616**	**-2.50**
	LiSi	**0.02**	**9.294**	-0.60	**9.294**	-0.60	**5.615**	**-2.52**

Tables 3-22**,** 3-23 and 3-24 indicate that by varying the density confinement radii of Li and Si at quantities which are about double the size of their corresponding wave function confinement radii, whilst within the density mode of parameterisation, tends to improve the results. Given results illustrated by Tables 3-22 to 3-24, it is noticeable that the application of thermal smearing does not necessarily improve the results. By considering the last row in Table 3-24, it is apparent that not much difference is yielded by including smearing during the structural relaxation of the LiSi using the derived SCC-DFTB parameter set. A bird's-eye view of Tables 3-11 through to 3-24, suggests that it is not necessary to use a large number of k-points during the development of SCC-DFTB parameter sets for the Li-Si system. These results generally show that parameter sets should not be quickly dismissed and deemed inaccurate because their performance can vary on various systems. It is on this note that it becomes necessary for the set developed in this work to be tested on various Li-Si systems.

3.7 SCC-DFTB Parameterisation of the Na-Si System

As discussed using Li-Si SCC-DFTB parameters, the development workflow begins with the selection and optimisation of DFT reference structures, and then the DFTB+ parameterisation follows. Similar to the Li-Si system, a set of SCC-DFTB parameters for the Na-Si is developed and presented in the summary that follows.

3.7.1 Reference DFT details used for the Na-Si

The geometry optimisation calculations on all reference systems were performed using the generalized gradient approximation (GGA) functional and double numerical plus polarisation (DNP) basis as implemented in the DMol^3 code embedded within the Materials Studio simulation package. The basis set used is analogous to the Gaussian double-zeta basis set. All the DFT calculations were conducted within periodic boundary conditions (PBC).

3.7.2 Structural properties of reference systems using DMol^3

Table 3-25. DFT calculated structural properties for Si, Na and NaSi systems

System	Functional	Global Orbital Cutoff	k-spacing (0.01/Å)	Lattice (Å)	
				This work	Experiment
Na	GGA-RPBE	6.4	24x24x24	a = 4.2852	4.29 [18]
Si	GGA-BLYP	6.5	18x18x18	a = 5.5353	5.43 [19]
NaSi	GGA-PBE	5.2	9x15x10	a = 12.0941 b = 6.5489 c = 11.0367	12.19 [20] 6.55 [20] 11.18 [20]

Table 3-25 presents the DFT calculated structural properties of the reference systems. Structure relaxation calculations were conducted on silicon, sodium and sodium silicide systems using DMol^3. The solid-state properties of the reference systems, Na (*Im-3m*), Si (*Fd-3m*), NaSi (*C2/c*), were converged using a k-point spacing of 0.01/ **Å**. The spacing used corresponds to 24x24x24, 18x18x18, 9x15x10 k-meshes for the Na, Si and NaSi respectively. The GGA-RPBE functional was employed on the geometry optimization of Na, the GGA-BLYP and GGA-PBE functionals were used on the Si and NaSi respectively. Various global orbital cutoff values were systematically sampled, and the values 6.4, 6.5, 5.2 were found to be suitable for Na, Si and NaSi respectively. The calculated lattice parameters for all the systems were found to agree with available experiments to within a difference less than 2%. These systems were then used as input models required for fitting using DFTB+.

Table 3-26. Parameterisation done by employing the potential mode of fitting, variation of the Na and Si covalent radii, various polynomial weighting and regularization penalty functions.

Parameter set	Cut-off Steps	Fit	Cut-off factor	Radii1 Na	Radii1 Si	Polynomial Degree	Total Error	Weight	Regularizer
Na-1.34-Si-0.91-GGA-P-Order-20-1.1-1.3.0	32	9	1.59	1.34	0.91	10	0.2613	0.1	None
Na-1.44-Si-1.01-GGA-P-Order-20-1.1-1.3.0	32	10	1.652	1.44	1.01	10	0.1867	0.1	None
Na-1.54-Si-1.11-GGA-P-Order-20-1.1-1.3.0	32	24	2.51	1.54	1.11	9	0.1310	0.1	None
Na-1.64-Si-1.21-GGA-P-Order-20-1.1-1.3.0	32	25	2.571	1.64	1.21	9	0.1120	0.1	None
Na-1.74-Si-1.31-GGA-P-Order-20-1.1-1.3.0	32	26	2.632	1.74	1.31	9	0.0987	0.1	None
Na-1.84-Si-1.41-GGA-P-Order-20-1.1-1.3.0	32	31	2.939	1.84	1.41	9	0.0925	0.1	None
Na-1.94-Si-1.51-GGA-P-Order-20-1.1-1.3.0	32	31	2.939	1.94	1.51	9	0.1021	0.1	None
Na-1.54-Si-1.11-GGA-P-Order-20-1.1-1.3.0wt0.2	32	9	1.59	1.54	1.11	10	0.1442	0.2	None
Na-1.54-Si-1.11-GGA-P-Order-20-1.1-1.3.0wt0.3	32	7	1.468	1.54	1.11	10	0.1922	0.3	None
Na-1.54-Si-1.11-GGA-P-Order-20-1.1-1.3.0wt0.4	32	7	1.468	1.54	1.11	10	0.1465	0.4	None
Na-1.54-Si-1.11-GGA-P-Order-20-1.1-1.3.0wt0.5	32	6	1.406	1.54	1.11	10	0.1784	0.5	None
Na-1.54-Si-1.11-GGA-P-Ord20-1.1-1.3.0-O-wt-0.1	32	27	2.694	1.54	1.11	10	0.1270	0.1	Oscillation
Na-1.54-Si-1.11-GGA-P-Ord20-1.1-1.3.0-O-wt-0.2	32	25	2.571	1.54	1.11	9	0.1714	0.2	Oscillation
Na-1.54-Si-1.11-GGA-P-Ord20-1.1-1.3.0-O-wt-0.3	32	25	2.571	1.54	1.11	10	0.1764	0.3	Oscillation
Na-1.54-Si-1.11-GGA-P-Ord20-1.1-1.3.0-O-wt-0.4	32	25	2.571	1.54	1.11	10	0.1221	0.4	Oscillation
Na-1.54-Si-1.11-GGA-P-Ord20-1.1-1.3.0-O-wt-0.5	32	25	2.571	1.54	1.11	9	0.1895	0.5	Oscillation
Na-1.54-Si-1.11-GGA-P-Ord20-1.1-1.3.0-O-wt-0.6	32	25	2.571	1.54	1.11	9	0.2295	0.6	Oscillation
Na-1.54-Si-1.11-GGA-P-Ord20-1.1-1.3.0-O-wt-0.7	32	25	2.571	1.54	1.11	9	0.1756	0.7	Oscillation

Table 3-26 presents the SCC-DFTB parameterisation for the Na-Si system done by employing the potential mode of fitting. During fitting, each parameterisation task was limited to 32 cut-off steps, and the maximum allowed polynomial order was set to 20, the scaling factor was confined to a minimum of 1.1 and a maximum of 3.0. Each parameterisation task generated 32 fits, and from each set of 32, the set with the lowest total error was selected. The third column in Table 3-26 reflects the number of fits identified as one with the lowest error within the parameterisation set. The covalent radii notated as Radii1 on the table, refer to the wave function confinement radii.

As reflected by the 5th and 6th columns of Table 3-26, considering the first 7 data rows from the top going down the table, the wave function confinement radius for Na was systematically varied in increments of 0.1 from 1.34 to 1.94 Bohr, whilst that of Si was varied in increments of 0.1 from 0.91 to 1.51. Except for the 7th row, the total error is gradually decreasing with an increase in covalent radii. The lowest error of 0.0925 corresponds to the parametrisation scheme wherein the wave function confinement radius for Na was set to 1.84 whilst that of Si was set to 1.41 Bohr. Considering these radii to be the upper bounds, a test was conducted to see if introducing an increasing measure of weighting on the parameterisation could improve the fitting accuracy.

A configuration wherein radii1 was fixed to 1.54 and 1.11 Bohr for Na and Si respectively was used, and is presented by the 8th through to the 11th data rows of Table 3-26. It was noted that applying weights on this configuration was generally increasing the total error than improve the accuracy, as fits with the lowest error were found to be within the first 10 steps corresponding to fits ranging from 6 – 9. To curb the error whilst weighting was systematically increased from 0.1 to 0.7, a regularizer was introduced and is shown by the last 7 rows of Table 3-26 from the bottom going up. A combination of the weights and an oscillation penalty function as the regularizer seemed to improve the accuracy. This was indicated by the parameter set obtained when the fitting weight was set to 0.4, corresponding to the least error among the 7 sets at the bottom portion of Table 3-26. To allow the parameterisation to better handle electronic properties we switch to the density mode of parameterisation, and the initial sets of the fitting tests are illustrated in Table 3-27.

Table 3-27 Parameterisation done through the density mode of fitting, a variation of the Na and Si covalent radii, and applying various perturbation weight-function widths.

Parameter set	Cut-off Steps	Fit	Cut-off factor	Radii1 - Na	Radii2 - Na	Radii1 - Si	Radii2 - Si	Polynomial Degree	Total Error	Perturb Weight-function-width
Na-1.54_2.78-Si-1.11_1.92-GGA-D-Order-20-1.1-1.3.0	32	14	1.897	1.54	2.78	1.11	1.92	10	0.5780	40
Na-1.54_2.88-Si-1.11_2.02-GGA-D-Order-20-1.1-1.3.0	32	14	1.897	1.54	2.88	1.11	2.02	10	0.5477	40
Na-1.54_2.98-Si-1.11_2.12-GGA-D-Order-20-1.1-1.3.0	32	5	1.345	1.54	2.98	1.11	2.12	11	0.5021	40
Na-1.54_3.08-Si-1.11_2.22-GGA-D-Order-20-1.1-1.3.0	32	14	1.897	1.54	3.08	1.11	2.22	10	0.6152	40
Na-1.54_3.18-Si-1.11_2.32-GGA-D-Order-20-1.1-1.3.0	32	4	1.284	1.54	3.18	1.11	2.32	11	0.8568	40
Na-1.54_3.28-Si-1.11_2.42-GGA-D-Order-20-1.1-1.3.0	32	14	1.897	1.54	3.28	1.11	2.42	10	0.6665	40
Na-1.54_3.38-Si-1.11_2.52-GGA-D-Order-20-1.1-1.3.0	32	14	1.897	1.54	3.38	1.11	2.52	10	0.6855	40
Na-1.54_5.9-Si-1.11_4.4-GGA-D-Order-20-1.1-1.3.0-wt-0.1_64-pWfW-40	64	16	1.552	1.54	5.9	1.11	4.40	10	0.97680000	40
Na-1.54_5.9-Si-1.11_4.4-GGA-D-Order-20-1.1-1.3.0-wt-0.1-64-pWfW-7.5	64	32	2.035	1.54	5.9	1.11	4.40	8	0.00009240	7.5
Na-1.54_5.9-Si-1.11_4.4-GGA-D-Order-20-1.1-1.3.0-wt-0.1-64-pWfW-15	64	14	1.492	1.54	5.9	1.11	4.40	14	0.00863000	15
Na-1.54_5.9-Si-1.11_4.4-GGA-D-Order-20-1.1-1.3.0-wt-0.1-64-pWfW-30	64	25	1.824	1.54	5.9	1.11	4.40	10	0.27560000	30
Na-1.64_6.0-Si-1.21_4.5-GGA-D-Order-20-1.1-1.3.0-wt-0.1-64-pWfW-7.5	64	33	2.065	1.64	6	1.21	4.50	8	0.00006802	7.5
Na-1.64_6.0-Si-1.21_4.5-GGA-D-Order-20-1.1-1.3.0-wt-0.1-64-pWfW-15	64	21	1.703	1.64	6	1.21	4.50	10	0.00994100	15

Table 3-28. Evaluation and selection of Na-Si SCC-DFTB parameter sets using the lattice parameters of Na, Si and NaSi crystal structures.

	Lattice (Å)											
Parameter set					NaSi							
	Na	**%diff**	**Si**	**%diff**	**a**	**%diff**	**b**	**%diff**	**c**	**%diff**	**$Diff_{ave}$**	
Experimental reference:	4.29		5.43		12.19		6.55		11.18			
Na-1.54_5.9-Si-1.11_4.4-GGA-D-Order-20-1.1-1.3.0-wt-0.1-64-pWfW-7.5	3.534	19.33	5.516	1.57	13.721	11.82	7.836	17.88	11.316	1.21	10.36	**S1**
Na-1.64_6.0-Si-1.21_4.5-GGA-D-Order-20-1.1-1.3.0-wt-0.1-64-pWfW-7.5	3.487	20.65	5.525	1.73	14.773	19.16	6.855	4.55	14.57	26.33	14.48	**S2**
Na-1.54_5.9-Si-1.11_4.4-GGA-D-Order-20-1.1-1.3.0-wt-0.1-64-pWfW-15	4.013	6.67	5.450	0.37	10.690	13.11	7.072	7.66	11.948	6.64	6.89	**S3**
Na-1.64_6.0-Si-1.21_4.5-GGA-D-Order-20-1.1-1.3.0-wt-0.1-64-pWfW-15	4.372	1.89	5.467	0.68	10.886	11.3	8.038	20.4	11.472	2.58	7.37	**S4**
S4_Alternative-6	4.129	3.82	5.587	2.85	11.847	2.85	6.752	3.04	11.14	0.36	2.58	**S5**

%diff == percentage difference with respect to experimental reference, $Diff_{ave}$ == average of the percentage difference for the respective parameter set

Table 3-27 presents the SCC-DFTB parameterisation for the Na-Si system via the density mode of fitting. The density mode makes it possible to vary radii1 and radii2 which respectively refer to the wave function and density confinement radii of the systems being used for fitting. The radii1 for Na and Si were fixed at 1.54 and 1.11 Bohr respectively. Considering the first 7 data rows in Table 3-27, the radii2 for Na and Si were systematically varied through increments of 0.1. For both systems, the radii were set to span a range of 3 units below and 3 units above a double-fold of their respective radii2. That is to say, when the radii1 for Na was set to 1.54 Bohr since a double fold of its radii2 would be 3.08 Bohr, then the range began from 2.78 to 3.38 Bohr as shown in the 6th column of Table 3-27. For Si, the radii ranged from 1.92 through to 2.52 Bohr.

Similar to the parameterisation configuration done when the potential mode was used, each parameterisation task was limited to 32 cut-off steps, and the maximum permissible polynomial order was set to 20, the scaling factor was confined to a minimum of 1.1 and a maximum of 3.0. The weight function width parameter which essentially specifies that the width of the normal function employed in the generation of weights, was set to 40% as shown by the first 7 data entries in the 11th column of Table 3-27. The resulting total error in the fitting did not seem to conform to a particular trend in that as the radii2 was linearly increased, the error both reduced and increased for some configurations. The parameter set with the lowest error of 0.5021 highlighted and located on the third data row from the top of the table going down, was observed to correspond to the parameterisation scheme with radii2 configured as 2.98 and 2.12 Bohr for Na and Si respectively.

To focus the emphasis on the atomic configurations within the central positions of the atoms for which a perturbation generator was used during the fitting, the perturb weight function width was decreased from 40 to 30, 15 and 7.5% as shown by the 7 rows counting from the bottom in Table 3-27. Whilst this was done, to allow for wider atomic configurations to be sampled, the number of permissible cut-off steps was raised to a maximum of 64. In addition to this, the radii2 was set to be about a double fold of the configuration that had initially produced a total error of 0.5021. That is to say, since for this error the radii2 was 2.98 Bohr for Na when 32 cut-off steps were employed, the radii2 was then set to 5.9 Bohr when 64 steps were used,

which is almost equivalent to 2.98 x 2. In the same manner, the radii2 for Si was set to 4.4 Bohr.

Interestingly, narrowing the perturb weight function width significantly improved fitting accuracy by reducing the total errors. Guided by the observation that the lowest total error in Table 3-26 wherein the potential mode was employed was noted to be 0.0925, corresponding to radii1 of 1.84 Bohr for Na, for comparison the radii1 was raised from 1.54 to 1.64 and captured in the last two rows in Table 3-27. The lowest error was seen to be 0.00006802, followed by 0.00009240, 0.00863000 and 0.00994100, which correspond to parameter sets with configurations wherein the weight function width was configured to 7.5 and 15 %. These parameter sets were selected for further evaluation and are presented by Table 3-28.

As illustrated by Table 3-28, the selected Na-Si SCC-DFTB parameter sets were evaluated using the lattice parameters of the reference Na, Si and NaSi structures. The four parameter sets selected from Table 3-27 and listed in Table 3-28 will be referred to as S1, S2, S3, and S4. The parameter sets S1 and S2 obtained when the perturb weight function width was set to 7.5%, underestimate the lattice parameters of pristine Na (*Im-3m*) by more than 19% but reproduce the Si (*Fd-3m*) lattice parameter to within 2% compared to the experiment reference values. Also, both S1 and S2 overestimate the ***a*** parameter of NaSi (*C2/c*) by more than 10%. S1 reproduces the ***c*** parameter to within 1.3% of the experimental reference value, but significantly overestimates the ***b*** parameter by 17.88%. Considering all the three reference structures, S1 and S2 have an average difference of more than 10% compared to experiments.

The parameter sets S3 and S4 generated by using a perturb weight function width of 15% handle the reference systems better than S1 and S2 as they yield average difference of less than 7.5% with respect to experimental reference lattice values. The parameter set S4 can reproduce the lattice parameters of the pristine Na and Si to within 2% of the available experimental reference. However, S4 underestimates the ***a*** lattice parameter by 11.3% and overestimates the ***b*** parameter by 20.4%. The S3 parameter set yields an average difference of 6.89% which is lower than that of S4 but underestimates the lattice parameter of Na by 6.67%. Since the interest in this work is to model Na-rich Si anodes, S4 is considered for further analysis. Since

a parameterisation task of 64 cut-off steps generates 64 fits and the fit with the lowest error is not always the most accurate, all the alternative fits from S4 were examined against the NaSi system. See Appendix D and E for reference. The 6th fit among the 64 fits was found to be a lot better as it yielded an average difference of 1.94% and the set is listed as S5.

A summary of the configuration used in developing the Na-Si SCC DFTB parameter set referred to as S5 and is used to study sodiated silicon in this work is presented by the table and discussion that follow.

Table 3-29. The compression radii used in calculating the confinement of the wave functions and densities presented by the Slater-Koster parameters

System	r_0 (radii1)	n_0 (radii2)
Na	1.64	6.0
Si	1.21	4.5

r_0 = the wave function confinement radius, n_0 = the density confinement radius

The density mode of the parameterisation was used. As captured in Table 3-29, the wave function,r_0, and density confinement radii, n_0, were varied. The n_0 of 1.64 and n_0 of 6.0 Bohr were applied on the Na system. For Si, 1.21 and 4.5 Bohr were used. In addition to the confinement radii, the quality of the parameterisation routine was set to fine; a minimum cut-off scaling radius factor of 1.1 and a maximum of 3.0 were used; a weight function width of 15 was employed on both the scale and perturb generator, and the bulk structures used for parameterisation were scaled within a maximum compression of 40% and maximum expansion of 60%. The SCC-DFTB parameterisation was done for the Na-Na, Si-Si, and Na-Si interaction pairs.

Chapter 4 **Validation and Application of Derived Li-Si and Na-Si Potentials**

This section presents the validations and application of the Li-Si and NaSi SCC-DFTB parameter sets developed in this work. The transferability of the Li-Si SCC-DFTB parameter set is assessed by calculating lattice constants of various lithium silicides, and partial density of states (PDOS) for bulk Si, as well as selected Li_xSi compositions. To demonstrate the employability of the Li-Si parameter set concerning temperature studies, the molecular dynamics of a Si supercell and the Li-rich silicide ($Li_{22}Si_5$) are presented. Since volume expansion is a major challenge in the implementation of Li-Si alloy-based anodes, the expansion of crystalline Si as a function of Li concentration is modelled as further validation. The Na-Si SCC-parameter set is validated against reference structures; its transferability and applicability are briefly shown using the optimisation Na-Si clathrates and the sodiation of Si

4.1 Transferability Tests of The SCC-DFTB Parameter Set

Table 4-1. Structural properties for bulk Si, Li and various lithium silicide systems.

System	Space group	No. atoms	Crystal System	at.% Li	at.% Si	a	%Diff	b	%Diff	c	%Diff	Bandgap (eV)	
Li	*Im-3m*	2	Cubic	100	0	3.51		3.51		3.51			Exp.
Li	*Im-3m*	2	Cubic	100	0	**3.721**	**6.01**	**3.721**	**6.01**	**3.721**	**6.01**		**Calc.**
Si	*Fd-3m*	8	Cubic	0	100	5.431		5.431		5.431		1.17	Exp.
Si	*Fd-3m*	8	Cubic	0	100	**5.46**	**0.53**	**5.46**	**0.53**	**5.46**	**0.53**	**2.301**	**Calc.**
LiSi	*I41/a*	32	Tetragonal	50	50	9.354		9.354		5.746		0.057	Exp.
LiSi	*I41/a*	32	Tetragonal	50	50	**9.321**	**-0.35**	**9.321**	**-0.35**	**5.638**	**-1.88**	**0.725**	**Calc.**
$Li_{12}Si_7$	*Pnma*	152	Orthorhombic	63.16	36.84	8.60		19.77		14.34			Exp.
$Li_{12}Si_7$	*Pnma*	152	Orthorhombic	63.16	36.84	**7.961**	**-7.43**	**19.096**	**-3.41**	**14.116**	**-1.56**		**Calc.**
Li_7Si_3	*P3212*	60	Hexagonal	70	30	7.629		7.629		18.009			Exp.
Li_7Si_3	*P3212*	60	Hexagonal	70	30	**7.358**	**-3.55**	**7.358**	**-3.55**	**18.038**	**0.16**		**Calc.**
$Li_{13}Si_4$	*Pbam*	34	Orthorhombic	76.47	23.53	7.99		15.21		4.43			Exp.
$Li_{13}Si_4$	*Pbam*	34	Orthorhombic	76.47	23.53	**7.849**	**-1.88**	**15.514**	**2.00**	**4.167**	**-5.95**		**Calc.**
$Li_{15}Si_4$	*I-43D*	76	Cubic	78.95	21.05	10.685		10.685		10.685			Exp.
$Li_{15}Si_4$	*I-43D*	76	Cubic	78.95	21.05	**10.271**	**-3.87**	**10.271**	**-3.87**	**10.270**	**-3.87**		**Calc.**
$Li_{21}Si_5$	*F-43m*	416	Cubic	80.77	19.23	18.71		18.71		18.71			Exp.
$Li_{21}Si_5$	*F-43m*	416	Cubic	80.77	19.23	**17.91**	**-4.28**	**17.91**	**-4.28**	**17.91**	**-4.28**		**Calc.**
$Li_{22}Si_5$	*F23*	432	Cubic	81.48	18.52	18.75		18.75		18.75			Exp.
$Li_{22}Si_5$	*F23*	432	Cubic	81.48	18.52	**18.92**	**0.91**	**18.92**	**0.91**	**18.92**	**0.91**		**Calc.**

Table 4-1 presents a set of results comprised of lattice constants and some bandgap values obtained using the parameter set developed herein. Although the assessment is primarily aimed at phases of lithium silicides as presented by the Li-Si phase diagram; properties of bulk Li and Si systems have been included for completeness.

The overall amount by which the lattice parameters of the lithium silicides are reproduced in comparison to experiments is found to be within a margin of 8% difference. A close inspection of the calculated lattice constants for the tetragonal LiSi indicates that ***a***=***b*** with values of 9.321 Å agree with experiments to within a 0.35% difference, whilst ***c*** with the value 5.638 Å, is within a difference of 1.88 %. In the orthorhombic $Li_{12}Si_7$ system, the ***a***, ***b*** and ***c*** parameters are underestimated by 7.43%, 3.41% and 1.56% respectively. A look at the hexagonal Li_7Si_3 illustrates that parameters ***a***=***b*** are underestimated by 3.55%, whilst ***c*** is slightly overestimated by 0.16%. For the orthorhombic $Li_{13}Si_4$, ***a*** and ***c*** are underestimated by 1.88% and 5.95% respectively, whilst ***b*** is overestimated by 2%. Lastly, for the cubic systems, $Li_{15}Si_4$, $Li_{21}Si_5$, and $Li_{22}Si_5$, the lattice constants were obtained to be with a difference of 3.87%, 4.28% and 0.91 % respectively. Generally, the slight over/underestimation could be adjusted by re-fitting for polytypes of silicon including the hexagonal, orthorhombic and tetragonal crystal systems. The structural relaxations done on the systems presented by Table 4-1 are assumed to be at 0K, and at this temperature, the theoretical bandgap of silicon is known to be about 1.17eV, and that of LiSi is known to be ~ 0.057eV for temperatures less than 450K. As seen from the calculated values, the Si bandgap was overestimated by 96.7%, whilst that of LiSi was extremely overestimated. Notwithstanding that traditional DFT under/over-estimates the bandgap in solids, these observations can be attributed to the fact that GGA-PBE was the functional used in the preparation of the applied DFT reference sample structures, and that these results are not explicitly inclusive of temperature effects. Better estimates could be yielded if a hybrid functional such as GGA-BLYP is applied to the samples and the systems are subjected to evaluations of temperature effects.

4.2 The Molecular Dynamics Results

4.2.1 Bulk silicon within the NVE ensemble

Table 4-2. Molecular dynamics properties of a silicon supercell at temperatures 1600K – 1700K

T (K)	Bandgap (Ha)	P_{ave} (GPa)	Fermi (eV)	Tot. E_{ave} (kcal/mol)	Kin. E_{ave} (kcal/mol)
1600	0.132	3.991	-2.769302	-412626.943	1201.280
1610	0.124	4.120	-2.868814	-412611.698	1209.066
1620	0.128	4.192	-4.022895	-412596.476	1216.376
1630	0.136	4.232	-2.418524	-412581.260	1224.432
1640	0.125	4.227	-2.610278	-412566.004	1231.707
1650	0.128	4.191	-3.045047	-412550.810	1239.649
1660	0.128	4.100	-2.306396	-412535.583	1247.348
1670	0.121	4.404	-3.884033	-412520.312	1254.254
1680	0.132	4.247	-2.191903	-412505.116	1261.557
1690	0.130	4.518	-2.364324	-412489.836	1269.458
1700	0.130	4.272	-3.746594	-412474.616	1276.772

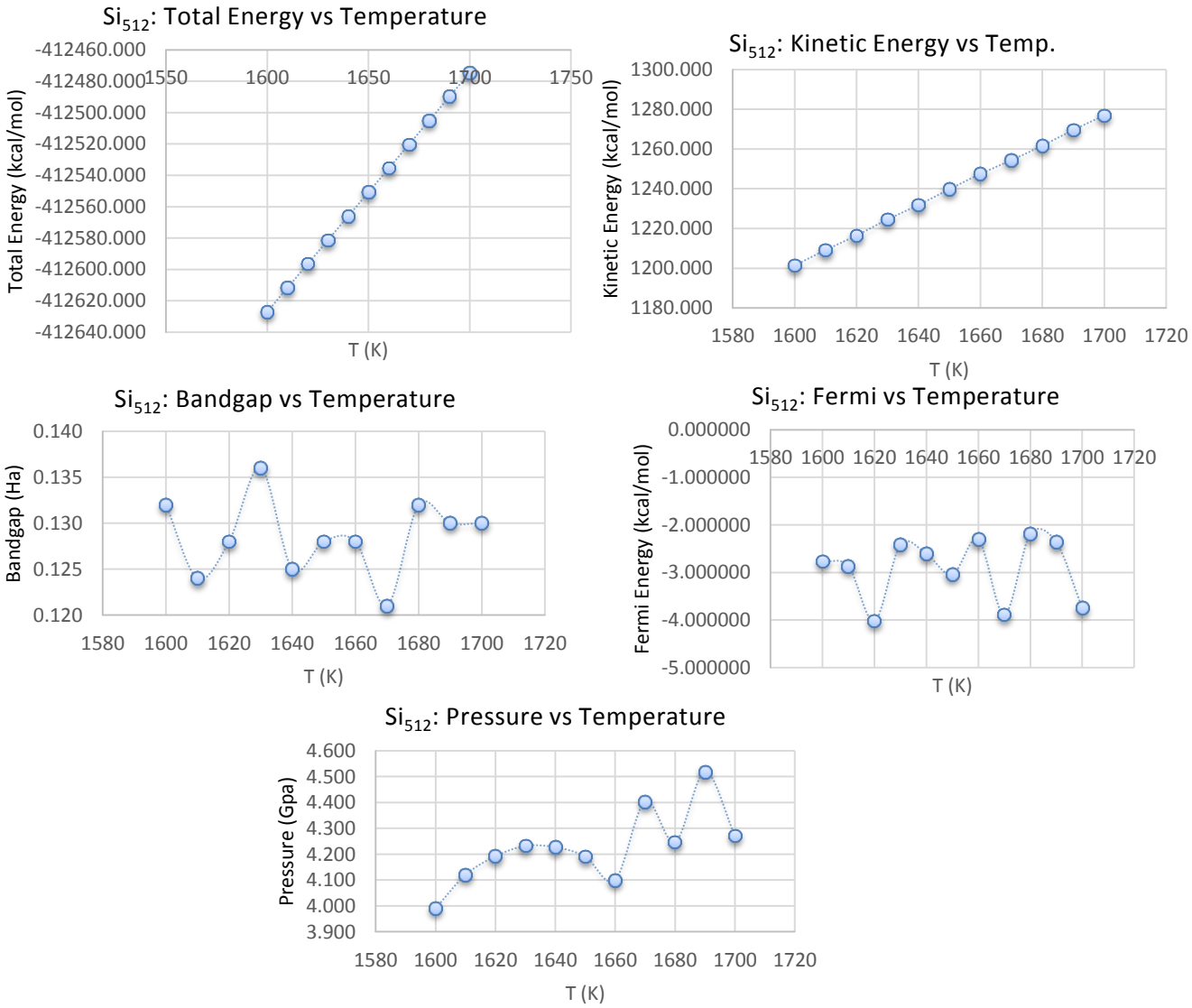

Figure 4-1. Graphical presentation of the molecular dynamics properties of silicon supercell

To validate the potentials, the molecular dynamic performance of cubic silicon was studied by using a supercell consisting of 512 atoms. The system was set to a microcanonical ensemble. As shown by Table 4-2, the temperature was systematically varied in increments of 10K from 1600K to 1700K. The simulation was allowed to run for 2ps at a time step of 1fs over a total of 2000 steps.

The graphical presentation of results captured in Table 4-2 as presented by Figure 4-1 illustrates that the gradient of the change in total energy as a function of temperature is positive, and the plot is linear, thus indicating a direct relationship between the two thermal quantities of silicon. This behaviour is expected as the simulation is done within constant energy conditions. A similar trend is noticed on the plot of the kinetic energy as a function of the change in temperature.

By considering how the bandgap and the Fermi energy vary consequent to temperature rise on the silicon supercell, it is noticed that there is no particular trend except that the dip at 1670K on the plots suggests a change in conductivity. Based on this observation, it could be inferred that silicon becomes more electronically conductive as temperature increases.

In principle pressure is a ratio of applied force to a surface area; and considering how pressure is gradually increasing from 1600K to 1630K and decreases until 1660K, only to then fluctuate afterward, this implicates a variation on the structural description of the silicon system. Theory suggests that silicon should begin melting around 1687K, however since this simulation was allowed to run over a small period, a concrete conclusion cannot be drawn because the statistical fluctuations that yield physical changes may have not been adequately sampled.

4.2.2 Bulk silicon within the NVT ensemble

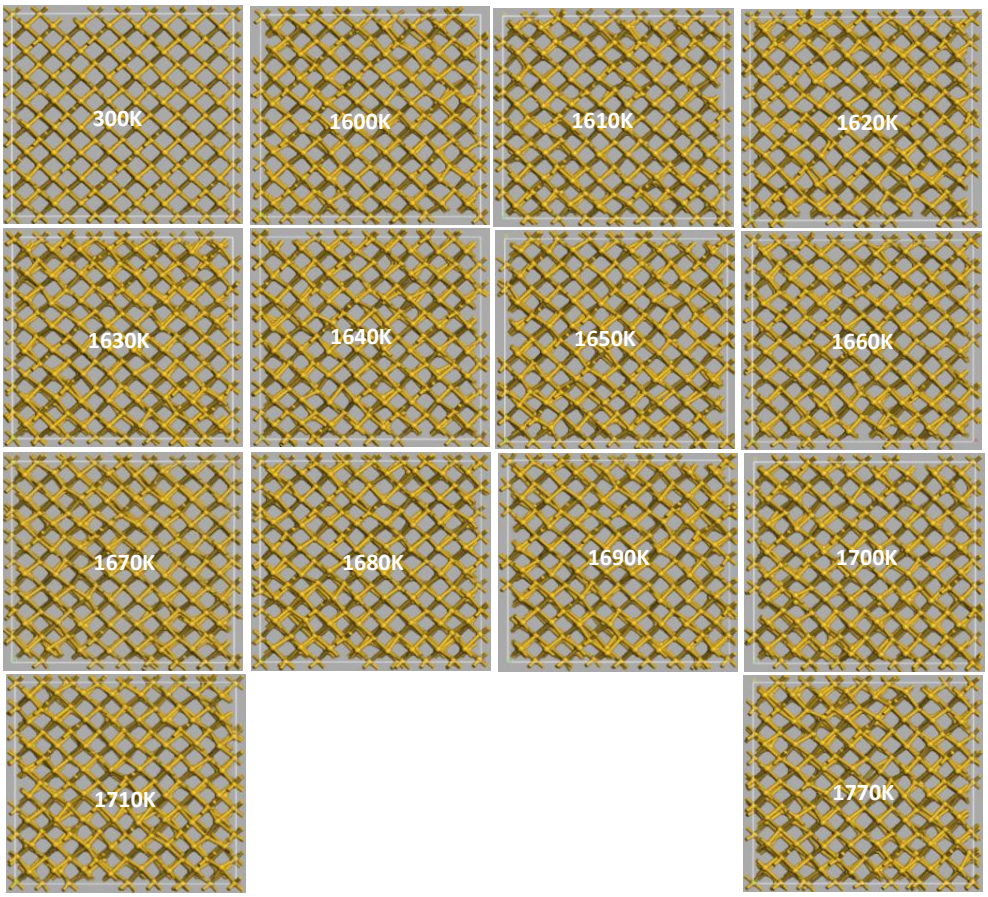

Figure 4-2. Silicon system at various temperatures ranging from 300K to 1770K

Molecular dynamics calculations were performed on a crystalline Si supercell consisting of 512 atoms. The silicon system was subjected to high temperatures ranging from 1600K to 1710K within constant moles, volume and temperature conditions (*i.e.* NVT ensemble). The temperature was controlled using the direct velocity scaling within a variation of 0K. The calculations were allowed to run for 10ps over 10000 steps at a time step of 1fs. These simulations were done in an attempt to reproduce the experimental melting point of silicon reported to be around 1687K. From the diagrams in Figure 4-2, it is shown that the system somewhat retained its crystallinity even beyond the theoretical melting point. This observation could either be attributed to suppression of statistical fluctuations imposed by the velocity scaling control method applied in the MD runs, or it could be that the system requires the introduction of a defect in one sub-lattice to stimulate the melting such as in fast ion conductors, or the S-K potentials merely overestimate the melting point, or the system requiring further equilibration before production runs.

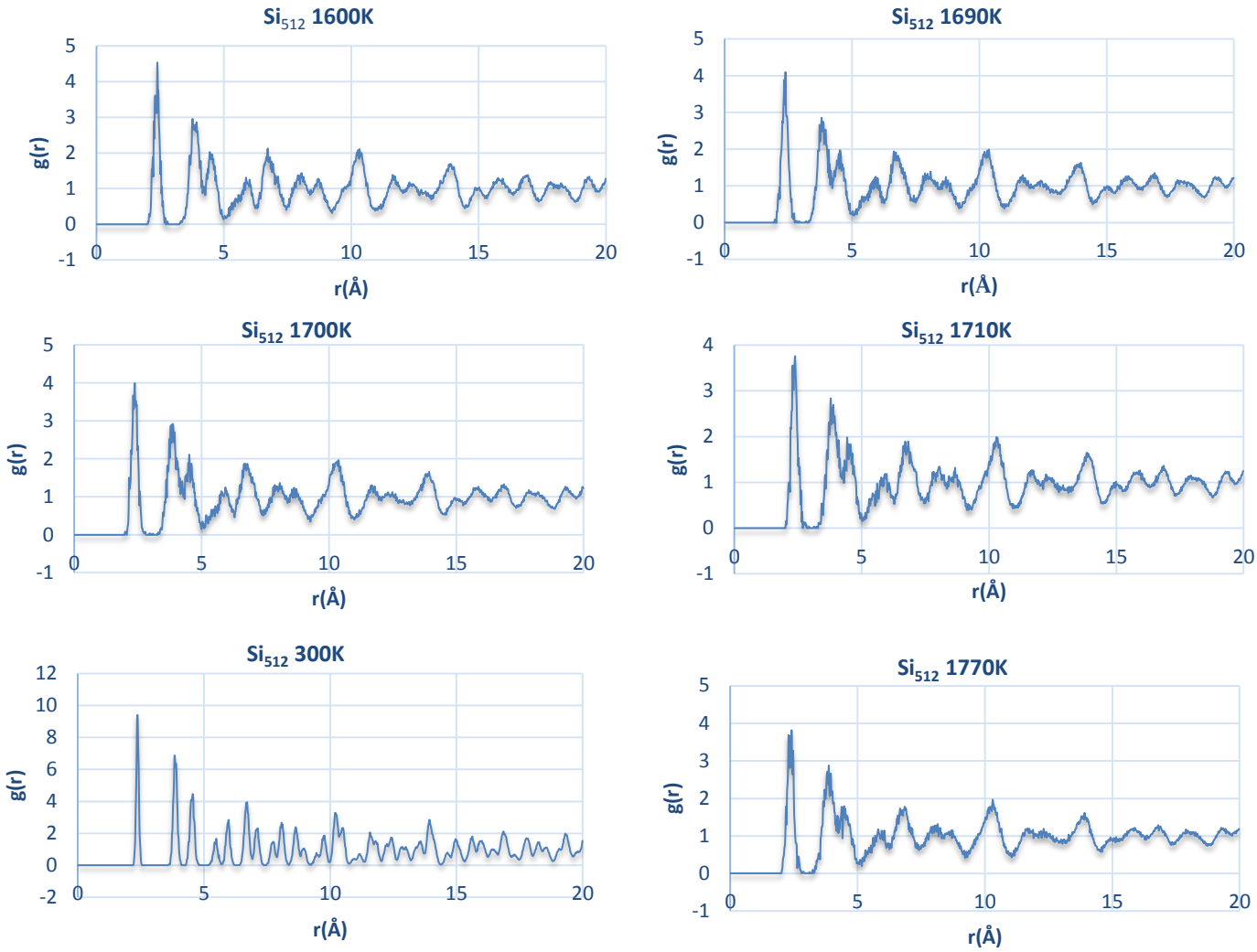

Figure 4-3. Radial distribution functions of bulk silicon

A look at the radial distribution functions (RDFs) corresponding to silicon systems as presented by Figure 4-3 for temperatures sampled from 1600K to 1710K in comparison to the system at 300K, highlights the presence of crystallinity in the structure. It is anticipated that crystallinity should be completely lost beyond the melting point of 1687K; however, it is evident that there is some ordering present within the radial distance of 20 Å. At the temperature of 1770K, silicon is considered to be within its liquid region. However, according to the RDF of Si in this work, the system is only approaching its melting state. It is however widely known that melting point is not a facile property to reproduce using empirical potentials. The semi-empirical potentials from the SCC-DFTB technique in this work may need to be re-fit to allow wider atomic environments of silicon to improve the melting point estimates.

4.2.3 Bulk $Li_{22}Si_5$ within the NVT ensemble

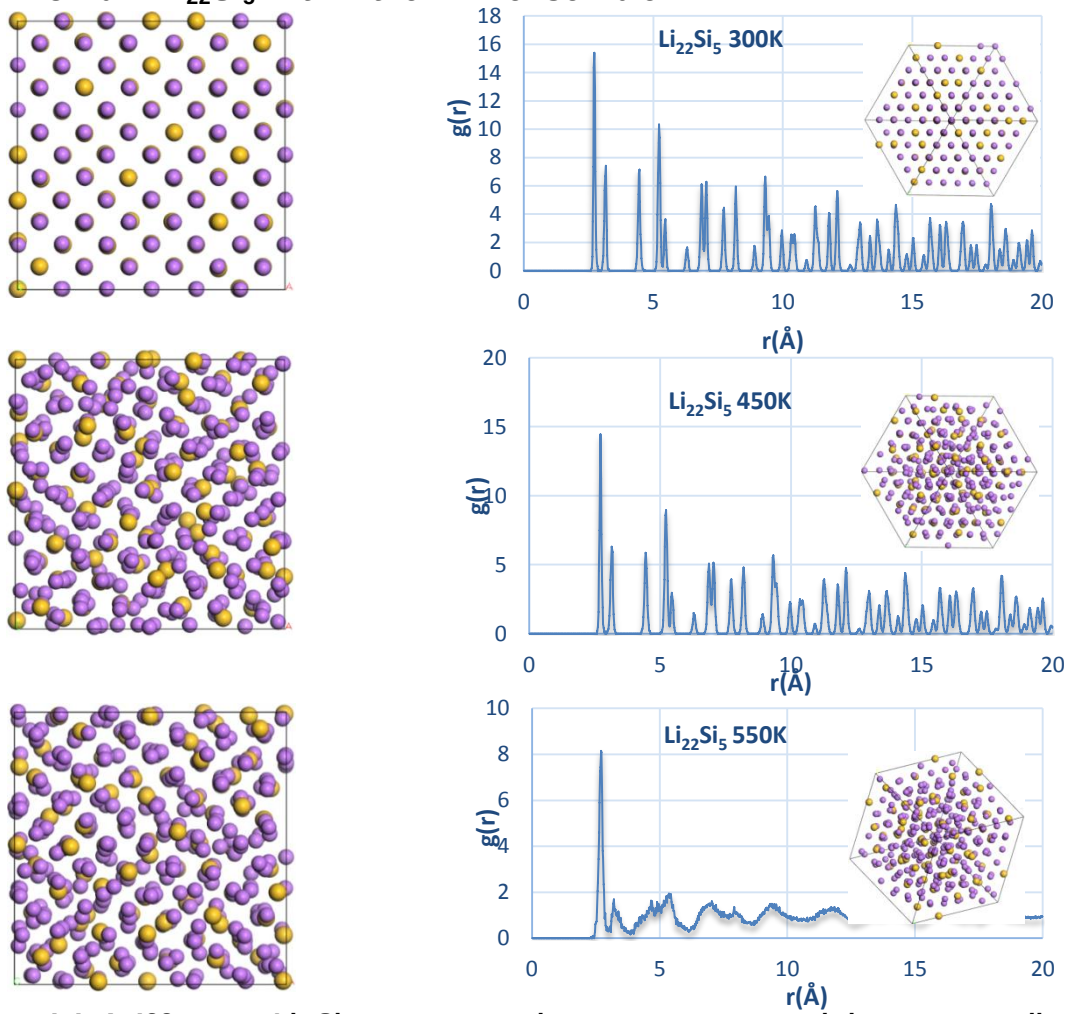

Figure 4-4. A 432 atoms $Li_{22}Si_5$ system at various temperatures and the corresponding radial distribution functions

The molecular dynamics of the most lithium-rich phase of silicon, $Li_{22}Si_5$, were investigated on a crystalline primary unit cell consisting of a total of 432 atoms. The system was subjected to temperatures ranging from 300K to 1780K within constant moles, constant volume and constant temperature conditions (*i.e.* NVT ensemble). The temperature was controlled using the direct velocity scaling within a variation of 0K. The calculations were allowed to run for a period of 0.5ps over 500 steps at a time step of 1fs. These calculations were done as a test to demonstrate the ability of the developed SCC-DFTB parameter set to study the thermal properties of lithiated silicon systems. For this purpose, the results for only three temperatures are illustrated in Figure 4-4. Consistent with the phase diagram [7] of the Li-Si system, $Li_{22}Si_5$ is anticipated to change in morphology at temperatures above 450K; and according to structures depicted by Figure 4-4, the system's atomic arrangement becomes disordered as temperature increases. Unlike at 300K, the radial distribution

function of $Li_{22}Si_5$ suggests that at 550K the system is beginning to melt because the function is seen to be with fewer peaks and exhibits a steady decay that moves closer to unity for radial distances beyond 10 Å. Despite the short simulation time, this observation proves the parameter sets to be functional for conducting temperature studies on the lithiated silicon phase $Li_{22}Si_5$.

4.3 Volume Expansion as Function of Li Insertion Into Crystalline Si

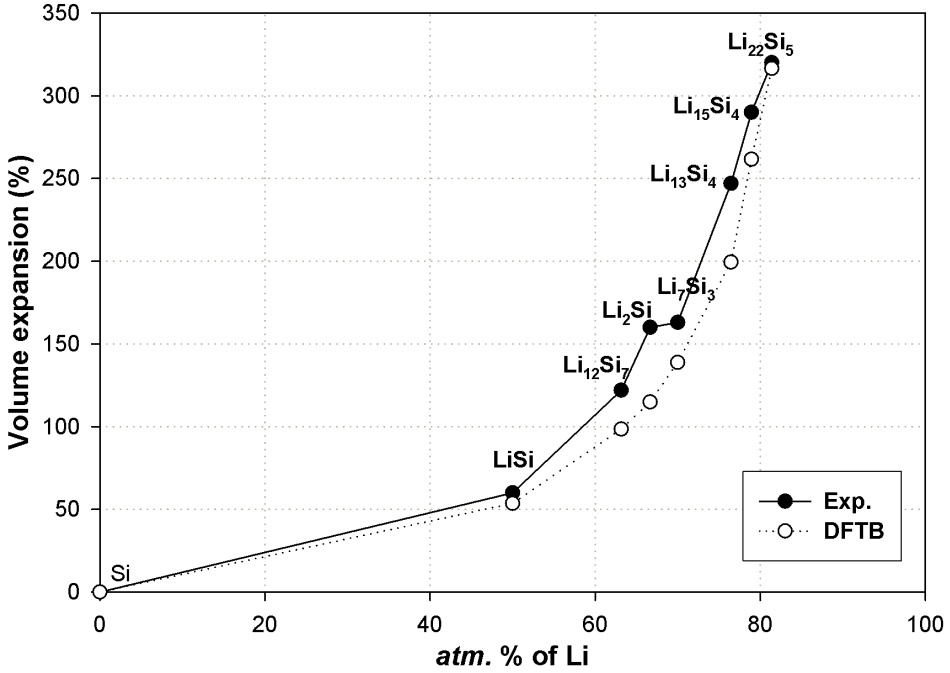

Figure 4-5 Experimental [162] and calculated volume density expansion (%) for various Li-Si alloys.

Table 4-4-3. The expansion of Si_8 as result of increasing the concentration of lithium atoms

			% Volume Expansion	
System	**Stoichiometric**	***atm % Li***	**Exp** [162]	**This Work**
LiSi	Li_1Si	50	60	53.6
$Li_{12}Si_7$	$Li_{1.71}Si$	63.16	122	
	$Li_{1.75}Si$ #	63.64		98.47
Li_7Si_3	$Li_{2.33}Si$	70	163	
	$Li_{2.375}Si$ #	70.37		138.8
$Li_{13}Si_4$	$Li_{3.25}Si$	76.47	247	199.35
$Li_{15}Si_4$	$Li_{3.75}Si$	78.95	290	261.57
$Li_{21}Si_5$ *	$Li_{4.2}Si$	80.77		
	$Li_{4.25}Si$ #	80.95		295.65
	$Li_{4.375}Si$ #	81.4		290.5
$Li_{22}Si_5$	$Li_{4.4}Si$	81.48	320	
	$Li_{4.5}Si$ #	81.82		316.45

Although not exact, the stoichiometric composition is close to that of the stable phase reported in theory.

$$\% \Delta V = \frac{V_f - V_i}{V_i} \times 100\% \quad \textbf{(4.1)}$$

Various configurations obtained by lithiating interstitial sites of a bulk 8 atom crystalline Si system were prepared. Li concentration was gradually increased by systematically adding a lithium atom into Si_8 interstitials. The first configuration in each concentration was selected. The primary guide for selecting the configuration was the low total energy per system. Each of the structures was relaxed using the following convergence criteria: energy, 0.02 kcal/mol; force, 0.1 kcal/mol/A; relaxation of cell shape and size allowed. Thermal smearing of 0.001 Ha was applied in relaxing the structures. Alloying materials can exhibit high volumetric and gravimetric capacities; however, the main challenge in the commercial implementation of silicon alloy-based anodes is their deleterious volume expansion (~300%) during charging and discharging. The various volume changes in the electrodes during cycling can lead to the degradation of electrochemical performance. Thus, understanding the characteristics of various lithiated silicon systems can positively aid the successful development of the Li-Si anode. The developed SCC-DFTB parameter set was further validated by modelling the volume expansion in crystalline Si as a function of Li content. The outcome is therefore presented by Figure 4-5 and Table 4-4-3. The expansion was determined from the geometrically optimised lithiated states by using equation (4.1). The procedure employed in lithiating silicon as described herein produced several systems with concentrations ranging from 11.11 to 82.22 *atm%* Li. For comparison to details reported from experimental work, the plot depicted by Figure 4-5, together with results in Table 4-1 was limited to seven lithiated states. The complete list of lithiated silicon systems produced using the SCC-DFTB parameter set is captured in Appendix B. It was observed that compositions ranging from 11.11 to 46.67 *atm%* Li yielded volume density expansion ranging from 4.98 to 34.37%. Furthermore, silicon was predicted to gradually expand in volume from 53.6% for LiSi phase which is composed of 50 *atm %* Li, to 261.57% for $Li_{15}Si_4$ with 78.95 atm % Li, and eventually shoots over 300% for $Li_{22}Si_5$ phase with the expansion at 316.45%. This trend is in agreement with experiments, as the expansion was reported to be 60%, 290% and 320% for LiSi, $Li_{15}Si_4$ as well as $Li_{22}Si_5$ respectively [162].

4.4 Partial Density of States for Selected Compositions of Li_xSi Systems

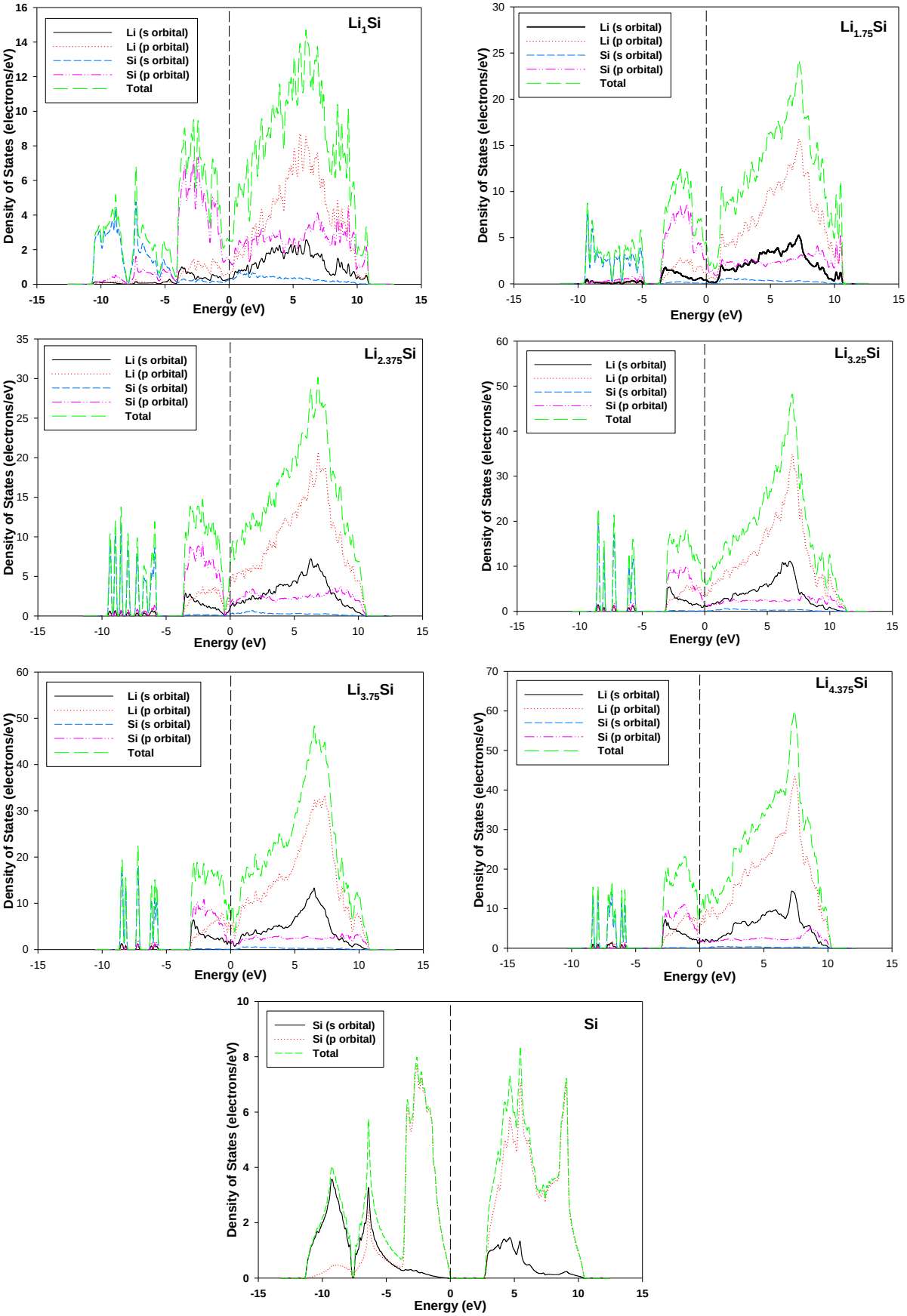

Figure 4-6 PDOS for Li_1Si, $Li_{1.75}Si$, $Li_{2.375}Si$, $Li_{3.25}Si$, $Li_{3.75}Si$, $Li_{4.375}Si$, and Si.

Theory suggests that silicon as a solid material exists as an intrinsic semiconductor. The bandgap on the plot of the calculated partial density of states (PDOS) for the pristine Si system agrees with the theory. A general observation of the PDOS of the lithiated silicon systems is that the introduction of lithium gives the systems a metallic signature. This quality is desirable in as far as electrical conductivity in battery applications is concerned. These plots also suggest it is likely to encounter more stable systems as the concentration of Li is gradually increased in various compositions of Si. The Fermi level though it is not within, but slightly towards the right of a pseudogap in the Li_1Si system, suggests that 50 *atm%* Li configuration is close to a known stable phase. For the $Li_{1.75}Si$ system, the Fermi level hinges on a peak, suggesting that the composition of 63.64 *atm%* Li in Si yields an unstable phase. In the $Li_{2.75}Si$ system, the pseudogap has moved slightly to the left, thus suggesting the configuration to be unstable but closer to a stable phase. As for the $Li_{3.25}Si$ and $Li_{3.75}Si$, the Fermi level is located inside a pseudogap; as such, this suggests that these systems correspond to stable phases. The Fermi level is almost in a pseudogap on the PDOS of the $Li_{4.375}Si$, and it indicates that the system is very close to a stable phase. Given that known stable phases of the Li-Si system generally exist as high temperatures phases, it is anticipated that compositions of systems that are expected to be reflected as stable by their PDOS may not be exact, as these calculations do not include temperature effects.

4.5 Mechanical Property Calculations Using Li-Si SCC-DFTB Parameters

Mechanical stability is important also for active materials used in batteries as their structural integrity or mechanical failure could translate to high performance or lead to undesirable effects such as degradation of capacity, short cycling life, and short-circuiting. Therefore these properties should be studied in candidate electrode materials such as Si. A supercell of the cubic Si crystal structure will be distorted by an amorphisation procedure; as such, the ability of the Li-Si SCC-DFTB parameter set to model the mechanical behaviour of Si is evaluated by calculating the mechanical properties of pristine Si and comparing calculated results with corresponding experimental values. Before the mechanical properties of cubic Si can be determined, the suitable maximum strain amplitude is sampled.

4.5.1 Mechanical properties of diamond Si

Table 4-4. Calculated independent elastic constants for Si *Fd-3m*. All quantities are in GPa

Strain Amplitude	Phase	C_{11}	Error +/-	C_{12}	Error +/-	C_{44}	Error +/-
0.001	Si	165.4713	0.0350	60.4489	0.0000	84.2641	0.0659
0.002	Si	165.4515	0.0732	60.4467	0.0000	84.2420	0.0212
0.003	Si	165.4275	0.1073	60.4371	0.0000	84.2200	0.0391
0.004	Si	165.4217	0.1450	60.4268	0.0000	84.1968	0.0313
0.005	Si	165.3946	0.1792	60.4145	0.0000	84.1697	0.0254
0.006	Si	165.3691	0.2159	60.3996	0.0000	84.1685	0.0519
0.007	Si	165.3440	0.2494	60.3871	0.0000	84.1525	0.0615
0.008	Si	165.3158	0.2840	60.3744	0.0000	84.1373	0.0710
0.009	Si	165.2895	0.3165	60.3626	0.0000	84.1234	0.0802
0.010	Si	165.2662	0.3488	60.3558	0.0000	84.1075	0.0898

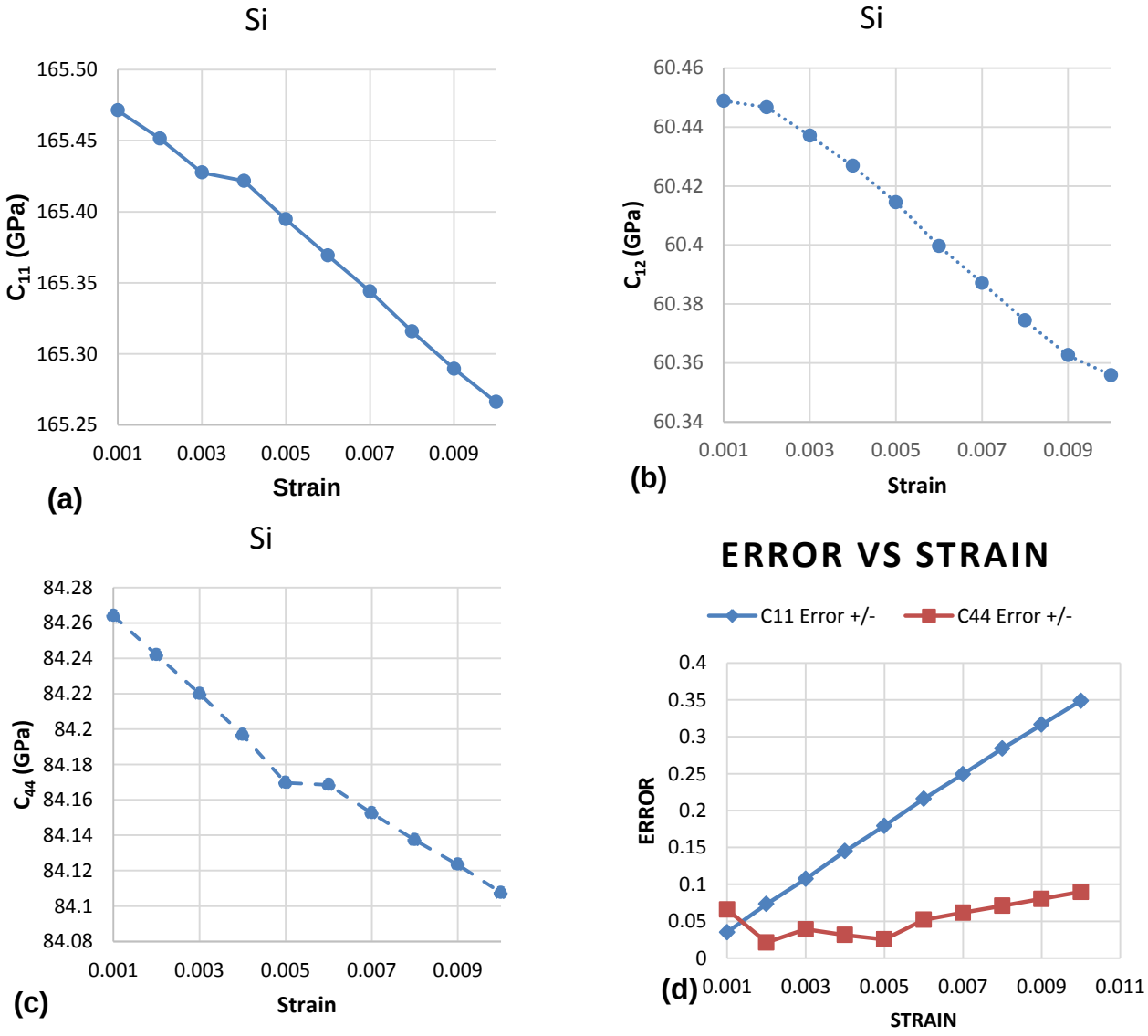

Figure 4-7. (a) – (c) A graphic presentation of the independent elastic constants C_{11}, C_{12}, C_{44} versus the maximum strain amplitude, and (d) a plot of the error versus strain amplitude applied on the cubic Si (*Fd-3m*).

Table 4-5. B: bulk modulus, G: shear modulus, and Y: Young's modulus in GPa K: compressibility, ϑ: Poisson ratio

		Reuss		Voigt		Hill				
Strain Amplitude	**Phase**	**B**	**G**	**B**	**G**	**B**	**G**	Y	**K (TGa)**	ϑ
0.001	Si	95.4564	67.8523	95.4564	71.5629	95.4564	69.7076	133.1230	10.4760	0.2676
0.002	Si	95.4483	67.8378	95.4483	71.5462	95.4483	69.6920	133.1024	10.4769	0.2676
0.003	Si	95.4372	67.8278	95.4372	71.5321	95.4372	69.6799	133.0953	10.4781	0.2676
0.004	Si	95.4251	67.8169	95.4251	71.5171	95.4251	69.6670	133.0867	10.4794	0.2676
0.005	Si	95.4078	67.8014	95.4078	71.4978	95.4078	69.6496	133.0672	10.4813	0.2675
0.006	Si	95.3895	67.7974	95.3895	71.4950	95.3895	69.6462	133.0518	10.4833	0.2675
0.007	Si	95.3728	67.7870	95.3728	71.4829	95.3728	69.6350	133.0347	10.4852	0.2675
0.008	Si	95.3549	67.7759	95.3549	71.4706	95.3549	69.6233	133.0143	10.4871	0.2675
0.009	Si	95.3382	67.7657	95.3382	71.4594	95.3382	69.6125	132.9951	10.4890	0.2675
0.010	Si	95.3259	67.7540	95.3259	71.4466	95.3259	69.6003	132.9748	10.4903	0.2675

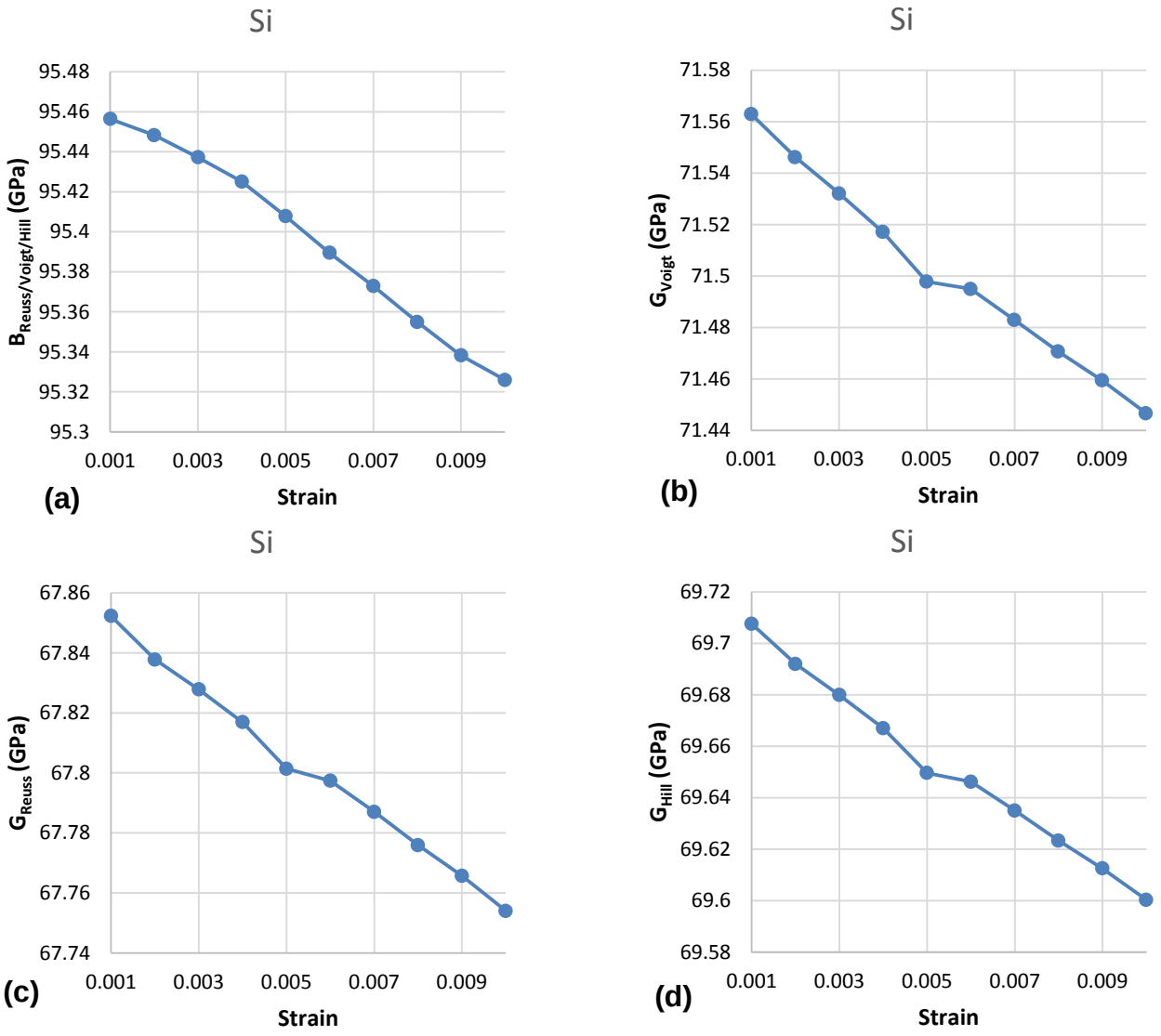

Figure 4-8. A graphic presentation of (a) the bulk and (b) – (d) shear moduli as a function of the strain amplitude applied on the cubic Si (*Fd-3m*).

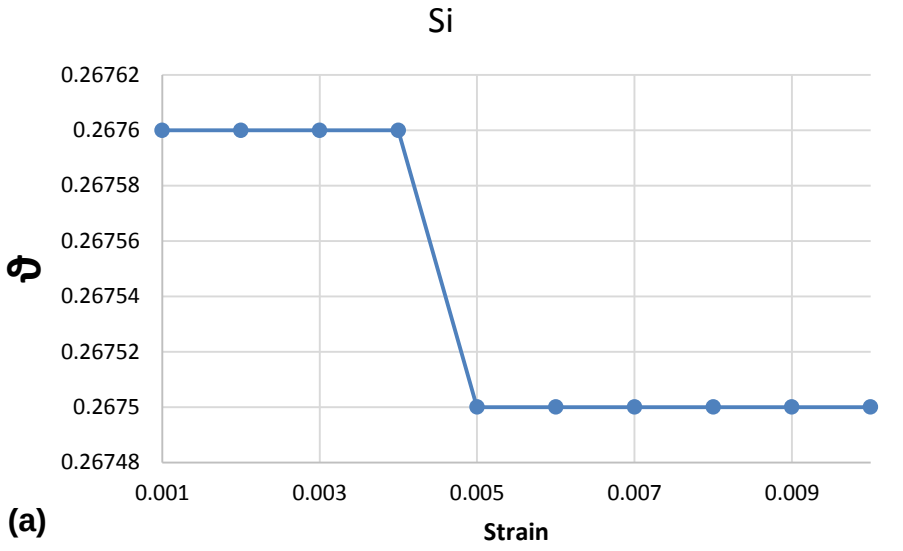

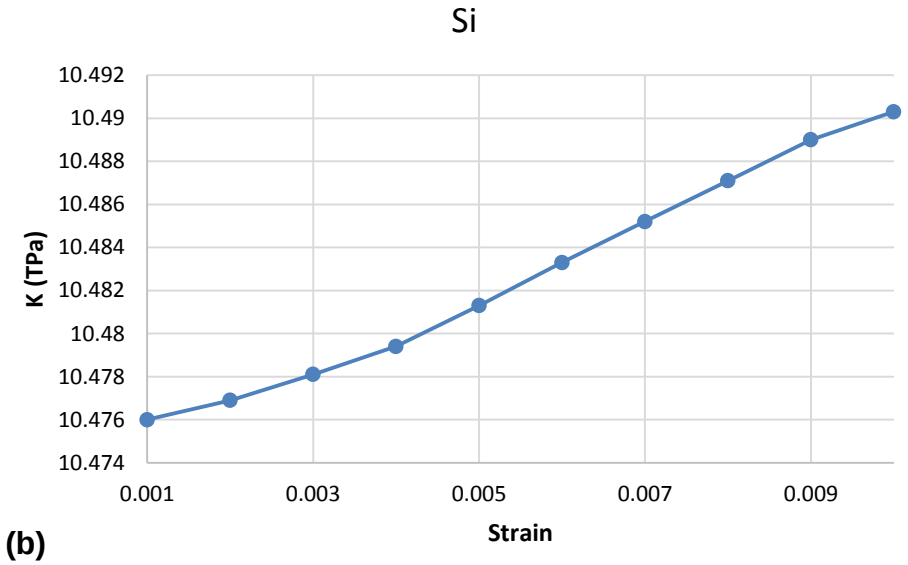

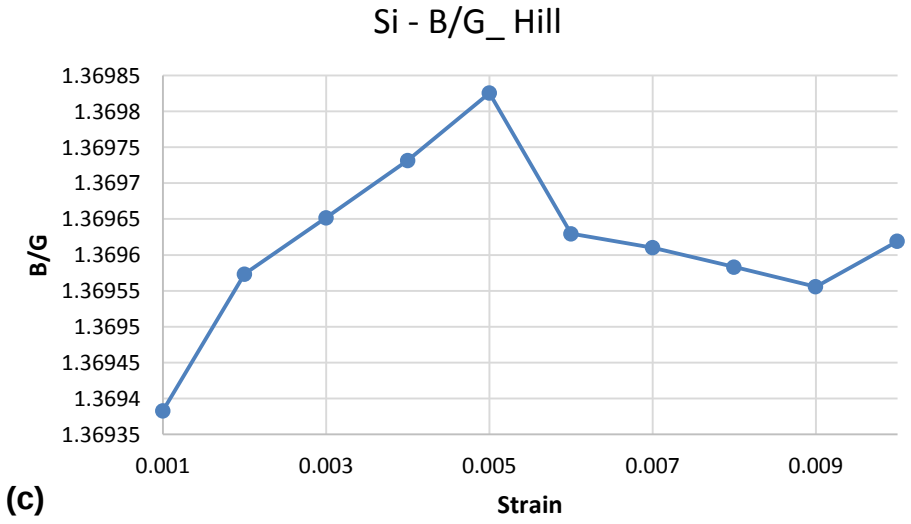

Figure 4-9. A graphic presentation of the (a) Poisson ratio, (b) compressibility, and (d) Pugh ratio as a function of the strain amplitude applied on the cubic Si (*Fd-3m*).

To determine the mechanical properties of given a system, its structure would have to be subjected to several strains. The distortions that result from the strains applied on a given structure, makes it possible for properties such as elastic constants, elastic moduli, and Poisson ratios to be calculated. It is necessary to sample the suitable maximum strain amplitude to be applied on a system under study so that computational noise can be minimalized and to ensure that the structure's region of linear elasticity should not be exceeded. Hence, the maximum strain amplitude was systematically varied from 0.001 to 0.010. Table 4-4, illustrates the calculated independent elastic constants for Si belonging to the *Fd-3m* space group. The silicon structure is cubic; hence, its crystal system has only three independent elastic constants, C_{11}, $C_{12,}$ and $C_{44,}$ with all values in GPa. As seen in Table 4-4 as well as from the graphical presentation depicted by Figure 4-7, the C_{ij} values are linearly decreasing by a very small margin (*i.e.* an average variation less than 0.03 %) as the strain amplitude is linearly increased. The computational error is less than 0.5 for all C_{11}, $C_{12,}$ and C_{44}. However, from a careful look at the errors in the C_{44}, it becomes apparent that the values are most minimal for strains within the maximum strain amplitude from 0.02 and 0.05; after, 0.05 the error seems to increase linearly increase.

Elastic moduli form part of fundamental and important properties in materials and are central to understanding mechanical behaviour. Table 4-5 illustrates the elastic moduli which are calculated using equations (2.26) and (2.27), the compressibility, K, as well as the Poisson ratio, ϑ. The bulk modulus is denoted by the letter B, G represents the shear modulus, and Y is Young's modulus, with all values in GPa. The Voigt, Reuss, and Hill represent the upper bound, lower bound and the arithmetic average of the two extremes respectively [163]. Since these moduli are computed using the C_{ij} values, it is generally anticipated the trends seen from the C_{ij}'s as the maximum strain amplitude increases should be similar for the moduli. Indeed, although the variation is very small (less than 0.025%), the bulk, shear, and young's moduli have an inverse proportionality towards the linear increase in strain amplitudes. As shown in Figure 4-9 (a), the Poisson ratio remains constant as the strain amplitude is systematically increased. However, a slight decrease is seen from the strain amplitude of 0.005. The Poisson ratio is generally expected to remain approximately constant within the elastic region of a material.

The B/G ratio, proposed by Pugh [164] is related to brittleness or ductility of materials. In principle, a high B/G ratio corresponds to ductility, while a low value is related to brittleness. The critical value distinguishing a ductile and brittle material is 1.75. Considering B and G values in Table 4-5 and the plot of the Pugh ratio depicted by Figure 4-9 (c), it is noticeable that the ratio seems to gradually increase with the increase in strain but an inflection point it encountered at the maximum strain amplitude of 0.005, from which the B/G ratio seems to linearly decrease. Nonetheless, the change in the ratio is minute and the average value is about 1.37, which is less than 1.75, hence implying that Si is brittle. This is consistent with what was reported in the literature [165].

Based on the observations discussed in the passages above, the maximum strain amplitude of 0.003 is selected. This value used to calculate and compare the mechanical properties of diamond silicon with those reported from experiments as well as theoretical studies, and the findings are presented by Table 4-6.

Table 4-6. A comparison of mechanical properties of Si (*Fd-3m*), values in GPa

Method	C_{11}	C_{12}	C_{44}	B	G	E	ϑ	Ref.
LDA	154.383	57.015	74.926	89.476	63.037	153.146	0.215	**This work**
GGA	152.168	56.842	75.034	88.32	64.91	156.13	0.19	[166]
SCC-DFTB	165.428	60.437	84.220	95.437	69.680	133.095	0.268	**This work**
Exp.	166	64	80	98				[167]

Considering the results shown in Table 4-6, it is noted that the values of the independent elastic constants, $\mathbf{C_{ij}}$, as estimated by the Li-Si SCC-DFTB parameters, satisfy the Born stability criteria for cubic crystals given by equation (2.25). Furthermore, the mechanical properties of Si *Fd-3m* as produced by the Li-Si SCC-DFTB parameters agree with experiments to within 6%. Relative to experiments, the LDA underestimated the C_{11}, C_{12}, and C_{44} by 7%, 11%, and 6% respectively. Except for the Poisson ratio of 0.215, which has a 12% difference, the LDA results calculated in this work agree to the DFT based results in reference [166] to within 3%.

4.6 Volume Expansion in Amorphous Silicon

The deleterious volume expansion in crystalline silicon consequent to lithiation necessitates the exploration of various morphologies and synthesis techniques, which can be used to buffer the expansion. As alluded to in the literature review found in this work, various parameters are usually applied to improve the performance of Si. This includes nano-structuring the active material, selecting an appropriate binder, choosing a suitable electrolyte, controlling particle size, using composites, balancing constituent concentrations and employing amorphous alloys.

Because of the improved capacity to host insertion species, amorphous systems are continually researched. It is, therefore, crucial to know by how much an amorphous material expands upon insertion to optimize the designed electrode system so that it can accommodate the expansion. It makes sense to expect that an amorphous material would undergo a linear volumetric expansion and expand isotropically with linearly increasing lithium content. Indeed, using atomic force microscopy and specially prepared samples, Beaulieu *et al* [168] illustrated that amorphous active materials do undergo a homogenous linear volumetric growth with a linearly increasing content.

Furthermore, the work by Timmons and Dahn [169], showed that particles composed of amorphous active materials undergo isotropic volume expansion upon lithium insertion, and confirmed that the volume expansion as a function of lithium content of an amorphous particle, can confidently be measured through *in situ* observations of a single particle of active material in plan view using an optical microscope. In this section, an SCC-DFTB based approach is used to probe into the expansion of amorphous silicon. A framework used to generate amorphous models is first presented, then the outcome of inserting Li within 33 to 50 atomic percent into amorphous Si is shown. The lithiation of amorphous Si is used as a basis to pave way for the use of Na and Mg in amorphous silicon in the future.

4.7 Framework for Generating the Amorphous Systems

A framework for generating the amorphous systems was developed and is briefly described as follows:

Geometry optimisation was conducted on a standard unit cell of crystalline silicon belonging to the *Fd-3m* space-group and consisting of 8 atoms using Slater-Koster

potentials within the DFTB+ code. A silicon supercell consisting of 512 atoms was then built from the optimised unit cell. Using LAMMPS [170], a classical molecular dynamics simulation code designed to run efficiently on parallel computers, the bulk amorphous silicon structure was generated through the melt and quench molecular dynamics technique, applied on a crystalline silicon supercell wherein the Stillinger-Weber [171] forcefield was employed.

Melt and Quench configurations were set up as follows: Time step 0.2 fs, 300K, 4500K, pressure 1atm, and using Stillinger-Weber forcefield.

Stage 1: The equilibration of the system was done using the NPT ensemble, the temperature of 300K, the pressure set to 1atm.The simulation was allowed to run for 50ps, using a time step 0.2fs, constrained isotropic, control method: nose-hoover T & P, sampling: 10000 samples, trajectory: 0 frames.

Stage 2: The system was then heated under the NPT ensemble, with temperatures ranging from 300K to 4500K, pressure kept at 1atm, simulation allowed to run for 100ps, using a time step of 0.2fs, constrained isotropic, control method: nose-hoover T & P, sampling: 10000 samples, trajectory: 0 frames.

Stage 3: The system was then cooled using the NVT ensemble, a temperature of 300K, pressure set to 1atm, the simulation allowed to run for 300ps, using a time step of 0.2fs, the control method: nose-hoover, sampling: 10000 samples, trajectory: 0 frames.

Stage 4: The system was then heated using NVT ensemble, with temperature ranging 300K to 4500K, the pressure kept at 1atm, the simulation allowed to run for 300ps, using a time step of 0.2fs, control method: nose-hoover, sampling: 10000 samples, trajectory: 0 frames

Stage 5: The system was cooled using the NVT ensemble, the temperature set to 300K, pressure at 1atm, simulation allowed to run for 50ps, using a time step of 0.2fs, the control method: nose-hoover, sampling: 10000 samples, trajectory: 0 frames

Stage 6: The system was then cooled using the NPT ensemble, the temperature set to 300K, the pressure at 1atm, the simulation allowed to run for 25ps, using a time

step of 0.2fs, constrained isotropic, control method: nose-hoover T & P, sampling: 10000 samples, trajectory: 0 frames.

Stage 7: The final cooling was done using the NPT ensemble, with the system at 300K, pressure of 1atm, the simulation set to run for 200ps, using a time step of 0.2fs, constrained isotropic, control method: nose-hoover T & P, sampling: 10000 samples, trajectory: 0 frames.

It is from all these stages that a bulk amorphous silicon system is generated.

4.8 Volume Expansion as Function of Li Insertion Into Amorphous Si

Table 4-7. Volume expansion resulting from lithiating amorphous Si from 33 to 50 *atm%* Li.

System	Stoichiometric	#atoms	*atm*% Li	*atm*% Si	Volume	ΔVol. (%)
Si512	a-Si	512	0	100	10723.5	0
Li256Li512	$Li_{0.5}Si$	768	33.3	66.7	11429.9	6.59
Li323Si512	$Li_{0.63}Si$	835	38.7	61.3	12120.7	13.03
Li358Si512	$Li_{0.7}Si$	870	41.1	58.9	12168.7	13.48
Li391Si512	$Li_{0.76}Si$	903	43.3	56.7	12188.3	13.66
Li404Si512	$Li_{0.79}Si$	916	44.1	55.9	12232.5	14.01
Li417Si512	$Li_{0.81}Si$	929	44.9	55.1	12258.0	14.31
Li512Si512	Li_1Si	1024	50	50	12287.0	14.58

Almost in a similar approach to the one used for crystalline Si (*c*-Si), amorphous silicon (*a*-Si) was lithiated in concentrations ranging from 33 to 50 atomic percent Li, to test the developed Li-Si SCC-DFTB potentials on amorphous systems, and to note the change in volume. As shown by Table 4-7, beginning with an unlithiated system, a supercell model of *a*-Si consisting of 512 atoms was relaxed using our Li-Si SCC-DFTB parameters and a respective volume of 10723.5 $Å^3$ was obtained. The relaxed *a*-Si was exported out of Materials Studio, and imported into a specialised intercalation software program [172; 173] to lithiate it. Since the Si was amorphous, Li atoms were inserted using an algorithm that placed the atoms into random positions within the Si structure. However, a minimum interatomic distance of 1.5 Å between any two Li atoms was maintained when this was done.

The first lithiated amorphous silicon, $Li_{0.5}Si$, consisting of a total of 768 atoms was prepared using the program and then imported into Materials Studio. To remove any possibly existing Li-Li close contacts, the amorphous Si lattice was constrained by fixing the positions of all Si atoms, leaving out the Li atoms. Using the universal forcefield, the $Li_{0.5}Si$ system was relaxed, therefore allowing the Li atoms to settle in positions without close contacts, after which the constraint on the Si was removed. To bring the total energy in the amorphous $Li_{0.5}Si$ to the ground-state, a structure relaxation procedure was performed and an equilibrium volume of 11429.9 $Å^3$ was noted. Comparing the $Li_{0.05}Si$ equilibrium volume to that of the unlithiated *a*-Si, relative volume expansion of 6.59% is noticed.

To increase the Li content in the amorphous Si, 67 Li atoms were inserted into the relaxed $Li_{0.5}Si$. This addition resulted with another system, $Li_{0.63}Si$, which had 38.7 *atm%* Li and a total of 835 atoms. The structure of $Li_{0.63}Si$ was then optimised and relative volume expansion of 13.03% was observed on the relaxed output. The concentration in the relaxed $Li_{0.63}Si$ was then raised to 41.1 *atm%* Li, resulting with $Li_{0.7}Si$, which had a total of 870 atoms. In a similar iterative manner, the lithiated amorphous, $Li_{0.7}Si$, was brought to equilibrium by performing a structure relaxation and its respective volume was 12168.7 $Å^3$, which corresponds to a relative expansion of 13.48%.

As presented by Table 4-7, the Li content in the amorphous Si was gradually increased up to 50 *atm%* Li, corresponding to Li_1Si, and consisting of a total of 1024 atoms. In going down the same table, it is evident that the amorphous Si is linearly expanding as a function of linearly increased Li content. Within the concentration range of 33 – 50 *atm%* Li in amorphous Si, the trend is consistent with the expectation previously alluded to and is also in agreement with the behaviour recorded in experiments. Given that the ultimate objective for developing functional Li-Si alloys would be for application in rechargeable batteries, it is perhaps also necessary that the electronic stability of these lithiated amorphous be interrogated.

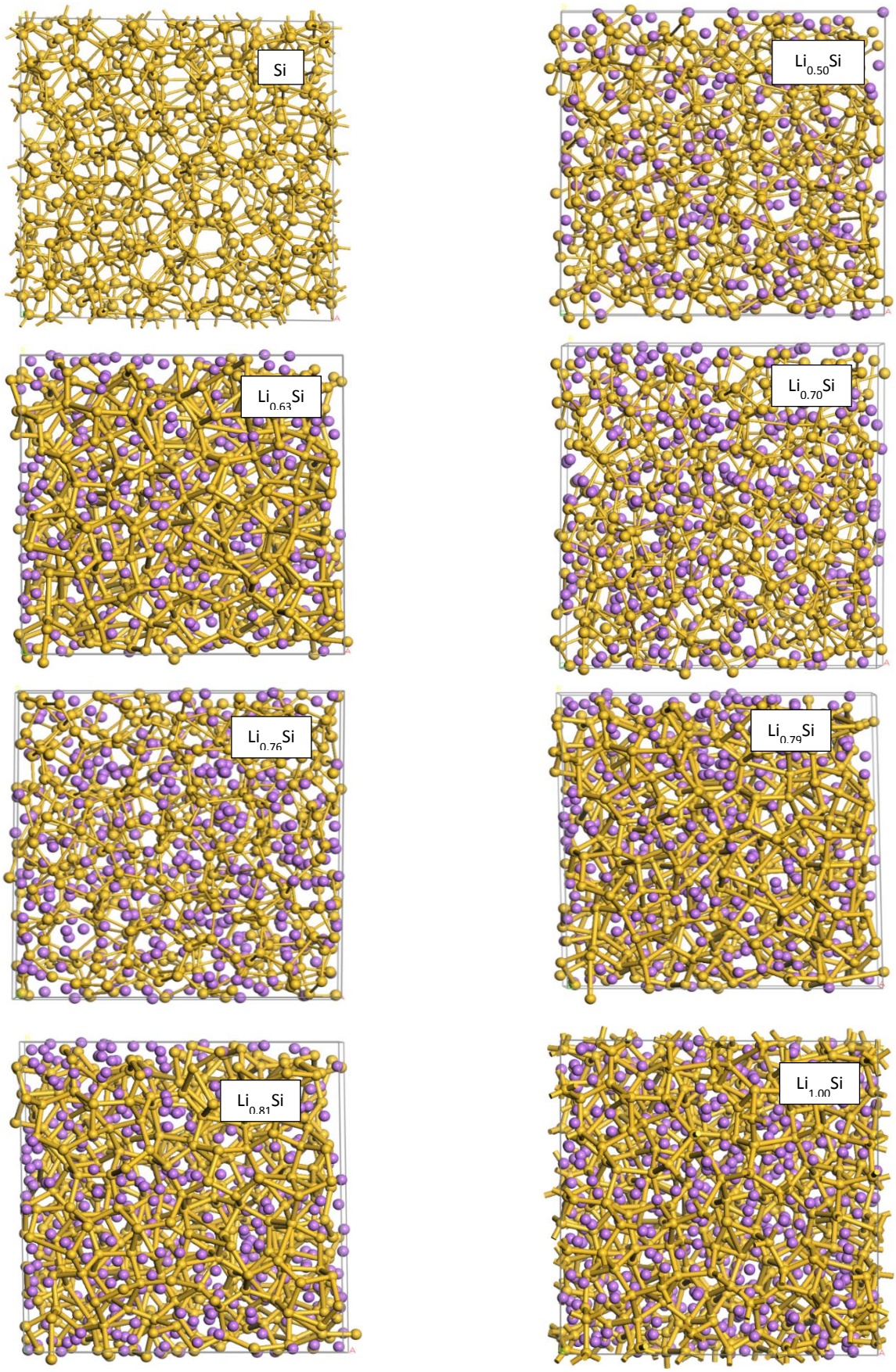

Figure 4-10. A graphical presentation of the lithiated amorphous silicon

4.9 Electronic Partial Density of States in Amorphous Li_xSi Alloys

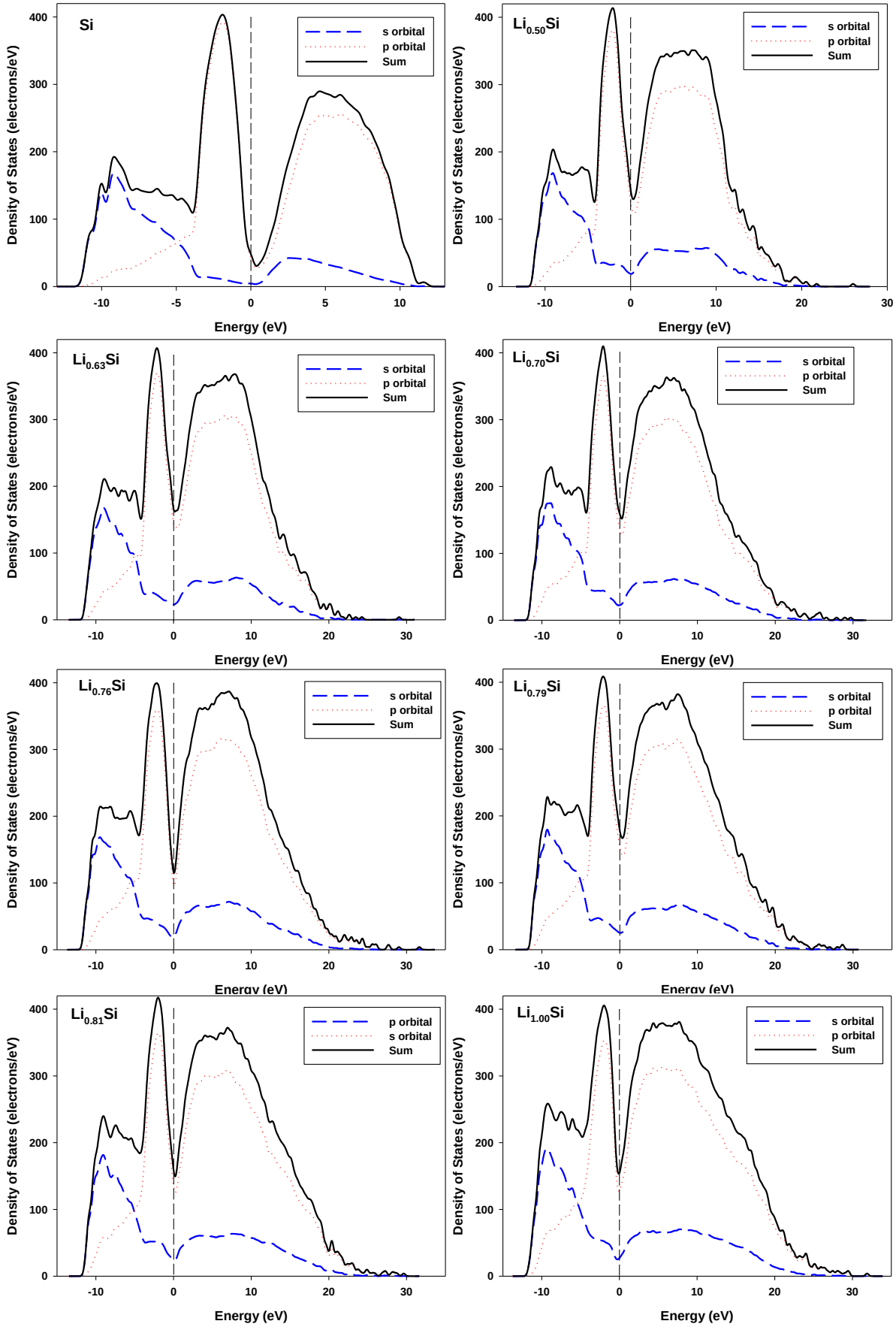

In principle, the electronic density of states, DOS, describes the number of electronic states per volume at each available energy level; and the electronic partial density of states, PDOS, can aid in the identification of which atom's electronic states contribute at given parts of the energy spectrum. Given that these systems in question are amorphous, we discuss the total orbital contributions from both Li and Si without specifically ascribing a contribution on the spectra per atomic species. The s, p, and sum on the PDOS refer to the combined contributions of the s orbital electrons, combined p orbital electron contribution, and sum refers to the total DOS resulting from combining all s and p contributions from both atomic species of the binary structure.

By considering the total PDOS graph of the unlithiated Si system and contrasting it with those of the lithiated systems, we note that its total DOS consists of fewer states around the Fermi level (represented by the dotted line). By virtue of having fewer atoms when unlithiated, this observation is generally expected because a relatively fewer number of electrons will exist in the system.

Considering the PDOS of these amorphous Li-Si alloys, we note that generally speaking the Fermi level is located around if not directly within the pseudogap. All these plots show that the major contribution around the Fermi level is from the p-orbitals of which the graphs are as well parabolic. The s-orbitals in all these lithiated amorphous systems are seen to exhibit states of about 30 electrons/eV. The p-orbitals of $Li_{0.63}Si$ and $Li_{0.79}Si$ appear to have about 140 electrons/eV states around the Fermi, whilst that of the $Li_{0.70}Si$ alloy has a DOS of about 130 electrons/eV. The p-orbital of $Li_{0.5}Si$ has a DOS of just under 120 electrons/eV whilst that of $Li_{0.81}Si$ as well as Li_1Si have a DOS of slightly above 120 electrons/eV.

The parabolic troughs of the total DOS in $Li_{0.76}Si$, $Li_{0.81}Si$, and Li_1Si are almost symmetrically split by the Fermi level, signifying a high probability of electronic stability. The $Li_{0.76}Si$ alloy portrays the lowest states in p-orbital and total DOS, with values of about 100 electrons/eV and 120 electrons/eV respectively. This suggests that among all these amorphous Li-Si alloys, the most stable composition would be that consisting of about 43.3 atm% Li.

4.10 Comparison of Volume Expansion in Crystalline and Amorphous Si as Result of Li Insertion Using SCC-DFTB

Table 4-8. Volume expansion of selected amorphous Si structures as a result of Li insertion

Stoichiometric	*atm*% Li	*atm*% Si	ΔVol. (%) a-Si
$Li_{0.5}Si$	33.3	66.7	6.59
$Li_{0.63}Si$	38.7	61.3	13.03
$Li_{0.76}Si$	43.3	56.7	13.66
Li_1Si	50	50	14.58

Table 4-9. Volume expansion of selected crystalline Si structures as a result of Li insertion

Stoichiometric	*atm*% Li	*atm*% Si	ΔVol. (%) c-Si
$Li_{0.5}Si$	33.33	66.7	12.67
$Li_{0.625}Si$	38.46	61.54	16.49
$Li_{0.75}Si$	42.86	57.14	31.21
Li_1Si	50	50	53.6

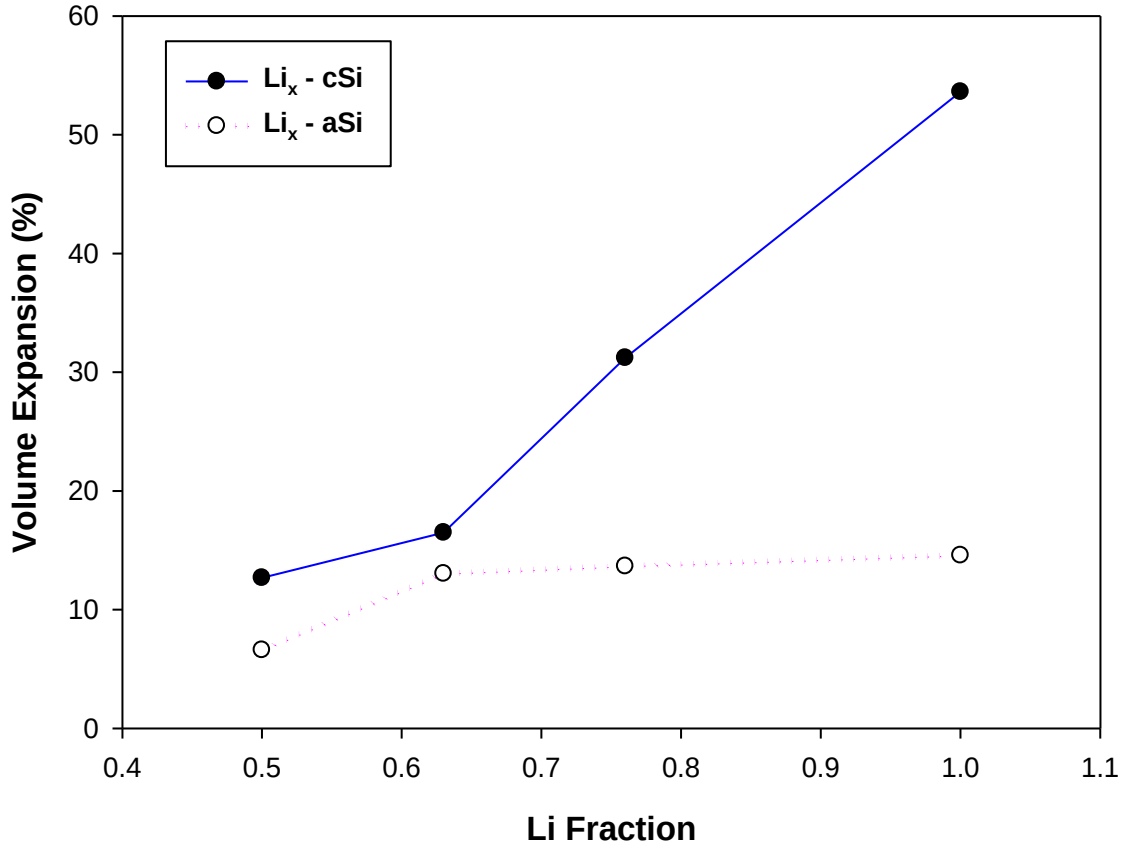

Figure 4-11. A graphical presentation of the volume expansion in amorphous and crystalline silicon as a result of increasing lithium content.

Tables 4-8 and 4-9 together with Figure 4-11 present a comparison between the relative volume expansions of amorphous silicon as a result of Li insertion with the relative volume expansion of crystalline silicon as a result of Li insertion. As shown, in Tables 4-7 and 4-8, lithium was inserted into amorphous silicon. Pure amorphous silicon was optimised, then a fraction of Li was inserted into the silicon, then the Li_x-aSi was optimised. The optimised structure was retrieved, and then the Li content was increased by the insertion of a fraction of Li atoms. Then the resulting composition was also then optimised. By iteratively increasing the Li content, the insertion was done accumulatively. The final volumes of the Li-aSi alloys were obtained, and have been tabulated in section 4.8 as Table 4-7. From these systems, a few compositions were selected to formulate Table 4-8. From the graphical presentation of the Li insertion into amorphous silicon and crystalline silicon, it can be deduced that the system is expanding in volume by a higher factor for the crystalline than for the amorphous host. For a selected concentration range (*i.e.* 33 to 50 *atm%* Li), the change in relative volume expansion as a result of increasing Li content is lower for the amorphous than for the crystalline silicon structure. This trend suggests that an amorphous host can potentially accommodate a larger amount of Li content than for a crystalline host. Also, the amorphous host seems to exhibit a buffering effect on the volume expansion. This is consistent with what has been reported in literature about hosts that are of a disintegrated structure; they tend to have abundant pores that effectively buffer the volume expansion.

4.11 Sodiation of Silicon

To computationally model the sodiation of silicon using the DFTB technique, similar to the context presented in the previous sections based on the Li-Si system in this thesis, an SCC-DFTB parameter set is required for the Na-Si system. At the time of writing, a parameter set that contains the Na-Si element on the DFTB website is the *matsci* library. However, the Na-Si pair in *matsci* library was developed for zeolites which are sorbate in state; as such, the library is not adapted for solids. Therefore, since the sodiation of silicon in this work is done based on solid states, it was necessary for the Na-Si SCC-DFTB parameter set to be developed in this respect. This section presents the validation and application of the Na-Si SCC-DFTB parameter set developed herein.

4.11.1 Validation of Na-Si SCC-DFTB parameter set

Table 4-10. The validation of Na-Si SCC-DFTB parameters

System	Bond	Length (Å)		Lattice (Å)	
		SCC-DFTB	Exp (Ref.)	SCC-DFTB	Experiment
Na	Na-Na	3.576	3.715	a = 4.129	4.29 [18]
Si	Si-Si	2.419	2.352	a = 5.587	5.43 [19]
NaSi	Na-Si	2.932	3.044	a = 11.847	12.19 [20]
	Na-Na	3.485	3.426	b = 6.752	6.55 [20]
	Si-Si	2.852	2.398	c = 11.139	11.18 [20]

Table 4-10 illustrates the validation of the newly developed Na-Si SCC-DFTB parameter set against the reference structure details used for parameterisation. The set can estimate the first nearest neighbour distance of the Na-Na bond in the bcc Na to within 3.75% relative to experiments. The approximated Si-Si bond length of 2.419 Å in FCC Si agrees with the experimental value of 2.352 Å to within 2.85%. The first nearest neighbour distance of the Na-Na, Na-Si, and the Si-Si in the monoclinic NaSi was estimated to within 1.73%, 3.68 %, and 18.93% respectively compared to experimental values. The huge percentage difference of the Si-Si bond suggests that the parameter set may need to be improved to better describe the bonding of silicon. Interestingly, as reflected in Table 4-10, the calculated equilibrium lattice parameters obtained by using the Na-Si SCC-DFTB parameters agreed with experiments to within 2.89% for Si (*Fd-3m*), 3.75% for Na (*Im-3m*) and 3.08% for NaSi (*C2/c*), which are reasonable for the DFTB method. After assessing the parameter set based on the reference structures is sensible to proceed to test for transferability.

4.11.2 Transferability test of the Na-Si SCC-DFTB parameter set

Table 4-11. Structural properties obtained using the Na-Si SCC-DFTB parameter set

System	Space group	#atoms	Lattice (Å)		%Diff
			Exp	Calc.	
Si	*Fd-3m*	8	a = 5.43	a = 5.587	2.89
Na	*Im-3m*	2	a = 4.29	a = 4.129	3.75
NaSi	*C2/c*	32	a = 12.19 b = 6.55 c = 11.18	a = 11.847 b = 6.752 c = 11.139	2.81 3.08 0.37
Na_4Si_{23}	*Pm-3n*	54	a = 10.197 [24]	a = 10.619	4.14
$NaSi_6$	*Cmcm*	28	a = 4.106 [22] b = 10.563 [22] c = 12.243 [22]	a = 4.131 b = 10.535 c = 13.986	0.61 0.27 14.24
Na_3Si_{17}	*Fd-3m*	160	a = 14.716 [23]	a = 15.477	5.17

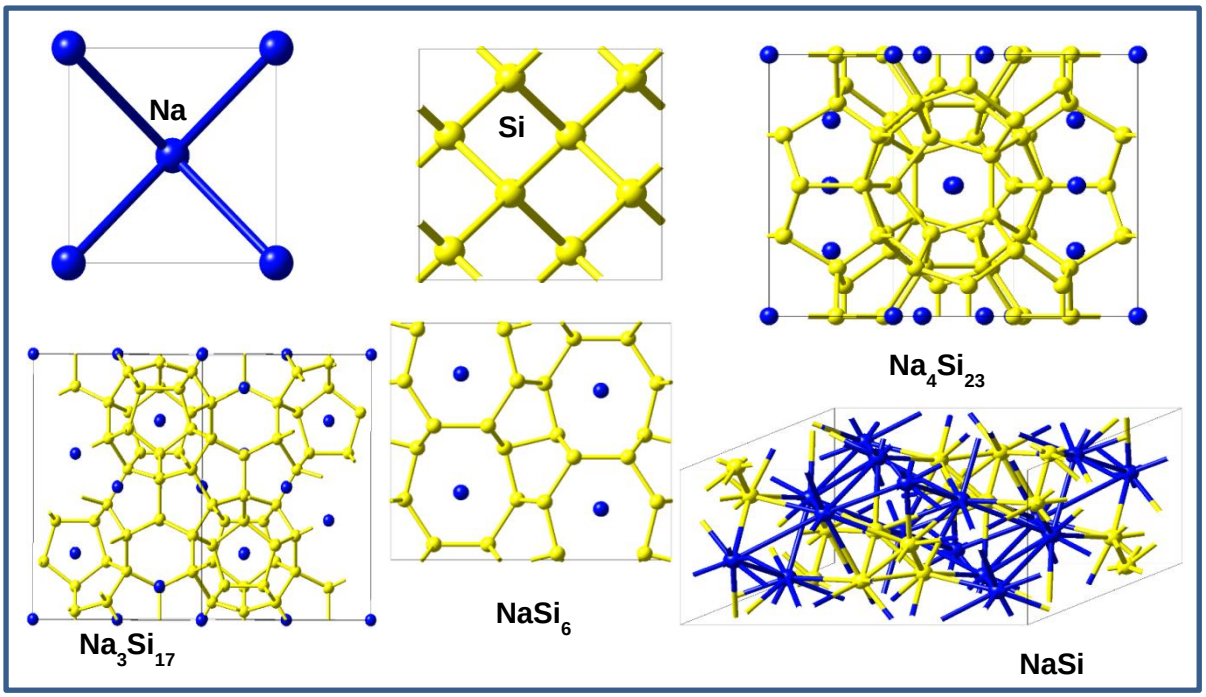

Figure 4-12. Illustration of Na, Si, Na_4Si_{23}, $NaSi_6$, Na_3Si_{17}, NaSi

Table 4-11, lists the reference structures used for fitting in the first three data rows, and the last three rows are Na-Si clathrates systems that were not used for fitting. Figure 4-12 graphically illustrates the structure of the reference structures (Na, Si, and NaSi) as well as the Na-Si clathrates (Na_4Si_{23}, $NaSi_6$, Na_3Si_{17}). It appears the Na-Si SCC-DFTB parameter set handles the geometry of cubic clathrates reasonably. That is to say, the calculated equilibrium lattice constant of 10.619Å for the cubic Na_4Si_{23} (also known as Na_8Si_{46}) agrees with experiments to within 4.14%, and for the cubic Na_3Si_{17} (also known as $Na_{24}Si_{136}$) the lattice parameter value of 15.477 Å agrees with experiments to within 5.17%. As for the orthorhombic $NaSi_6$, the ***a*** and ***b*** lattice parameters are in excellent agreement with experimental values, as they differ by only 0.61% and 0.27% respectively. However, the SCC-DFTB parameter overestimates the ***c*** parameter by 14.24%. Since the set generally handles most of the systems tested on reasonably well, perhaps the accuracy in better handling a variety of bond coordination can be improved by applying regularizer in the parameterisation routine. Nonetheless, it is not necessary to discard developed set on this basis. To further evaluate the ability of the Na-Si SCC-DFTB parameter set to handle even more complex geometries, similar to the Li-Si system, a test is done on the sodiation of crystalline and amorphous silicon, but with few compositions.

4.12 Sodium Insertion Into Crystalline and Amorphous Silicon

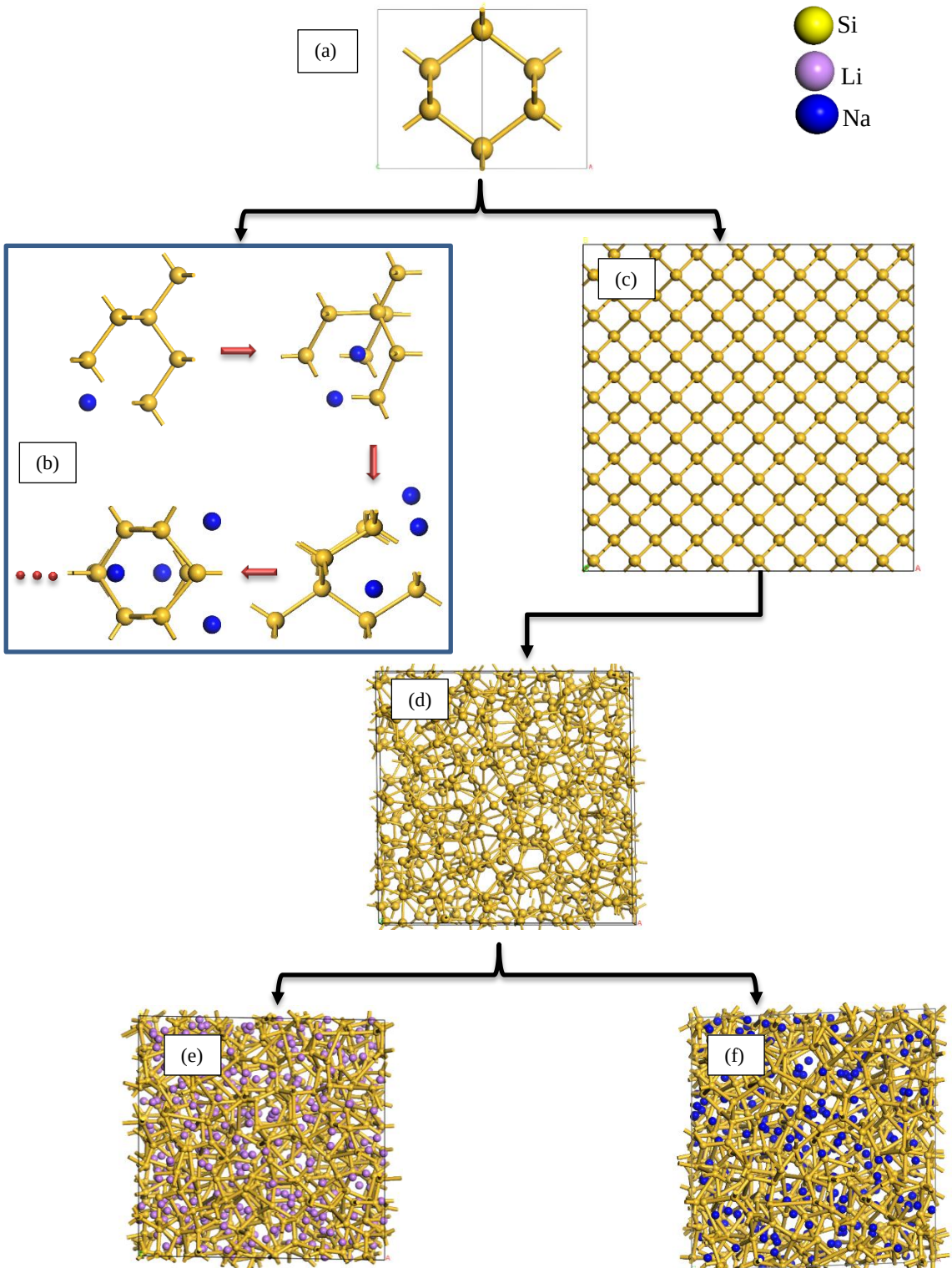

Figure 4-13. Graphical presentation of silicon sodiation and a step-wise graphical illustration of the creation of intercalated amorphous Si structures. (a) A standard unit cell of bulk Si, (b) systematic Na insertion into bulk Si, (c) a crystalline Si supercell with 512 atoms, (d) bulk amorphous Si, (e) amorphous Si with 50 *atm* % Li, (f) amorphous Si with 50 *atm* % Na.

Figure 4-13 presents a step-wise graphical illustration of the sodiation of silicon and a step-wise graphical illustration of the creation of amorphous Si structures. Using the insights generated from the work done in lithiating crystalline silicon, a similar approach was used for sodiating silicon. The variation in volume when sodium is inserted into crystalline silicon was modelled using the SCC-DFTB approach.

As shown in Figure 4-13, the workflow takes a form that starts from a standard unit cell of bulk Si. Sodium is systematically inserted into the interstitials of bulk Si. When this is done, the volume changes are then compared to those reported for the Li-Si system. In principle, this process of inserting sodium into silicon is intended to predict what could potentially occur when the sodium-silicon alloy is employed in rechargeable batteries.

4.12.1 Sodium Insertion Into Crystalline Silicon (*c*-Si)

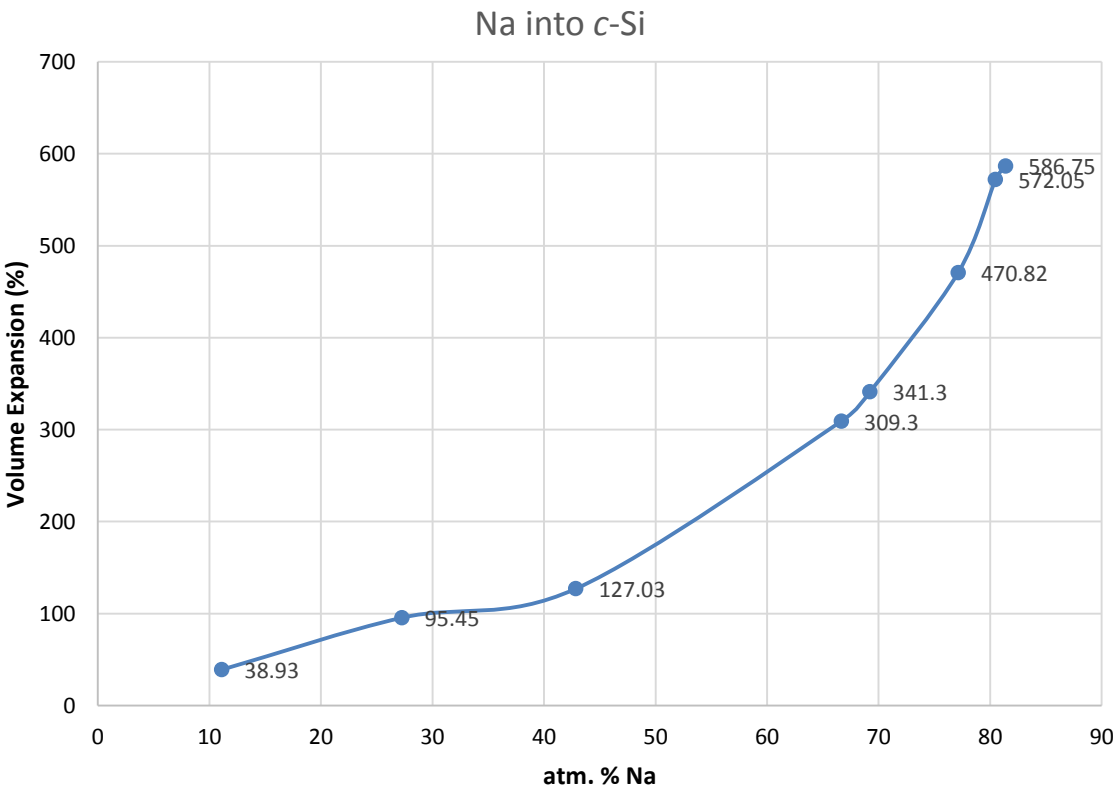

Figure 4-14. Volume expansion of crystalline Si as a function of Na intercalation

The Na-Si SCC-DFTB parameter set predicts that Na insertion into *c*-Si will result with an enormous volume expansion going beyond 400% at 77 *atm%* Na, and will be above 500% for concentrations exceeding 80 *atm%* Na.

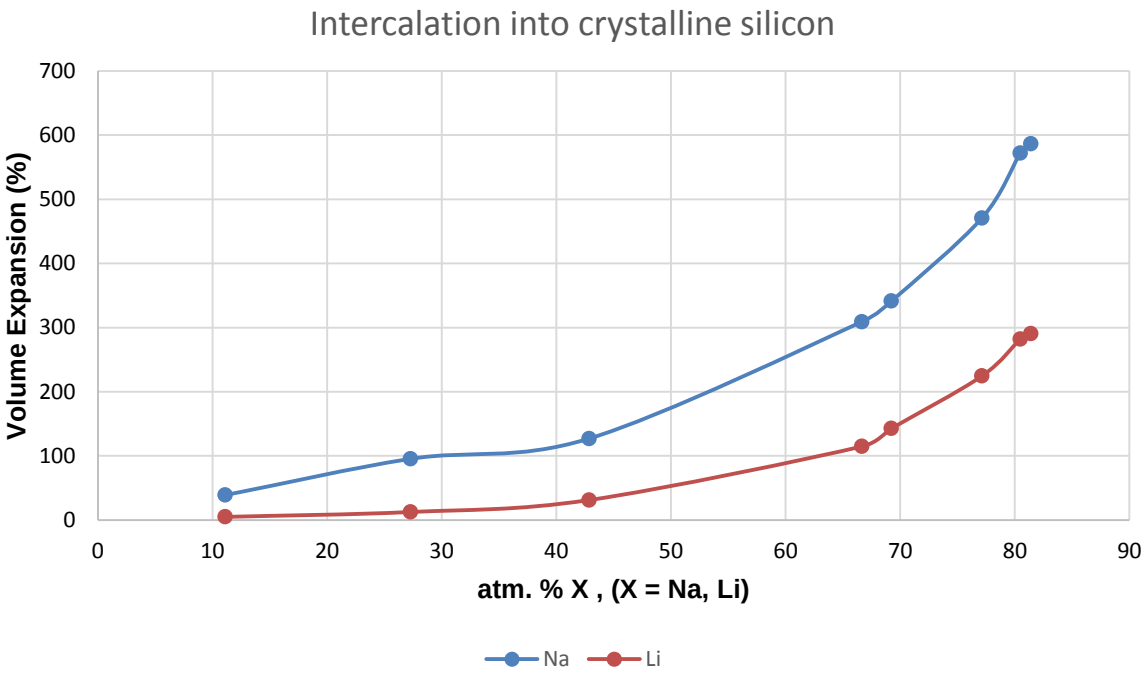

Figure 4-15. Comparison between the expansion of Si as result of Na intercalation with Li intercalation

Table 4-12. Comparison of Si volume expansion as a result of Li to Na insertion

Conc. *atm.* %	Na-Si Vol. Expa.	Li-Si Vol Expa.	Na/Li Vol. Expa.
11.11	38.93	4.98	7.82
27.27	95.45	12.57	7.59
42.86	127.03	31.21	4.07
66.67	309.3	114.84	2.69
69.23	341.3	142.71	2.39
77.14	470.82	224.59	2.1
80.49	572.05	282.26	2.03
81.4	586.75	290.5	2.02

As depicted by Figure 4-15 and captured in Table 4-12, a comparison between how crystalline silicon expands in volume as a result of Na intercalation and Li intercalation shows that Na would likely result in more adverse effects. As shown in the 4th column (Na/Li Vol. Exp.), for concentrations ranging from 66.67 – 81.4 *atm %*, *c*-Si expanded by at least twice as much when intercalated with Na than when Li is used. This suggests that unless effective methods for buffering the extreme volume expansions can be devised and employed, c-Si would not be suitable for application as an anode in Na-ion batteries.

4.12.2 Bulk amorphous silicon with 33 *atm%* Na

System	$Na_{0.5}Si$	$Na_{0.5}Si$
# Atoms	768	768
Volume	10341.3 Å³	12427.9 Å³
α	90°	88.69639
β	90°	90.19472
γ	90°	87.84536
Geometry	Unrelaxed	Relaxed
Morphology	Bulk	Bulk

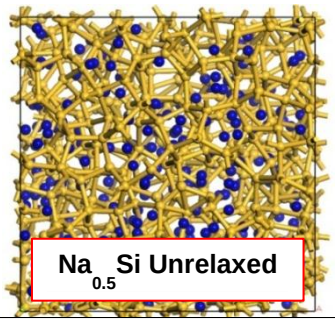

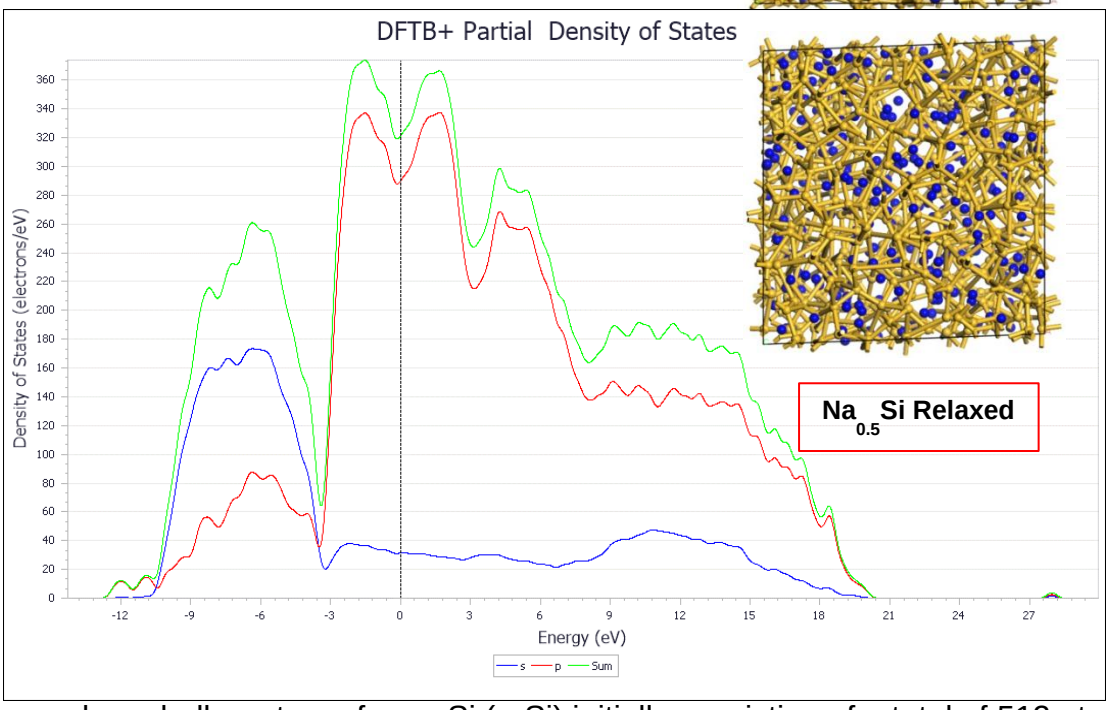

An amorphous bulk system of pure Si (*a*-Si) initially consisting of a total of 512 atoms was optimised. 256 atoms of Na were then randomly added into the optimised a-Si structure. The 768 atoms amorphous Na-Si system which now was composed of 33 *atm%* Na had a volume of 10431.3 Å³ before relaxation. The sodiated *a*-Si was then brought to equilibrium by employing the Na-Si SCC-DFTB parameter set in performing a structure relaxation. The volume of the resulting slightly distorted $Na_{0.5}Si$ structure increased to 12427.9 Å³, which represents a 15.89% expansion relative to the unsodiated optimised a-Si that had a volume of 10723.5 Å³. This expansion in a-Si is 6x less than in *c*-Si, meaning *a*-Si would be more preferred for Na-ion batteries. At 33 *atm%* Na, the volume expansion in a-Si is more than 2x that of Li at the same concentration (*i.e.* a-Si expands by 6.59% at 33 *atm%* of Li). This is anticipated since Na has a larger atomic (2.27 Å) and ionic (1.02 Å) radii compared to Li (1.82 Å & 0.76 Å respectively). Despite this expansion, the PDOS shows that the structure of $Na_{0.5}Si$ is somewhat stable since the Fermi is located amid the pseudogap on the total DOS.

Chapter 5 **Cluster Expansion Applied on the M – Si Alloys (M= Li, Na, Mg)**

It has already been highlighted in previous chapters that due to its theoretical capacity, Si has potential use as a high energy density electrode material in rechargeable batteries when alloyed to Li. Furthermore, the need for various functional intercalants of Si has also been alluded to. The phase diagram of the Li-Si system has been extensively reported in available literature, however, not so much work has been explored for the Na-Si and Mg-Si systems in perspective of the energy storage application.

It has also been previously mentioned in this work that compositional and configurational search necessary for screening new materials is traditionally done through costly experimentation in laboratories, and it entails a lot of effort and time. In this section, a 'virtual laboratory' is mimicked by employing the strength of a machine-learning-powered technique, cluster expansion, embedded within the UNCLE code, to screen potential materials based on the alloy of Si with Li, Na and Mg.

A preliminary crystal structure search is done using the FCC and BCC symmetries. Where possible, the mechanical and electronic stabilities of predicted structures are evaluated using SCC-DFTB. The cluster expansion technique is essentially coupled with the SCC-DFTB to pave way for future investigations on new materials. On one hand, the cluster expansion can help identify candidate new materials which can be used to broaden the training set required for DFTB parameterisation of the Slater-Koster potentials, and on the other hand, it can be used to produce stable structures from which larger systems with complex morphologies such as those with a Nano architectural design.

The crystal structure search in this section aims to predict viable M – Si alloy (M= Li, Na, Mg) compositions and stable phases that could potentially be further investigated for guiding the design of high energy density electrodes. It is noted that despite that Li-Si alloys have been widely studied, the material space for this system has possibly not been fully exhausted; furthermore, the crystal search on the Li-Si

system is done as a framework validator that establishes a bridge of insights through which the Na-Si and Mg-Si systems could be explored.

5.1 Ground-State Phase Structure Predictions for Li-Si

5.1.1 Miscible constituents and miscibility gap mode of the cluster expansion

Building on the theoretical background of the cluster expansion method as presented in section 2.6 of this thesis, and before structure predictions can be done, it is perhaps necessary to highlight the two modes/model types (*viz.* miscible constituents and miscibility gap mode) that the iterative processes in the cluster expansion use as part of the convergence evaluation. To distinguish the two model types, the heats of formation $\Delta H_f(\vec{\sigma})$ are evaluated for all structures in the training set as defined by the following equation:

$$\Delta H_f(\vec{\sigma}) = \frac{E_{DFT}(\vec{\sigma}) - \sum n_i(\vec{\sigma}) E^i_{DFT}}{\sum n_i(\vec{\sigma})} \quad \textbf{(5.1)}$$

where $E_{DFT}(\vec{\sigma})$ describes the DFT total energy of the structure $\vec{\sigma}$, $n_i(\vec{\sigma})$ is the number of atoms of atomic species i contained in $\vec{\sigma}$, and E^i_{DFT} denotes the DFT total energy of the pure phase of atomic species i. The sums go over all the type of atoms contained in the structure $\vec{\sigma}$.

The models with miscible constituents have structures with negative ΔH_f, signifying thermodynamically stable ordered structures, while models with a positive ΔH_f, wherein none of the ordered structures are thermodynamically stable and phase separation occurs, and consequently have a miscibility gap.

5.1.1.1 Miscible constituents

If a model has miscible constituents, structures with the lowest ΔH_f at a given concentration (see Figure 5-1 that follows) are the most important, and the cluster expansion (CE) should be most accurate for those. To achieve this, structures predicted by the cluster expansion to be more favourable (*i.e.* those with a lower ΔH_f) and are not yet part of the training set, are added to the training set. This is done iteratively until no new structures are predicted by CE to be more favourable

than those already included in the training set. At this stage, the CE has converged and from all considered structures, the thermodynamically stable ones are identified.

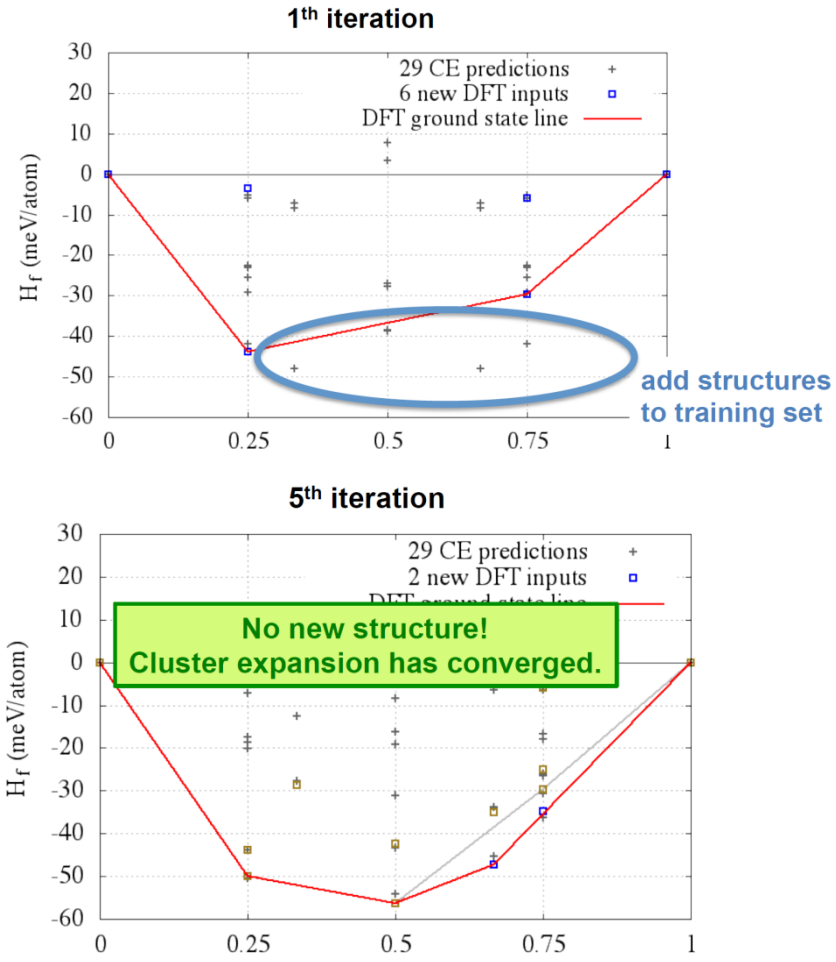

Figure 5-1. Illustration of a ground-state binary diagram with miscible constituents.

5.1.1.2 Miscibility gap

If a model is phase separating, then no stable ordered structures exist apart from the two pure phases and in this case, all structures are of equal importance to the cluster expansion. As shown by Figure 5-2, the model is said to reflect a miscibility gap. Thus, the selection procedure of structures to be added to the training set has to improve the quality of the cluster expansion for all considered structures, regardless of their formation energies ΔH_f.

The stochastic nature of the genetic algorithm is used to determine how good or bad the energies of the structures are predicted by the cluster expansion. Numerous cluster expansions are performed using an identical training set. The energies of all considered structures are then predicted by these multiple J's, and the standard deviations of the predicted energies are evaluated. Structures with the highest

standard deviation are those whose description by the cluster expansion is the worst. Therefore, these are iteratively added to the training set.

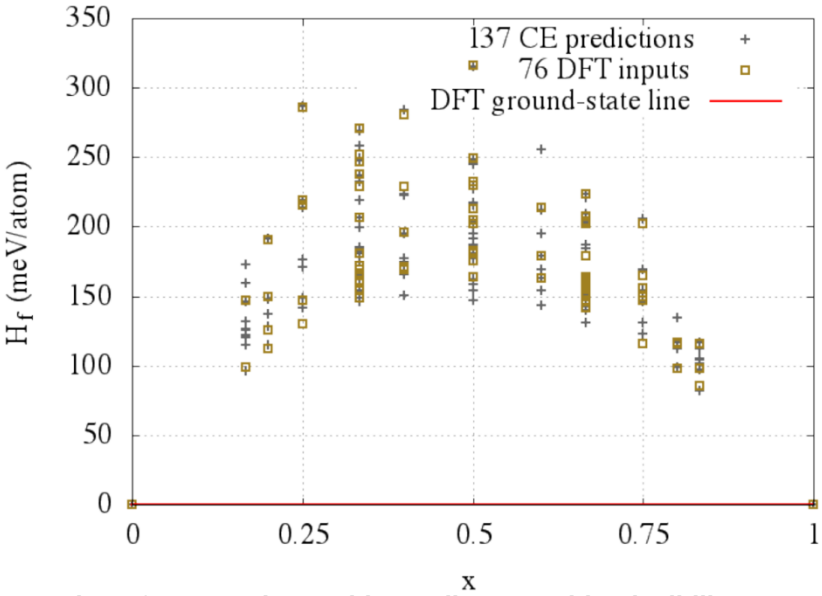

Figure 5-2. Illustration of a ground-state binary diagram with miscibility gap.

5.1.2 Structure predictions from Li, Si belonging to the *Fm-3m* symmetry

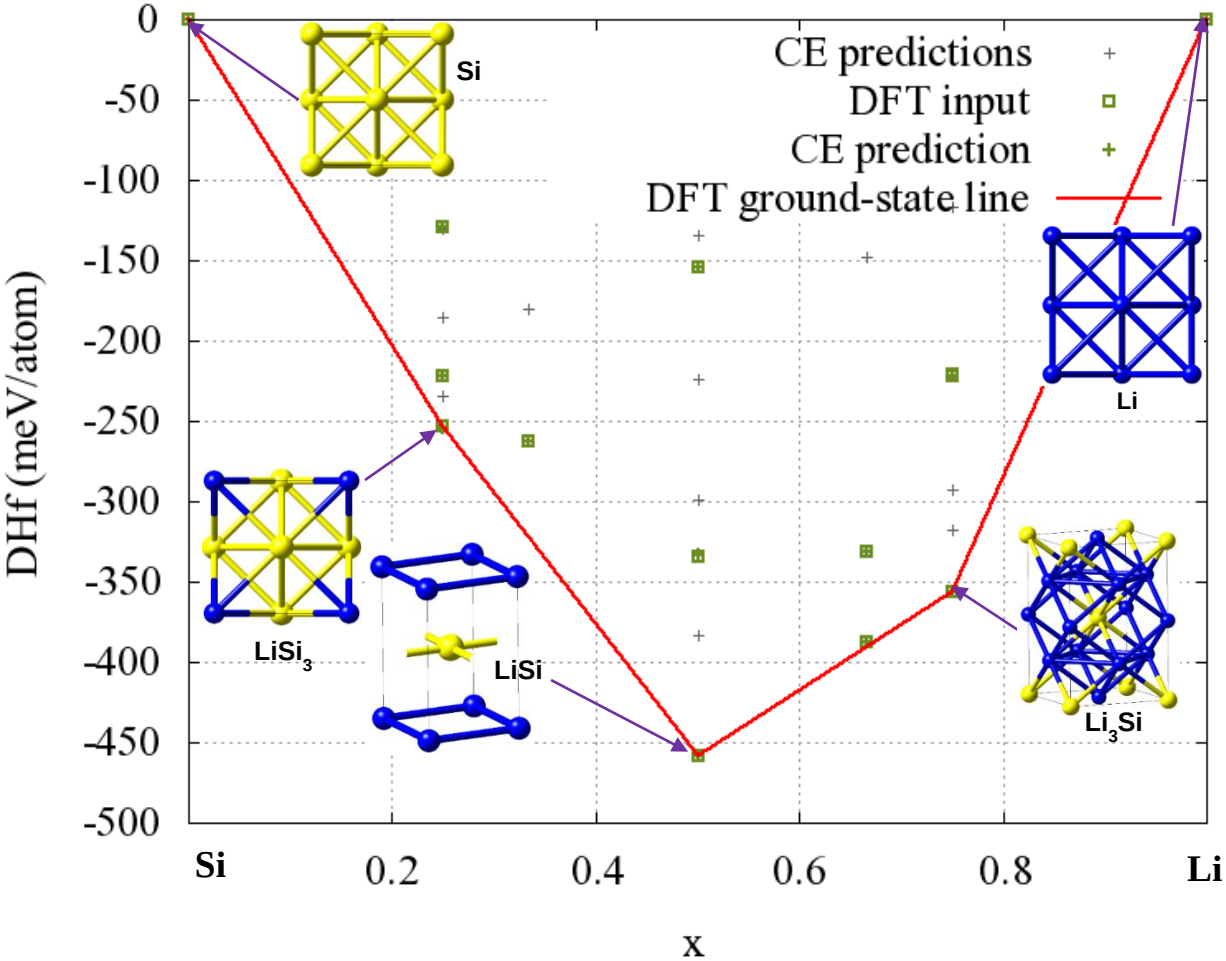

Figure 5-3. Calculated binary ground-state diagram of Si-Li emanating from a grid search using the FCC-based system considering structures of up to 16 basis atoms.

Table 5-1. A listing of the structures that constitute the DFT ground-state line, their compositions *x* and formation energies DHf from the Si-Li cluster expansion.

# x(1:k,1:nC)	DHf / atom [eV]	structure title	cell formula	space group
0.0000000000	1.0000000000	0.0000000000	ce2	Si	Fm-3m
0.2500000000	0.7500000000	-0.2536335000	ce29	LiSi3	Pm-3m
0.5000000000	0.5000000000	-0.4587745000	ce4	LiSi	P4/mmm
0.7500000000	0.2500000000	-0.3564175000	ce15	Li3Si	I4/mmm
1.0000000000	0.0000000000	0.0000000000	ce1	Li	Fm-3m

Table 5-2. A summary of the iterative optimization progress

Iteration	no. of struc.	no. of new struc.	CVS [meV/pos.]	% struc. with SD below 5 meV	new structures
0	0	2	-	-	ce1 ce2
0	0	6	-	-	ce1 ce18 ce10 ce9 ce27 ce2
1	6	4	13	-	ce29 ce16 ce6 ce28
2	10	3	1.4	-	ce23 ce3 ce26
3	13	3	3.6	-	ce25 ce4 ce13
4	16	1	0.37	-	ce15
5	17	0	0.25	-	

Table 5-3. Comparison of energies E and formation energies DHf in eV (counted per active atom position) as predicted by the cluster expansion and as calculated by the computational engine (DFT).

Energy differences to the structure at the ground state line (GSL) for each composition x are listed.

# no.	x(1:k,1:nC)		E_DFT	D(E_DFT,E_CE)	E_CE	DHf_DFT	DHf_CE	Dist to GSL DFT	title	cell formula	space group
1	0.00000	1.00000	-4.8651740000	0.0000001000	-4.8651739000	0.0000000000	0.0000000000	0.0000000000	ce2	Si	Fm-3m
2	0.25000	0.75000	-4.3196000000	-0.0003996001	-4.3199996001	-0.1945295000	-0.1949291501	0.0591040000	ce23	LiSi3	C2/m
3	0.25000	0.75000	-4.3467557500	0.0001482816	-4.3466074684	-0.2216852500	-0.2215370184	0.0319482500	ce27	LiSi3	Cmmm
4	0.25000	0.75000	-4.3668055000	0.0001141575	-4.3666913425	-0.2417350000	-0.2416208925	0.0118985000	ce25	LiSi3	I4/mmm
5	0.25000	0.75000	-4.3787040000	-0.0000292598	-4.3787332598	-0.2536335000	-0.2536628098	0.0000000000	ce29	LiSi3	Pm-3m
6	0.33333	0.66667	-4.1042526667	-0.0001205499	-4.1043732166	-0.2258833333	-0.2260039166	0.0961305000	ce10	LiSi2	I4/mmm
7	0.33333	0.66667	-4.1405826667	0.0002849258	-4.1402977408	-0.2622133333	-0.2619284408	0.0598005000	ce9	LiSi2	Immm
8	0.50000	0.50000	-3.5972607500	0.0001663108	-3.5970944392	-0.2122937500	-0.2121274392	0.2464807500	ce16	Li2Si2	R-3m
9	0.50000	0.50000	-3.6704135000	0.0001114990	-3.6703020010	-0.2854465000	-0.2853350010	0.1733280000	ce3	LiSi	R-3m
10	0.50000	0.50000	-3.7188537500	-0.0001276145	-3.7189813645	-0.3338867500	-0.3340143645	0.1248877500	ce18	Li2Si2	C2/m
11	0.50000	0.50000	-3.8437415000	0.0002100292	-3.8435314708	-0.4587745000	-0.4585644708	0.0000000000	ce4	LiSi	P4/mmm
12	0.66667	0.33333	-3.2787196667	-0.0002849258	-3.2790045925	-0.3871550000	-0.3874398925	0.0033815000	ce6	Li2Si	Immm
13	0.75000	0.25000	-2.8661347500	-0.0003224666	-2.8664572166	-0.2212712500	-0.2215936666	0.1351462500	ce26	Li3Si	Cmmm
14	0.75000	0.25000	-2.8663130000	0.0002585451	-2.8660544549	-0.2214495000	-0.2211909049	0.1349680000	ce28	Li3Si	Pm-3m
15	0.75000	0.25000	-2.9242865000	0.0004495770	-2.9238369230	-0.2794230000	-0.2789733730	0.0769945000	ce13	Li3Si	C2/m
16	0.75000	0.25000	-3.0012810000	-0.0002760065	-3.0015570065	-0.3564175000	-0.3566934565	0.0000000000	ce15	Li3Si	I4/mmm
17	1.00000	0.00000	-1.9047600000	-0.0000001000	-1.9047601000	0.0000000000	0.0000000000	0.0000000000	ce1	Li	Fm-3m

In order to obtain the converged bulk cluster expansion depicted by Figure 5-3, an FCC-based Li unit cell belonging to the *Fm-3m* space group was used, wherein Si atoms were added onto the 4a Wyckoff-position. A configurational space search of 4 unit cells leading to 16 basis atoms was considered. The genetic algorithm was used for fitting the cluster expansion.

The cluster expansion scheme was set up such that the permissible maximum number of structures added within each iteration was 5. Five structures were used to initialise the first iteration. The scheme was set to use the automatic treatment of the miscible constituents. The convergence criterion for optimizing the cluster expansion was 5meV/ atomic position, and to assess the quality of the predictions, 5 cluster expansions were used for each iteration. Lastly, a total permissible number of iteration to conduct the ground-state search was chosen to be 20.

As reflected on Table 5-2, which presents the summary of the iterative optimisation progress within the cluster expansion, the 5th column remained empty, meaning that the optimisation scheme did not switch to a miscibility gap mode. This suggests that a system with stable structures has been produced. From iteration numbered 5 in Table 5-2, it can be detected that a total of 17 structures were contained in the training set, of which besides the pure Li and Si systems, 3 Li-Si phases were located on the ground-state tie-line. As seen in Table 5-1, the three thermodynamically stable phases are $LiSi_3$ (Pm-3m), LiSi (P4/mmm) and Li_3Si (I4/mmm). A cross-validation score of 0.25 meV/atomic position was obtained as noted on the 5th iteration in Table 5-2**,** which is very good as it greatly satisfies our specified convergence criterion.

Consider Table 5-3, the energy difference captured on the 4th column as *D(E_DFT, E_CE)*, compares the DFT input energy (located within the 3rd column, E-DFT) with the predicted energy (5th column, E_CE). From this calculation, it is noted that $LiSi_3$, LiSi, Li_3Si were predicted as stable phases with respect to the pure phases of Li and Si.

Given that to calculate the binary ground-state diagram depicted as in Figure 5-3, the search was done by moving from Si to Li on the concentration range, it was necessary to use a similar cluster expansion scheme to assess the outcome when the opposite is carried out. (*I.e*. A search from the Li concentration moving to Si across the range, provided that the two starting systems are isostructural and the same cluster expansion framework is used). The following results were obtained.

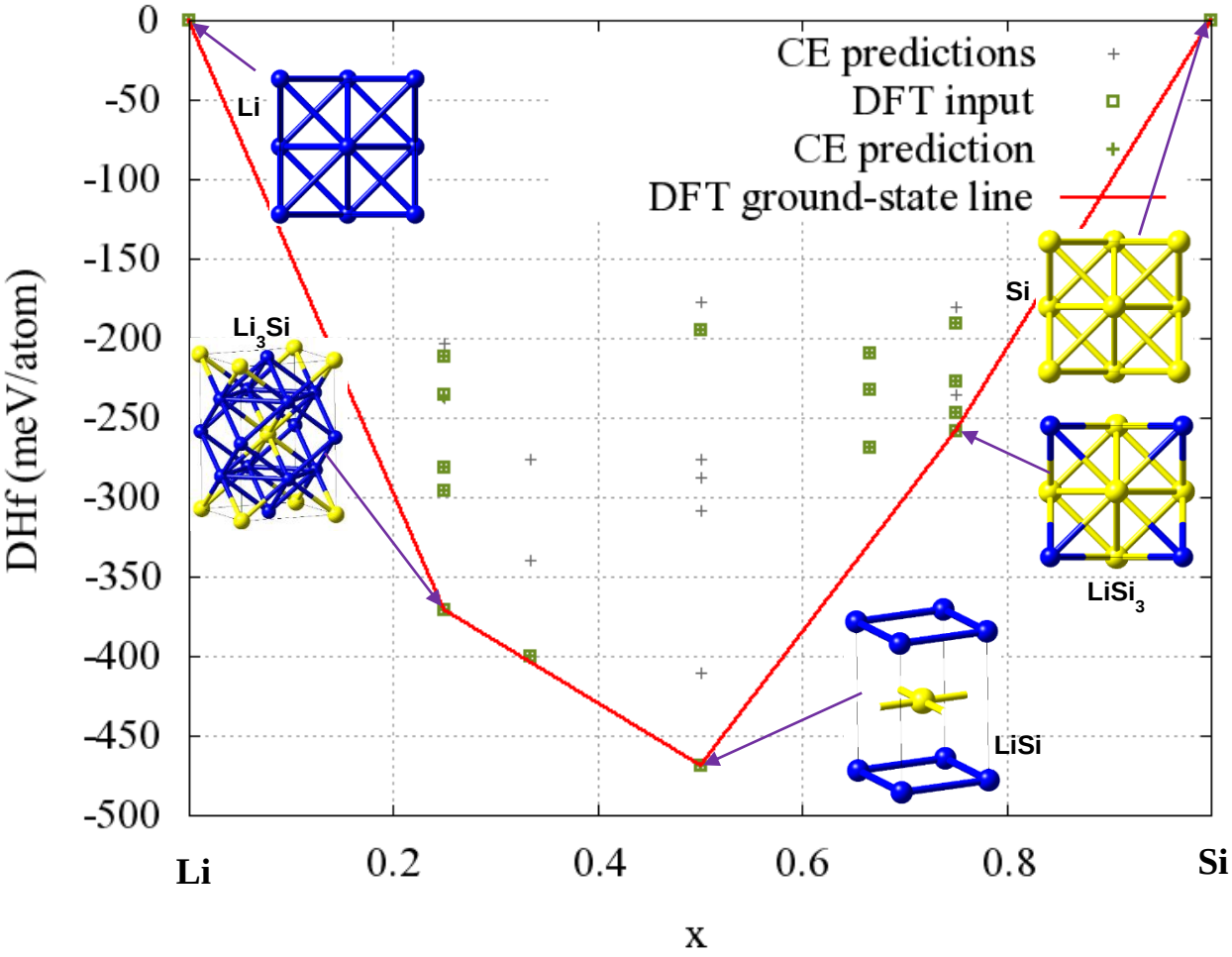

Figure 5-4. Calculated binary ground-state diagram of Li-Si emanating from a grid search using the FCC-based system considering structures of up to 16 basis atoms.

Table 5-4. A listing of the structures that constitute the DFT ground-state line, their compositions *x* and formation energies DHf.

The structures constituting the DFT ground state line, their compositions x and formation energies DHf are:

# x(1:k,1:nC)	DHf / atom [eV]	structure title	cell formula	space group
0.0000000000	1.0000000000	0.0000000000	ce2	Li	Fm-3m
0.2500000000	0.7500000000	-0.3705282500	ce25	Li3Si	I4/mmm
0.5000000000	0.5000000000	-0.4683610000	ce4	LiSi	P4/mmm
0.7500000000	0.2500000000	-0.2584910000	ce28	LiSi3	Pm-3m
1.0000000000	0.0000000000	0.0000000000	ce1	Si	Fm-3m

Table 5-5. A summary of the iterative optimization progress

Iteration	no. of struc.	no. of new struc.	CVS [meV/pos.]	% struc. with SD below 5 meV	new structures
0	0	2	-	-	ce1 ce2
0	0	7	-	-	ce5 ce14 ce23 ce4 ce19 ce1 ce2
1	7	4	0.71	-	ce25 ce9 ce6 ce28
2	11	3	0.26	-	ce29 ce7 ce15
3	14	1	0.35	-	ce27
4	15	2	0.034	-	ce22 ce26
5	17	0	0.12	-	

Table 5-6. Comparison of energies E and formation energies DHf in eV (counted per active atom position) as predicted by the cluster expansion and as calculated by the computational engine (DFT).

Energy differences to the structure at the ground state line (GSL) for each composition x are listed.

# no.	x(1:k,1:nC)		E_DFT	D(E_DFT,E_CE)	E_CE	DHf_DFT	DHf_CE	Dist to GSL DFT	title	cell formula	space group
1	0.00000	1.00000	-1.8855610000	-0.0000000133	-1.8855610133	0.0000000000	0.0000000000	0.0000000000	ce2	Li	Fm-3m
2	0.25000	0.75000	-2.8420910000	-0.0001748150	-2.8422658150	-0.2116200000	-0.2117948100	0.1589082500	ce27	Li3Si	Cmmm
3	0.25000	0.75000	-2.8663882500	-0.0001085935	-2.8664968435	-0.2359172500	-0.2360258385	0.1346110000	ce29	Li3Si	Pm-3m
4	0.25000	0.75000	-2.9115675000	0.0002103051	-2.9113571949	-0.2810965000	-0.2808861899	0.0894317500	ce22	Li3Si	Pmmm
5	0.25000	0.75000	-2.9259035000	0.0000246297	-2.9258788703	-0.2954325000	-0.2954078653	0.0750957500	ce23	Li3Si	C2/m
6	0.25000	0.75000	-3.0009992500	-0.0000341290	-3.0010333790	-0.3705282500	-0.3705623740	0.0000000000	ce25	Li3Si	I4/mmm
7	0.33333	0.66667	-3.2785440000	-0.0001576199	-3.2787016199	-0.3997696667	-0.3999272844	0.0033695000	ce9	Li2Si	Immm
8	0.50000	0.50000	-3.5697885000	0.0000747311	-3.5697137689	-0.1944075000	-0.1943327722	0.2739535000	ce19	Li2Si2	P4/nmm
9	0.50000	0.50000	-3.8437420000	0.0000903712	-3.8436516288	-0.4683610000	-0.4682706322	0.0000000000	ce4	LiSi	P4/mmm
10	0.66667	0.33333	-4.0814713333	-0.0000403916	-4.0815117250	-0.2094836667	-0.2095240672	0.1189640000	ce5	LiSi2	P-3m1
11	0.66667	0.33333	-4.1038123333	-0.0000286255	-4.1038409588	-0.2318246667	-0.2318533010	0.0966230000	ce7	LiSi2	I4/mmm
12	0.66667	0.33333	-4.1406143333	0.0001737222	-4.1404406111	-0.2686266667	-0.2684529533	0.0598210000	ce6	LiSi2	Immm
13	0.75000	0.25000	-4.3104480000	-0.0000857435	-4.3105337435	-0.1901570000	-0.1902427552	0.0683340000	ce14	LiSi3	P4/mmm
14	0.75000	0.25000	-4.3469887500	0.0000856003	-4.3469031497	-0.2266977500	-0.2266121613	0.0317932500	ce26	LiSi3	Cmmm
15	0.75000	0.25000	-4.3667692500	-0.0001548103	-4.3669240603	-0.2464782500	-0.2466330720	0.0120127500	ce15	LiSi3	I4/mmm
16	0.75000	0.25000	-4.3787820000	0.0001359965	-4.3786460035	-0.2584910000	-0.2583550152	0.0000000000	ce28	LiSi3	Pm-3m
17	1.00000	0.00000	-4.8652010000	0.0000000200	-4.8652009800	0.0000000000	0.0000000000	0.0000000000	ce1	Si	Fm-3m

By considering Figure 5-4 together with tables 5-4 through to 5-6, it is evident that the cluster expansion essentially produced a similar outcome compared to that presented Figure 5-3. Once more, a total of 17 structures were contained in the training set, of which besides the pure Li and Si systems, 3 Li-Si phases lie on the ground-state tie-line. As seen in Table 5-5, a very good cross-validation score of 0.12 meV/atomic position was obtained. As listed in Table 5-1 and Table 5-4, the same set of stable structures are predicted. I.e. From the comparative calculation, it is again noted that $LiSi_3$, LiSi, Li_3Si were predicted as thermodynamically stable phases with respect to the pure phases of Li and Si.

To sample a broader range of possible structures, a larger configurational space consisting of 5 unit cells was explored. The outcome of the respective cluster expansion is presented by the following set of results.

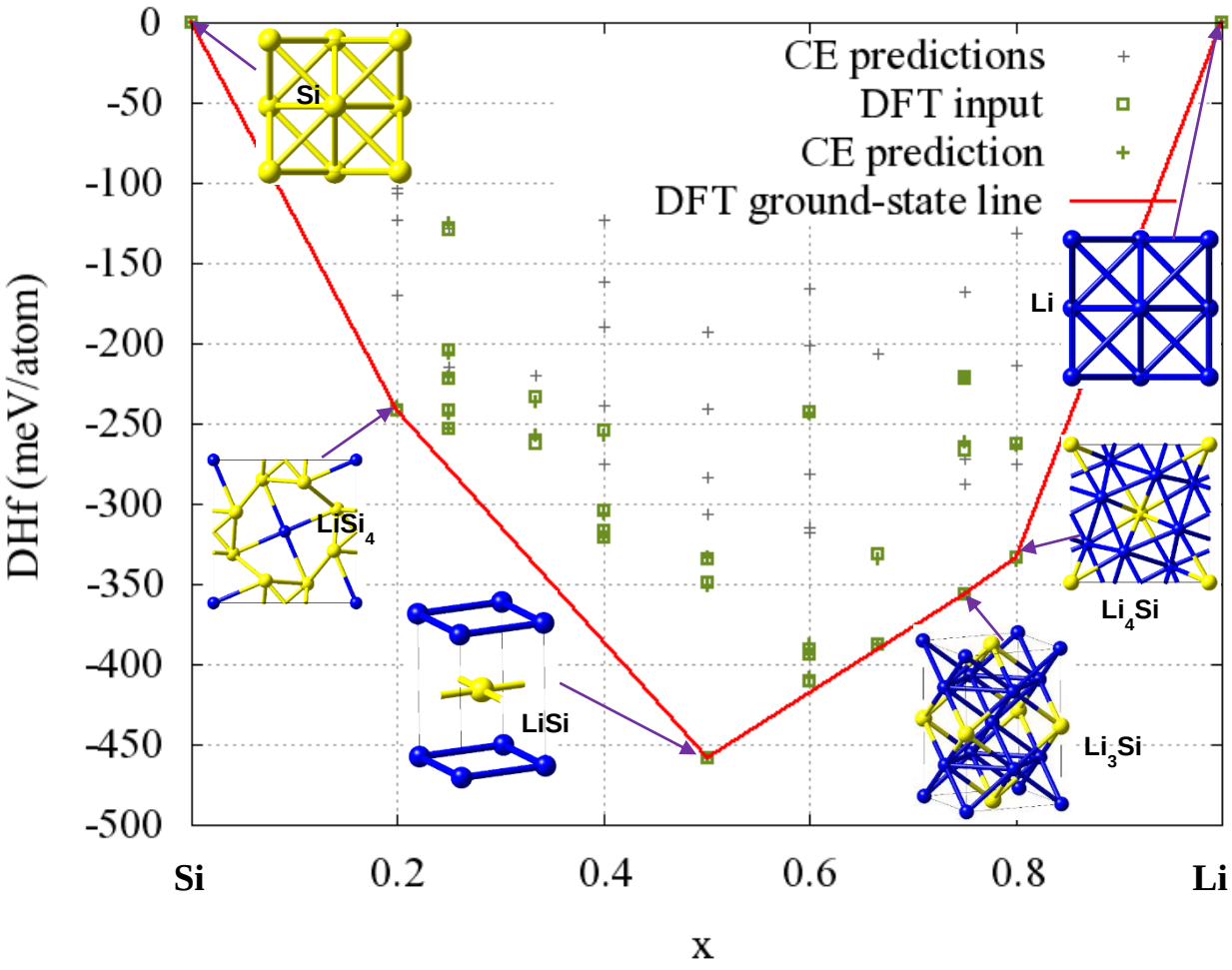

Figure 5-5. Calculated binary ground-state diagram of Li-Si emanating from a grid search using the FCC-based system considering structures of up to 20 basis atoms.

Besides the pure systems, as presented by the table in appendix F, 4 Li-Si allows were predicted to be thermodynamically stable. Namely, $LiSi_4$ (I4/m), LiSi (P4/mmm), Li_3Si (I4/mmm) and Li_4Si (Fm-3m).

Table 5-7. Summary of the iterative optimization progress

Iteration	no. of struc.	no. of new struc.	CVS [meV/pos.]	% struc. with SD below 5 meV	new structures
0	0	2	-	-	ce1 ce2
0	0	7	-	-	ce38 ce20 ce32 ce18 ce29 ce1 ce2
1	7	5	0.31	-	ce9 ce54 ce6 ce57 ce15
2	12	4	0.24	-	ce25 ce47 ce4 ce55
3	16	2	0.31	-	ce39 ce28
4	18	3	0.13	-	ce27 ce10 ce49
5	21	1	0.0029	-	ce56
6	22	1	0.11	-	ce12
7	23	5	5.3	-	ce26 ce46 ce7 ce21 ce41
8	28	1	1.7	-	ce23
9	29	0	2.5	-	

Table 5-8. A comparison of energies E and formation energies DHf in eV (counted per active atom position) as predicted by the cluster expansion and as calculated by the computational engine (DFT).

Energy differences to the structure at the ground state line (GSL) for each composition x are listed.

# no.	x(1:k,1:nC)		E_DFT	D(E_DFT,E_CE)	E_CE	DHf_DFT	DHf_CE	Dist to GSL DFT	title	cell formula	space group
1	0.00000	1.00000	-4.8651730000	-0.0000000852	-4.8651730852	0.0000000000	0.0000000000	0.0000000000	ce2	Si	Fm-3m
2	0.20000	0.80000	-4.5144208000	0.0015753875	-4.5128454125	-0.2413296000	-0.2397541243	0.0000000000	ce57	LiSi4	I4/m
3	0.25000	0.75000	-4.2541140000	0.0038130797	-4.2503009203	-0.1290432500	-0.1252300814	0.1485269167	ce21	LiSi3	R-3m
4	0.25000	0.75000	-4.3295452500	-0.0019578766	-4.3315031266	-0.2044745000	-0.2064322878	0.0730956667	ce23	LiSi3	C2/m
5	0.25000	0.75000	-4.3467547500	0.0013600568	-4.3453946932	-0.2216840000	-0.2203238543	0.0558861667	ce27	LiSi3	Cmmm
6	0.25000	0.75000	-4.3668055000	-0.0025126234	-4.3693181234	-0.2417347500	-0.2442472845	0.0358354167	ce25	LiSi3	I4/mmm
7	0.25000	0.75000	-4.3787037500	0.0002083919	-4.3784953581	-0.2536330000	-0.2534245193	0.0239371667	ce29	LiSi3	Pm-3m
8	0.33333	0.66667	-4.1121713333	-0.0026619260	-4.1148332593	-0.2338013333	-0.2364631692	0.1041697778	ce10	LiSi2	I4/mmm
9	0.33333	0.66667	-4.1406426667	0.0048175202	-4.1358251465	-0.2622726667	-0.2574550564	0.0756984444	ce9	LiSi2	Immm
10	0.40000	0.60000	-3.9354932000	-0.0032255439	-3.9387187439	-0.2544838000	-0.2577092528	0.1318080667	ce46	Li2Si3	R-3m
11	0.40000	0.60000	-3.9851682000	-0.0017982056	-3.9869664056	-0.3041588000	-0.3059569145	0.0821330667	ce47	Li2Si3	Immm
12	0.40000	0.60000	-3.9979836000	-0.0012514192	-3.9992350192	-0.3169742000	-0.3182255281	0.0693176667	ce56	Li2Si3	C2/m
13	0.40000	0.60000	-4.0018188000	-0.0003232042	-4.0021420042	-0.3208094000	-0.3211325131	0.0654824667	ce49	Li2Si3	I4/mmm
14	0.50000	0.50000	-3.7188537500	0.0001879912	-3.7186657588	-0.3338852500	-0.3336971662	0.1248877500	ce18	Li2Si2	C2/m
15	0.50000	0.50000	-3.7341565000	-0.0019496416	-3.7361061416	-0.3491880000	-0.3511375490	0.1095850000	ce20	Li2Si2	I4_1/amd
16	0.50000	0.50000	-3.8437415000	0.0004508015	-3.8432906985	-0.4587730000	-0.4583221059	0.0000000000	ce4	LiSi	P4/mmm
17	0.60000	0.40000	-3.3319128000	-0.0004524750	-3.3323652750	-0.2429852000	-0.2434375809	0.1748439000	ce38	Li3Si2	R-3m
18	0.60000	0.40000	-3.4797054000	-0.0024074200	-3.4821128200	-0.3907778000	-0.3931851259	0.0270513000	ce39	Li3Si2	Immm
19	0.60000	0.40000	-3.4828274000	0.0058894661	-3.4769379339	-0.3938998000	-0.3880102399	0.0239293000	ce41	Li3Si2	I4/mmm
20	0.60000	0.40000	-3.4991204000	0.0016010141	-3.4975193859	-0.4101928000	-0.4085916919	0.0076363000	ce55	Li3Si2	C2/m
21	0.66667	0.33333	-3.2223043333	-0.0036080396	-3.2259123729	-0.3307373333	-0.3343452779	0.0597958333	ce7	Li2Si	I4/mmm
22	0.66667	0.33333	-3.2787113333	-0.0000620352	-3.2787733685	-0.3871443333	-0.3872062734	0.0033888333	ce6	Li2Si	Immm
23	0.75000	0.25000	-2.8661637500	0.0008642230	-2.8652995270	-0.2212975000	-0.2204331807	0.1351157500	ce26	Li3Si	Cmmm
24	0.75000	0.25000	-2.8663130000	-0.0001651554	-2.8664781554	-0.2214467500	-0.2216118091	0.1349665000	ce28	Li3Si	Pm-3m
25	0.75000	0.25000	-2.9115700000	0.0050139980	-2.9065560020	-0.2667037500	-0.2616896557	0.0897095000	ce12	Li3Si	Pmmm
26	0.75000	0.25000	-3.0012795000	0.0001900853	-3.0010894147	-0.3564132500	-0.3562230684	0.0000000000	ce15	Li3Si	I4/mmm
27	0.80000	0.20000	-2.7592872000	-0.0011704371	-2.7604576371	-0.2624414000	-0.2636117401	0.0709222000	ce32	Li4Si	C2/m
28	0.80000	0.20000	-2.8302094000	-0.0015642137	-2.8317736137	-0.3333636000	-0.3349277167	0.0000000000	ce54	Li4Si	I4/m
29	1.00000	0.00000	-1.9047640000	-0.0000001000	-1.9047641000	0.0000000000	0.0000000000	0.0000000000	ce1	Li	Fm-3m

As shown in Table 5-7, the cluster expansion optimization finished successfully with a cross-validation score of 2.5 meV/pos on the last iteration. This value as well satisfies the convergence criterion used in the scheme. As a result of using a wider configurational search from the 5 unit cells (*i.e.* a grid search using the FCC-based system considering structures of up to 20 basis atoms), the total number of structures in the training set increased to 29 as illustrated by Table 5-8. From the produced structures, two new phases were predicted to be thermodynamically stable. *I.e.* $LiSi_4$ and Li_4Si are now found on the ground-state line.

At this point, it is noted that the ground-state search using the Fm-3m symmetry in the FCC parent lattice yields similar outcomes when screening from Li to Si and from Si to Li side of the concentration regime. It is possible to predict additional structures when a wider configurational space is employed. Now, a different symmetry (*Im-3m*) which presents the BCC parent lattice is explored, and the details that follow illustrate the outcome of the respective cluster expansion.

5.1.3 Structure predictions from Li belonging to the *Im-3m* space group

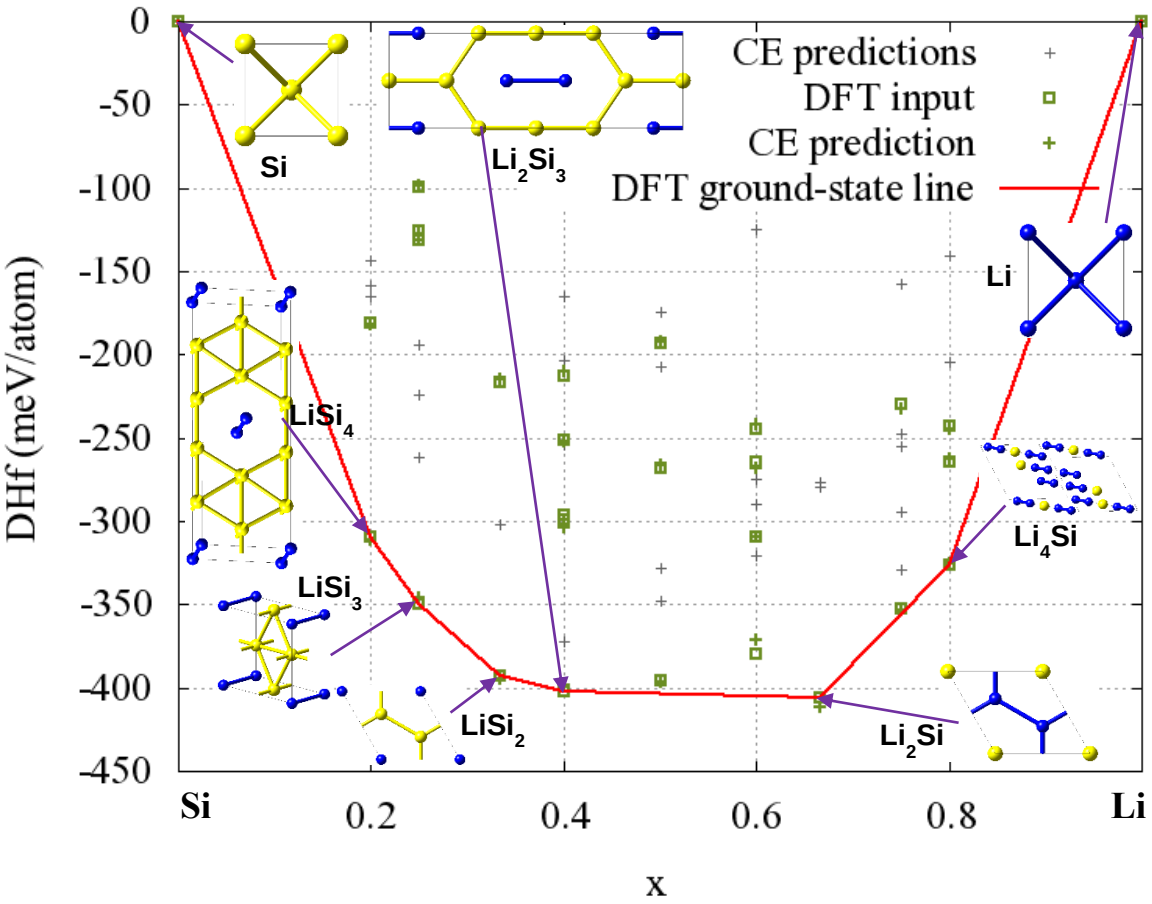

Figure 5-6. Calculated binary ground-state diagram of Li-Si emanating from a grid search using the BCC-based system considering structures of up to 10 basis atoms.

Table 5-9. Summary of the iterative optimization progress

Iteration	no. of struc.	no. of new struc.	CVS [meV/pos.]	% struc. with SD below 5 meV	new structures
0	0	2	-	-	ce1 ce2
0	0	7	-	-	ce46 ce22 ce40 ce56 ce41 ce1 ce2
1	7	5	0.6	-	ce10 ce25 ce15 ce47 ce53
2	12	5	0.65	-	ce51 ce9 ce23 ce20 ce44
3	17	5	0.0027	-	ce27 ce4 ce36 ce6 ce31
4	22	5	0.24	-	ce49 ce17 ce39 ce26 ce33
5	27	1	2.3	-	ce54
6	28	0	2.9	-	

Table 5-10. A comparison of energies E and formation energies DHf in eV (counted per active atom position) as predicted by the cluster expansion and as calculated by the computational engine (DFT).

Energy differences to the structure at the ground state line (GSL) for each composition x are listed.

# no.	x(1:k,1:nC)		E_DFT	D(E_DFT,E_CE)	E_CE	DHf_DFT	DHf_CE	Dist to GSL DFT	title	cell formula	space group
1	0.00000	1.00000	-4.8924660000	-0.0000000615	-4.8924660615	0.0000000000	0.0000000000	0.0000000000	ce2	Si	Im-3m
2	0.20000	0.80000	-4.4761506000	-0.0003158667	-4.4764664667	-0.1811400000	-0.1814558313	0.1281412000	ce53	LiSi4	R-3m
3	0.20000	0.80000	-4.6042918000	-0.0016975106	-4.6059893106	-0.3092812000	-0.3109786752	0.0000000000	ce51	LiSi4	C2/m
4	0.25000	0.75000	-4.2445792500	0.0003036434	-4.2442756066	-0.0989325000	-0.0986288278	0.2511267500	ce25	LiSi3	Fm-3m
5	0.25000	0.75000	-4.2715932500	-0.0018993170	-4.2734925670	-0.1259465000	-0.1278457882	0.2241127500	ce23	LiSi3	P4/mmm
6	0.25000	0.75000	-4.2767490000	0.0002269739	-4.2765220261	-0.1311022500	-0.1308752473	0.2189570000	ce27	LiSi3	R-3m
7	0.25000	0.75000	-4.4957060000	0.0040258559	-4.4916801441	-0.3500592500	-0.3460333652	0.0000000000	ce22	LiSi3	P2/m
8	0.33333	0.66667	-4.1136903333	0.0021658059	-4.1115245274	-0.2169833333	-0.2148175095	0.1757036667	ce10	LiSi2	I4/mmm
9	0.33333	0.66667	-4.2893940000	-0.0020683450	-4.2914623450	-0.3926870000	-0.3947553270	0.0000000000	ce9	LiSi2	P-3m1
10	0.40000	0.60000	-3.9099322000	0.0019491420	-3.9079830580	-0.2123770000	-0.2104278488	0.1896658000	ce44	Li2Si3	I4/mmm
11	0.40000	0.60000	-3.9491584000	-0.0004876608	-3.9496460608	-0.2516032000	-0.2520908516	0.1504396000	ce49	Li2Si3	R-3m
12	0.40000	0.60000	-3.9937230000	-0.0029109039	-3.9966339039	-0.2961678000	-0.2990786947	0.1058750000	ce56	Li2Si3	C2/m
13	0.40000	0.60000	-3.9965756000	-0.0050661376	-4.0016417376	-0.2990204000	-0.3040865284	0.1030224000	ce46	Li2Si3	Fmmm
14	0.40000	0.60000	-4.0995980000	0.0034558286	-4.0961421714	-0.4020428000	-0.3985869621	0.0000000000	ce47	Li2Si3	C2/m
15	0.50000	0.50000	-3.5918910000	0.0013339285	-3.5905570715	-0.1930635000	-0.1917295753	0.2105040000	ce20	Li2Si2	Fd-3m
16	0.50000	0.50000	-3.6671860000	0.0025470519	-3.6646389481	-0.2683585000	-0.2658114519	0.1352090000	ce4	LiSi	Pm-3m
17	0.50000	0.50000	-3.7947827500	-0.0006541135	-3.7954368635	-0.3959552500	-0.3966093674	0.0076122500	ce17	Li2Si2	P2_1/m
18	0.60000	0.40000	-3.3448046000	0.0026946784	-3.3421099216	-0.2447048000	-0.2420101386	0.1603874000	ce36	Li3Si2	I4/mmm
19	0.60000	0.40000	-3.3646482000	-0.0038469087	-3.3684951087	-0.2645484000	-0.2683953256	0.1405438000	ce40	Li3Si2	I4/mmm
20	0.60000	0.40000	-3.4092172000	-0.0006455784	-3.4098627784	-0.3091174000	-0.3097629953	0.0959748000	ce41	Li3Si2	R-3m
21	0.60000	0.40000	-3.4797786000	0.0082027942	-3.4715758058	-0.3796788000	-0.3714760227	0.0254134000	ce39	Li3Si2	C2/m
22	0.66667	0.33333	-3.3070566667	-0.0049939514	-3.3120506181	-0.4061086667	-0.4111026437	0.0000000000	ce6	Li2Si	P-3m1
23	0.75000	0.25000	-2.8816570000	-0.0027137237	-2.8843707237	-0.2296487500	-0.2323625102	0.1265917500	ce26	Li3Si	R-3m
24	0.75000	0.25000	-3.0042952500	-0.0014453032	-3.0057405532	-0.3522870000	-0.3537323398	0.0039535000	ce15	Li3Si	Fm-3m
25	0.80000	0.20000	-2.7454778000	-0.0016050843	-2.7470828843	-0.2428334000	-0.2444385273	0.0834862000	ce31	Li4Si	C2/m
26	0.80000	0.20000	-2.7673004000	0.0023715697	-2.7649288303	-0.2646560000	-0.2622844733	0.0616636000	ce54	Li4Si	I4/m
27	0.80000	0.20000	-2.8289640000	0.0008305558	-2.8281334442	-0.3263196000	-0.3254890872	0.0000000000	ce33	Li4Si	R-3m
28	1.00000	0.00000	-1.9051890000	0.0000000692	-1.9051889308	0.0000000000	0.0000000000	0.0000000000	ce1	Li	Im-3m

Figure 5-6 presents the calculated binary ground-state diagram of Li-Si system resulting from a grid search using the BCC parent lattice considering structures of up to 10 basis atoms. The converged cluster expansion as depicted by Figure 5-6 was obtained by adding Si atoms onto the Li (Im-3m) 2a Wyckoff-position. A configurational space search of 5 unit cells over a max of 40 iterations of the genetic algorithm was used for fitting the cluster expansion. As shown in Table 5-9, the cluster expansion optimization finished successfully with a cross-validation score of 2.9 meV/pos on the last iteration. According to Table 5-10, which gives a comparison of energies and formation energies as predicted by the cluster expansion and the DFT engine, all the formation energies from the cluster expansion are negative. This implies the model used is comprised of miscible constituents. As seen from the same table, a total of 28 crystalline structures were predicted. Of these structures, beside the pure systems, as listed in appendix G, 6 Li-Si alloys ($LiSi_4$, $LiSi_3$, $LiSi_2$, Li_2Si_3, Li_2Si and Li_4Si) were predicted to be thermodynamically stable.

5.2 Correlations of structural stability from electronic density of states

Using the DFTB+ code, the Li-Si SCC-DFTB parameters are employed to calculate the electronic partial density of states (PDOS) of the Li-Si alloys predicted from the FCC-based cluster expansion. These calculations are done to further evaluate the structural stability of phases predicted to be thermodynamically stable by cluster expansion. To assess the structural stability, we consider the position of the Fermi level, E_f, (depicted as a dashed line going through 0 on the energy spectrum) on total

DOS. It is perhaps also necessary to highlight that the calculations are done at zero pressure and 0K.

5.2.1 DFTB+ calculated electronic partial density of states for structures on the ground-state search tie-line of the FCC-based Li-Si cluster expansion. The Fermi level (E_F) has been aligned to 0 eV

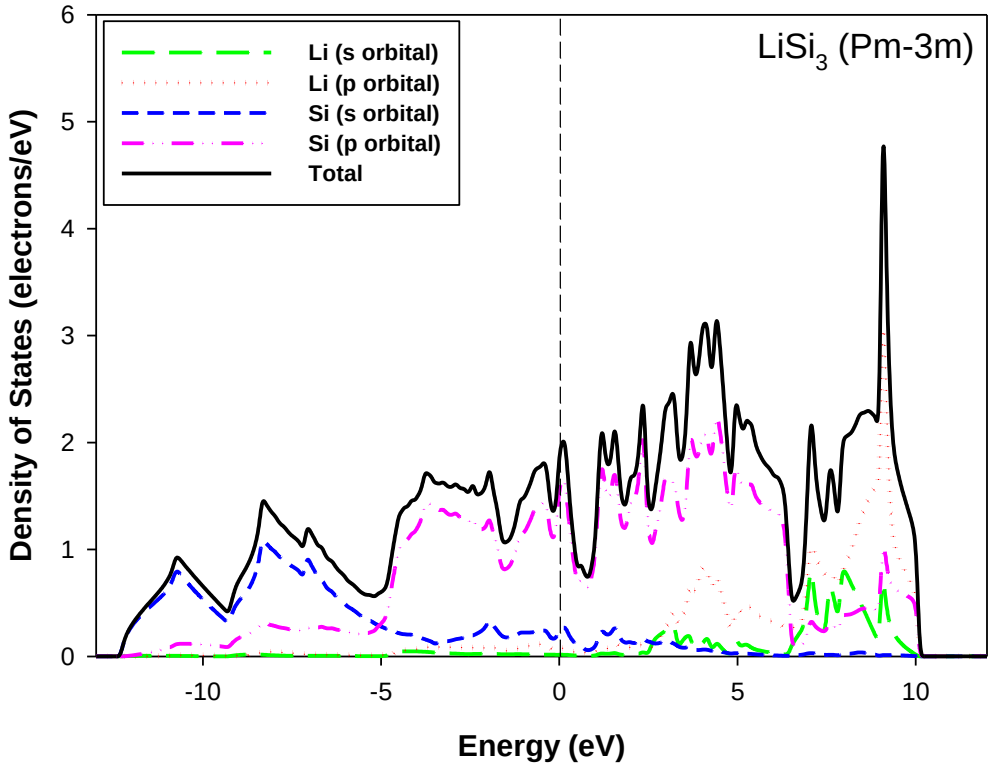

Figure 5-7. The electronic partial density of states (PDOS) for the $LiSi_3$ (trigonal, *Pm-3m*) structure at 0GPa and 0K.

Figure 5-7 shows the PDOS of the trigonal $LiSi_3$ structure in the absence of external pressure and the simulation is assumed to be done at 0K. As seen on the plot, the major contribution in the vicinity of the Fermi level is from electron states in the p orbital of the Si atoms. Considering the total DOS, E_f lies toward the anti-bonding region of the pseudogap. This suggests the Pm-3m $LiSi_3$ phase would be unstable at 0GPa. The number of electronic states at the Fermi, $N(E_f)$ appears to be somewhat low (~1.5 electrons/eV) and, the narrow conduction bandwidth relative to the valance band suggests the $LiSi_3$ to be metastable. Perhaps higher stabilization of this phase can be achieved under different thermodynamic conditions such as introducing pressure.

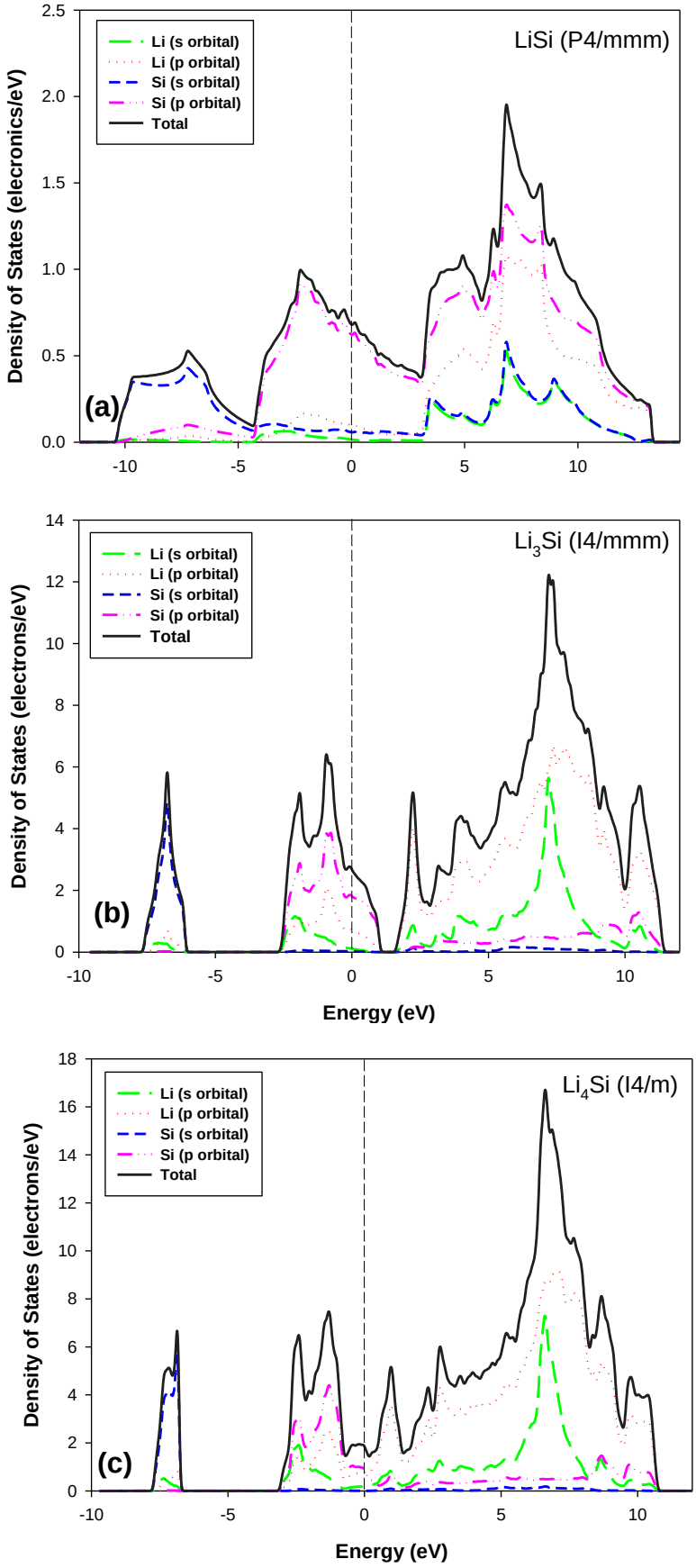

Figure 5-8. The electronic partial density of states (PDOS) for the (a) LiSi (*P4/mmm*), (b) Li_3Si (*I4/mmm*), and (c) Li_4Si (*I4/m*) tetragonal structures at 0GPa and 0K.

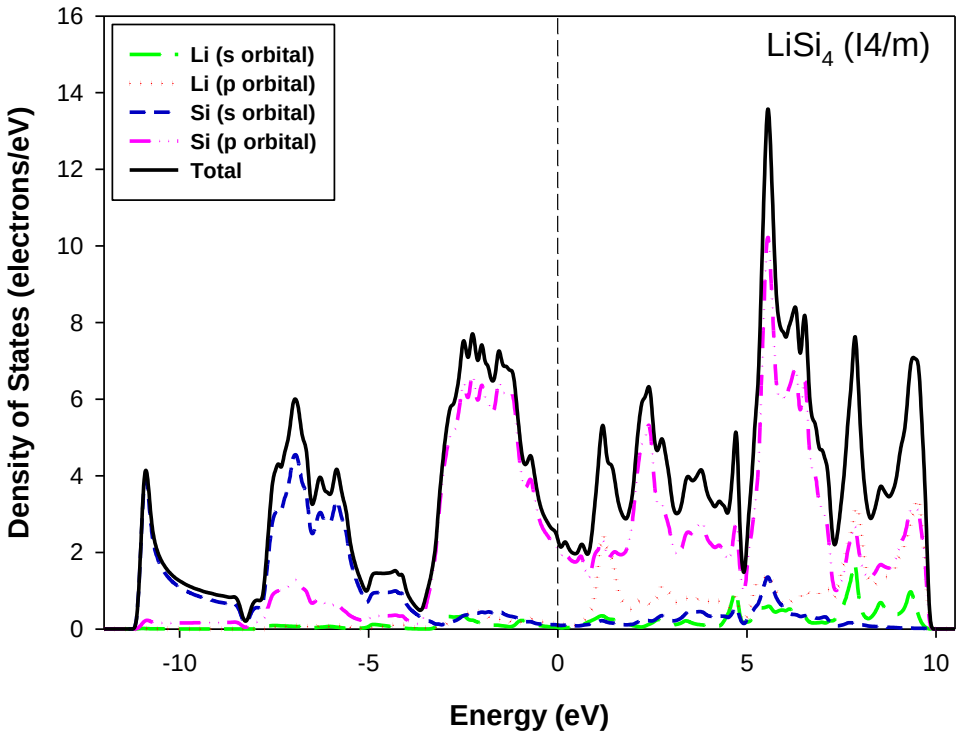

Figure 5-9. The electronic partial density of states (PDOS) for the $LiSi_4$ (*I4/m*) tetragonal structure at 0GPa and 0K.

Figures 5-8 and 5-9 depict the electronic partial density of states for the LiSi (*P4/mmm*), Li_3Si (*I4/mmm*), Li_4Si (*I4/m*), and $LiSi_4$ (*I4/m*) tetragonal structures calculated in the absence of any external pressure and temperature influence. For all these four binary tetragonal Li-Si alloys, it is observed that the major contribution at the Fermi level stems from electronic states in the p orbitals of Si atoms. It is noted that for the most Li-rich phase in the set, Li_4Si (*I4/m*), there is almost an overlap between the Li and Si p orbital contributions, however, the Si p orbital intercepts the Fermi at a value slightly higher than that of Li. It is possible that with the application of external pressure, the electrons around the Fermi may distribute in a manner that slightly gives Li the upper hand.

The total DOS of LiSi (*P4/mmm*) does not show a very well pronounced pseudogap, however, it seems the E_f falls into the small dip on the DOS. In addition, the number of electrons in the Fermi, $N(E_f)$, is quite low (i.e. ~0.68 electrons/eV); hence this suggests the LiSi (*P4/mmm*) phase to be metastable. The predicted metastability of the LiSi *P4/mmm* structure in this work is in agreement with the work by Morris *et al* [174] wherein this phase was predicted to be metastable using *Ab initio* random structure searching (AIRSS) method, and was proposed to become more stable above 2.5GPa.

The total DOS for the Li_3Si (*I4/mmm*) crystal structure shows no deep valley at the E_f. The Fermi level is seen to fall onto a broad peak of the DOS, and the conduction bandwidth of this phase is broad. These attributes suggest the Li_3Si to be unstable at 0GPa. This behaviour suggests that Li_3Si (*I4/mmm*) is likely to be more stable at high pressure.

Considering the total DOS for the Li_4Si (*I4/m*) at 0GPa, a deep valley in the vicinity of the Fermi level exists. The E_f falls onto a small locally flat peak in the pseudogap, meaning a small perturbation of E_f consequent to influence such as external pressure would not constitute very large variations in the number of electrons at E_f. Therefore, it is predicted that the Li_4Si (*I4/m*) would be structurally stable when pressure is applied to it. Interestingly, this observation agrees with the work by Zhang *et at* [175], in which the Li_4Si (*I4/m*) was reported to become more stable above 40.5GPa.

As for the tetragonal $LiSi_4$ (*I4/m*), the PDOS plot exhibits a deep valley and a narrow conduction bandwidth. Like in the other Li-Si alloys discussed in the paragraphs above, the major contribution in the E_f is due to electrons in the p orbitals of the Si atoms. Furthermore, E_f falls onto the bonding region of the total DOS. Hence, the phase is predicted to be structurally stable.

5.2.2 DFTB+ calculated electronic partial density of states for structures on ground-state search tie-line of the BCC-based Li-Si cluster expansion.

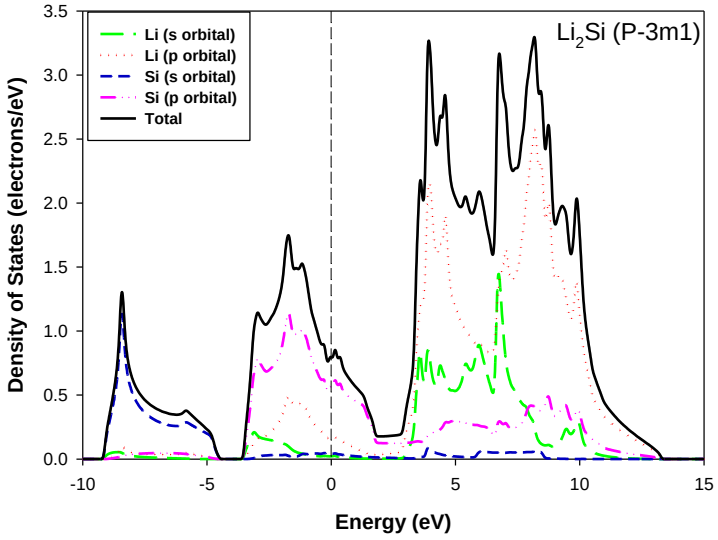

Figure 5-10. The electronic partial density of states (PDOS) for the Li_2Si (trigonal, *P-3m1*), structure at 0GPa and 0K.

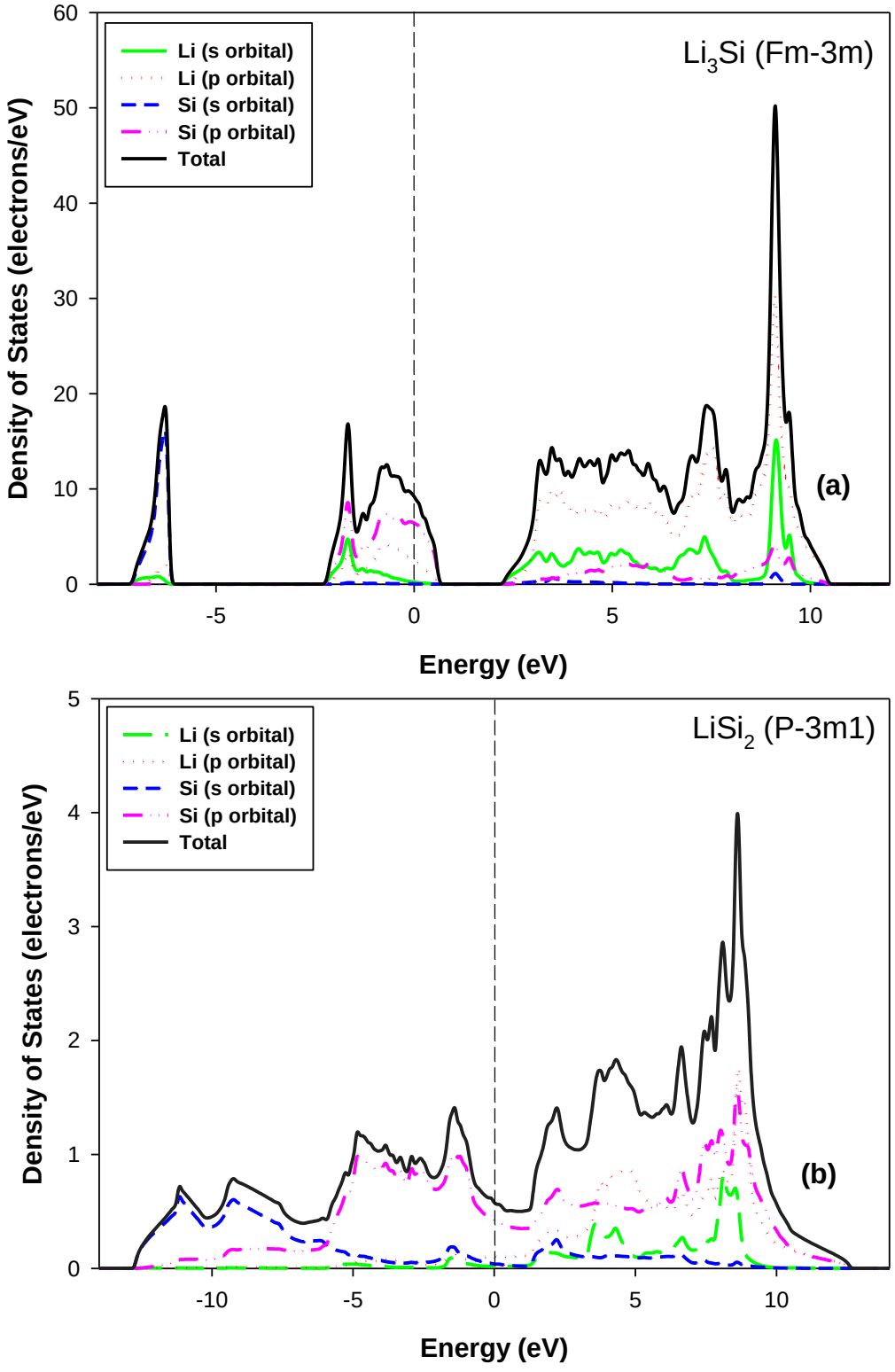

Figure 5-11. The electronic partial density of states (PDOS) for the (a) Li_3Si (cubic, *Fm-3m*), and (b) $LiSi_2$ (trigonal, *P-3m1*) structures at 0GPa and 0K.

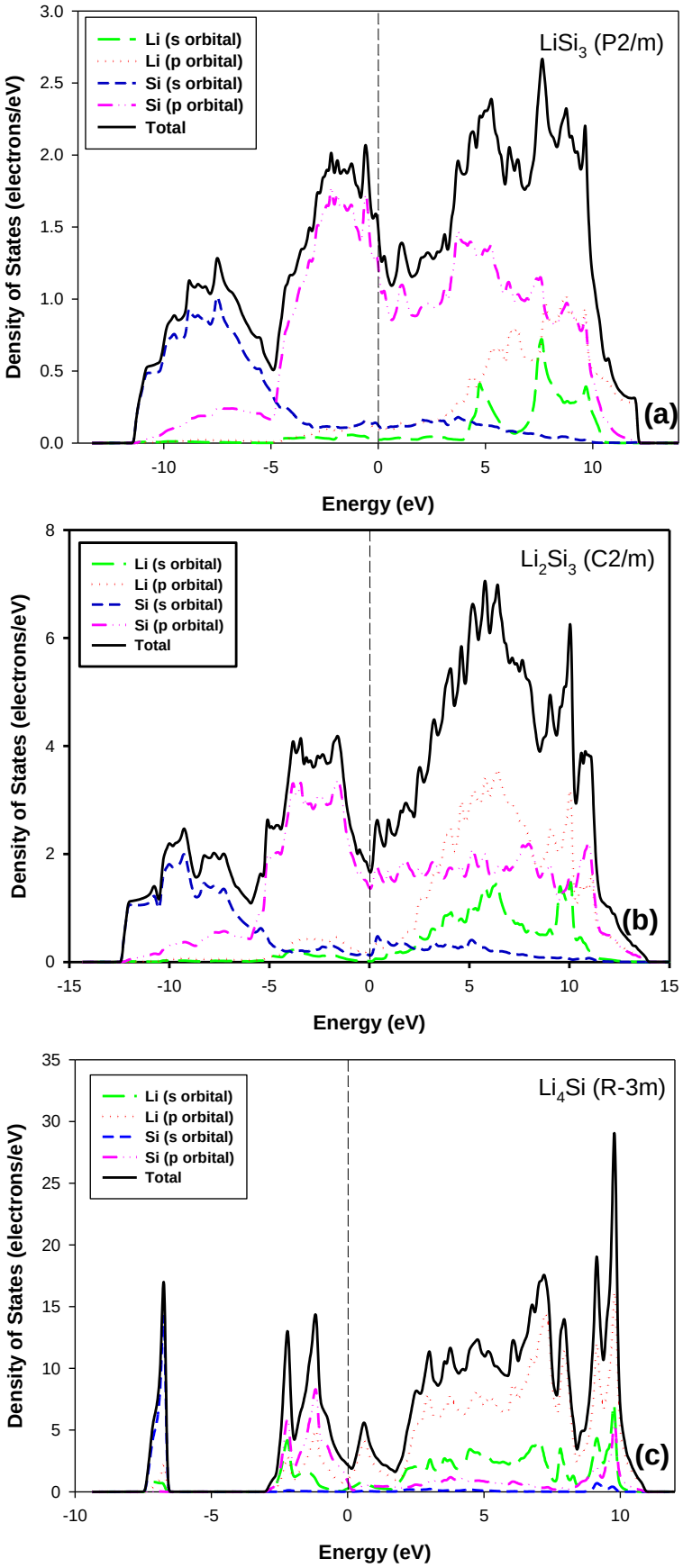

Figure 5-12. The electronic partial density of states (PDOS) for the (a) $LiSi_3$ (monoclinic, *P2/m*), (b) Li_2Si_3 (monoclinic, *C2/m*), and (c) Li_4Si (trigonal, *R-3m*) structures at 0GPa and 0K.

Figures 5-10, 5-11 and 5-12 depict the electronic partial density of states for the trigonal Li_2Si (*P-3m1*), cubic Li_3Si (*Fm-3m*), trigonal $LiSi_2$ (*P-3m1*), monoclinic $LiSi_3$ (*P2/m*), monoclinic Li_2Si_3 (*C2/m*), and trigonal Li_4Si (*R-3m*) structures calculated in the absence of any external pressure and temperature influence. Except for Li_4Si (*R-3m*) that shows an approximately equivalent contribution of the Li and Si p orbitals at the Fermi level, all these depict a major contribution stemming from the p orbital electron states of Si atoms.

By focusing on the total DOS for all structures predicted using the bcc-based parent lattice, it is apparent that: E_f fall into a small pseudogap on the DOS of Li_2Si (*P-3m1*) and $N(E_f)$ has a small value (~0.8 electrons/eV), thus suggesting the phase to be metastable. The Fermi is located on a broad peak with $N(E_f)$ of approximately 9 electrons/eV for the cubic Li_3Si (*Fm-3m*). Hence, it is predicted that this phase would be structurally unstable at 0K. However, stability can be improved. Zhang *et al* [175] predicted this phase to be a low-pressure phase that becomes more stable above 8.4GPa. The E_f falls exactly on the pseudogap for the trigonal Li_2Si (*P-3m1*), monoclinic Li_2Si_3 (*C2/m*) and trigonal Li_4Si (*R-3m*) binary alloys. This implies the structures are to likely be structurally stable. Interestingly, Zhang *et al* [175] predicted these structures to be more stable above 25GPa. As for the monoclinic $LiSi_3$ (*P2/m*), its total DOS does not portray any pseudogap at E_f. Hence, it shows that the phase is not structurally stable at 0K.

It is good practice to cross-reference predictions done using simulations with any available experimental information and other theoretical or computer-based methods. This helps to establish a basis from which the predicted materials properties can be validated and it, in turn, establish some level of accuracy of the modelling approach. Having said that, we proceed to relate our predictions with any other available work obtainable from literature. As listed in the table that follows, a corresponding agreement on most of our crystal structure predictions was found on the swarm-intelligence based work by Zhang *et al* [175].

Table 5-11. Li-Si alloys predicted through genetic algorithm implemented within UNCLE code.

Method	Structure	Space group	Crystal type	Method
UNCLE (this work)	Li_4Si	*R-3m*	Trigonal	CALYPSO [175]
UNCLE (this work)	Li_4Si	*I4/m*	Tetragonal	CALYPSO [175]
UNCLE (this work)	Li_3Si	*I4/mmm*	Tetragonal	
UNCLE (this work)	Li_3Si	*Fm-3m*	Cubic	CALYPSO [175]
UNCLE (this work)	Li_2Si_3	*C2/m*	Monoclinic	
UNCLE (this work)	Li_2Si	*P-3m1*	Trigonal	
UNCLE (this work)	LiSi	*P4/mmm*	Tetragonal	CALYPSO [175]
UNCLE (this work)	$LiSi_2$	*P-3m1*	Trigonal	
UNCLE (this work)	$LiSi_3$	*P2/m*	Monoclinic	
UNCLE (this work)	$LiSi_3$	*Pm-3m*	Cubic	
UNCLE (this work)	$LiSi_4$	*I4/m*	Tetragonal	CALYPSO [175]
UNCLE (this work)	$LiSi_4$	*C2/m*	Monoclinic	

Using the universal cluster expansion technique, crystal structure predictions of binary alloys in the Li-Si system were performed utilizing the genetic algorithm as implemented within the UNCLE code. The structure search was done using the solid Li belonging to the *Fm-3m* and *Im-3m* symmetries, as well as the solid Si with the Fm-3m symmetry. The Li-Si system has been widely studied using various approaches, most work has been achieved by experimental and first-principles techniques; although very minimal, recently the use of intelligence-based techniques on the system has emerged.

In this work, as shown in Table 5-11, 12 new crystalline Li-Si alloys were predicted to be thermodynamically stable. Among these twelve alloys, 5 [*viz.* LiSi, Li_4Si (*I4/m* & *R-3m*), $LiSi_4$, Li_3Si] of the structures were also proposed in the predictive work by Zhang *et al* [175], in which a different approach (*viz.* the particle swarm-intelligence-based code, CALYPSO [176]) was used. We note that although predictive techniques used between the current work (UNCLE) and CALYPSO are different, part of the commonality can be attributed to Fm-3m symmetry of the elemental Li and Si solids used as parent structures from which crystal structure screening was done.

5.2.3 Effect of pressure on the stability of predicted Li-Si alloys

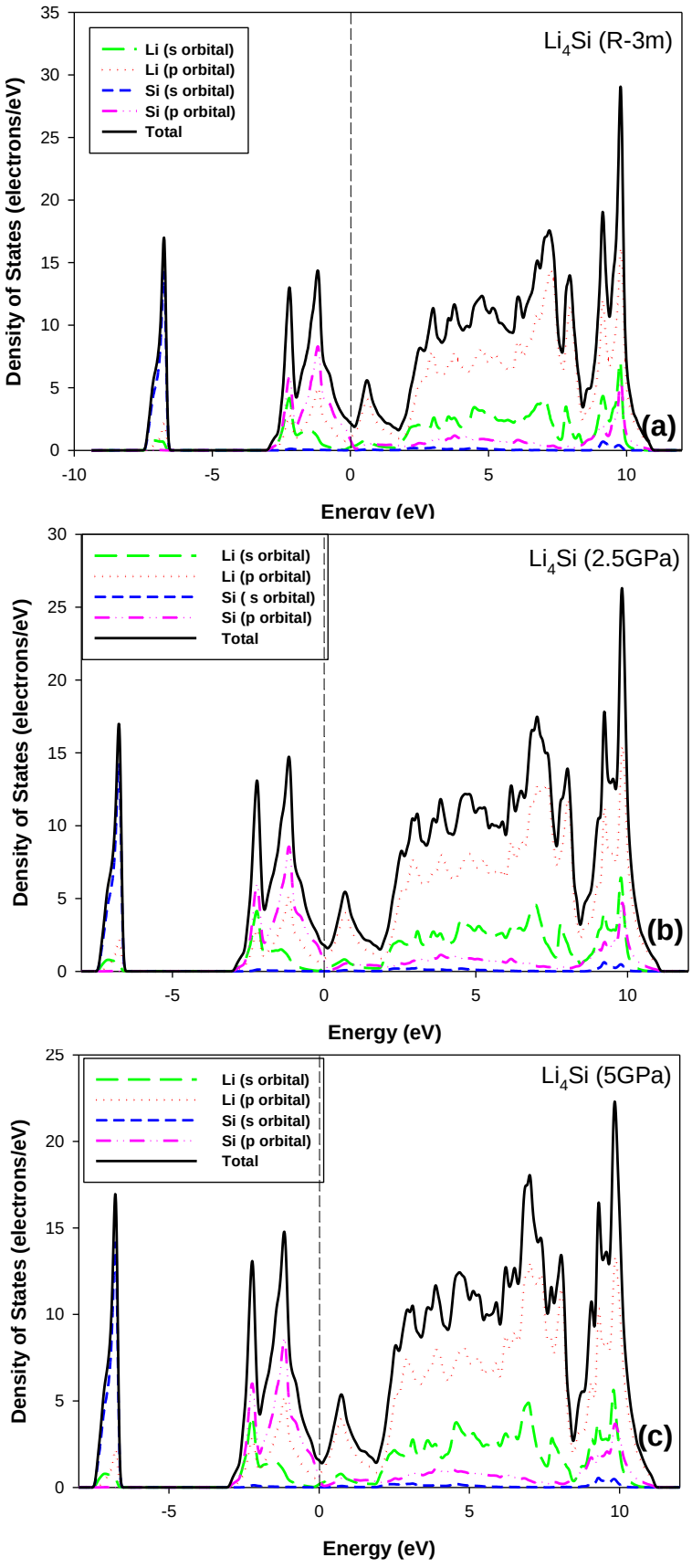

Figure 5-13. The electronic partial density of states (PDOS) for the hexagonal (a) Li_4Si (*R-3m*) at 0GPa (b) Li_4Si (*R-3m*) at 2.5GPa, and (c) Li_4Si (*R-3m*) at 5GPa.

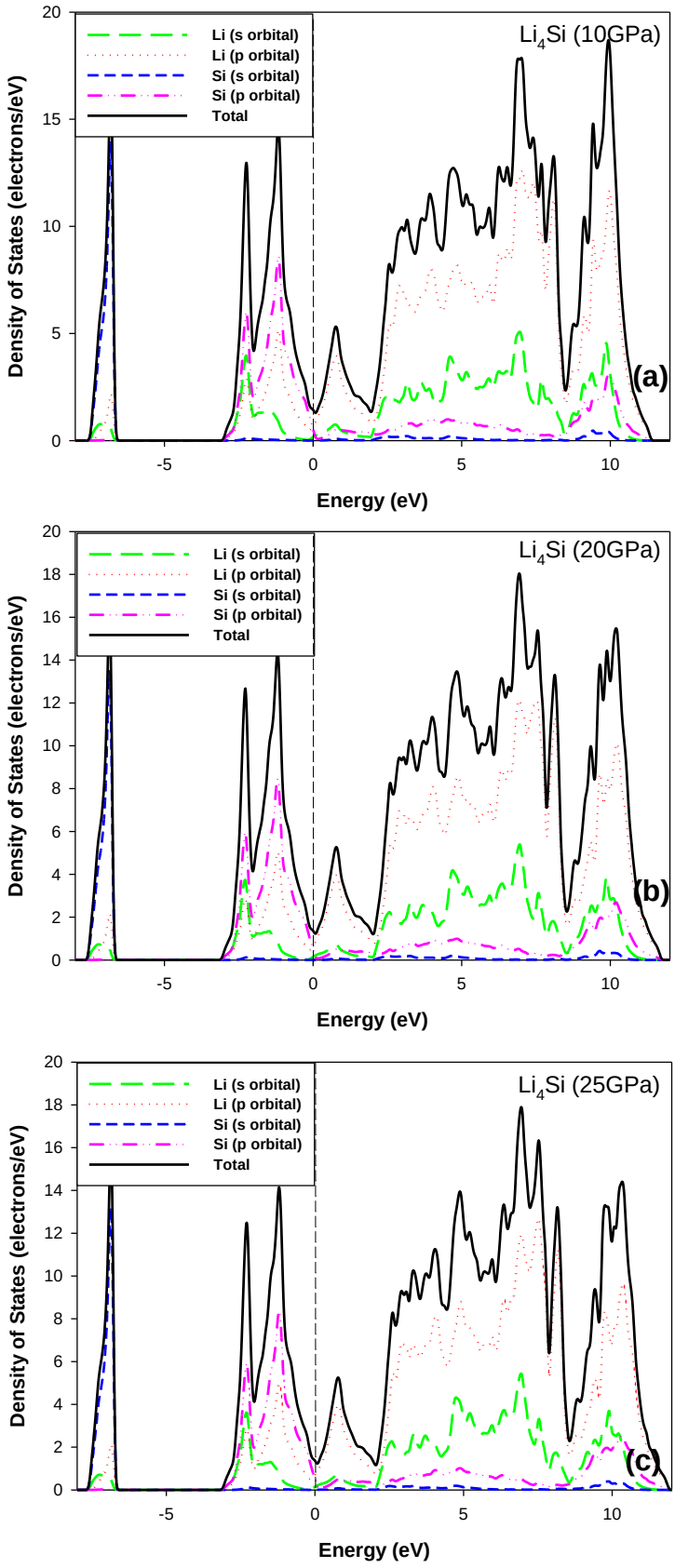

Figure 5-14. The electronic partial density of states (PDOS) for the hexagonal (a) Li_4Si (*R-3m*) at 10GPa (b) Li_4Si (*R-3m*) at 20GPa, and (c) Li_4Si (*R-3m*) at 25GPa.

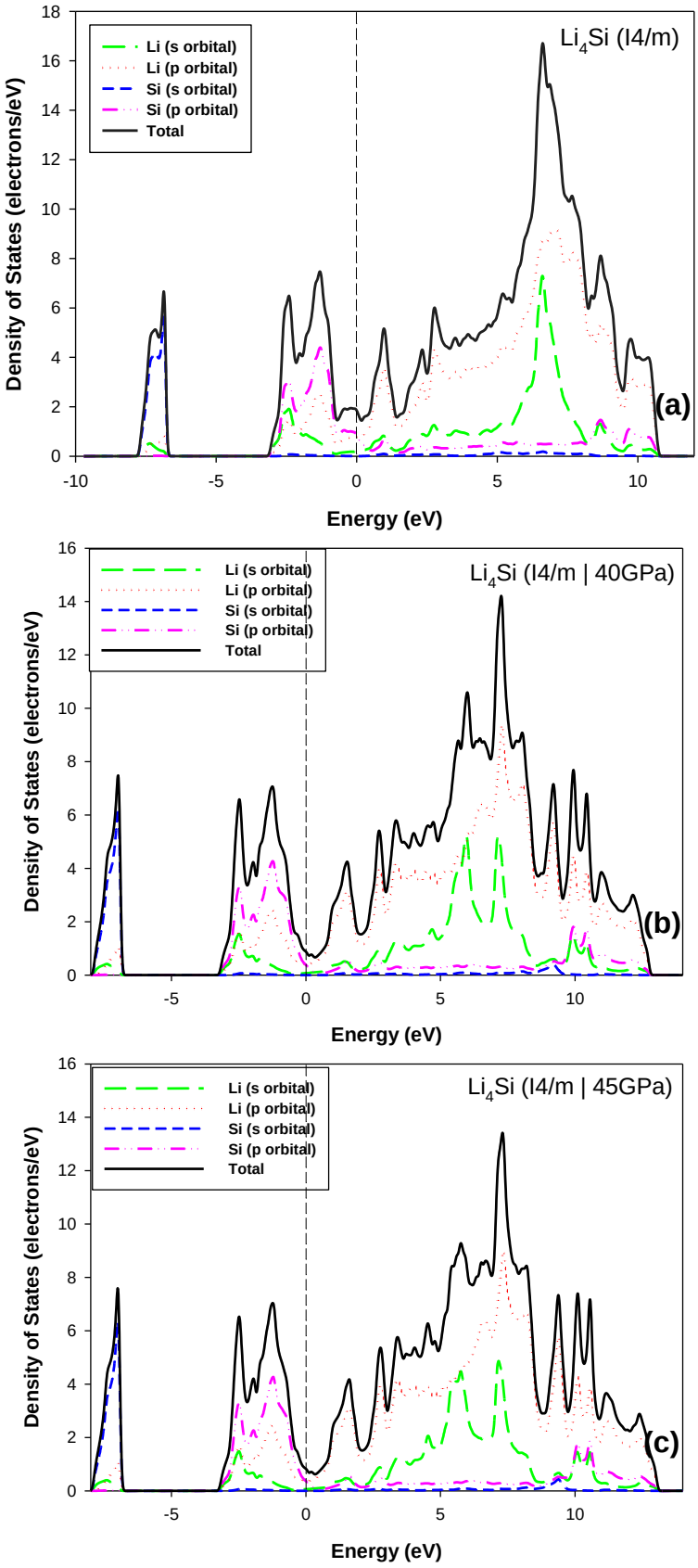

Figure 5-15. The electronic partial density of states (PDOS) for the tetragonal (a) Li_4Si (*I4/m*) at 0GPa (b) Li_4Si (*I4/m*) at 40GPa, and (c) Li_4Si (*I4/m*) at 45GPa.

The phase diagram published by Okamoto [7] lists the $Li_{4.4}Si$ phase (corresponding to $Li_{22}Si_5$) as the most lithium-rich phase. $Li_{4.4}Si$ was reported to exhibit high-energy-density, which is an attractive attribute for application in rechargeable batteries. In this work, the hexagonal Li_4Si (*R-3m*) and tetragonal Li_4Si (*I4/m*) phases (corresponding to $Li_{12}Si_3$) were predicted to be thermodynamically stable using cluster expansion. Zhang *et al* predicted the hexagonal Li_4Si phase to be a low-pressure phase that becomes stable above 8.4GPa and the tetragonal phase to be a high-pressure phase that becomes more stable above 40.5GPa. Since the PDOS for the Li-Si alloys presented in sections 5.2.1 and 5.2.2 of this thesis were calculated at 0K and 0GPa, pressure was later introduced during the structure relaxation of a few selected systems to see how it affects their stability. The outcome on the Li_4Si compound is illustrated by figures 5-13, 5-14 and 5-15. On Figure 5-13, the *R-3m* Li_4Si is subjected to pressure of 2.5GPa to 5GPa, and in Figure 5-14 it ranges from 10GPa to 25GPa. In all hexagonal Li_4Si structures within the 0 – 25GPa, the Fermi is situated exactly in the pseudogap. As pressure is being increased the energy redistribution of the electrons does not significantly alter the band shapes on the DOS. The major contribution at the Fermi level is noted to be equivalently from the Li and Si p orbitals since the PDOS of the Li and Si atoms overlap. Furthermore, the Fermi remains localised within the deep valley. Hence, the Li_4Si (*R-3m*) is seen to maintain its structural stability globally within the range 0 – 25GPa. Considering Figure 5-15, it is evident that the minor locally flat peak in the vicinity of the Fermi at 0GPa is removed by application of external pressure at 40GPa and 45GPa. However, the perturbation does not destabilize the structure of the tetragonal Li_4Si I4/m) but improves its stability. The witnessed stability at 40 – 45GPa is consistent with the report by Zhang *et al* [175]. In collectively scrutinizing the PDOS graphs of Li_4Si (*R-3m*) and Li_4Si (*I4/m*) structures under the influence of external pressure, it can be noticed the parabolicity of the DOS in the vicinity of the Fermi is increasing. Fewer and fewer electron states are located at E_f and the minimum at this region is therefore lowered even further. The Li-Si SCC-DFTB parameter is thus seen to widely confirm the stability of the Li-Si alloys predicted by the cluster expansion technique. The successful development and insights acquired based on the Li-Si framework which combine the SCC-DFTB method with the Cluster Expansion method, allow for probing the Na-Si material space and other compounds that may be considered candidate active materials for batteries.

5.3 Ground-State Phase Structure Predictions for Na-Si

Sodium is isoelectronic to lithium and has been earmarked one of the candidate intercalation elements for silicon-based anodes. The Na-Si system has not been extensively studied as much as Li-Si systems; hence, not many Na-Si structures have been discovered as yet. In this section, the universal cluster expansion technique is used to conduct a crystal structure prediction intended to possibly identify new systems that could be further studied in the future. As a test, the grid search based on the *Fm-3m* symmetry parent lattice is conducted.

5.3.1 Structure predictions from Si *Fm-3m*

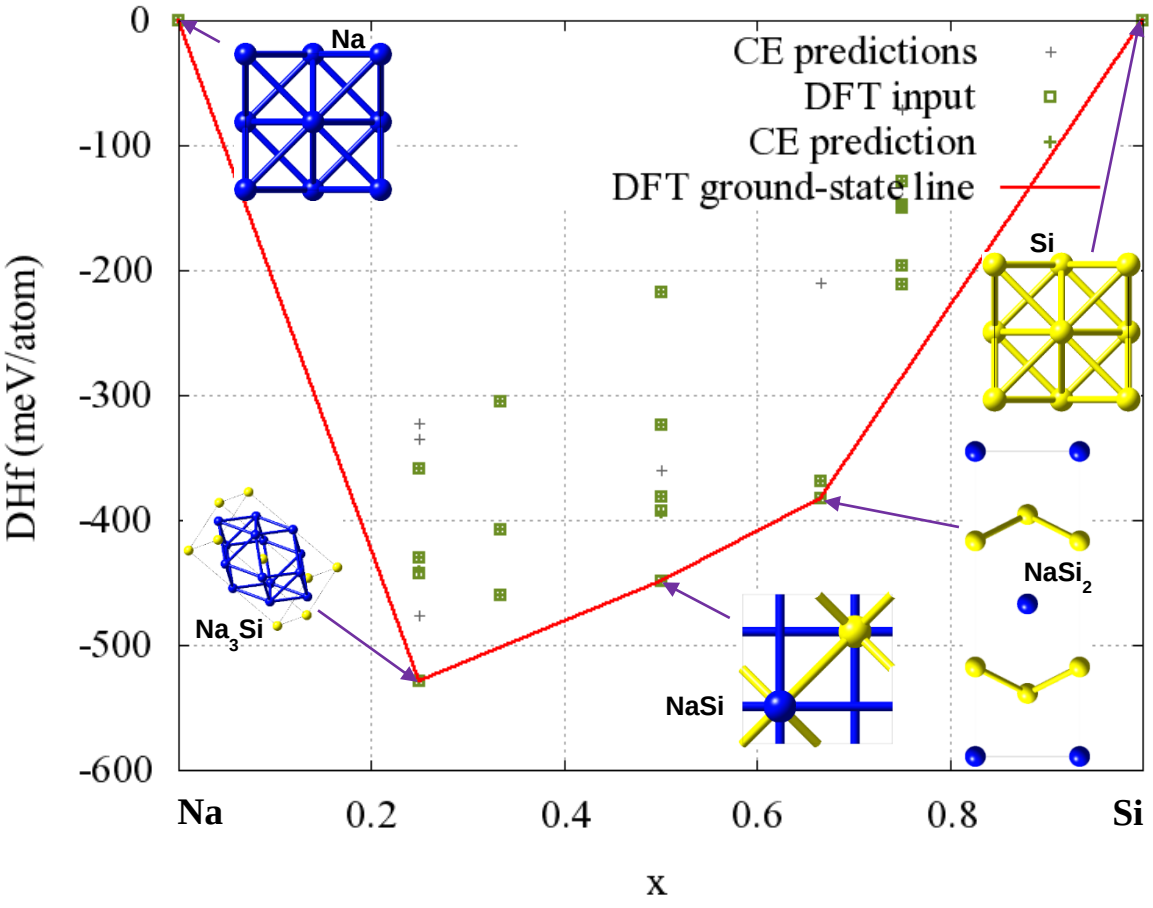

Figure 5-16. Calculated binary ground-state diagram of Na-Si emanating from a grid search using the FCC-based system considering structures of up to 16 basis atoms.

Table 5-12. Summary of the iterative optimization progress

Iteration	no. of struc.	no. of new struc.	CVS [meV/pos.]	% struc. with SD below 5 meV	new structures
0	0	2	-	-	ce1 ce2
0	0	7	-	-	ce13 ce4 ce20 ce19 ce15 ce1 ce2
1	7	5	22	-	ce25 ce10 ce16 ce6 ce28
2	12	3	2.1	-	ce29 ce7 ce14
3	15	3	0.11	-	ce21 ce8 ce3
4	18	2	0.43	-	ce9 ce26
5	20	1	0.11	-	ce27
6	21	0	0.39	-	

Table 5-13. A comparison of energies E and formation energies DHf in eV (counted per active atom position) as predicted by the cluster expansion and as calculated by the computational engine (DFT).

Energy differences to the structure at the ground state line (GSL) for each composition x are listed.

# no.	x(1:k,1:nC)		E_DFT	D(E_DFT,E_CE)	E_CE	DHf_DFT	DHf_CE	Dist to GSL DFT	title	cell formula	space group
1	0.00000	1.00000	-0.5448540000	-0.0000000789	-0.5448540789	0.0000000000	0.0000000000	0.0000000000	ce2	Na	Fm-3m
2	0.25000	0.75000	-1.9842250000	-0.0000094160	-1.9842344160	-0.3592842500	-0.3592935818	0.1692752500	ce21	Na3Si	R-3m
3	0.25000	0.75000	-2.0551842500	-0.0000140028	-2.0551982528	-0.4302435000	-0.4302574186	0.0983160000	ce27	Na3Si	Cmmm
4	0.25000	0.75000	-2.0674692500	0.0008607877	-2.0666084623	-0.4425285000	-0.4416676281	0.0860310000	ce29	Na3Si	Pm-3m
5	0.25000	0.75000	-2.1535002500	0.0000123854	-2.1534878646	-0.5285595000	-0.5285470304	0.0000000000	ce25	Na3Si	I4/mmm
6	0.33333	0.66667	-2.2901153333	0.0000110190	-2.2901043144	-0.3051456667	-0.3051345617	0.1967769167	ce8	Na2Si	P-3m1
7	0.33333	0.66667	-2.3920120000	0.0000222718	-2.3919897282	-0.4070423333	-0.4070199756	0.0948802500	ce10	Na2Si	I4/mmm
8	0.33333	0.66667	-2.4450396667	-0.0000248591	-2.4450645257	-0.4600700000	-0.4600947731	0.0418525833	ce9	Na2Si	Immm
9	0.50000	0.50000	-2.9229375000	0.0001086984	-2.9228288016	-0.2179100000	-0.2178012121	0.2307387500	ce3	NaSi	R-3m
10	0.50000	0.50000	-3.0283272500	0.0000135402	-3.0283137098	-0.3232997500	-0.3232861204	0.1253490000	ce20	Na2Si2	I4_1/amd
11	0.50000	0.50000	-3.0862137500	0.0000545960	-3.0861591540	-0.3811862500	-0.3811315645	0.0674625000	ce16	Na2Si2	R-3m
12	0.50000	0.50000	-3.0978690000	-0.0011859288	-3.0990549288	-0.3928415000	-0.3940273393	0.0558072500	ce4	NaSi	P4/mmm
13	0.50000	0.50000	-3.1536762500	0.0000180739	-3.1536581761	-0.4486487500	-0.4486305867	0.0000000000	ce19	Na2Si2	P4/nmm
14	0.66667	0.33333	-3.7942836667	-0.0000096452	-3.7942933119	-0.3691983333	-0.3692078856	0.0130533333	ce7	NaSi2	I4/mmm
15	0.66667	0.33333	-3.8073370000	0.0000248591	-3.8073121409	-0.3822516667	-0.3822267146	0.0000000000	ce6	NaSi2	Immm
16	0.75000	0.25000	-3.9140575000	-0.0000093840	-3.9140668840	-0.1289432500	-0.1289525392	0.1577455000	ce15	NaSi3	I4/mmm
17	0.75000	0.25000	-3.9326592500	-0.0000095889	-3.9326688389	-0.1475450000	-0.1475544942	0.1391437500	ce26	NaSi3	Cmmm
18	0.75000	0.25000	-3.9353597500	0.0008720244	-3.9344877256	-0.1502455000	-0.1493733809	0.1364432500	ce28	NaSi3	Pm-3m
19	0.75000	0.25000	-3.9814595000	0.0000106103	-3.9814488897	-0.1963452500	-0.1963345449	0.0903435000	ce14	NaSi3	P4/mmm
20	0.75000	0.25000	-3.9961100000	0.0000110190	-3.9960989810	-0.2109957500	-0.2109846363	0.0756930000	ce13	NaSi3	C2/m
21	1.00000	0.00000	-4.8652010000	-0.0000001000	-4.8652011000	0.0000000000	0.0000000000	0.0000000000	ce1	Si	Fm-3m

Presented as Figure 5-16, the binary ground-state diagram of the Na-Si system was obtained by adding a Na atom onto the 4a Wyckoff position in Si (*Fm-3m*) and performing a grid search considering structures of up to 16 basis atoms over a configurational space of 4 unit cells. As depicted in Table 5-12, the 5th column remained empty, meaning the model did not switch to a miscibility gap mode, and the cluster expansion optimization finished successfully with a cross-validation score of 0.39 meV/pos. Considering Table 5-13, it is noticeable that all the formation energies (in column 7, DHf_CE) have negative values, suggesting that the model is comprised of miscible constituents. The same table reflects a list of 21 structures that have been produced by the cluster expansion, of which 5 are found to line on the ground-state tie-line. As such, beside the pure systems, as shown in appendix H, 3 thermodynamically stable Na-Si structures (*i.e.* Na_3Si, NaSi & $NaSi_2$) are predicted.

Considering the experimental work by Sangster *et al* [21], the Na-Si phase diagram lists NaSi and $NaSi_2$. With the former being classified as belonging to the space group *C2/c* and the latter's space group is not identified. Recently, Sung *et al* [177], in their predictive work, employed the *ab intio* evolutionary crystal structure search method and reported $NaSi_2$ to be stable at 20GPa in the *Fd-3m* space group. The work by Sung *et al* [177] does not only report the $NaSi_2$ but also includes Na_3Si

(*P6/mmm*), Na_2Si (*P6/mmm*) and the zintle phase NaSi. The difference in the current work on the predicted Na-Si alloys lies on the symmetries of the common compositions.

The universal cluster expansion technique in this work classified the three predicted structures, Na_3Si, NaSi & $NaSi_2$, as belonging to the space groups *I4/mmm*, *P4/nmm* and *Immm* respectively. Hence their respective crystal types are tetragonal for Na_3Si and NaSi, and $NaSi_2$ is orthorhombic. The NaSi and $NaSi_2$ systems have been reported in the available literature, however, in a different symmetry. The predictions in this work suggest that the Na-Si systems have various polymorphs that are worth noting and investigating further. The Na rich phase, Na_3Si has not to the best our knowledge been reported in experiments based literature as yet. At this point, it is perhaps necessary to further evaluate stability CE predicted crystal Na-Si structures using the electronic partial density of states. To do so, the Na-Si SCC-DFTB parameter set developed in this work is employed.

5.3.2 DFTB+ calculated electronic partial density of states for structures on ground-state search tie-line of the FCC-based Na-Si cluster expansion.

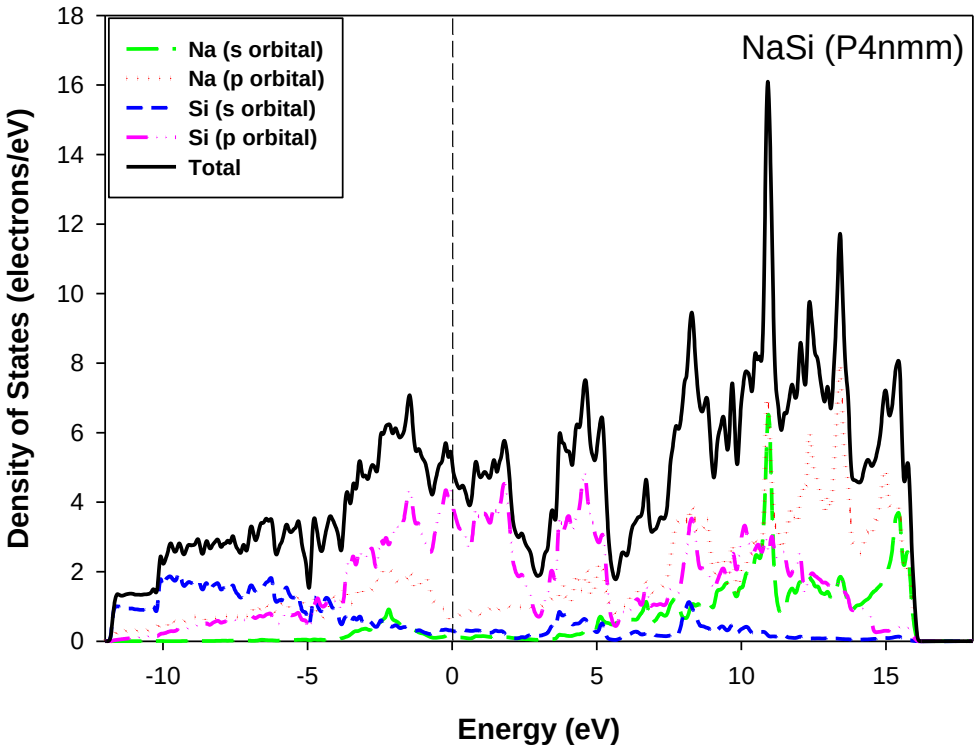

Figure 5-17. The electronic partial density of states (PDOS) for the (a) NaSi (tetragonal, P4nmm) structure at 0GPa and 0K.

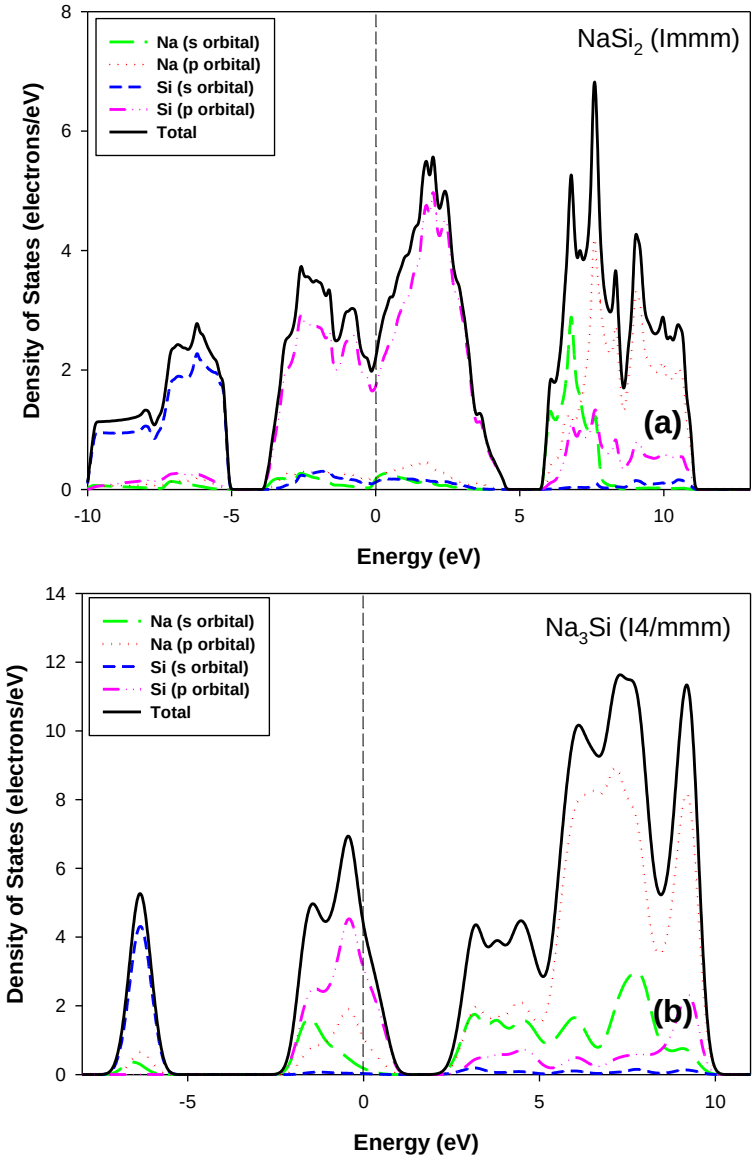

Figure 5-18. The electronic partial density of states (PDOS) for the (a) $NaSi_2$ (orthorhombic, *Immm*), and (b) Na_3Si (tetragonal, *I4/mmm*) structures at 0GPa and 0K.

Figures 5-17 and 5-18 show the PDOS of the tetragonal NaSi (*P4nmm*), orthorhombic $NaSi_2$ (*Immm*) and tetragonal Na_3Si structures in the absence of external pressure and temperature. As seen on all the three plots, the major contribution in the vicinity of the Fermi level is from electron states in the p orbital of the Si atoms. Considering the total DOS of the zintle phase, NaSi, it is deduced that no deep valley exists at E_f. E_f appears to nudge a sharp peak and this suggests that a perturbation would result with a significant alteration in the number of electrons in that region. Furthermore, the width of the conduction band on the PDOS is broader than that of the width of the valance band. Hence, these aspects suggest that the tetragonal NaSi (*P4nmm*) is structurally unstable at low pressure.

On the other hand, the DOS of orthorhombic $NaSi_2$ (*Immm*) depicts a deep valley in the vicinity of the Fermi. The Fermi level falls on the deep valley; thus, it can be deduced that the phase is structurally stable, and perhaps an external pressure may raise the stability a bit higher.

The PDOS of the Na-rich phase, Na_3Si (*I4/mmm*) illustrates the E_f hinges towards the bonding region of a broad peak on the total DOS. This behaviour suggests that the structure is metastable and applying pressure may just stabilize the crystal structure. To assess such possibility it is necessary to external pressure when the atomic positions and cell parameters are optimised through a structure relaxation.

In the section that follows, Na_3Si (*I4/mmm*) is subjected to an external pressure ranging from 2.5GPa – 25GPa.

5.3.3 Pressure introduced in the optimization of bulk Na_3Si primary cell

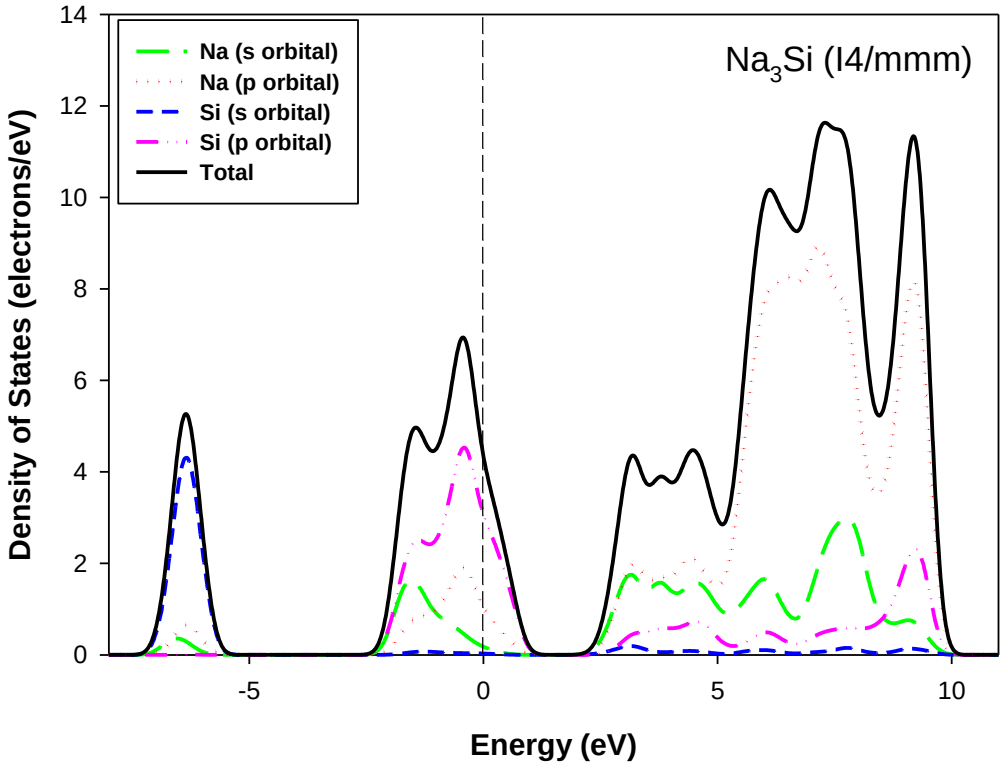

Figure 5-19. The electronic partial density of states (PDOS) for the tetragonal (a) Na_3Si (*I4/mmm*) at 0GPa.

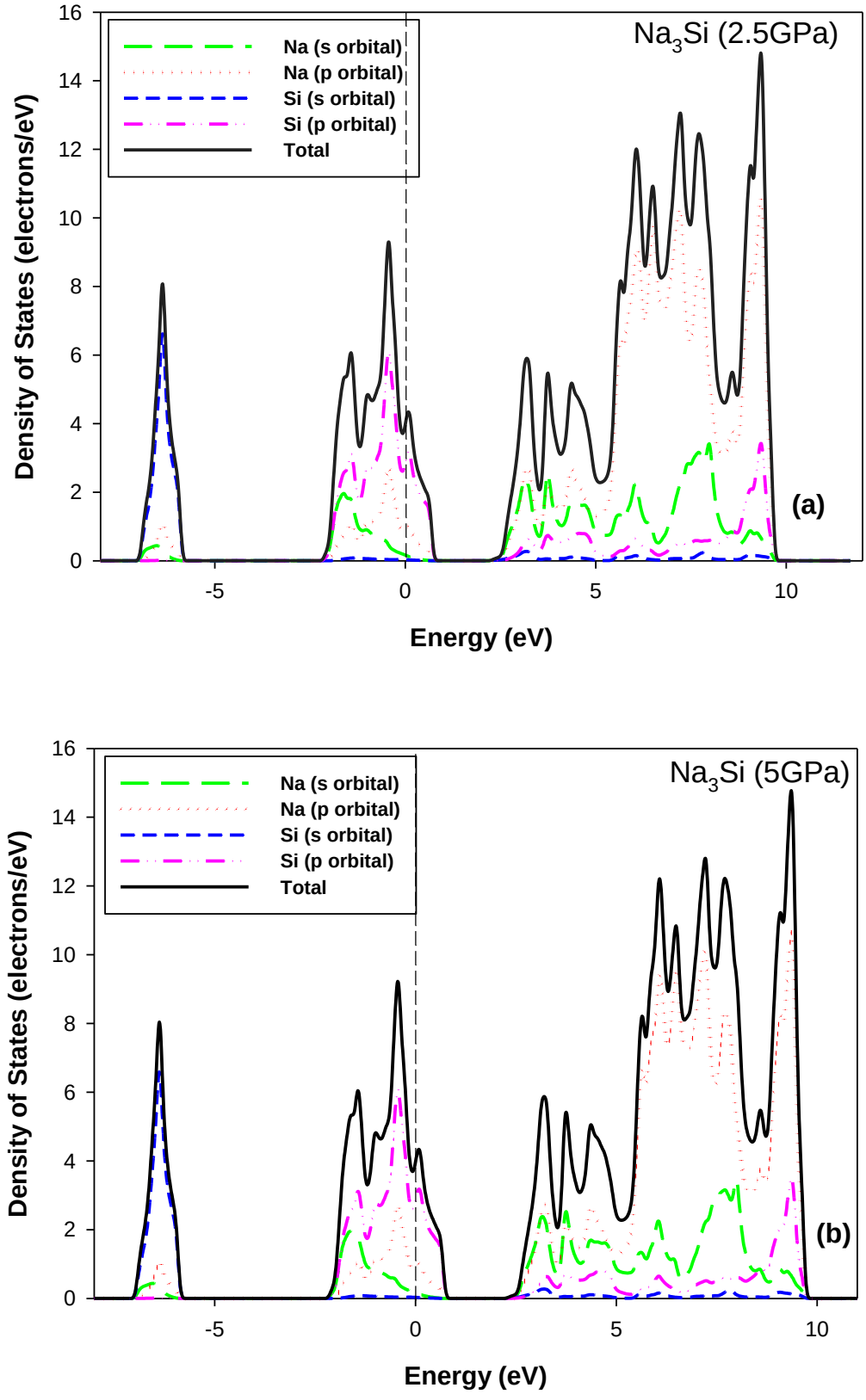

Figure 5-20. The electronic partial density of states (PDOS) for the tetragonal (a) Na_3Si (*I4/mmm*) at 2.5GPa and (b) Na_3Si (*I4/mmm*) at 5GPa.

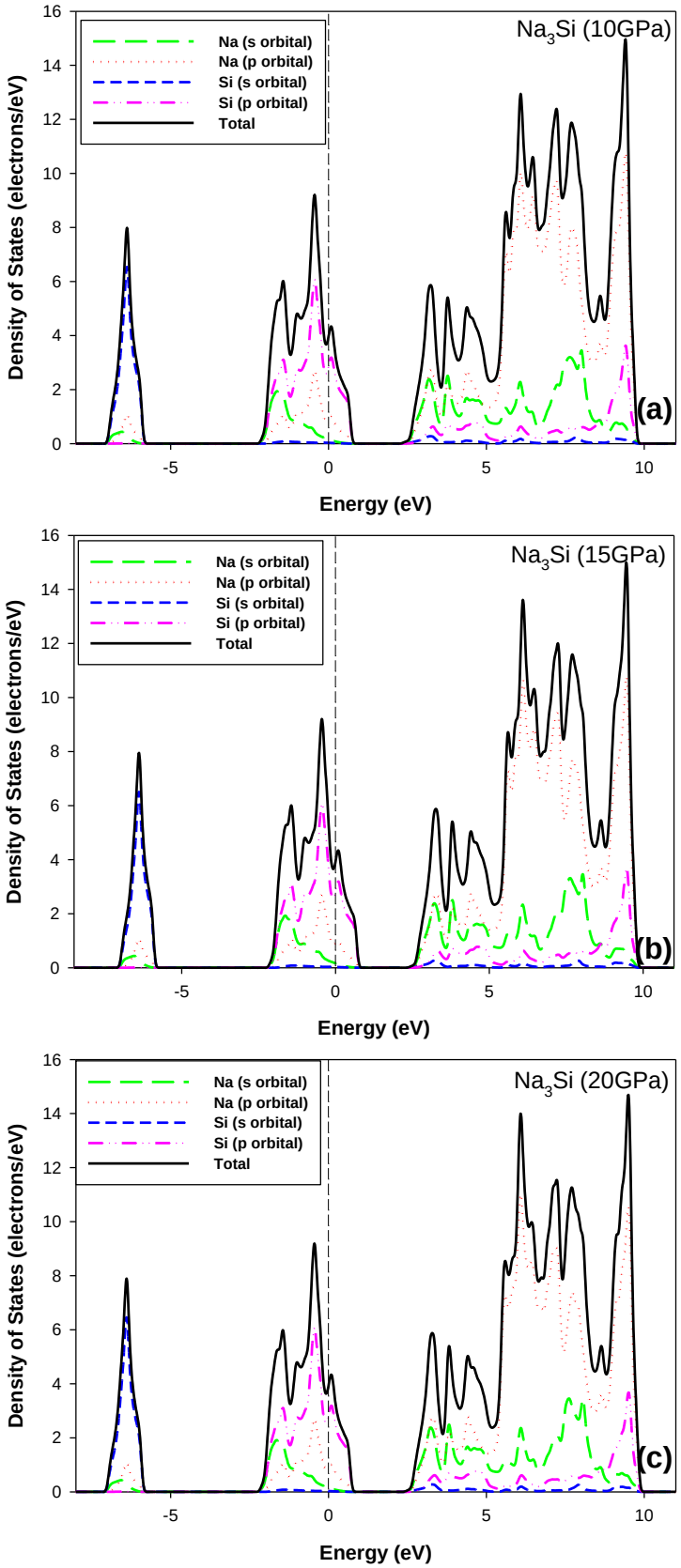

Figure 5-21. The electronic partial density of states (PDOS) for the tetragonal (a) Na_3Si (*I4/mmm*) at 10GPa, (b) Na_3Si (*I4/mmm*) at 15GPa, and (c) Na_3Si (*I4/mmm*) at 20GPa.

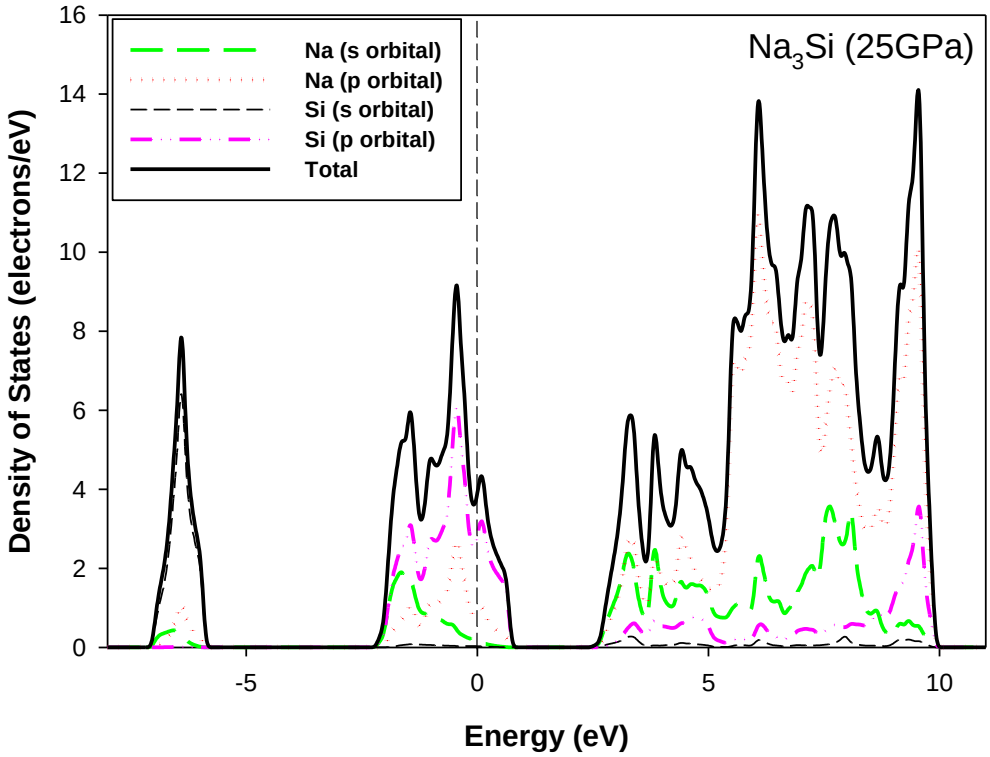

Figure 5-22. The electronic partial density of states (PDOS) for the tetragonal Na_3Si (*I4/mmm*) at 25GPa.

Figure 5-19 through to Figure 5-22 illustrates the electronic partial density of states for the tetragonal Na_3Si (*I4/mmm*) calculated using the Na-Si SCC-DFTB parameters developed herein. Initially, the PDOS was determined in the absence of external pressure, and then an external pressure of 2.5GPa was introduced to the system. As shown by Figure 5-20 (a), the pressure induces a small pseudogap on the total DOS. The Fermi level is seen to fall within the pseudogap.

The external pressure of 5GPa was applied to the Na_3Si crystal structure. A shown by Figure 5-20 (b), the shape of the bands at this pressure compared with the shape at 2.5GPa seems not to have changed by much. The external pressure was systematically raised by increments of 5GPa spanning a range from 10GPa to 25GPa. Again, the PDOS graphs do not appear to have changed in shape. This suggests that the external pressure did not drastically redistribute electronic states across the energy spectrum. As such, the crystal globally keeps its state of stability in the pressure ranges explored. Also, the number of electrons at the Fermi level is not greatly lowered, hence it can be deduced that SCC-DFTB parameters predict Na_3Si to be metastable in the 2.5GPa – 25GPa pressure range.

5.4 Preliminary Ground-State Phase Structure Predictions for Mg-Si

Na and Mg are considered alternatives for Li-ion based electrodes. Although Na and Mg batteries would not exhibit better performance compared with Li-ion batteries, they are considered to be more economic. Unlike Li and Na which donate single electrons, the ability of Mg to donate two electrons makes it interesting for energy storage applications. In this section, though not within the scope of this work, cluster expansion is employed a test to screen Mg-Si alloys that could be explored for study in the context of energy storage.

5.4.1 Structure predictions from Si *Fm-3m*

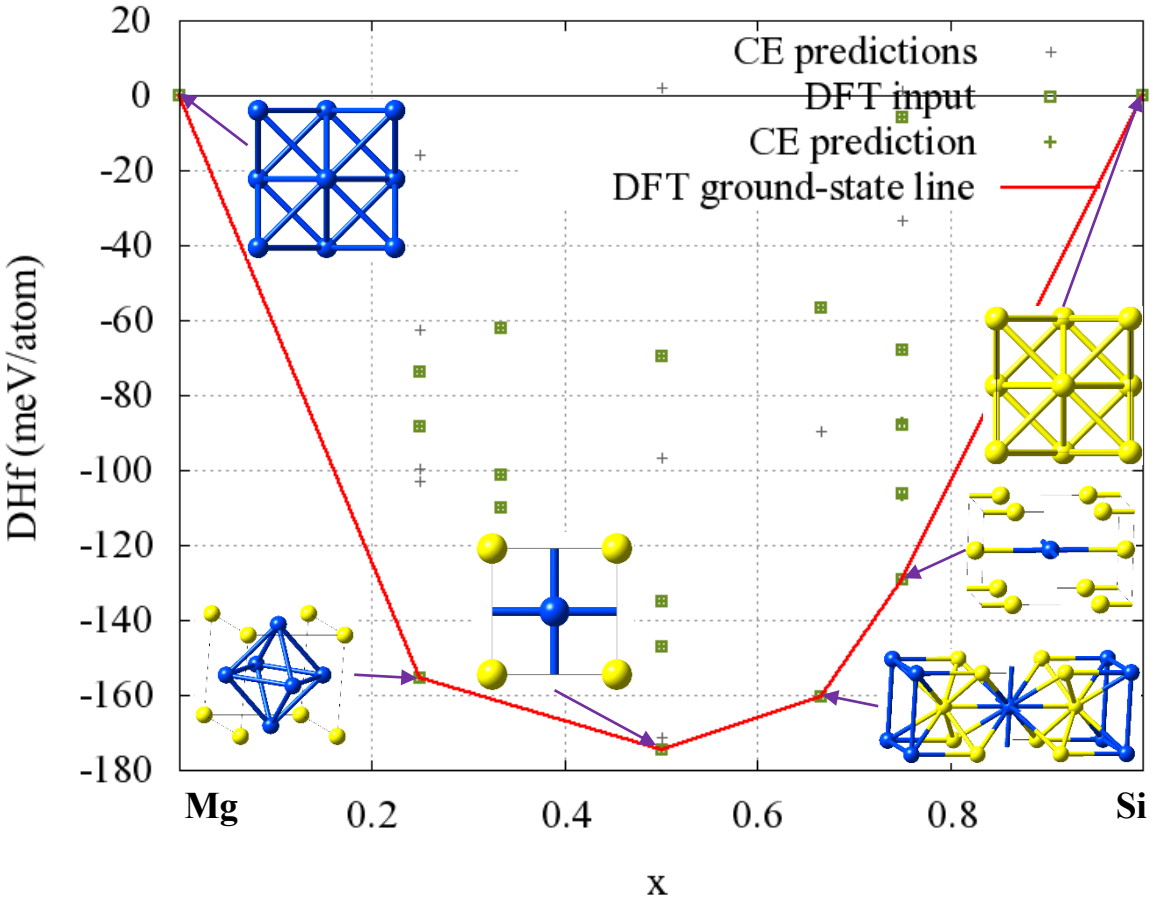

Figure 5-23. Calculated binary ground-state diagram of Mg-Si emanating from a grid search using the FCC-based system considering structures of up to 16 basis atoms.

Table 5-14. Summary of the iterative optimization progress

Iteration	no. of struc.	no. of new struc.	CVS [meV/pos.]	% struc. with SD below 5 meV	new structures
0	0	2	-	-	ce1 ce2
0	0	7	-	-	ce7 ce19 ce29 ce10 ce12 ce1 ce2
1	7	5	0.46	-	ce25 ce9 ce4 ce6 ce28
2	12	2	0.25	-	ce20 ce15
3	14	4	0.3	-	ce27 ce8 ce16 ce11
4	18	1	0.033	-	ce26
5	19	0	0.02	-	

Table 5-15. A comparison of energies E and formation energies DHf in eV (counted per active atom position) as predicted by the cluster expansion and as calculated by the computational engine (DFT).

Energy differences to the structure at the ground state line (GSL) for each composition x are listed.

# no.	x(1:k,1:nC)		E_DFT	D(E_DFT,E_CE)	E_CE	DHf_DFT	DHf_CE	Dist to GSL DFT	title	cell formula	space group
1	0.00000	1.00000	-1.4916460000	0.0000000882	-1.4916459118	0.0000000000	0.0000000000	0.0000000000	ce2	Mg	Fm-3m
2	0.25000	0.75000	-2.4087970000	-0.0000136447	-2.4088106447	-0.0737622500	-0.0737759770	0.0815960000	ce27	Mg3Si	Cmmm
3	0.25000	0.75000	-2.4235590000	-0.0000129556	-2.4235719556	-0.0885242500	-0.0885372879	0.0668340000	ce25	Mg3Si	I4/mmm
4	0.25000	0.75000	-2.4903930000	-0.0000286112	-2.4904216112	-0.1553582500	-0.1553869435	0.0000000000	ce29	Mg3Si	Pm-3m
5	0.33333	0.66667	-2.6783486667	0.0000123668	-2.6783362998	-0.0621843333	-0.0621720469	0.0995930000	ce8	Mg2Si	P-3m1
6	0.33333	0.66667	-2.7175250000	0.0000100629	-2.7175149371	-0.1013606667	-0.1013506842	0.0604166667	ce10	Mg2Si	I4/mmm
7	0.33333	0.66667	-2.7262620000	-0.0000114237	-2.7262734237	-0.1100976667	-0.1101091707	0.0516796667	ce9	Mg2Si	Immm
8	0.50000	0.50000	-3.2481157500	-0.0000170294	-3.2481327794	-0.0696922500	-0.0697093559	0.1049232500	ce16	Mg2Si2	R-3m
9	0.50000	0.50000	-3.3133995000	0.0000197676	-3.3133797324	-0.1349760000	-0.1349563089	0.0396395000	ce19	Mg2Si2	P4/nmm
10	0.50000	0.50000	-3.3253310000	0.0000089210	-3.3253220790	-0.1469075000	-0.1468986555	0.0277080000	ce20	Mg2Si2	I4_1/amd
11	0.50000	0.50000	-3.3530390000	0.0000348476	-3.3530041524	-0.1746155000	-0.1745807289	0.0000000000	ce4	MgSi	P4/mmm
12	0.66667	0.33333	-3.7971710000	0.0000172614	-3.7971537386	-0.0564883333	-0.0564711445	0.1038683333	ce7	MgSi2	I4/mmm
13	0.66667	0.33333	-3.9010393333	-0.0000114237	-3.9010507570	-0.1603566667	-0.1603681629	0.0000000000	ce6	MgSi2	Immm
14	0.75000	0.25000	-4.0278487500	0.0000170294	-4.0278317206	-0.0060365000	-0.0060195412	0.1229962500	ce11	MgSi3	R-3m
15	0.75000	0.25000	-4.0899247500	-0.0000101762	-4.0899349262	-0.0681125000	-0.0681227468	0.0609202500	ce26	MgSi3	Cmmm
16	0.75000	0.25000	-4.1095537500	0.0000343041	-4.1095194459	-0.0877415000	-0.0877072665	0.0412912500	ce15	MgSi3	I4/mmm
17	0.75000	0.25000	-4.1282670000	-0.0000293292	-4.1282963292	-0.1064547500	-0.1064841498	0.0225780000	ce28	MgSi3	Pm-3m
18	0.75000	0.25000	-4.1508450000	0.0000154245	-4.1508295755	-0.1290327500	-0.1290173961	0.0000000000	ce12	MgSi3	Pmmm
19	1.00000	0.00000	-4.8652010000	0.0000000647	-4.8652009353	0.0000000000	0.0000000000	0.0000000000	ce1	Si	Fm-3m

A cluster expansion of the Mg-Si was performed based on an FCC parent lattice. Figure 5-23 depicts the binary ground-state diagram of Mg-Si system. As shown by Table 5-14, the cluster expansion converged successfully with an excellent cross-validation score of 0.02 meV/atomic position; and Table 5-15 depicts 19 predicted structures. Besides the pure systems, as listed in appendix I, four Mg-Si alloys were predicted to be thermodynamically stable. That is Mg_3Si (*Pm-3m*), MgSi (*P4/mmm*), $MgSi_2$ (*Immm*) and $MgSi_3$ (*Pmmm*). Since, the major objective would be to study large complex systems using SCC-DFTB, to model Mg-Si alloys, a parameter set in this respect would be required. The *magsil* parameter set available on the DFTB.org website was developed for chrysotile nanotube structures and therefore is limited for our context. Hence, a new set would need to be developed.

5.5 Exploring the Nano-architectural Design of New Active Material for Future Battery Electrodes

As alluded to in the literature review, strategies being explored to address the challenges of energy storage such as volume expansion, short cycling life, inadequate energy densities include the use of porous and nanostructured materials. Furthermore, in some cases, the amorphization of materials being used is reported to contribute to improved performances. For instance, the experimental work done by Li *et al* [178] reported that the performance of Li-ion batteries was seen to improve when amorphous nanosized silicon composed of a hierarchically porous structure was employed. Also, in the same work, it was indicated that the amorphous feature of the silicon nanoparticles aid in the relief of stress induced by volume expansion consequent to lithiation, and the feature enhances structural stability which promotes longer cycling lifetime. Also, Lee *at al* [179] demonstrated that amorphous composites can be used to improve capacity retention, the electrochemical performance of Li-ion battery anodes. Lim *et al* [96] by experimentally studying the sodiation of amorphous silicon, demonstrated that the amorphization of silicon can be used as part of design strategies applicable for Na-ion batteries.

In this subsection, structures predicted via cluster expansion are used to simulate silicon-based nanostructures. For illustrative purposes, Li-Si and Na-Si based nanospheres are designed. The nanospheres which can be thought of as nanoparticles are designed and their structural stability is evaluated through the analysis of their electronic density of states. The objective is to demonstrate that the combination of SCC-DFTB with Cluster Expansion can be used as a tool for compositional and structural optimization of novel electrodes earmarked for the next generation of rechargeable batteries.

5.5.1 Designing nanostructured material from structures predicted by the machine learning powered cluster expansion.

5.5.1.1 Li-Si based nanostructure

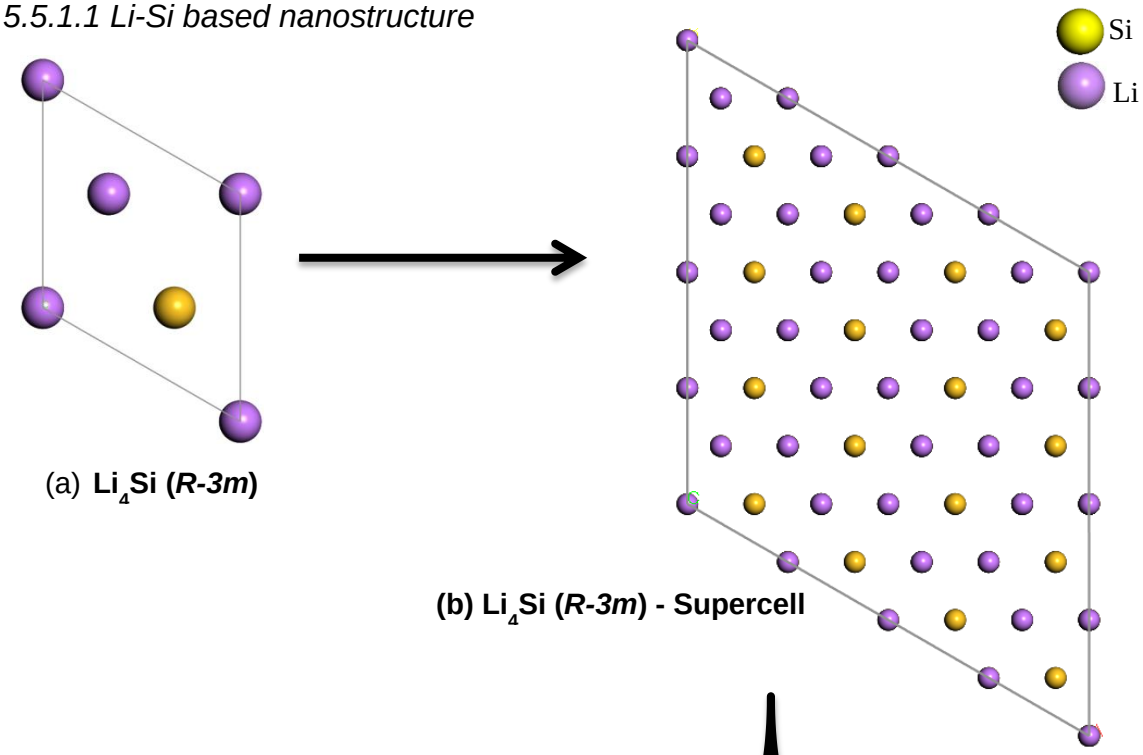

(a) **Li_4Si (*R-3m*)**

(b) Li_4Si (*R-3m*) - Supercell

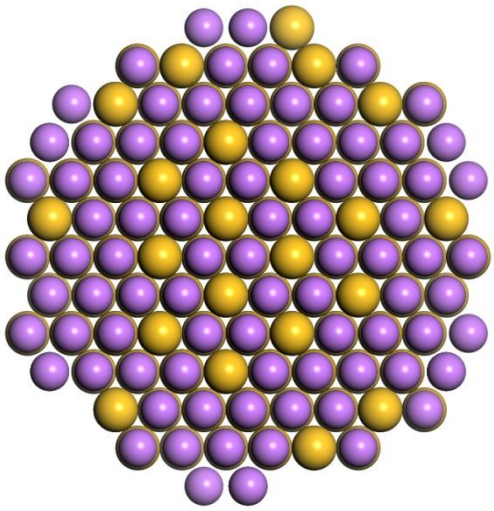

(c) $Li_{3.993}Si$ - Nano sphere

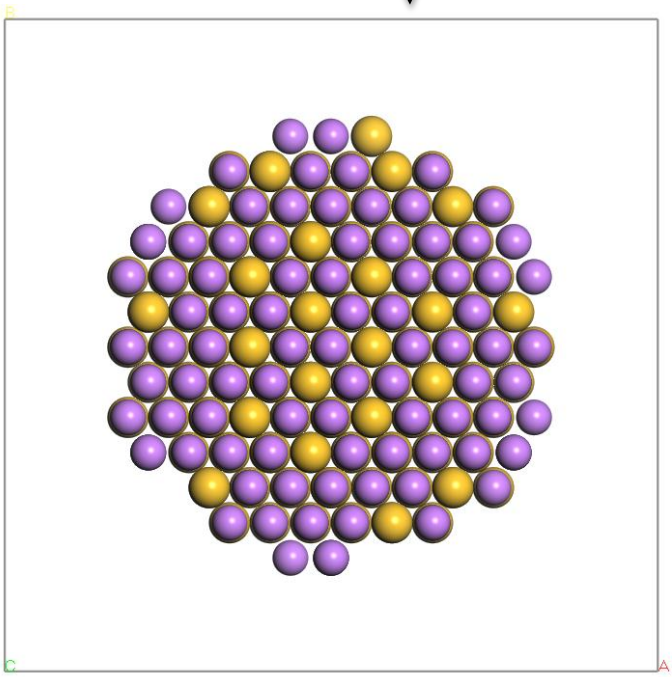

(d) $Li_{3.993}Si$ - Nano sphere [PBC]

Figure 5-24. Schematic presentation of the design of nano-structured electrode material from predicted Li-Si alloys.

Figure 5-24 shows a schema through which electrodes with a nano-architecture can be designed using structures that were predicted to be stable from cluster expansion. The stability of the nanostructures is further assessed using SCC-DFTB parameters. The crystalline lithium-rich phase (a) Li_4Si (*R-3m*) was predicted to be thermodynamically stable via a machine-learning-powered cluster expansion technique. A supercell comprised of a total of 960 atoms was built from a primary unit cell of Li_4Si and volume for this system was noted to be 13698.9 $Å^3$. A structure relaxation operation was performed using the bulk Li_4Si supercell, and the volume of the relaxed system was 13698.4 $Å^3$.

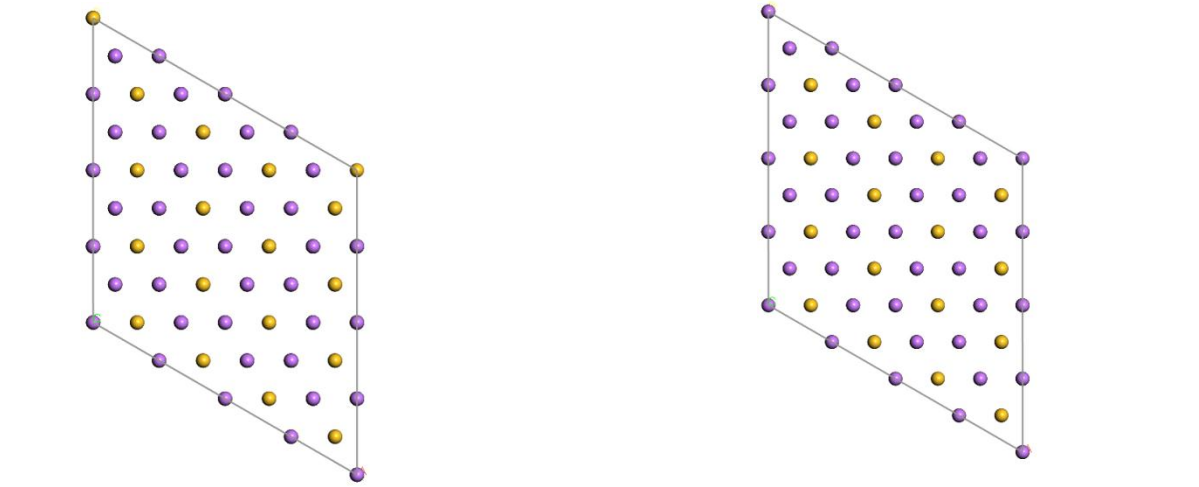

(a) **Li_4Si (*R-3m*) – Supercell - Unrelaxed** **(b)** **Li_4Si (*R-3m*) – Supercell - Relaxed**

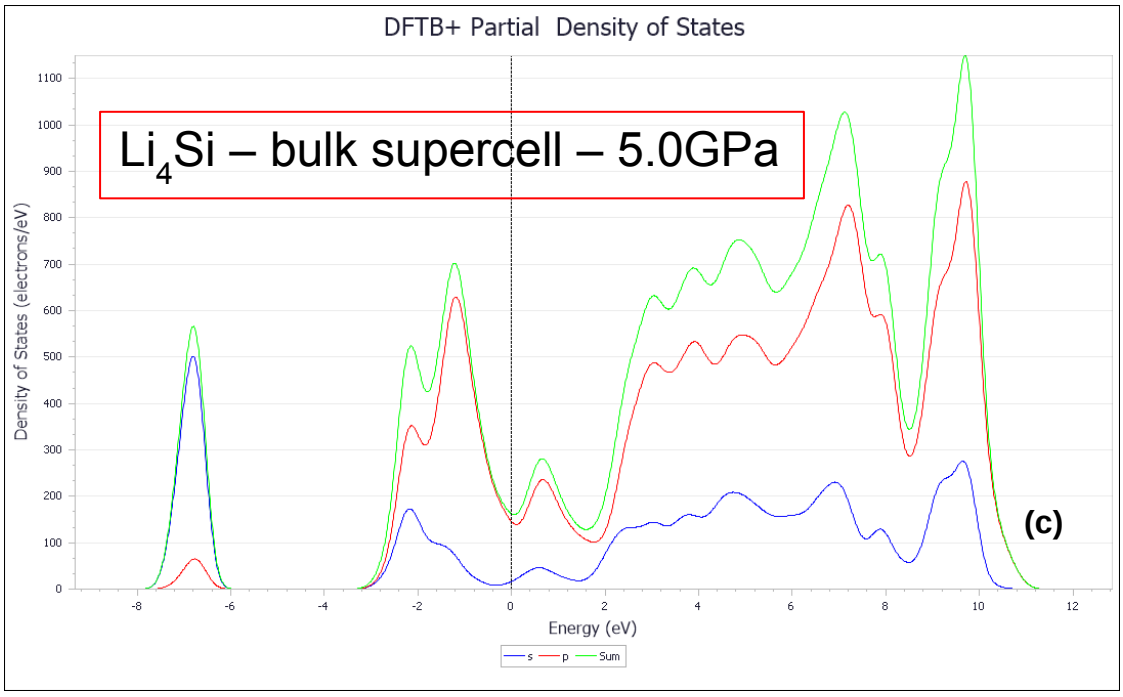

Figure 5-25. The illustration of the (a) unrelaxed and (b) relaxed supercell of the trigonal $LiSi_4$ (*R-3m*) crystal structure and (c) the latter's electronic partial density of states (PDOS) at 5GPa and 0K.

From the PDOS of the relaxed crystalline Li_4Si supercell illustrated by Figure 5-25, it can be seen on the total DOS that the Fermi level is located exactly within a parabolic pseudogap with a minimum around 160 electrons/eV. Hence, this suggests that the supercell is stable. From this supercell, a Li-Si nanostructure of a spherical morphology with a total number of 739 atoms was built. As depicted by Figure 5-26, two systems were generated, (c) a non-periodic nanosphere constituted of 591 Li atoms and 148 Si atoms with a net charge of 0.017 and (d) a nanosphere within periodic boundary conditions (PBC) comprised of an equivalent number of atoms. The cell size of the nanosphere PBC was set to 40 Å, 40 Å, 40 Å on the ***a***, ***b***, ***c*** lattice parameter. The cell was constructed such that there is space around the nanosphere to minimize the possible effects of artificial self-interaction. The structures of two nanospheres were optimised to bring the total system energy to ground-state.

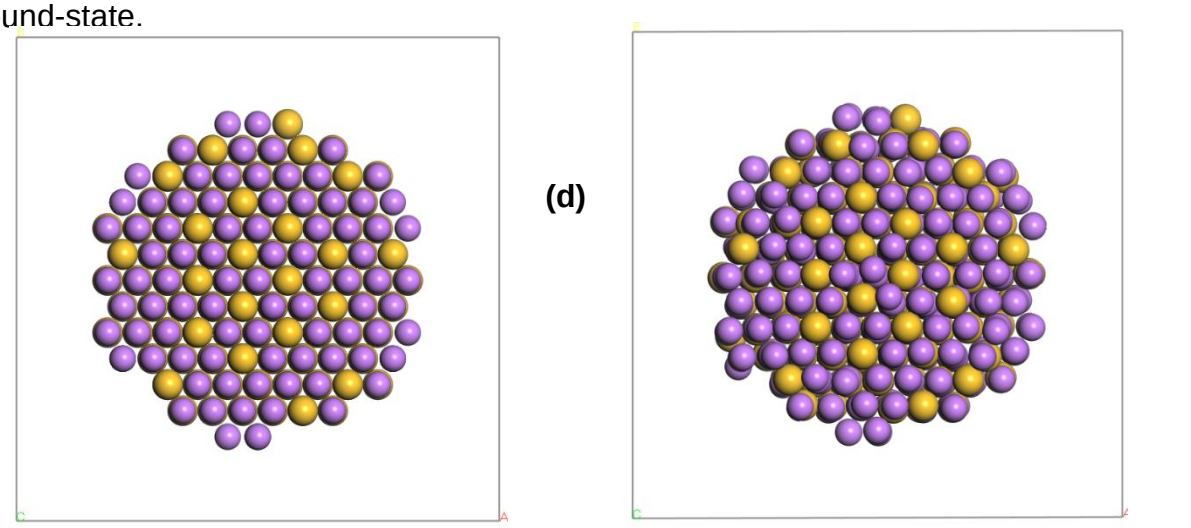

(d)

$Li_{3.99}Si$ – Nanosphere – Unrelaxed [PBC]

$Li_{3.99}Si$ – Nanospere – Relaxed [PBC]

(c)

$Li_{3.99}Si$ – Nanosphere - Unrelaxed

$Li_{3.99}Si$ – Nanospere - Relaxed

Figure 5-26. Illustration of the $Li_{3.99}Si$ nanosphere before and after structural relaxation done within and without periodic boundary conditions (PBC).

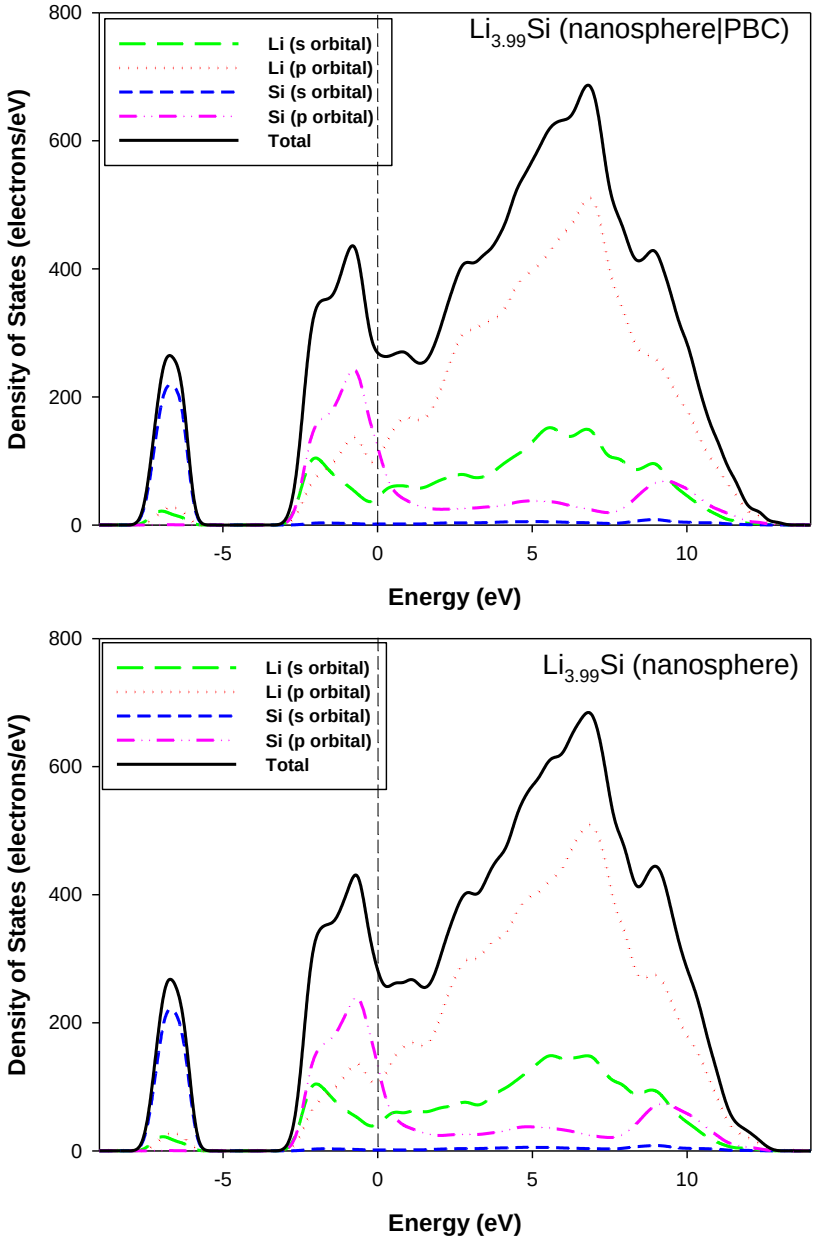

Figure 5-27. The electronic partial density of states (PDOS) for the $Li_{3.99}Si$ nanospheres at 0GPa and 0K.

Figure 5-27 shows the PDOS graphs for the relaxed $Li_{3.99}Si$ nanosphere when periodic boundary conditions are used and when no used. The structure relaxations were done in the absence of external pressure and temperature. As noticed on both plots, the Li and Si p orbitals almost have equivalent contribution at the Fermi level, with electron states in the p orbital of the Si atoms contributing just slightly more. Considering the total DOS, it is observed that E_f falls within but more toward the bonding region of the pseudogap. This suggests that with and without periodic boundary conditions, the $Li_{3.99}Si$ nanosphere exhibited structural stability. This

behaviour is consistent with the observation from the bulk Li_4Si (*R-3m*) crystal structure.

5.5.1.2 Na-Si based nanostructure

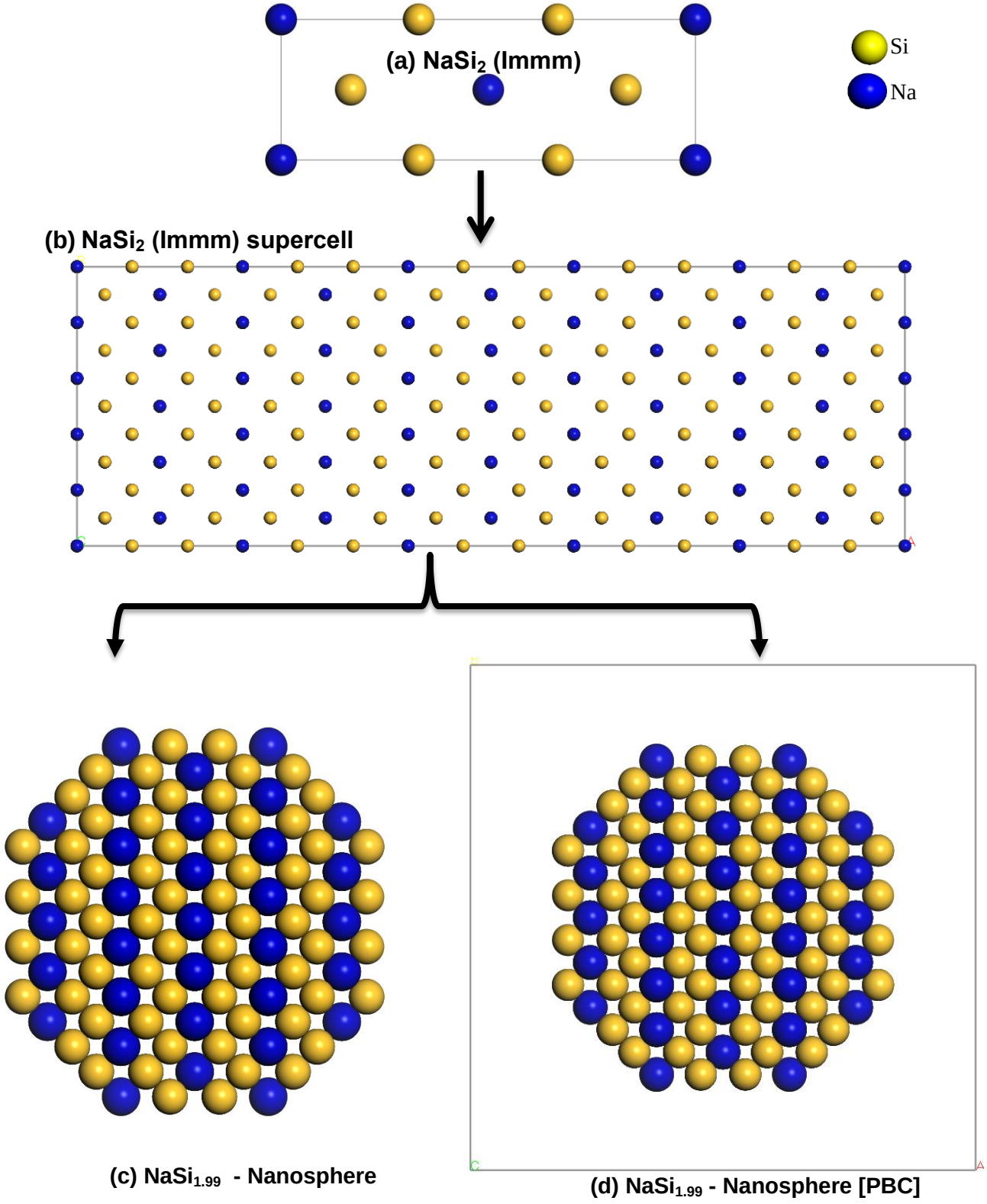

Figure 5-28. Schematic presentation of the design of nano-structured electrode material from predicted Na-Si alloys.

Using insights generated from the framework illustrated from the Li-Si binary alloy systems, the workflow can now be employed on the Na-Si alloy as presented by Figure 5-28, and perhaps other systems. Using the predicted $NaSi_2$ and Na_3Si binary structures, supercell structures of these systems are generated and optimised. The supercell of $NaSi_2$ consists of a total of 750 atoms, whilst that of Na_3Si consists of 1000 atoms. From the optimised supercells, Na-Si nanostructures were built.

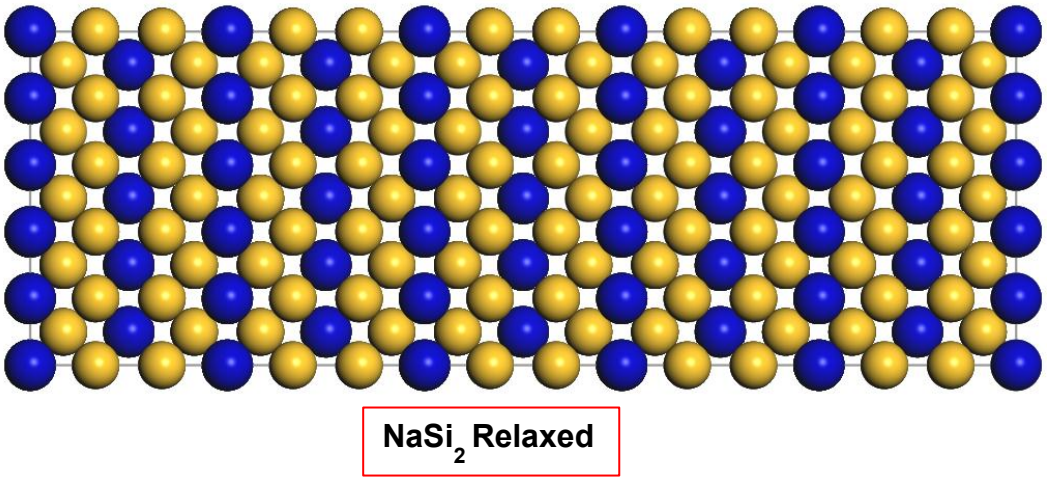

Figure 5-29. A presentation of (a) the crystal structure of a relaxed 1000 atom supercell of the orthorhombic $NaSi_2$ (*Immm*) and (b) its electronic partial density of states (PDOS) at 0GPa and 0K.

Figure 5-29 presents a relaxed $NaSi_2$ crystalline supercell structure consisting of 1000 atoms, together with its corresponding PDOS at 0GPa and 0K. From Figure 5-29, it is evident that the major contribution at the Fermi level stems from the Si p-orbital. The total DOS of $NaSi_2$ falls within the pseudogap and therefore suggests that this phase is structurally stable.

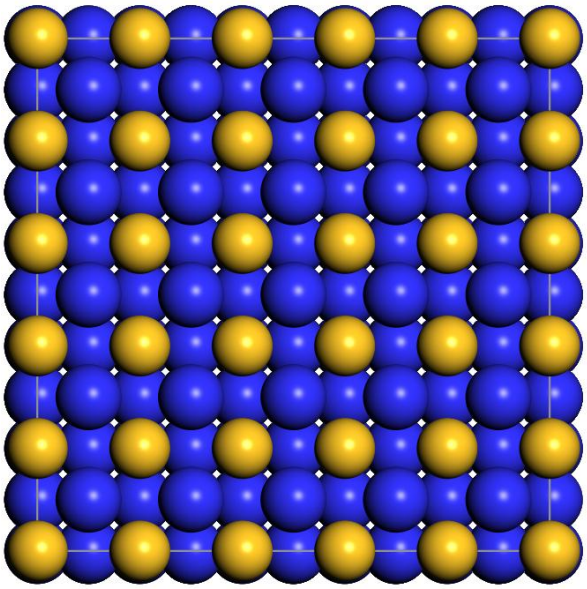

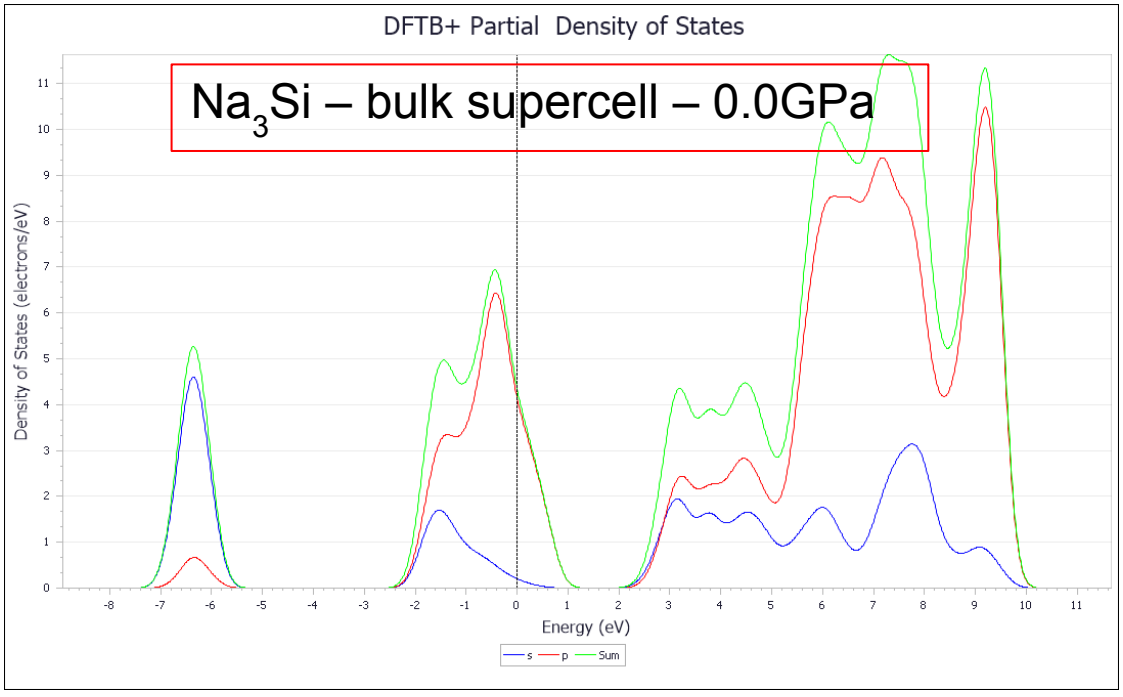

Figure 5-30. A presentation of (a) the crystal structure of a relaxed 1000 atom supercell of the tetragonal Na_3Si (*I4/mmm*) and (b) its electronic partial density of states (PDOS) at 0GPa and 0K.

Figure 5-30 shows the PDOS of the 1000 atom supercell generated from the tetragonal Na_3Si (I4/mmm) structure in the absence of external pressure and temperature. Similar to the unit cell from which the supercell was built, E_f hinges toward the bonding region of a broad peak on the total DOS. Also the case of the supercell, the behaviour suggests that the structure is metastable.

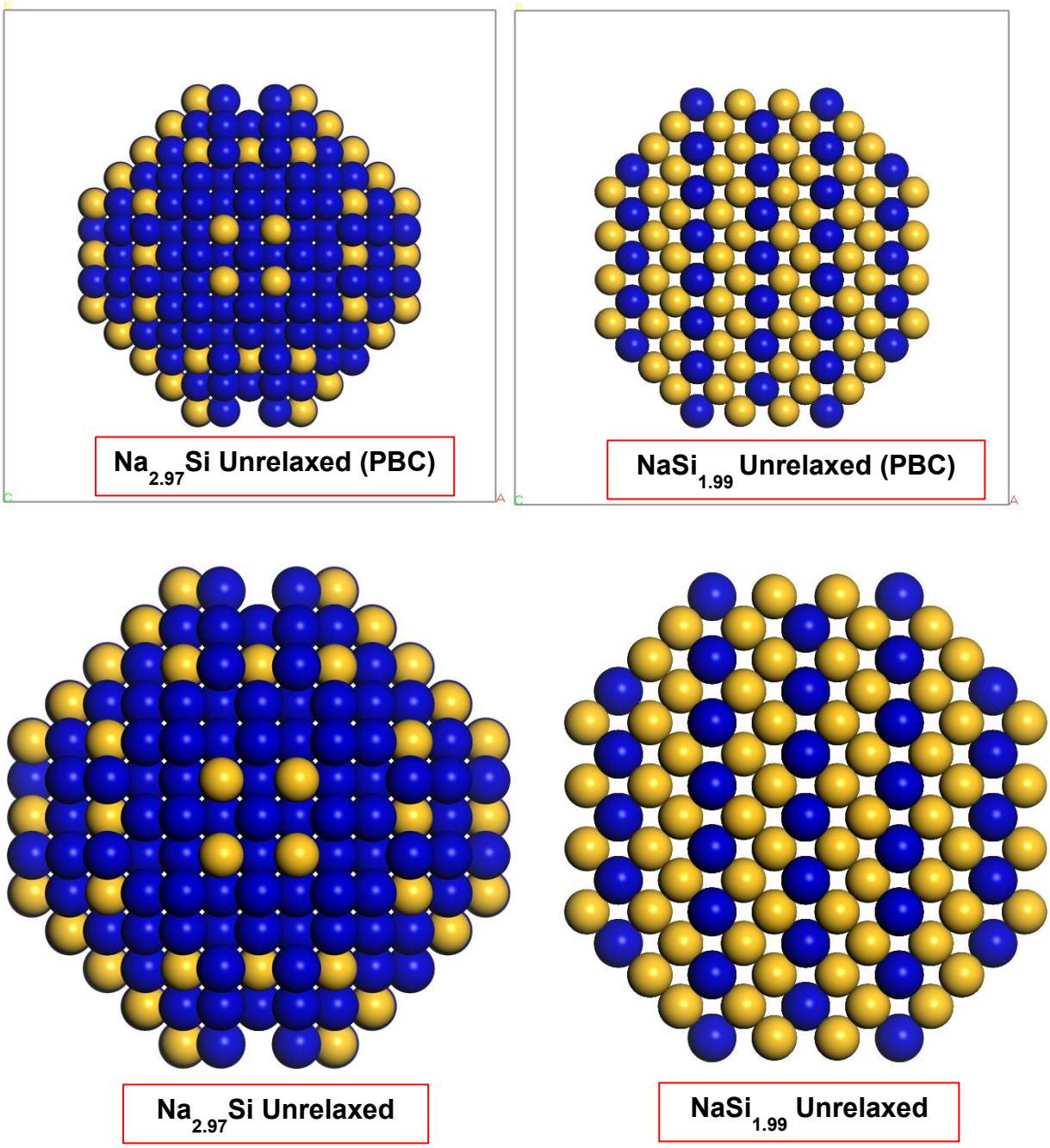

Figure 5-31. A graphical illustration of the $Na_{2.97}Si$ and $NaSi_{1.99}$ nanospheres before structural relaxation done within and without periodic boundary conditions (PBC).

Similar to the development of nanospheres designed from supercell of structures predicted through cluster expansion and further studied via the SCC-DFTB approach, nanostructures based on the Na-Si can be built. Figure 5-31 illustrates the $Na_{2.97}Si$ and $NaSi_{1.99}$ nanospheres built from Na_3Si (*I4/mmm*) and $NaSi_2$ (*Immm*) respectively. Figure 5-32 shows a presentation of (a) the relaxed 591 atom $Na_{2.97}Si$ nanosphere (b) its volumetric properties and (c) PDOS in the absence of external pressure and temperature. The similar to the unit cell and supercell from the nanosphere was built, E_f is seen to hinge toward the bonding region of a broad peak on the total DOS. This suggests that the $Na_{2.97}Si$ nanosphere is metastable.

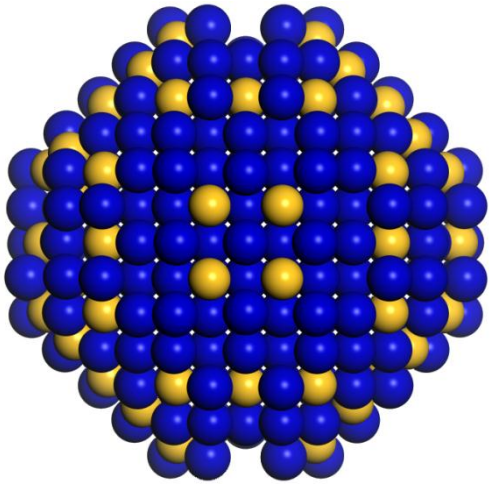

(a) $Na_{2.97}Si$ Relaxed

(b)

System	$Na_{2.97}Si$	$Na_{2.97}Si$
# Atoms	591	591
Volume	13251.30 Å³	13327.82 Å³
Geometry	Unrelaxed	Relaxed
Morphology	Nanosphere	Nanosphere

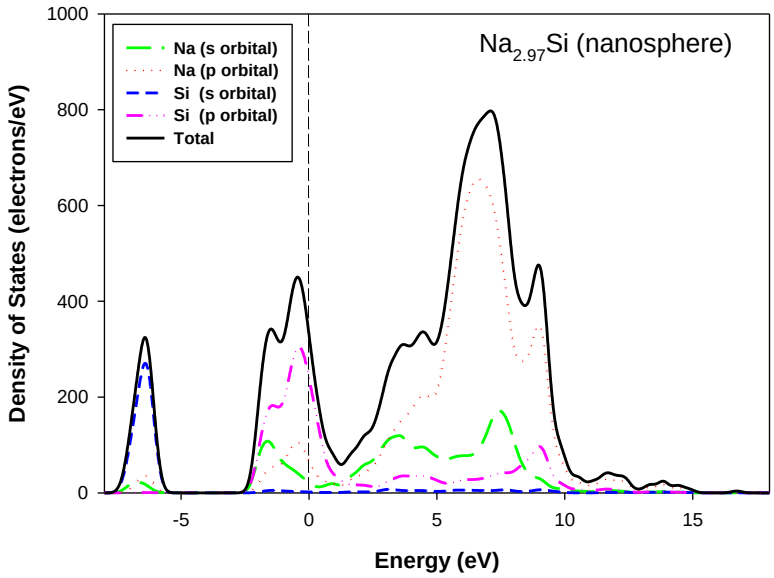

(c)

Figure 5-32. A presentation of (a) the relaxed 591 atom $Na_{2.97}Si$ nanosphere (b) volumetric properties and (c) its electronic partial density of states (PDOS) at 0GPa and 0K.

5.5.1.3 An assessment of ground-state sodium-silicon nanospheres

As shown in Figure 5-31, two sodium-silicon nanospheres based on the predicted Na_3Si and $NaSi_2$ were built, *i.e.* $Na_{2.97}Si$ and $NaSi_{1.99}$ nanospheres. Structure relaxation calculations were performed on the nanospheres to bring them to the ground-state. Using an HPC server node equipped with an Intel® Xeon® Gold 6140 Processor [180] with 36 logical CPU cores, 192GB of random access memory, 100Gb/s interconnection network links, and a BeeGFS parallel file system [181], it took 15 days 10 hours 7 minutes and 36 seconds to bring $Na_{2.97}Si$ to ground-state. The structure relaxation calculation of the $NaSi_{1.99}$ nanosphere ran for over a month and at the time of writing was still running, but an inspection of the interim results showed that the set criteria for convergence would eventually be met with time. In light of the insights obtained from the efforts made to bring the two nanospheres to ground-state, it was necessary to highlight a few aspects that aided the progress and results produced.

Geometry optimisation algorithms within the DFTB+ code as implemented in Materials Studio simulation package

The DFTB+ code in Materials Studio has four geometry optimisation algorithm options that can be used in calculations. Namely, the Smart, Steepest Descent [182], Conjugate Gradient [183], Quasi-Newton and the adjusted basis set Newton-Raphson (ABNR) [184] algorithms. The choice of which algorithm to select when relaxing a structure of a given material depends primarily on the size of the structure and the optimisation state in which the calculation is with respect to the energy minimum. Detailed presentations of the algorithms can be found elsewhere [158]. Hence, only a few aspects of these algorithms are highlighted in this work.

The Smart algorithm is a cascade implementation of the Steepest Descent, ABNR, and quasi-Newton algorithms. The Steepest Descent relies on the energy gradients and can result in very slow convergence near the minimum due to the gradient approaching zero. It is most suited to the relaxation of poorly refined crystallographic models which would exhibit large gradients and configurations that are far from the minimum. Hence, it is recommended that the Steepest Descent algorithm be used for the initial 10 – 100 steps when optimising large structures or systems with high distortion; then to complete the optimisation to convergence, the conjugate gradient

and/or a Newton-Raphson optimiser can be used. The conjugate gradient and the Newton-Raphson algorithms are most suitable for calculations involving large systems. Unlike the Newton-Raphson methods which pose higher memory requirements, the conjugate algorithm requires lesser memory. However, ABNR is reckoned to be suitable for many applications. Hence, where necessary, it is employed in optimising the nanospheres built herein.

Table 5-16. Volume of Na-Si models before and after geometry optimisation

System	Space group	Morphology	Algorithm	#Atoms	P (GPa)	Unrelaxed Vol. ($Å^3$)	Relaxed Vol. ($Å^3$)	ΔVol. (%)	Notes
$NaSi_2$	Immm	Bulk - Unit cell	Smart	6	0	111.972	110.053	-1.71	
$NaSi_2$	Immm	Bulk - Supercell	Smart	750	0	13756.7	13765	0.06	
$NaSi_{1.99}$		Nanosphere	Steepest Descent	637	0	13874.77	13521.27	-2.55	□
$NaSi_{1.99}$		Nanosphere	ABNR	637	0	13521.27	13378.63	-1.05	†
$NaSi_{1.99}$		Nanosphere	ABNR	637	0	13874.77	13378.63	-3.58	§
Na_3Si	I4/mmm	Bulk - Unit cell	Smart	8	0	169.809	151.825	-10.59	
Na_3Si	I4/mmm	Bulk - Unit cell	Smart	8	2.5	169.809	151.245	-10.93	
Na_3Si	I4/mmm	Bulk - Supercell	Smart	1000	2.5	18905.7	18904.0	-0.01	
Na_3Si	I4/mmm	Bulk - Supercell	Steepest Descent	512	2.5	9679.71	9677.08	-0.03	□
Na_3Si	I4/mmm	Bulk - Supercell	ABNR	512	2.5	9677.08	9677.31	0.00	
Na_3Si	I4/mmm	Bulk - Supercell	Smart	512	0	9679.71	9714.04	0.35	
$Na_{2.97}Si$		Nanosphere	Smart	591	0	13251.3	13327.82	0.58	

□ Calculation allowed a maximum of 100 iterations.
† Intermediate result obtained at the 270th iteration. NB: Calculation was still running at the time of writing.
§ Evaluation of volume taking the effect of both the steepest descent and ABNR algorithm into account.

By focusing on the volume change in the systems used, Table 5-16 presents a comparison of the trends in the $NaSi_2$ and Na_3Si based systems. As listed in Table 5-16, a primary unit cell of the predicted Na_3Si (*I4/mmm*) system consisting of 8 atoms was optimised using the smart algorithm, both in the presence of an external pressure of 2.5GPa and in the absence of pressure. Before geometry optimisation, the unrelaxed structure had a cell volume of 169.809 $Å^3$**.** At ground-state, the cell volume contracted by approximately 10.93% to 151.245 $Å^3$ when an external pressure was introduced; and the system contracted by about 10.58% to a volume of 151.825 $Å^3$ in the absence of external pressure. The reason for introducing pressure

was to see the extent of its influence on the cell volume since pressure was previously learned to improve the stability of the Na_3Si system. Given that $NaSi_2$ was revealed to be stable without external pressure, the geometry optimisation of a primary unit cell of the system comprised of a total of 6 atoms was conducted at 0GPa. The $NaSi_2$ structure was brought to the ground-state using the smart algorithm within the DFTB+ environment. Before optimisation, the cell volume was 111.972 $\mathbf{Å^3}$, and after the geometry optimisation $NaSi_2$ contracted by 1.7% bringing the equilibrium volume to 110.053 $\mathbf{Å^3}$**.** A contraction of the crystal structure is observed on the unit cells for both Na_3Si and $NaSi_2$.

As listed in Table 5-16, a supercell consisting of a total of 750 atoms was generated from the ground-state $NaSi_2$ primary cell. Two other supercells were built from the ground-state Na_3Si structure, one with 1000 atoms and the other with 512 atoms. The reason for developing two supercells from Na_3Si was to demonstrate the ability of the Na-Si SCC-DFTB parameters to model relatively larger sodium-rich systems. The smart algorithm was successfully used to bring the bulk 750 atom $NaSi_2$ and 1000 atom Na_3Si structures to the ground-state. The volume change for these bulk supercell structures was very marginal. The bulk $NaSi_2$ supercell structure marginally expanded by 0.06%, and the bulk Na_3Si supercell structure contracted by 0.01%.

The steepest descent algorithm was employed in the optimisation of the 512 atom bulk Na_3Si structure; interestingly, as presented in Figure 5-33 the system converged in less than 10 optimisation steps. And the volume contracted by 0.03%. The ABNR algorithm was then used on the output, and it was noted that the volume change on the Na_3Si structure was very close to zero (*i.e.* 0.002%). This suggests that the energy gradients were easily brought to a minimum. For comparison, an unrelaxed 512 atom Na_3Si structure was optimised using the smart algorithm. Similar to the other three cases, the change was very marginal, that is, it expanded by 0.35%. Concerning the Na_3Si, as already mentioned, a nanosphere consisting of 591 atoms was generated from the 1000 atom supercell.

The volume adjustments on the supercells indicate that the pre-optimisation of the unit cells from which the larger bulk structures were generated, contributed significantly to bringing the cell parameters to the ground-state. Hence, only negligible changes are noted.

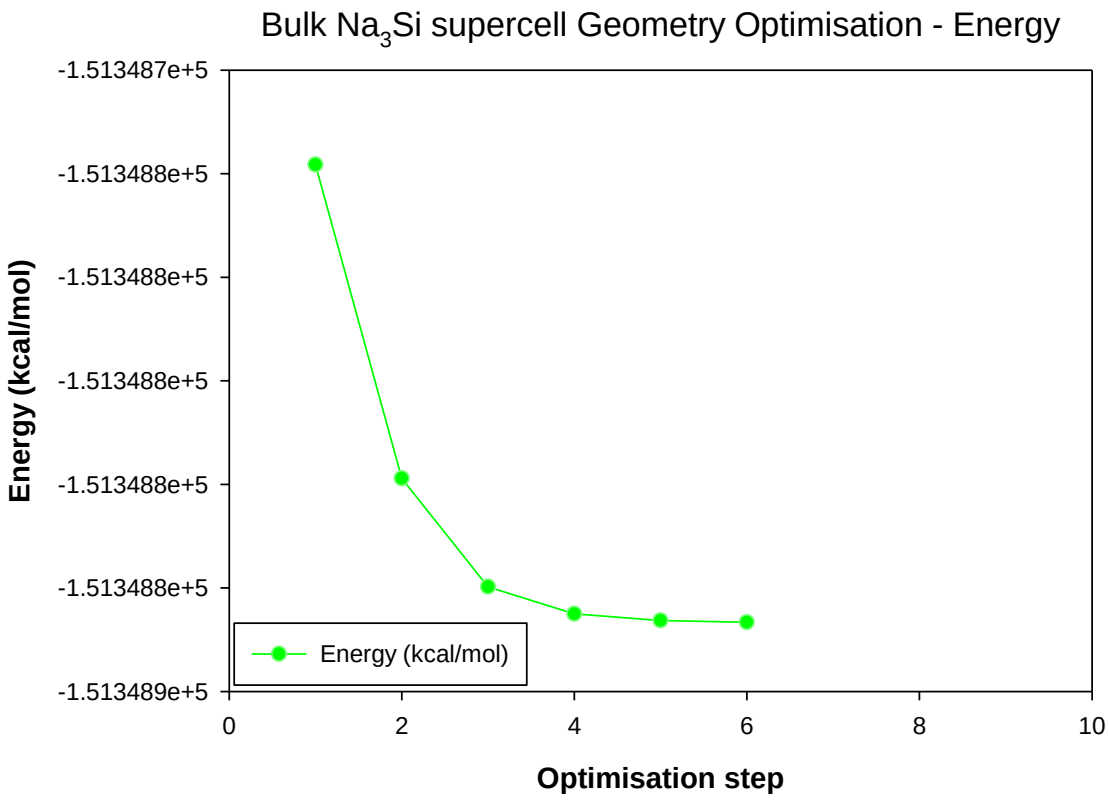

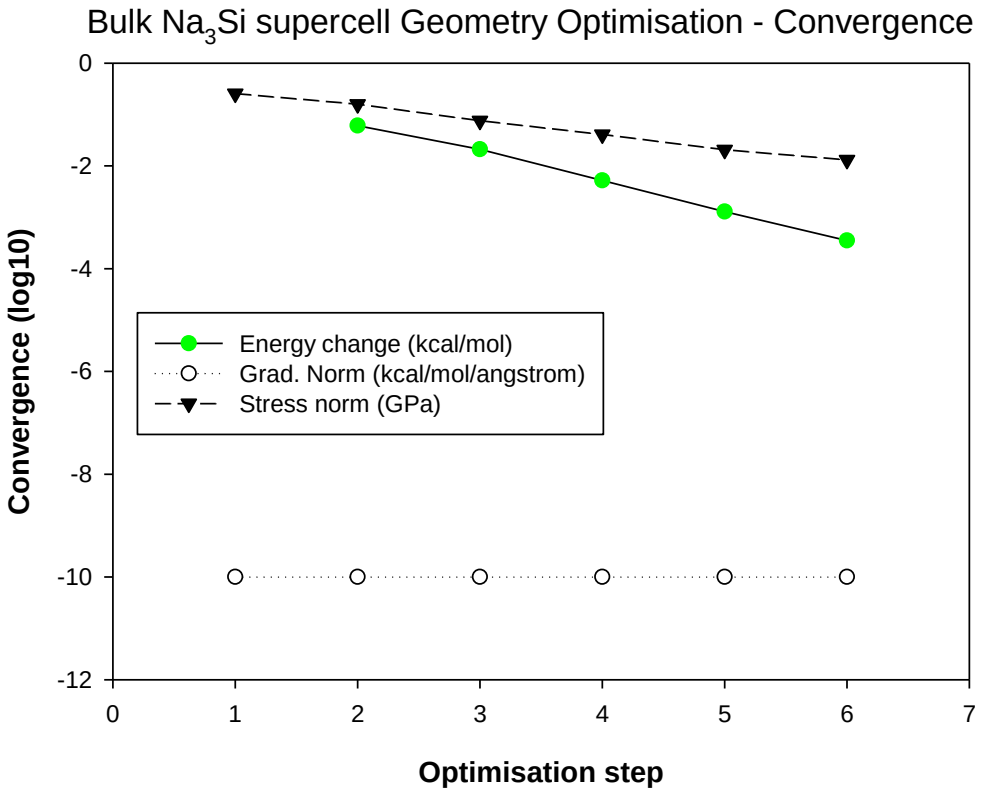

Figure 5-33. Convergence plots for the 512 atom bulk Na_3Si structure obtained using the steepest descent algorithm.

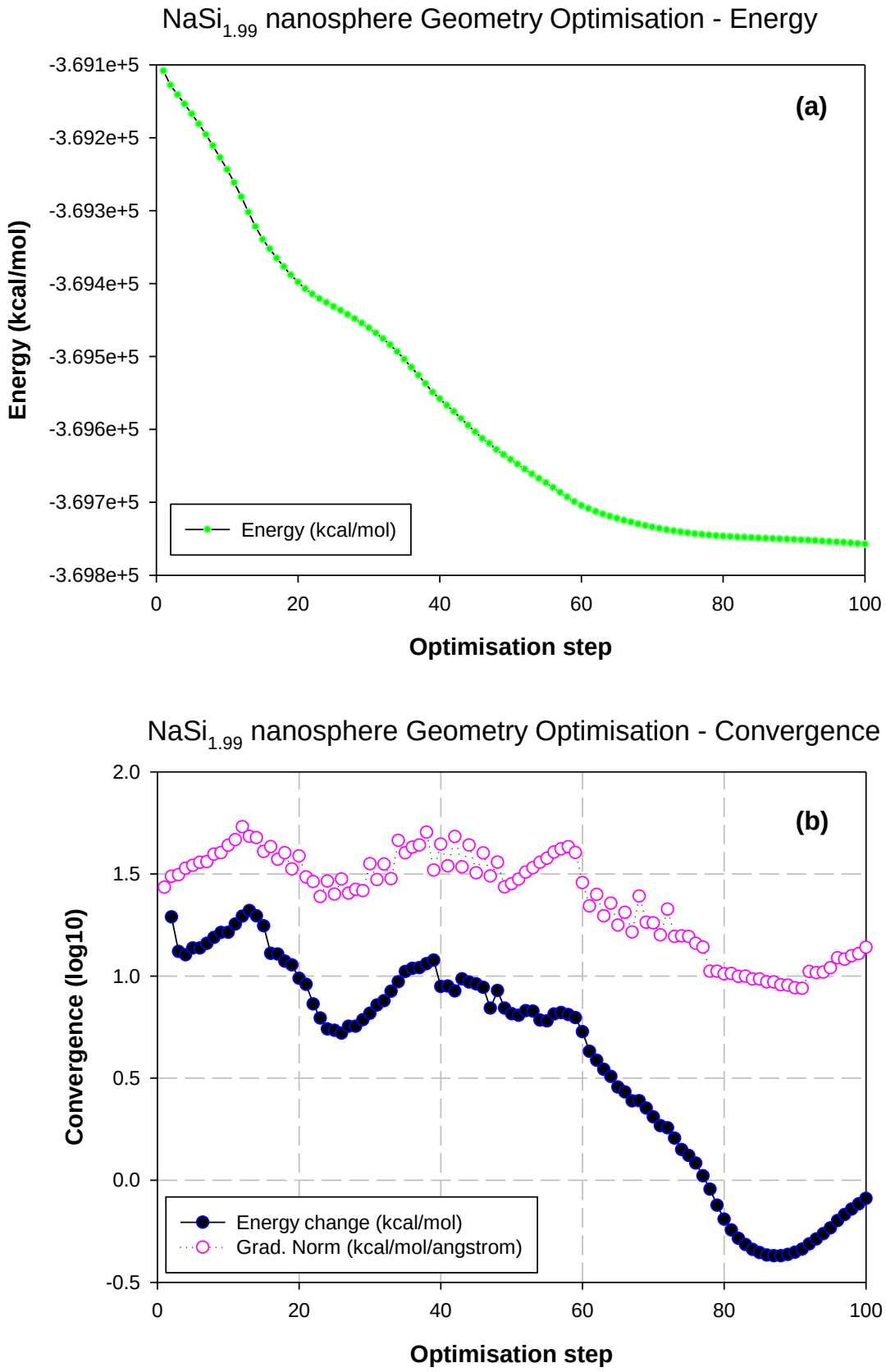

Figure 5-34. Convergence plots for (a) the $NaSi_{1.99}$ nanosphere energy and (b) $NaSi_{1.99}$ up to the 100th optimisation step obtained using the steepest descent algorithm.

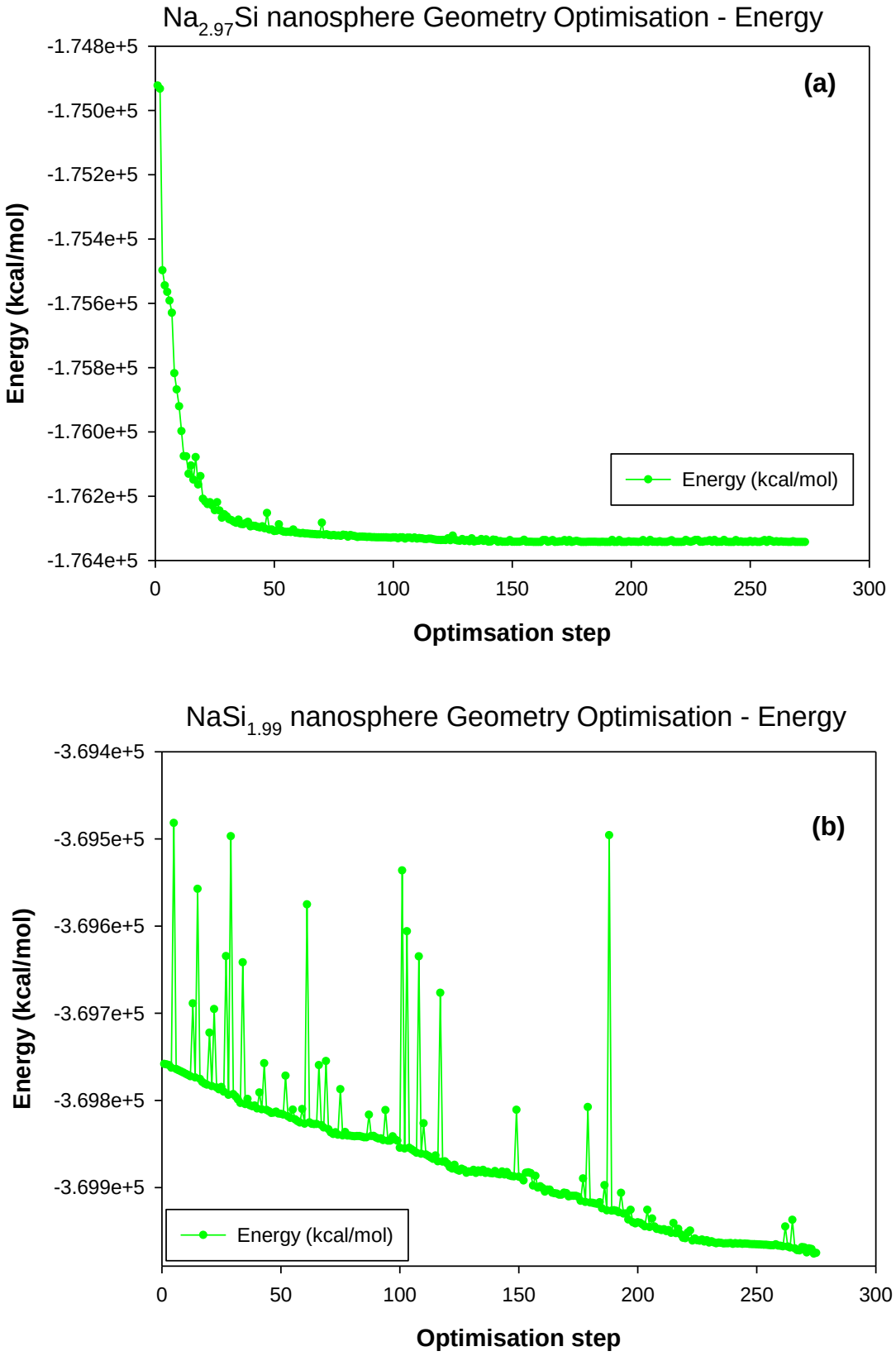

Figure 5-35. Comparison of the energy convergence plots for (a) the $Na_{2.97}Si$ nanosphere at full optimisation and (b) $NaSi_{1.99}$ up to the 270th optimisation step.

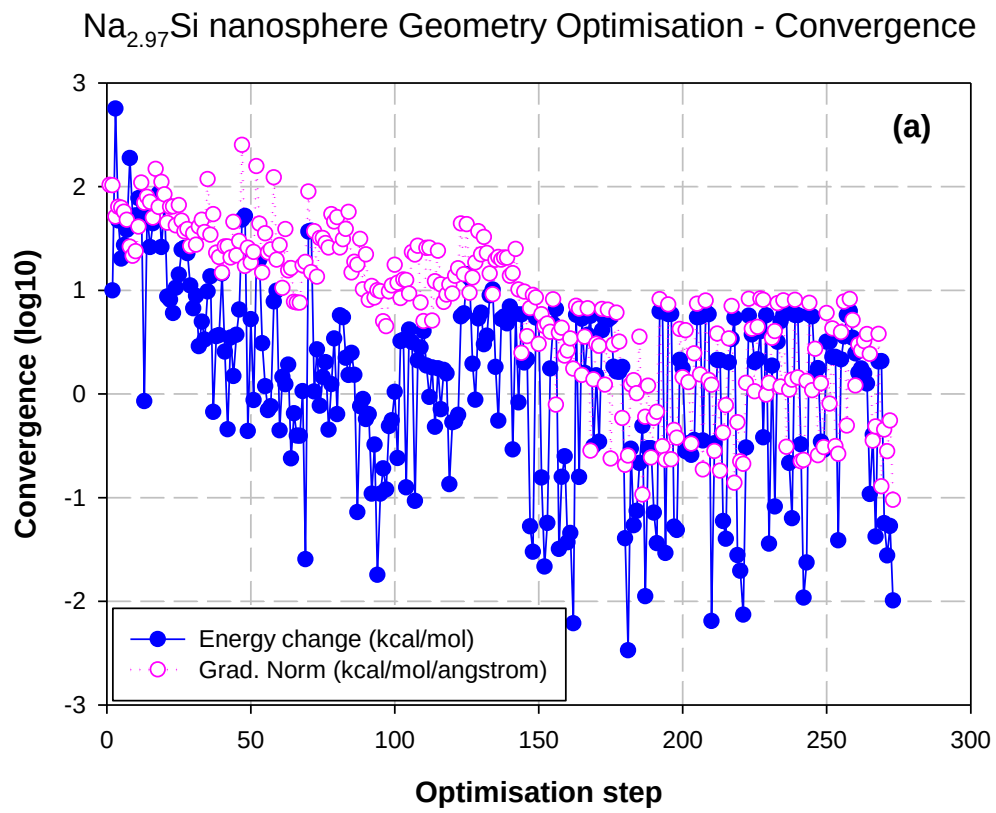

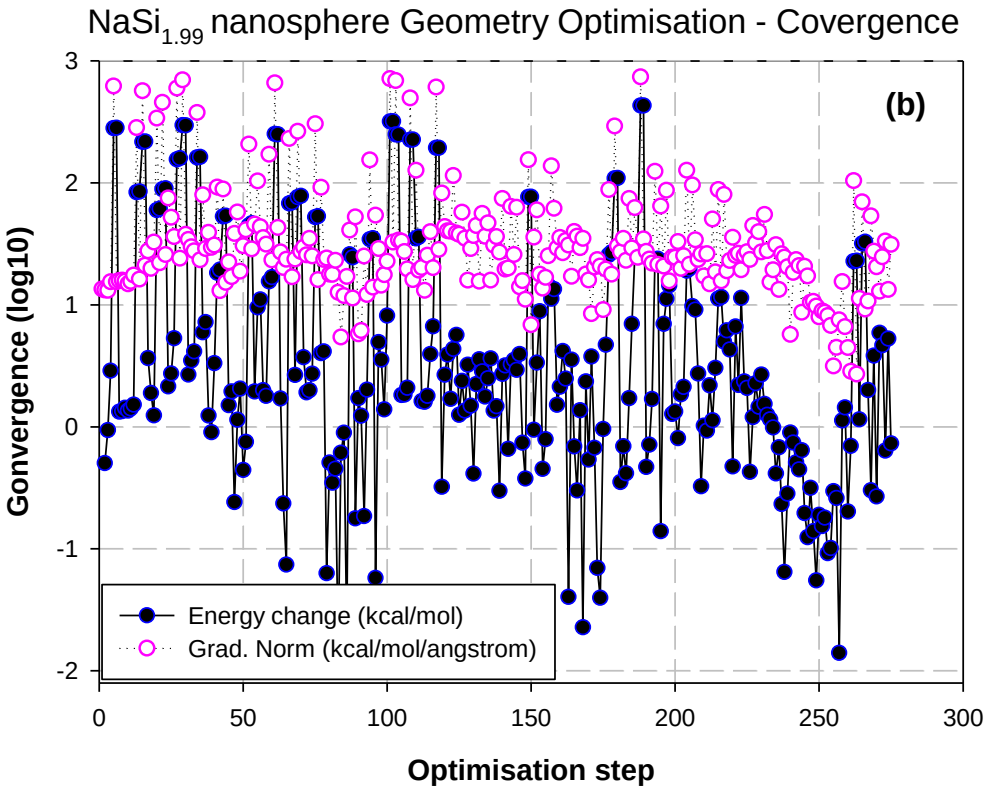

Figure 5-36. Convergence plots for (a) the $Na_{2.97}Si$ nanosphere at full optimisation and (b) $NaSi_{1.99}$ up to the 270th optimisation step obtained using the ABNR algorithm.

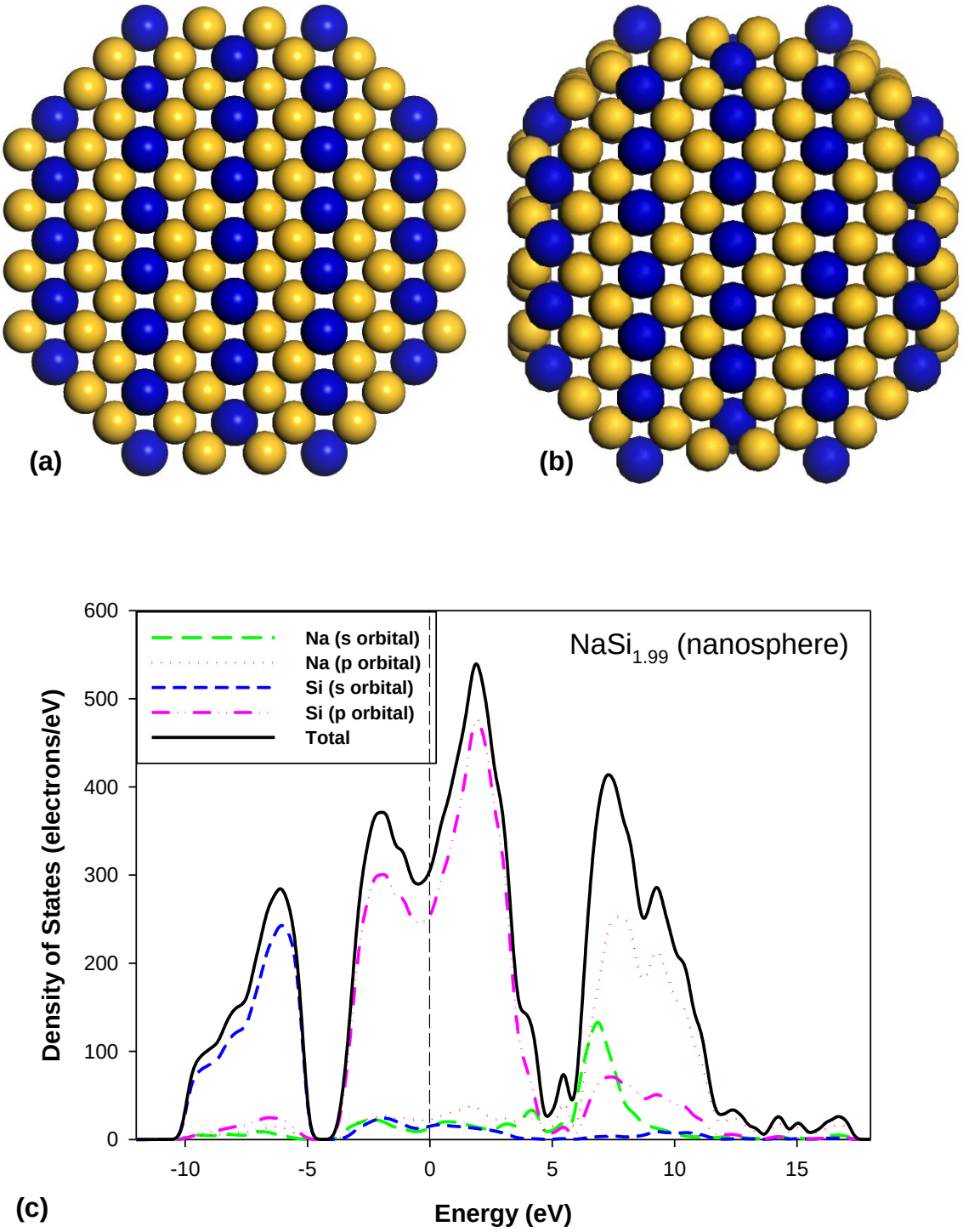

Figure 5-37. A graphic presentation of the (a) unrelaxed $NaSi_{1.99}$ nanosphere, (b) $NaSi_{1.99}$ nanosphere at 270th iteration of optimisation conducted using the ABNR algorithm and (c) the electronic partial density of states (PDOS) for the $NaSi_{1.99}$ nanosphere at the 270th step.

As reflected in Table 5-16, nanosphere models were generated from ground-state crystalline supercell structures and then optimised. It has already been illustrated with the $Na_{2.97}Si$ nanosphere that SCC-DFTB can be used to model systems of a nano-architecture. Table 5-16, brings to the fore, finer details that are worth noting to pave way for more progressive developments. Considering the data listed in the table for nanospheres it is noticeable that systems of more than 500 atoms were used. Also, it is indicated that several algorithms were employed. The $Na_{2.97}Si$ nanosphere was successfully brought to equilibrium by using the smart algorithm. Similar to the case of bulk crystalline structures, the volume changed marginally. Slight relative volume expansion of about 0.58% was perceived. However, relative to the contraction in the Na_3Si primary cell, it can be deduced that the systems generally contracted. Although it worked for the bulk crystalline structure over about 16 days, the smart algorithm was not able to bring the $NaSi_{1.99}$ nanosphere model consisting of a total of 637 atoms to convergence in the same duration. By noting the technicalities together with the model size, it became necessary to review the approach. To kick-start the optimisation process, the $NaSi_{1.99}$ was first treated with the steepest descent algorithm wherein the calculation was permitted a maximum of 100 steps. As shown in Figure 5-34, the energy was brought down and it began to level off from around the 60^{th} step. The steepest descent algorithm was able to localise the gradient norm around unity and bring the energy change closer to zero; however, all 100 steps were used. At the 100^{th} step, the nanosphere contracted by about 2.55% bringing the volume of the nanosphere to 13527.27 $\mathbf{Å^3}$**.** After treating the $NaSi_{1.99}$ nanosphere with the steepest descent algorithm, the ABNR algorithm was then used to continue the geometry optimisation process. The model was subjected to convergence criteria set such that the energy change should be below 0.02kcal/mol and a maximum permissible number of 10000 optimisation steps. The ABNR calculation on the nanosphere did not abruptly terminate but continued to run over a month, in addition to the time that had been spent using the steepest descent algorithm. The prolonged duration in an attempt to achieve convergence prompted a comparison of the behaviour exhibited the $NaSi_{1.99}$ to the $Na_{2.97}Si$ nanosphere. An intermediate model was extracted at the 270^{th} step; its convergence plots were inspected. Figures 5-35 and 5-36, illustrate that the calculation was nearing the set convergence, in that as seen in Figure 5-35 the energy begins to level off from

around the 225th step, and in Figure 5-36, it is apparent that the gradient norm of $NaSi_{1.99}$ is approaching unity whilst the energy change is approaching zero. In addition to the evaluation of the convergence plots, the electronic partial density of states was calculated. The graphic presentation of the $NaSi_{1.99}$ nanosphere at the 270th step compared to its unrelaxed state depicted in Figure 5-37 reflects a contraction. As demonstrated by the PDOS of the $NaSi_{1.99}$ nanosphere in Figure 5-37, a pseudogap exists in the vicinity of the Fermi level. The major contribution is witnessed to emanate from the p orbital of the Si atoms. The Fermi level falls within the pseudogap thus predicting structural stability. Furthermore, in a DFT study by Choe *et al* [185], contraction of a host lattice was reported in the sodiation of one of the orthorhombic TiO_2 phases. The contraction in the predicted Na-Si structures in this work suggests that further probing into the sodiation of nanospheres may be useful. However, what can be drawn from the exploration conducted herein is that the SCC-DFTB technique can be instrumental to the studies of nanostructures comprised of sizes that may be intractable for DFT.

Chapter 6 **Conclusion and Recommendations**

A computational materials science research workflow that uniquely combines several techniques including the Self-Consistent Density functional-based Tight Binding (SCC-DFTB) through the DFTB+ code, classical molecular dynamics technique via the Large-scale Atomic/Molecular Massively Parallel Simulator (LAMMPS), the density function theory (DFT) through the $DMol^3$ code and the machine-learning-powered cluster expansion approach embedded within the MedeA-UNiversal CLuster Expansion (UNCLE) simulation package has been presented. The approach and observations are summarised in the passages that follow.

The parameterisation of the approximate Self-Consistent Charge Density Functional-based Tight Binding (SCC-DFTB) for the Li-Si system has been presented. A procedural approach required for the successful development of Slater-Koster potentials has been shown. The configurations necessary to improve and refine the accuracy of the resulting parameter sets have been discussed. The SCC-DFTB parameter set in this work has been developed to handle environments that consist of Li-Li, Li-Si and Si-Si interaction pairs. The developed parameter set has been shown to produce good geometric properties of bulk Si, Li and LiSi in comparison to the reference DFT samples and available experimental values.

By conducting a molecular dynamics assessment on a silicon supercell, the parameter set has been demonstrated to handle a system of over 500 atoms at high temperatures. A trial to melt a 512 atom silicon system was done, and since the system was not melted in this work, in the future, a revised approach such as introducing a defect in one sub-lattice may be necessary. The molecular dynamics of the most lithium-rich phase of silicon, $Li_{22}Si_5$, was investigated on a crystalline primary unit cell consisting of a total of 432 atoms. This was done to demonstrate the ability of the developed SCC-DFTB parameter set to study the thermal properties of lithiated silicon systems. Despite having run the simulation over a short time, the radial distribution function of $Li_{22}Si_5$ at 550K was found to be consistent with the phase diagram of the Li-Si system.

The transferability of the parameter set has been assessed by calculating the lattice constants for known stable phases of the Li-Si system. The results were found to generally be within a margin of less than 8% difference, with some values such as that of the cubic $Li_{22}Si_5$ being less than 1% different from experiments. The set was shown to be compatible with various crystalline systems present on the Li-Si phase diagram. It was noted that the accuracy of the developed set can be further improved by fitting for polytypes of silicon, and by using hybrid functionals where applicable, to yield better electronic property estimates. Nonetheless, in comparison to the percentage difference range for the estimation of geometric properties of about 3.62% seen in literature [186], wherein SCC-DFTB was applied, the parameter set in the work herein is reasonably transferable because it handles a broad range of Li-Si phases although fitted to one.

A silicon system of a unit cell with 8 atoms was successfully lithiated to the maximum Li concentration. The expansion suggested by the theory was successfully modelled using the SCC-DFTB parameter set developed in this work. It was shown that silicon gradually expands in volume from 53.6% for LiSi phase which is composed of 50 *atm %* Li, to 261.57% for $Li_{15}Si_4$ with 78.95 *atm %* Li, and eventually shoots over 300% for $Li_{22}Si_5$ phase with the expansion at 316.45%, which is in agreement to experiments [162]. The Partial Density of States of the sampled lithiated systems were calculated to illustrate that the technique can be used to determine electronic properties as well.

The ability of the Li-Si SCC-DFTB parameter set to model the mechanical behaviour of Si was assessed by calculating the mechanical properties of pristine Si. A comparison of the calculated results to corresponding experimental values was presented. The parameter set was able to produce the mechanical properties of cubic Si (*Fd-3m*) to within a difference of 6% to the reference experimental values.

The set was further employed in modelling the volume expansion of amorphous silicon. A framework for generating amorphous silicon (*a*-Si) was presented. The expansion of *a*-Si as a result of lithiation with the 33 – 50 *atm* % Li was modelled. Consistent with experiments, it was illustrated that when Li was systematically inserted into *a*-Si model, *a*-Si linearly expanded with an increase in Li content. Unlike the *c*-Si system, wherein the Li-Si SCC-DFTB parameter set predicted the volume

expansion from 12.67% (for the $Li_{0.5}Si$) to 53.6% (for the Li_1Si) for the 33 – 50 *atm* % Li, *a*-Si exhibited a relative volume expansion that ranges from 6.59% (for $Li_{0.5}Si$) to 14.58% (for Li_1Si). Furthermore, using the electronic density of states analysis, the structural stability of the amorphous Li-Si alloys was examined.

As an alternative of Li for rechargeable batteries and as guided by interests reported in the available literature, the sodiation of Si was explored. Using knowledge and lessons learned from the Li-Si framework, the parameterisation of the approximate SCC-DFTB for the Na-Si was presented. The Na-Si SCC-DFTB parameter set was demonstrated to produce the equilibrium lattice parameters which agree with experiments to within 2.89% for Na (*Im-3m*), 3.75% for Si (*Fd-3m*), and 3.08% for NaSi (*Fd-3m*); which are structures that were used for during fitting. To test the transferability, three sodium silicide compounds of the clathrate crystal structure (i.e. the *Pm-3n* Na_8Si_{46}, the *Cmcm* $NaSi_6$ and *Fd-3m* $Na_{24}Si_{136}$) were geometrically optimised. With respect to the equilibrium lattice parameters, the Na-Si SCC-DFTB parameter set was shown to agree with experiments to within 4.14% for the cubic Na_8Si_{46} and 5.17% for the cubic $Na_{24}Si_{136}$. As for the orthorhombic $NaSi_6$, the ***a*** and ***b*** lattice parameters are in excellent agreement with experiments to within 0.61% and 0.27% respectively. However, the ***c*** parameter was overestimated by 14.24%.

By employing the approach used in modelling the Li insertion into silicon, the sodiation of *c*-Si was modelled. It was predicted that *c*-Si expands by over 400% at 77 *atm* % Na and shoots above 500% for concentrations exceeding 80 *atm* % of Na. A comparison between how *c*-Si expands as a result of lithiation to the expansion consequent to sodiation was done. For concentrations ranging from 66.6 - 81.4 *atm* %, *c*-Si was seen to expand by at least twice as much when sodiated than when lithiated. Hence, implying that *c*-Si may not be suitable for Na-ion batteries. As a test, the ability of the Na-Si SCC-DFTB parameter to handle complex geometries was shown by modelling the expansion a-Si at 33 *atm* % Na. It was perceived that at this concentration, *a*-Si expanded 6 times less than when *c*-Si was used. Hence, suggesting that *a*-Si would be more preferable for Na-ion batteries. In comparing the sodiation of *a*-Si to the lithiation of *a*-Si at 33 *atm* %, due to sodium's larger atomic and ionic radii, *a*-Si expanded to 15.89% for Na, whereas for Li the volume expansion was 6.58%. Despite the 15.89% volume expansion, the PDOS of the amorphous $Na_{0.5}Si$ (corresponding the 33 *atm* % Na) predicted the structure to be

stable since the Fermi level was located within a pseudogap. Using the Li-Si and the Na-Si SCC-DFTB parameter sets, it was illustrated that amorphisation appears to lower the magnitude by which Si expands, therefore agreeing with experiments in that amorphous structures are reported to exhibit a buffering effect towards volume expansion.

The material space for the Li-Si system was explored through a ground-state crystal structure prediction conducted through cluster expansion. Using the FCC and BCC parent lattice in the grid search, 12 thermodynamically stable Li-Si alloys were predicted by the genetic algorithm, *viz*. the trigonal Li_4Si (*R-3m*), tetragonal Li_4Si (I4/m), tetragonal Li_3Si (*I4/mmm*), cubic Li_3Si (*Fm-3m*), monoclinic Li_2Si_3 (*C2/m*), trigonal Li_2Si (*P-3m1*), tetragonal LiSi (P4/mmm), trigonal $LiSi_2$ (*P-2m1*), monoclinic $LiSi_3$ (*P2/m*), cubic $LiSi_3$ (*Pm-3m*), tetragonal LiSi4 (I4/m) and monoclinic $LiSi_4$ (*C2/m*). Among the twelve alloys, five [*viz.* LiSi, Li_4Si (*I4/m* & *R-3m*), $LiSi_4$, Li_3Si] of the structures were consistent with the predictive work by Zhang *et al* [175], in which a particle swarm-intelligence-based code, CALYPSO [176] was used.

The structural stabilities of the predicted Li-Si alloys were studied. It was demonstrated that with the introduction of external pressure, the stability of some structures can be improved. For some structures such as the lithium-rich phase, Li_4Si (*R-3m*), the shape of the bands on the electronic partial density of states graph did not significantly change for pressures ranging from 0 – 25GPa. Hence, the Li_4Si (*R-3m*) phase was predicted to globally maintain its structural stability with the range 0 – 25GPa. In studying the PDOS, the Li_4Si (*I4/m*) was noted to be more stable at 40GPa and 45GPa, which is consistent with the prediction made by Zhang *et al* [175].

Using the insights acquired based on the Li-Si framework in which the SCC-DFTB method was combined with cluster expansion, a test for exploring the Na-Si material space was done. Besides the pristine Na (*Fm-3m*) and Si (*Fm-3m*) systems, three thermodynamically stable Na-Si alloys (*i.e.* the *I4/mmm* Na_3Si, *P4/nmm* NaSi and *Immm* $NaSi_2$) were predicted from a grid search that used the FCC parent lattice and considered structures with up to 16 basis atoms. Using Na-Si SCC-DFTB parameters developed in this work, a correlation of the total DOS in the vicinity of the Fermi level depicted on PDOS graphs, the structural stabilities of the three Na-Si

were further evaluated. NaSi (*P4/nmm*) was shown to be unstable at 0GPa, $NaSi_2$ (Immm) was found to be stable and the Na-rich Na_3Si phase was noted to exhibit metastability. Upon application of external pressure ranging from 2.5 – 25GPa on Na_3Si, the Fermi level was seen to move into a pseudogap, hence suggesting that Na_3Si (*I4/mmm*) would be a high-pressure phase.

Expanding on the groundwork laid from the cluster expansion for the Li-Si and Na-Si alloys, the Mg-Si system was tested through the cluster expansion technique to illustrate that the approach can be used to rapidly screen a variety of materials. The ground-state crystal structure search predicted 4 thermodynamically stable Mg-Si alloys; and they are Mg_3Si (*Pm-3m*), MgSi (*P4/mmm*), $MgSi_2$ (*Immm*) and $MgSi_3$ (*Pmmm*).

Lastly, candidate electrode materials with nano-architectural features were simulated by means of designing nanospheres from the predicted Li-Si and Na-Si crystal structures. The simulated nanoparticles were composed of more than 500 atoms, the supercell models from which the nanospheres were designed consisted of up to 1000 atoms. The crystal structures of these large systems were brought to equilibrium through geometry optimizations carried out using a DFTB-based code. Hence, the ability of the SCC-DFTB approach to handle large systems compared to DFT was demonstrated. The stability of the nanospheres was examined, and the link between SCC-DFTB to cluster expansion was established. The workflow present in this work paves the way to rapid material discovery, that is highly sought in the era of the fourth industrial revolution, to address and meet energy demands that are consequent to digital transformations as well as the birth of new technologies.

Recommendations:

The results presented in this work show great promise towards the further development of models and studies conducted through SCC-DFTB parameterisation. With just a few adjustments to the parameterisation framework presented herein, several studies which are important for the promotion of the successful design of high energy density electrodes in rechargeable batteries can be conducted. Furthermore, Cao *et al* [187] presented a review of the cluster expansion formalism and demonstrated how machine learning improves the predictive accuracy

cluster expansion. The work also illustrated the ability of the cluster expansion technique to predict surfaces and nanostructured materials. Hence, these aspects strengthen the workflow proposed in this work.

According to literature, the scientific community is exploring the use of systems consisting of silicon nanostructures [188], amorphous silicon systems [189], and the use of carbon composites [190] to improve electrode performance. The nanostructured silicon and nano-composites of Si-based electrodes are reported to exhibit the potential to overcome the volume expansion and poor cyclability in lithiated Si. The potential success is generally attributed to their many open channels which act as ideal expansion buffers. The composites are also seen to exhibit the capacity to withstand the stress induced by the anisotropic volume changes in Si, and yield improved electrochemical performances.

Although these features are interesting, the effect of the microstructure of lithiated nanostructured Si, together with its evolution from crystal to amorphous structure on the electrochemical performance of Li-ion batteries remains unclear. The mechanical integrity of electrode materials is important for battery performance and needs further exploration. Thus, based on the findings in this work, the following are recommended:

- The development of refined Li-Si and Na-Si SCC-DFTB parameters to model the mechanical behaviour of Li-Si and Na-Si alloys.
- Employ molecular dynamics using SCC-DFTB to study temperature effects.
- Use cluster expansion to predict properties of surfaces and nanostructures based on the Na-Si system, and to screen viable composite structures.
- Explore the use of SCC-DFTB to model charging and discharging in amorphous nanospheres

REFERENCES

[1] B. Scrosati, J. Garche. (2010). Lithium batteries: Status, prospects and future. *J. Power Sources , 195*, 2419-2430.

[2] P. Taheri, S. Hsieh, M. Bahrami. (2011). Investigating electrical contact resistance losses in lithium-ion battery assemblies for hybrid and electric vehicles. *J. Power Sources , 196*, 6525-6533.

[3] U. S. Kim, C. B. Shin, C. -S. Kim. (2009). Modeling for the scale-up of a lithium-ion polymer battery. *J. Power Sources , 189*, 841-846.

[4] A. Daemmrich. (2017). Invention, Innovation Systems, and The Fourth Industrial Revolution. *Technol. Innov. , 18*, 257 - 265.

[5] L. Guoping, H. Yun, W. Aizhi. (2017). Fourth Industrial Revolution: Technological Drivers, Impacts and Coping Methods. *Chin. Geogra. Sci. , 27*, 626 - 637.

[6] M. Lee, J. J. Yun, A. Pyka, D. Won, F. Kodama, G. Schiuma, H. Park, J. Jeon, K. Park, K. Jung; M. Yan, S. Lee, X. Zhao. (2018). How to Respond to the Fourth Industrial Revolution, or the Second Information Technology Revolution? Dynamic New Combinations Between Technology, Market, and Society through Open Innovation. *J. Open Innov. Technol. Mark. Complex. , 4*, 21: 1 - 24.

[7] H. Okamoto. (1990). The Li-Si (Lithium-Silicon) System. *Bull. of Alloy Phase Diagr.* , 306-312.

[8] J. Evers, G. Oehlinger, G. Sextl. (1993). High-pressure synthesis of LiSi: three-dmensional network of three-bonded Si- ions. *Angew. Chem. Int. Ed. Engl. , 32*, 1442-1444.

[9] L. A. Stearns, J. Gryko, J. Diefenbacher, G. K. Ramachandran, P. F. McMillane. (2003). Lithium monosilicide (LiSi), a low-dimensional silicon-based material prepared by high pressure synthesis: NMR and vibrational spectroscopy and electrical properties characterization. *J. Solid State Chem. , 173*, 251-258.

[10] M. Zeilinger, D. Benson, U. Haussermann, T. F. Fassler. (2013). Single crystal growth and thermodynamic stability of $Li_{17}Si_4$. *Chem. Mater. , 25*, 1960-1967.

[11] R. Ramirez, R. Nesper, H. G. von Schnering. (1986). The electronic structure of crystalline $Li_{21}Si_5$. *Z. Naturforsch , 41a*, 1267-1282.

[12] R. Nesper, H. G. von Schnering. (1987). $Li_{21}Si_5$, a zintle phase as well as a hume-rothery phase. *J. Solid State Chem. , 70*, 48-57.

[13] U. Frank, W. Miller, H. Schaefer. (1975). On the Phase $Li_{13}Si_4$. *Z. Naturforsch B , 30*, 10-13.

[14] S. Dupke, T. Langer, R. Pottgen, M. Winter, H. Eckert. (2012). Structural and dynamic characterization of $Li_{12}Si_7$ and $Li_{12}Ge_7$ using Sold State NMR. *Solid State Nucl. Magn. Reson. , 42*, 17-25.

[15] V. L. Chevrier, J. W. Zwanzinger, J. R. Dahn. (2010). First principles study of Li-Si phases: charge transfer, electronic structure, and lattice vibrations. *J. Alloys Compd. , 496*, 25-36.

[16] M. Gu, Z. Wang, J. G. Connell, D. E. Perea, L. J. Lauhon, F. Gao, C. Wang. (2013). Electronic origin for the phase transition from amorphous Li_xSi to crystalline Li15Si4. *ACS Nano* , 6303-6309.

[17] R. A. Huggins. (1999). Lithium alloy negative electrodes. *J. Power Sources , 13*, 81-82.

[18] B. Böhm, W. Klemm. (1939). Zur Kenntnls des Verhaltens der Alkalimetalle zueinander. *Z. anorg. allg. Chem. , 243*, 69 - 85.

[19] D. N. Batchelder, R.O. Simmons. (1964). Lattice Constants and Thermal Expansivities of Silicon and of Calcium Fluoride between 6° and 322°K. *J. Chem. Phys.* , 2324 - 2329.

[20] J. Witte, H. G. Von Schnering, W. Klemm. (1964). Das Verhalten der Alkalimetalle zu Halbmetallen. XI. Die Kristallstruktur von NaSi und NaGe. *Z. anorg. allg. Chem. , 327*, 260 - 273.

[21] J. Sangster, A. D. Pelton. (1992). The Na-Si (Sodium-Silicon) System. *J. Phase Equilib. , 13*, 67-69.

[22] O. O. Kurakevych, T. A. Strobel, D. Y. Kim, T. Muramatsu, V. V. Struzhkin. (2013). Na-Si clathrates are high-pressure phases: A melt-based route to control stoichiometry and properties. *Crys. Growth Des. , 13*, 303 - 307.

[23] M. Beekman, M. Baitinger, H. Borrmann, W. Schnelle, K. Meier, G. S. Nolas, Y. Grin. (2009). Preparation and Crystal Growth of $Na_{24}Si_{136}$. *J. Am. Chem. Soc. , 131*, 9642 - 9643.

[24] M. Beekman, E. N. Nenghabi, K. Biswas, C. W. Myles, M. Baitinger, G. S. Nolas. (2010). Framework contraction in Na-stuffed Si(cF136). *Inorg. Chem. (12) , 49*, 5338 - 5340.

[25] K. I. Ramachandran, G. Deepa, K. Namboori. (2008). *Computational Chemistry and Molecular Modeling, Principles and Applications* (1st ed.). Berlin, Germany: Springer-Verlag Berlin Heidelberg.

[26] N. Attig, P. Gibbon, Th. Lippert. (2011). Trends in supercomputing: The European path to exascale. *Comput. Phys. Commun. , 182*, 2041 - 2046.

[27] K. Ohno, K. Esfarjani, Y. Kawazoe. (2018). *Computational Materials Science: From Ab Initio to Monte Carlo Methods* (2nd ed.). Berlin, Germany: Springer-Verlag GmbH, part of Springer Nature.

[28] Weinan, E. (2011). *Principles of Multiscale Modeling* (1st ed.). Cambridge: Cambridge University Press.

[29] M. Elstner, G. Seifert. (2014). Density functional tight binding. *Phil. Trans. R. Soc. A , 372*, 20120483: 1-12.

[30] R. Jose, S. Ramakrishna. (2018). Materials 4.0: Materials big data enabled materials discovery. *Appl. Mater. Today , 10*, 127 - 132.

[31] A. Fernández, C. Fernández, J. Á. Miguel-Dávilab, M. Á. Condeb, V. Matellán. (2019). Supercomputers to improve the performance in higher education: A review of the literature. *Comput. Educ. , 128*, 353 - 364.

[32] T. Sterling, M. Anderson, M. Brodowicz. (2018). *High Performance Computing, Modern Systems and Practices.* Cambridge, United States: Morgan Kaufmann.

[33] H. Zhang, M. Diehl, F. Roters, D. Raabe. (2016). A virtual laboratory using high resolution crystal plasticity simulations to determine the initial yield surface for sheet metal forming operations. *Int. J. Plast.* , 111 - 138.

[34] C. Li, Y. Jiang, P. Fang. (2019). Innovation in Advanced Manufacturing Driven By Supercomputing. *Procedia CIRP , 83*, 584 - 589.

[35] T. M. Mitchell. (1999). Machine learning and data mining. *Commun Acm , 42*, 31 - 36.

[36] Y. Liu, T. Zhao, W. Ju, S. Shi. (2017). Materials discovery and design using machine learning. *J. Materiomics , 3*, 159 - 177.

[37] J. Schmidt, M. R. Marques, S. Botti, M. A. L. Marques. (2019). Recent advances and applications of machine learning in solid state materials. *npj Comput. Mater. , 5*, 83: 1-36.

[38] J. Wei, X. Chu, X.-Y. Sun, K. Yun, H.-X. Deng, J. Chen, Z. Wei, M. Lei. (2019). Machine learning in materials science. *InfoMat , 1*, 335 - 358.

[39] R. K. Vasudevan, K. Choudhary, A. Mehta, R. Smith, G. Kusne, F. Tavazza, L. Vleck, M. Ziatdinov, S. V. Kalinin, J. Hattrick-Simpers. (2019). Materials science in the artificial intelligence age: high-throughput library generation, machine learning, and a pathway from correlations to the underpinning physics. *MRS Commun. , 9*, 821 - 838.

[40] J. J. Möller, W. Körner, G. Krugel, D. F. Urban, C. Elsässer. (2018). Compositional optimization of hard-magnetic phases with machine-learning models. *Acta Materialia , 153*, 53 - 61.

[41] J. Jung, J. I. Yoon, H. K. Park, J. Y. Kim, H. S. Kim. (2019). An efficient machine learning approach to establish structure-property linkages. *Comput. Mater. Sci. , 156*, 17 - 25.

[42] A. Cecen, H. Dai, Y. C. Yabansu, S. R. Kalidini, L. Song. (2018). Material structure-property linkages using three-dimensional convolutional neural networks. *Acta Materialia , 146*, 76 - 84.

[43] C. Wen, Y. Zhang, C. Wang, D. Xue, Y. Bai, S. Antonov, L. Dai, T. Lookman, Y. Su. (2019). Machine learning assisted design of high entropy alloys with desired property. *Acta Materialia , 170*, 109 - 117.

[44] N. Artrith, A. Urban, G. Ceder. (2018). Constructing first-principles phase diagrams of amorphous Li_xSi using machine-learning-assisted sampling with an evolutionary algorithm. *J. Chem. Phys. , 148*, 241711: 1-8.

[45] J. E. Mayer, E. Montroll. (1941). Mollecular distribution. *J. Chem. Phys. , 9*, 2 - 16.

[46] Q. Wu, B. He, T. Song, J. Gao, S. Shi. (2016). Cluster expansion method and its application in computational materials science. *Comput. Mater. Sci. , 125*, 243-254.

[47] S. Muller. (2003). Bulk and surface ordering phenomenoa in binary metal alloys. *J. Phys.: Condens. Matter , 15*, R1429-R1500.

[48] T. Nagaura, K. Tozawa. (1990). Lithium ion rechargeable battery. *Prog. Batt. Sol. Cells , 9*, 209-217.

[49] J. M. Tarascon. (2010). Key challenges infuture Li-battery research. *Phys. Trans. R. Soc. A , 368*, 3227-3241.

[50] M. Verbrugge, E. Tate. (2004). Adaptive state of charge algorithm for nickel metal hydride batteries including hysteresis phenomena. *J. Power Sources , 126*, 236-249.

[51] P. Taheri, M. Bahrami. (2012). Temperature rise in prismatic polymer lithium-ion batteries: an analytic approach. *SAE Int. J. Passeng. Cars - Electron. Electr. Syst. , 5*, 0334-13.

[52] G. -H. Kim, K. Smith, J. Ireland, A. Pesaran. (2012). Fail-safe design for large capacity lithium-ion battery systems. *J. Power Sources , 210*, 243-253.

[53] G. G. Amatucci, C. N. Schmutz, A. Blyr, C. Sigala, A. S. Gozdz, D. Larcher, J. M. Tarascon. (1997). Materials' effects on the elevated and room temperature performance of $C/LiMn_2O_4$ Li-ion batteries. *J. Power Sources , 69*, 11-25.

[54] V. Ramadesigan, P. W. C. Northrop, S. De, S. Santhanagopalan, R. D. Braatz, V. R. Subramanian. (2012). Modelling and simualtion of lithium-ion batteries from a systems engineering perspective. *J. Electrochem. Soc. , 159*, R31-R45.

[55] T. M. Kumar, T. S. D. Kumari, A. M. Stephan. (2009). Carbonaceous anode materials for lithium-ion batteries - the road ahead. *J. Indian Inst. Sci. , 89*, 393-424.

[56] B. Scrosati. (2000). Recent adavances in lithium battery materials. *Electrochim. Acta , 45*, 2461-2466.

[57] A. K. Shukla, T. P. Kumar. (2008). Materials for next-generation lithium batteries. *Curr. Sci. , 94*, 314-331.

[58] J. Chen, L. Yang, S. Fang, Y. Tang. (2010). Synthesis of sawtooth-like $Li_4Ti_5O_{12}$ nanosheets as anode materials for Li-ion batteries. *Electrochim. Acta , 55*, 6656-6600.

[59] A. N. Dey. (1971). Electrochemical alloying of lithium in organic electrolytes. *J. Electrochem. Soc , 118*, 1547-1549.

[60] W. -J. Zhang. (2011). A review of the electrochemical performance fo alloy anodes for lithium batteries. *J. Power Sources , 196*, 13-24.

[61] P. R. Shearing, N. P. Brandon, J. Gelb, R. Bradely, P. J. Withers, A. J. Marquis, S. Copper, S. J. Harris. (2012). Multi length scale microstuctural investigations of a commercially available Li-ion battery electrode. *J. Electrochem. Soc. , 159*, A1023-A1027.

[62] G. B. Less, J. H. Seo, S. Han, A. M. Sastry, J. Zausch, A. Latz, S. Schmidt, C. Wieser, D. Kehrwald, S. Fell. (2012). Mirco-scale modelling of Li-ion batteries: parameterization and validation. *J. Electrochem. Soc. , 159*, A697-A704.

[63] T. Hutzenlaub, S. Thiele, R. Zengerle, C. Ziegler. (2012). Three-dimensional reconstruction of a $LiCoO_2$ Li-ion battery cathode. *Electrochem. Solid-State Lett. , 15*, A33-A36.

[64] P. G. Bruce. (2008). Energy storage beyond the horizon: Rechargeable lithium batteries. *Solid State Ion. , 179*, 752-760.

[65] H. Wu, Y. Cui. (2012). Designing nanostructured Si anodes for high energy lithium ion batteries. *Nano Today , 7*, 414-429.

[66] H. Zhao, C. Jiang, X. He, J. Ren, C. Wan. (2008). Preparation of micro-porous membrane electrodes and their application in preparing anodes of rechargeable lithium batteries. *J. Membrane Sci. , 310*, 1-6.

[67] G. Centi; S. Peranthoner. (2010). Problems and perspectives in nanostructured carbon-based electrodes for clean and sustainable energy. *Catal. Today , 150*, 151-162.

[68] W. Wang, P. N. Kumta. (2007). Reversible high capacity nanocomposite anodes of Si/C/SWNTs for rechargeable Li-ion batteries. *J. Power Sources , 172*, 650-658.

[69] R. R. Zhao, G. Z. Ma, L. C. Zhu, A. J. Li, H. Y. Chen. (2012). An improved carbon-coating method for $LiFePO_4$/C composite derived from Fe^{3+} precursor. *Int. J. Electrochem. Sci. , 7*, 10923-1092.

[70] S. W. Oh, S. -T. Myung, S. -M. Oh, K. H. Oh, K. Amine, B. Scrosati, Y. -K. Sun. (2010). Double carbon coating of $LiFePO_4$ as high rate electrode for rechargeable lithium batteries. *Adv. Mater. , 22*, 4842-4845.

[71] K. Wang, R. Cai, T. Yuan, X. Yu, R. Ran, Z. Shao. (2009). Process investigation, electrochemical characterization and optimization of $LiFePO_4$/C composite from mechanical activiation using sucrose as carbon source. *Electrochim. Acta , 54*, 2861-2868.

[72] J. D. Wilcox, M. D. Deoff, M. Marcinek, R. Kostecki. (2007). Factors influencing the quality of carbon coatings $LiFePO_4$. *J. Electrochem. Soc. , 154*, A389-A395.

[73] N. Dimov, S. Kugino, M. Yoshio. (2003). Carbon-coated silicon as anode material for lithium ion bateries: Advantages and limitations. *Electrochim. Acta , 48*, 1579-1587.

[74] J. Guo, X. Chen, C. Wang. (2010). Carbon scaffold structured silicon anodes for lithium-ion batteries. *J. Mater. Chem. , 20*, 5035-5040.

[75] J. Saint, M. Morcrette, D. Larcher, l. Laffont, S. Beattie, J. -P. Peres, D. Talaga, M. Couzi, J. -M. Tarascon. (2007). Towards a fundamental understanding of the

improved electrochemical performance of silicon-carbon composites. *Adv. Funct. Mater. , 17*, 1765-1774.

[76] J. Yang, M. Winter, J. O. Besenhard. (1996). Small particle size multiphase Li-alloy anodes for lithium-ion-batteries. *Solid State Ion. , 90*, 281-287.

[77] J. Yang, Y. Takeda, N. Imanishi, T. Ichikawa, O. Yamamoto. (2000). $SnSb_x$-based composite electrodes for lithium ion cells. *Solid State Ion. , 135*, 175-180.

[78] J. Wolfenstine. (2003). $CaSi_2$ as an anode for lithium-ion batteries. *J. Power Sources , 124*, 241-245.

[79] N. Ding, J. Xu, Y. Yao, G. Wegner, I. Lieberwirth, C. Chen. (2009). Improvement of cyclability of Si as anode for Li-ion batteries. *J. Power Sources , 192*, 644-651.

[80] J. Li, H. M. Dahn, L. J. Krause, D. -B. Le, J. R. Dahn. (2008). Impact of binder choice on the performance of α-Fe_2O_3 as a negative electrode. *J. Electrochem. Soc. , 115*, A812-A816.

[81] J. Li, R. R. Lewis, J. R. Dahn. (2007). Sodium carboxymethyl cellulose a potential binder for Si negative electrodes for Li-ion batteries. *Electrochem. Solid-State Lett. , 10*, A17-A20.

[82] N. Ding, J. Xu, Y. X. Yao, G. Wegner, X. Fang, C. H. Chen, I. Lieberwirth. (2009). Determination of the difussion coefficient of lithium ions in nano-Si. *Solid State Ion. , 180*, 222-225.

[83] H. Jung, M. Park, Y. G. Yoon, G. B. Kim, S. K. Joo. (2003). Amorphous silicon anode for lithium-ion rechargeable batteries. *J. Power Sources , 115*, 346-351.

[84] M. N. Obrovac, L. Christensen. (2004). Structural changes in silicon anodes during lithium insertion/extraction. *Electrochem. Solid-State Lett. , 7*, A93-A96.

[85] J. Shu, M. Shui, D. Xu, D. Wang. (2012). A comparative study of overdischarge behaviours of cathode materials for lithium-ion batteries. *J. Solid State Electrochem. , 16*, 819-824.

[86] Y. Qin, T. Feng, Z. Li, Z. Sun. (2011). Structural, optical and electrical properties of amorphous silicon thin fiilms prepared by sputtering with different targets. *App. Surf. Sci. , 257*, 7993-7996.

[87] T. Takamura, S. Ohara, M. Uehara, J. Suzuki, K. Sekine. (2004). A vacuum deposited Si film having a Li extraction capacity over 2000 mAh/g with a long cycle life. *J. Power Sources , 129*, 96-100.

[88] J. M.Tarascon. (2010). Is lithium the new gold? *Nat. Chem. , 2*, 510.

[89] A. Sonoc, J. J. (2014). A review of lithium supply and demand and a preliminary investigation of a room temperature method to recylce lithium ion batteries to recover lithium and other materials. *Procedia CIRP , 15*, 289-293.

[90] K. M. Abraham. (1982). Intercalation positive electrodes for rechargeable sodium cells. *Solid State Ion. , 7* (3), 199-212.

[91] Z. Lan, M. Chen, X. Xu, C. Xiao, F. Wang, Y. Lu, Y. Jiang, J. Jiang. (2017). Investigations on molybdenum dinitride as a promising anode material for Na-ion batteries from first-principle calculations. *J. Alloys Compd. , 702*, 875-881.

[92] J. Cui, S. Yao, J. -K Kim. (2017). Recent progress in rational design of anode materials for high-performance Na-ion batteries. *Energy Storage Mater. , 7*, 64-114.

[93] K. Nejati, A. Hosseinian, L. Edjilali, E. Vessally. (2017). The effect of structural curvature on the cell voltage of BN nanotube based Na-ion batteries. *J. Mol. Liq. , 229*, 167-171.

[94] E. Edison, R. Satish, W. C. Ling, N. Bucher, V. Aravindan, S. Madhavi. (2017). Nanostructured intermetallic $FeSn_2$-carbonaceous composites as highly stable anode for Na-ion batteries. *J. Power Source , 343*, 296-302.

[95] S. C. Jung, D. S. Jung, J. W. Choi, Y. -K. Han. (2014). Atom-level understanding of the sodiation process in silicon anode material. *J. Phys. Chem. Lett. , 5*, 1283-1288.

[96] C. -H. Lim, T. -Y. Huang, P. -S. Shao, J. -H. Chien, Y. -T. Weng, H. -F. Huang, B. J. Hwang, N. -L. Wu. (2016). Exerimental study on sodiation of amorphous silicon for use as sodium-ion battery anode. *Electrochim. Acta , 211*, 265-272.

[97] S. Aladinli, F. Bordet, K. Ahlbrecht, J. Tubke. (2017). Compositional graphitic cathode investigation and structural characterization tests for Na-based dual-ion battery applications using ethylene carbonate: ethyl methyl carbonate-based electrolyte. *Electrochem. Acta , 228*, 503-512.

[98] J. C. Slater, G. F. Koster. (1954). Simplified LCAO method for the periodic potential problem. *Phys. Rev. , 94*, 1498-1524.

[99] S. L. Candelaria, Y. Shao, W. Zhou, X. Li, J. Xia, J. -G. Zhang, Y. Wang, J. Liu, J. Li, G. Cao. (2012). Nanostructuresd carbon for energy storage and conversion. *Nano Energy , 1*, 195-220.

[100] D. Fautex, R. Koksbang. (1993). Rechargeable lithium battery anode: Alternatives to metallic lithium. *J. Appl. Electrochem. , 34*, 1-10.

[101] S. D. Beattie, D. Larcher, M. Mocrette, B. Simon, J. M. Tarascon. (2008). Si electrode for Li-ion batteries - A new way to look at an old problem. *J. Electrochem. Soc. , 155*, A158-A163.

[102] L. Y. Beaulieu, K. W. Eberman, R. L. Turner, L. J. Krause, J. R. Dahn. (2001). Colossal reversible volume changes in lithium alloys. *Electrochem. Solid-State Lett. , 4*, A137-A140.

[103] W. Kohn, L. J. Sham. (1965). Self-consistent equations including exchange and correlation effects. *Phys. Rev. , 140*, A1133-A1138.

[104] B. Aradi, B. Hourahine, Th. Frauenheim. (2007). DFTB+, a sparse matrix-based implementation of the DFTB method. *J. Phys. Chem. A , 111*, 5678-5684.

[105] *BIOVIA Materials Studio* | *Material Modeling & Simulation Software Application*. (n.d.). Retrieved December 08, 2016, from Accelrys Web site: http://accelrys.com/products/collaborative-science/biovia-materials-studio/

[106] D. Lerch, O. Wieckhorst, G. L. Hart, R. W. Forcade, S. Muller. (2009). UNCLE: a code for constructing cluster expansions for arbitrary lattices with minimal user-input. *Modelling Simul. Mater. Sci. Eng. , 17*, 0550003: 1-19.

[107] M. C. Payne, D. C. Allan, T. A. Arias, J. D. Joannopoulos. (1992). Iterative minimization techniques for ab inito total-energy calculations: molecular dynamics and conjugate gradients. *Rev. Mod. Phys. , 64*, 1045-1097.

[108] P. Hohenberg, W. Kohn. (1964). Inhomogeneous electron gas. *Phys. Rev. , 136*, B864-B871.

[109] A. E. Mattsson, P. A. Schultz, M. P. Desjarlais, T. R. Mattsson, K. Leung. (2005). Designing meaningful density functional theory calculations in materials science - a primer. *Modelling Simul. Mater. Sci. Eng. , 13*, R1-R31.

[110] J. P. Perdew, A. Zunger. (1981). Self-interaction correction to density-functional approximations for many-electron systems. *Phys. Rev. B , 23*, 5048-5079.

[111] J. P. Perdew, Y. Wang. (1992). Accurate and simple analytical represention of the electron-gas correlation energy. *Phys. Rev. B , 45*, 13244-13249.

[112] J. P. Perdew, K. Burke, M. Ernzerhof. (1996). Generalized gradient approximation made simple. *Phys. Rev. Lett. , 77*, 3865-3868.

[113] J. P. Perdew, J. A. Chevary, S. H. Vosko, K. A. Jackson, M. R. Pederson, D. J. Singh, C. Fiolhais. (1992). Atoms, molecules, solids, and surfaces: applications of the generalized approximation for exchange and correlation. *Phys. Rev. B , 46*, 6671-6687.

[114] A. D. Becke. (1988). Density-functional exchange-energy approximation with correct asymptotic behavior. *Phys. Rev. A , 38*, 3098-3100.

[115] C. Lee, W. Yang, R. G. Parr. (1988). Development of the Colle-Salvetti correlation-energy formula into a functional of the electron density. *Phys. Rev. B , 37*, 785-789.

[116] G. Seifert, J. -O. Joswig. (2012). Density-functional tight binding - an approximate density-functional theory method. *WIREs Comput. Mol. Sci. , 2*, 456-465.

[117] C. M. Goringe, D. R. Bowler, E. Hernandez. (1997). Tight-binding modelling of materials. *Rep. Prog. Phys. , 60*, 1447-1512.

[118] N. Zonias, P. Lagoudakis, C. -K. Skylaris. (2010). Large-scale first principles and tight-binding functional theory calculations on hydrogen-passivated silicon nanorods. *J. Phys. Condens. Matter , 22*, 025303: 1-10.

[119] C. M. Maupin, B. Aradi, G. A. Voth. (2010). The self-consistent charge density functional tight binding method applied to liquid water and the hydrated excess proton: Benchmark simualtions. *J. Phys. Chem. B , 114*, 6922-6931.

[120] D. Porezag, T. Frauenheim, T. Kohler, G. Seifert, R. Kaschner. (1995). Construction of tight-binding potentials on the basis of density functional theory: Application to carbon. *Phys. Rev. B , 51*, 12947-12957.

[121] M. Elstner, D. Porezag, G. Jungickel, J. Elstner, M. Haugk, S. Suhai, G. Seifert, T. Frauenheim. (1998). Self-consistent-charge density-functional tight-binding method for simulations of complex materials properties. *Phys. Rev. B , 58*, 7260-7268.

[122] C. Kohler, G. Seifert, U. Gerstmann, M. Elstner, H. Overhof, T. Frauenheim. (2001). Approximate density-functional calculations of spin density density in large molecular systems and complex solids. *Phys. Chem. Chem. Phys. , 3*, 5109-5114.

[123] T. Niehaus, S. Suhai, F. D. Salla, P. Lugli, M. Elstner, G. Seifert, T. Fraunheim. (2001). Tight-binding approach to time-dependent density-functional response theory. *Phys. Rev. B , 63*, 085108: 1-9.

[124] D. J. Chadi. (1979). (110) Surface atomic structures of covalent and ionic semiconductors. *Phys. Rev.B , 19*, 2074-2082.

[125] B. Aradi, B. Hourahine, Th. Frauenheim. (2007). DFTB+, a sparse matrix-based implementation of the DFTB method. *J. Phys. Chem. A , 111*, 5678-5684.

[126] D. Porezag, T. Frauenheim, T. Kohler, G. Seifert, R. Kaschner. (1995). Construction of tight-binding potentials on the basis of density functional theory: Application to carbon. *Phys. Rev. B , 51*, 12947-12957.

[127] W. Foulkes, R. H. (1989). Tight-binding models and desnsity-functional theory. *Phys. Rev. B , B40*, 12520-12536.

[128] Q. Cui, M. E. (2001). A QM/MM Implementation of the Self-Consistent Charge Density Functional Tight Binding (SCC-DFTB) Method. *J. Phys. Chem. , B105*, 569-585.

[129] Y. Yang, H. Y. (2007). Extension of the Self-Consistent Charge Density-Functional Tight-Binding Method: Third-Order Expansion of the Density Functional Theory Total Energy and Introduction of a Modified Effective Coulomb Interaction. *J. Phys. Chem. , A111*, 10861-10873.

[130] C. Köhler, T. F. (2007). Treatment of Collinear and Noncollinear Electron Spin within an Approximate Density Functional Based Method. *J. Phys. Chem. , A111*, 5622-5629.

[131] M. Gaus, Q. C. (2011). DFTB3: Extension of the Self-Consistent-Charge Density-Functional Tight-Binding Method (SCC-DFTB). *J. Chem. Theory Comput. , 7*, 931-948.

[132] M. Elstner, G. S. (2014). Density functional tight binding. *Phil. Trans. R. Soc. , A372*, 20120483.

[133] S. Pal, D. J. (2016). Nonadiabatic Molecular Dynamics for Thousands Atom Systems: A Tight-Binding Approach toward PYXAID. *J. Chem. Theory Comput. , 12*, 1436-1448.

[134] H. Jones. (1937). The phase boundaries in binary alloys, part 2: thetheory of the α, β phase boundaries. *Proc. Phys. Soc. , 49*, 250 -257.

[135] P. Ravindran, R. Asokamani. (1997). Correlation between electronic structure, mechanical properties and phase stability in intermetallic compounds. *Bull. Mater. Sci. , 20*, 613 - 622.

[136] Tibane, M. M. (2011). *Phase stability study of Pt-Cr and Ru-Cr binary alloys.* PhD Thesis: University of Limpopo.

[137] R. Yu, J. Zhu, H. Q. Ye. (2010). Calculations of single-crystal elastic constants made simple. *Comput. Phys. Commun. , 181*, 671 - 675.

[138] M. Born. (1940). On the stability of crystal lattices. *Math. Proc. Cambridge Philos. Soc. , 36*, 160 - 172.

[139] F. Mouhat, F.-X. Coudert. (2014). Necessary and sufficient stability conditions in various crystal systems. *Phys. Rev. B , 90*, 224104: 1-4.

[140] L. Verlet. (1967). Computer "Experiments" on Classical Fluids. I. Thermodynamical Properties of Lennard-Jones Molecules. *Phys. Rev.* , 98-103.

[141] S. Nosé. (1991). Constant temperature molecular dynamics methods. *Prog. Theor. Phys., Suppl.* , 1-46.

[142] H. J. C. Berendsen, J. P. M. Postma, W. F. van Gunsteren, A. DiNola, J. R. Haak. (1984). Molecular dynamics with coupling to an external bath. *J. Chem. Phys.* , 3684-3690.

[143] T. C. Le, D. A. Winkler. (2016). Discovery and optimization of materials using evolutionary approaches. *Chem. Rev. , 116*, 6107 - 6132.

[144] L. M. Schmitt. (2001). Fundamental study: Theory of genetic algorithms. *Theor. Comput. Sci. , 259*, 1 - 61.

[145] H. Bhasin, S. Bhatia. (2011). Application of genetic algorithims in machine learning. *IJCSIT , 2*, 2412 - 2415.

[146] P. C. Jennings, S. Lysgaard, J. S. Hummelshøj, T. Vegge, T. Bligaard. (2019). Genetic algorithms for computational materials discovery accelerated by machine learning. *npj Comput. Mater.* , 46: 1 - 6.

[147] J. M. Sanchez, F. Ducastelle, D. Gratias. (1984). Generalized cluster description of multicomponent systems. *Physica A , 128*, 334-350.

[148] E. Ising. (1925). Beitrag zur Theorie des Ferromagnetismus. *Z. Phys.* , 253-258.

[149] S. Arlot, A. Celisse. (2010). A survey of cross-validation procedures for model selection. *Stat. Surv. , 4*, 40 -79.

[150] G. Kresse, J. Furthmüller. (1996). Efficient iterative schemes for ab initio total-energy calculations using plane-wave basis set. *Phys. Rev. B , 16*, 11169 - 11186.

[151] G. Kresse, J. Furthmüller. (1996). Effeciency of ab-initio total energy calaculation for metals and semiconductors using a plane-wave basis set. *Comp. Mater. Sci , 6*, 15 - 50.

[152] E. Wimmer, H. Krakauer, M. Weinert, A. J. Freeman. (1981). Full-potnetial self-consistent linearized-augmented-plane-wave method for calculating the electronic structure of molecules and surfaces: O_2 molecule. *Phys. Rev. B. , 24*, 864 - 875.

[153] M. Weinert, E. Wimmer, A. J. Freeman. (1982). Total-energy all electron density functional method for bulk solids and surfaces. *Phys. Rev. B , 26*, 4571 - 4578.

[154] G. L. W. Hart, R. W. Forcade. (2008). Algorithm for generating derivative structures. *Phys. Rev. B , 77*, 224115: 1-12.

[155] G. L. W. Hart, R. W. Forcade. (2009). Generating derivative structures from multilattices: Algorithm and application to hcp alloys. *Phys. Rev. B , 80*, 014120: 1-8.

[156] B. Delly. (2010). Time dependent density functional theory with DMol3. *J. Phys.: Condens. Matter. , 22*, 384209: 1-6.

[157] H. J. Monkhorst, J. D. Pack. (1976). Special points for brillouin-zone integrations. *Phys. Rev. B , 13*, 5188-5192.

[158] BIOVIA, Dassault Systemes. (2018). Materials Studio. San Diego:Dassault Systemes.

[159] Y. Kubota, M.C.S. Escano, H. Nakanishi, H. Kasai. (2008). Electronic Structure of LiSi. *J. Alloys Compd.* , 151 – 157.

[160] M.R. Nadler, C.P.Kempter. (1959). Crystallographic Data 186. Lithium. *Anal. Chem.* , 2109-2109.

[161] J. J. Low, M. L. Kreider, D. P. Pulsifer, A. S. Jones, T. H. Gilani. (2009). Band gap energy in silicon. *Am. J. Undergrad. Res. , 8*, 29-34.

[162] B. A. Boukamp, G. C. Lesh, R. A. Huggins. (1981). All-solid lithium electrodes with mixed conductor matrix. *J. Electrochem. Soc. , 128*, 725-729.

[163] R. Hill. (1952). The elastic behaviour of a crystalline aggregate. *Proc. Phys. Soc. Lond.* , 349 - 354.

[164] S. F. Pugh. (1954). XCII. Relations between the elastic moduli and the plastic properties of polycrstalline pure metals. *Lond .Edinb. Dubl. Phil. Mag. , 45*, 823 - 843.

[165] J. J. Gilman. (1993). Why Silicon Is Hard. *Sci. Mag. , 261*, 1436 - 1439.

[166] V. B. Shenoy, P. Johari, Y. Qi. (2010). Elastic softening of ammorphous and crystalline Li-Si Phases with increasing Li concentration: A first-principle study. *J. Power Sources , 195*, 6825 - 6830.

[167] J. J. Hall. (1967). Electronic Effects in the Elastic Constants of n-Type Silicon. *Phys. Rev. , 161*, 756 - 761.

[168] L. Y. Beaulieu, T. D. Hatchard, A. Bonakdarpour, M. D. Fleischauer, J. R. Dahn. (2003). Reaction of Li with Alloy Thin Films Studied by In Situ AFM. *J. Electrochem. Soc. , 150*, A1457 - A1464.

[169] A. Tommons, J. R. Dahn. (2007). Isotropic volume expansion of particles of amorpous metallic alloys in composite negative electrodes for Li-ion batteries. *J. Electrochem. Soc. , 154*, A444 - A448.

[170] S. J. Plimpton. (1995). Fast Parallel Algorithms for Short-Range Molecular Dynamics. *J. Comp. Phys. , 117* (1), 1-19.

[171] F. H. Stillinger, T. A. Weber. (1985). Computer simulation of local order in condensed phases of silicon. *Phys. Rev. B , 31*, 5262-5271.

[172] K. M. Kgatwane. (2011). *Atomistic simulation studies of lithiated MnO_2 nanostructures.* (Thesis write-up for MSc to PhD conversion): Univeristy of Limpopo.

[173] T. T. Sayle, K. Kgatwane, P. E. Ngoepe, D. C. Sayle. (2016). 'Breathing-crystals' the origin of electrochemical activity of mesoporous Li–MnO_2. *J. Mater. Chem. A , 4*, 6456 - 6464.

[174] A. J. Morris, C. P. Grey, C. J. Pickard. (2014). Thermodynamically stable lithium silicides and germanides from density functional theory calculations. *Phys. Rev. B , 90*, 054111: 1-9.

[175] S. Zhang, Y. Wang, G. Yang, Y. Ma. (2016). Silicon framework-based lithium silicides at high pressures. *ACS Appl. Mater. Interfaces , 8*, 16761-16767.

[176] Y. Wang, J. Jv, L. Zhu, Y. Ma. (2012). CALYPSO: A method for crystal structure prediction. *Comput. Phys. Comm. , 183*, 2063-2070.

[177] H.-J. Sung, W.H. Han, I.-H. Lee, K.J. Chang. (2018). Superconducting open-framework allotrope of silicon at ambient pressure. *Phys. Rev. Lett. , 120*, 157001: 1-6.

[178] W. Li, X. Guo, Y. Lu, L. Wang, A. Fan, M. Sui, H. Yu. (2017). Amorphous nanosized silicon with hierachically porous structures for high-performance lithium ion batteries. *Energy Storage Mater. , 7*, 203 - 208.

[179] S.-S. Lee, C.-M. Park. (2018). Amorphous silicon dioxide-based composites for high-performance Li-ion battery anodes. *Electrochim. Acta , 284*, 220 - 225.

[180] Corporation, I. (n.d.). *Intel® Xeon® Gold 6140 Processor (24.75M Cache, 2.30 GHz) Product Specifications*. Retrieved from https://ark.intel.com/content/www/us/en/ark/products/120485/intel-xeon-gold-6140-processor-24-75m-cache-2-30-ghz.html

[181] ThinkParQ. (n.d.). *BeeGFS-ThinkParQ*. Retrieved from https://thinkparq.com/products/beegfs/

[182] M. Levitt, S. Lifson. (1969). Refinement of protein conformations using a macromolecular energy minimization procedure. *J. Mol. Biol. , 46*, 269-279.

[183] R. Fletcher, C. M. Reeves. (1964). Function minimization by conjugate gradients. *Comput. J. , 7*, 149-154.

[184] W. H. Press, B. P. Flannery, S. A. Teukolsky, W. T. Vetterling. (1986). *Numerical Recipes, The Art of Scientific Computing.* Cambridge: Cambridge University Press.

[185] S.-H. Choe, C.-J. Yu, K.-C. Ri, J.-S. Kim, U.-G. Jong, Y.-H. Kye, S.-N. Hong. (2019). First-principles study of Na_xTiO_2 with trigonal bipyramid structures: an insight into sodium-ion battery anode applications. *Phys. Chem. Chem. Phys.* , 8408-8417.

[186] G. Dolgonos, B. Aradi, N. H. Moreira, T. Frauenheim. (2010). An Improved Self-Consistent-Charge Density-Functional Tight-Binding (SCC-DFTB) Set of Parameters for Simulation of Bulk and Molecular Systems Involving Titanium. *J. Chem. Theory Comput.* , 266-278.

[187] L. Cao, C. Li, T. Mueller. (2018). The use of cluster expansion to predict the structures and properties of surfaces and nanostructured materials. *J. Chem. Inf. Model. , 58*, 2401 - 2413.

[188] Md. A. Rahman, G. Song , A. I. Bhatt , Y. C. Wong , C. Wen. (2016). Nanostructured Silicon Anodes for High-Performance Lithium-Ion Batteries. *Adv. Funct. Mater.* , 647–678.

[189] C. -H. Lim, T. -Y. Huang, P. -S. Shao, J. -H. Chien, Y. -T. Weng, H.-F. Huang, B. J. Hwang, N. -L. Wu. (2016). Experimental Study on Sodiation of Amorphous Silicon for Use as Sodium-Ion Battery Anode. *Electrochim. Acta* , 265–272.

[190] Q. Zhao, Y. Huang, X. Hu. (2016). A Si/C nanocomposite anode by ball milling for highly reversible sodium storage. *Electrochem. Commun.* , 8–12.

[191] R. R. Zhao, G. Z. Ma, L. C. Zhu, A. J. Li, H. Y. Chen. (2012). An improved carbon-coating method for $LiFePO_4$/C composite derived from Fe^{3+} precursor. *Int. J. Electrochem. Sci. , 7*, 10923-1092.

[192] N. Dimov, S. Kugino, M. Yoshio. (2003). Carbon-coated silicon as anode material for lithium ion bateries: Advantages and limitations. *Electrochim. Acta , 48*, 1579-1587.

[193] L. Y. Beaulieu, K. W. Eberman, R. L. Turner, L. J. Krause, J. R. Dahn. (2001). Colossal reversible volume changes in lithium alloys. *Electrochem. Solid-State Lett. , 4*, A137-A140.

[194] C. Lee, W. Yang, R. G. Parr. (1988). Development of the Colle-Salvetti correlation-energy formula into a functional of the electron density. *Phys. Rev. B , 37*, 785-789.

[195] S. W. Oh, S. -T. Myung, S. -M. Oh, K. H. Oh, K. Amine, B. Scrosati, Y. -K. Sun. (2010). Double carbon coating of $LiFePO_4$ as high rate electrode for rechargeable lithium batteries. *Adv. Mater. , 22*, 4842-4845.

[196] J. D. Wilcox, M. D. Deoff, M. Marcinek, R. Kostecki. (2007). Factors influencing the quality of carbon coatings LiFePO4. *J. Electrochem. Soc. , 154*, A389-A395.

[197] M. C. Payne, D. C. Allan, T. A. Arias, J. D. Joannopoulos. (1992). Iterative minimization techniques for ab inito total-energy calculations: molecular dynamics and conjugate gradients. *Rev. Mod. Phys. , 64*, 1045-1097.

[198] A. Sonoc, J. Jeswiet. (2014). A review of lithium supply and demand and a preliminary investigation of a room temperature method to recylce lithium ion batteries to recover lithium and other materials. *Procedia CIRP , 15*, 289-293.

[199] C. Köhler, Th. Frauenheim, B. Hourahine, G. Seifert, M. Sternberg. (2007). Treatment of Collinear and Noncollinear Electron Spin within an Approximate Density Functional Based Method. *J. Phys. Chem. , A111*, 5622-5629.

[200] C.-Y. Chou, M. Lee, G. S. Hwang. (2015). A Comparative First-Principles Study on Sodiation of Silicon, Germanium, and Tin for Sodium-Ion Batteries. *J. Phys. Chem. C* , 14843−14850.

[201] Z. Cui, F. Gao, Z. Cui, J. Qu. (2012). A second nearest-neighbor embedded atom method interatomic potential for Li-Si alloys. *J. Power Sources , 207*, 150 - 159.

[202] (2014). In R. Yazami, *Nanomaterials for Lithium-Ion Batteries: Fundamentals and Applications* (p. 386). Broken Sound Parkway N.W: CRC Press, Taylor & Francis Group LLC.

[203] Y. Yang, H. Yu, D. York, Q. Cui, M. Elstner. (2007). Extension of the Self-Consistent Charge Density-Functional Tight-Binding Method: Third-Order Expansion of the Density Functional Theory Total Energy and Introduction of a Modified Effective Coulomb Interaction. *J. Phys. Chem. , A111*, 10861-10873.

[204] X.-H. Li, H.-L. Cui, R.-Z. Zhang. (2019). Mechanical, acoustical, and optical properties of several Li-Si alloys: a first-principle study. *J. Zhejiang Univ-Sci A (App Phys & Eng) , 20*, 614 - 626.

[205] W. Foulkes, R. Haydock. (1989). Tight-binding models and density-functional theory. *Phys. Rev. B , B40*, 12520-12536.

[206] S. Pal, D. J. Trivedi, A. V. Akimov, B. Aradi, T. Frauenheim, O. V. Prezhdo. (2016). Nonadiabatic Molecular Dynamics for Thousands Atom Systems: A Tight-Binding Approach toward PYXAID. *J. Chem. Theory Comput. , 12*, 1436-1448.

[207] S. J. Clark, M. D. Segall, C. J. Pickard, P. J. Hasnip, M. I. J. Probert, K. Refson, M. C. Payne. (2005). First principles methods using CASTEP. *Z. Kristallogr. , 220*, 567 - 570.

[208] S. C. Jung, D. S. Jung, J. W. Choi, Y.-K. Han. (2014). Atom-Level Understanding of the Sodiation Process in Silicon Anode Material. *J. Phys. Chem. Lett.* , 1283−1288.

[209] Q. Cui, M. Elstner, E. Kaxiras, T. Frauenheim, M. Karplus. (2001). A QM/MM Implementation of the Self-Consistent Charge Density Functional Tight Binding (SCC-DFTB) Method. *J. Phys. Chem. , B105*, 569-585.

[210] M. Gaus, Q. Cui, M. Elstner. (2011). DFTB3: Extension of the Self-Consistent-Charge Density-Functional Tight-Binding Method (SCC-DFTB). *J. Chem. Theory Comput. , 7*, 931-948.

[211] M. J. Phasha, P. E. Ngoepe, H. R. Chauke, D. G. Pettifor, D. Nguyen-Mann. (2010). Link between structural and mechanical stability of fcc- and bbc-based ordered Mg-Li alloys. *Intermetallics , 18*, 2083 - 2089.

[212] M. Elstner, G. Seifert. (2014). Density functional tight binding. *Phil. Trans. R. Soc. , A372*, 20120483.

[213] G. Simmons, H. Wang. (1971). *Single crystal elastic constants and calculated aggregate properties: a handbook.* Cambridge: Massachusetts: MIT Press.

[214] J. M. Tarascon. (2010). Is lithium the new gold? *Nat. Chem. , 2*, 510.

[215] K. Wang, R. Cai, T. Yuan, X. Yu, R. Ran, Z. Shao. (2009). Process investigation, electrochemical characterization and optimization of $LiFePO_4$/C composite from mechanical activiation using sucrose as carbon source. *Electrochim. Acta , 54*, 2861-2868.

[216] F. Fan, S. Huang, H. Yang, M. Raju, D. Datta, V. B. Shenoy, A. C. van Duin, S. Zhang, T. Zhu. (2013). Mechanical properties of amorphous Li_xSi alloys: a reactive force field study. *Model. Simul. Mater. Sci.* , 074002: 1-15.

[217] D. Uxa, B. Jerliu, E. Hüger, L. Dörrer, M. Horisberger, J. Stahn, H. Schmidt. (2019). On the Lithiation Mechanism of Amorphous Silicon Electrodes in Li-Ion Batteries. *J. Phys. Chem. C , 123*, 22027 - 22039.

[218] P. Hohenberg, W. Kohn. (1964). Inhomogeneous electron gas. *Phys. Rev. , 136*, B864-B871.

[219] L. -Y. Kuo, A. Moradabadi, H. -F. Huang, B. -J. Hwang, P. Kaghazchi. (2017). Structure and ionic conductivity of the solid electrolyte interphase layer on tin anodes in Na-ion batteries. *J. Power Sources , 341*, 107-113.

APPENDIX

A. Research presentations and papers

1. The development of SCC-DFTB parameters for the Li-Si system, CHPC National Conference, Velmore Hotel Estate, Pretoria, 3-7 December 2017
2. Density functional tight binding study of lithium silicon systems, Center for Nanoscale Materials, Argonne National Laboratory, Chicago, IL, USA, 25 November 2014
3. Computational modelling of lithiated silicon systems, 5th Annual Faculty of Science and Agriculture Postgraduates Research Day, Bolivia Lodge, Polokwane, 02 – 03 October 2014
4. Density functional tight-binding (DFTB) study of Si as an anode material, 57th South African Institute of Physics conference, University of Pretoria, 9 – 13 July 2012
5. Tight-binding study of Si as an anode in portable energy storage devices, 3rd Academy of Science of South Africa Young Scientists Conference, CSIR International Convention Centre, 16 – 18 October 2012
6. Systematic validation of tight-binding potentials for Li-ion battery electrode materials, Materials Modelling Centre, University of Limpopo, 27 September 2012

To be published:

(i) Katlego W. Phoshoko, Phuti E. Ngoepe, *The development of SCC-DFTB parameters for the Li-Si and Na-Si systems*, Materials Modelling Centre, University of Limpopo, South Africa

(ii) Katlego W. Phoshoko, Phuti E. Ngoepe, *The nano-architectural design of Li and Na Ion Battery Anodes using UNCLE and SCC-DFTB*, Materials Modelling Centre, University of Limpopo, South Africa

B. Lithium insertion into bulk silicon

#Li	(at. %) Li	Configuration	Etot (DFTB+)	Initial Vol	Final Vol	Δ Vol	Vol Expansion
1	11.11	Li1_Si8_1-1	-284.987846	168.379	170.87	1.48	4.98
2	20	Li2_Si8_1-1	-291.5959651	175.368	178.265	1.65	9.52
3	27.27	Li3_Si8_1-1	-297.4834524	184.932	183.227	-0.92	12.57
4	33.33	Li4_Si8_1-1	-304.1414425	192.938	183.388	-4.95	12.67
5	38.46	Li5_Si8_1-1	-311.2410041	216.111	189.605	-12.26	16.49
6	42.86	Li6_Si8_1-1	-318.3886792	228.842	213.568	-6.67	31.21
7	46.67	Li7_Si8_1-1	-325.6639453	243.571	218.713	-10.21	34.37
8	50	Li8_Si8_1-1	-330.2668689	261.92	250.017	-4.54	53.6
9	52.94	Li9_Si8_1-1	-339.7986558	254.484	238.079	-6.45	46.27
10	55.56	Li10_Si8_1-1	-346.8676767	259.903	240.534	-7.45	47.78
11	57.89	Li11_Si8_1-1	-350.8413649	305.089	274.109	-10.15	68.4
12	60	Li12_Si8_1-1	-358.0036533	318.791	286.405	-10.16	75.96
13	61.9	Li13_Si8_1-1	-363.403273	327.867	305.4	-6.85	87.63
14	63.64	Li14_Si8_1-1	-369.2194773	336.683	323.052	-4.05	98.47
15	65.22	Li15_Si8_1-1	-374.8232983	353.563	333.456	-5.69	104.87
16	66.67	Li16_Si8_1-1	-380.8997564	364.53	349.694	-4.07	114.84
17	68	Li17_Si8_1-1	-387.1488069	387.85	355.776	-8.27	118.58
18	69.23	Li18_Si8_1-1	-391.9053747	409.465	395.05	-3.52	142.71
19	70.37	Li19_Si8_1-1	-397.9067916	415.35	388.693	-6.42	138.8
20	71.43	Li20_Si8_1-1	-406.091785	420.495	396.946	-5.6	143.87
21	72.41	Li21_Si8_1-1	-408.8857916	441.469	403.253	-8.66	147.75
22	73.33	Li22_Si8_1-1	-418.8146646	447.881	409.232	-8.63	151.42
23	74.19	Li23_Si8_1-1	-419.6182834	495.532	480.038	-3.13	194.92
24	75	Li24_Si8_1-1	-427.3265637	506.92	490.324	-3.27	201.24
25	75.76	Li25_Si8_1-1	-432.1165954	526.193	497.321	-5.49	205.54
26	76.47	Li26_Si8_1-1	-437.1079447	535.158	487.251	-8.95	199.35
27	77.14	Li27_Si8_1-1	-441.3783357	553.032	528.33	-4.47	224.59
28	77.78	Li28_Si8_1-1	-446.426734	562.977	556.61	-1.13	241.97
29	78.38	Li29_Si8_1-1	-451.9643042	581.274	572.346	-1.54	251.63
30	78.95	Li30_Si8_1-1	-457.0868973	593.845	588.521	-0.9	261.57
31	79.49	Li31_Si8_1-1	-461.2857377	614.146	594.655	-3.17	265.34
32	80	Li32_Si8_1-1	-468.709302	640.593	619.109	-3.35	280.36
33	80.49	Li33_Si8_1-1	-472.6969702	645.572	622.189	-3.62	282.26
34	80.95	Li34_Si8_1-1	-479.0281843	682.19	643.993	-5.6	295.65
35	81.4	Li35_Si8_1-1	-489.7886525	676.143	635.61	-5.99	290.5
36	81.82	Li36_Si8_1-1	-490.8262191	695.16	677.843	-2.49	316.45
37	82.22	Li37_Si8_1-1	-495.2399924	723.049	711.64	-1.58	337.21

C. MD on a Silicon supercell with 512 atoms. Ensemble: NVT, 1fs, 10000 steps, 10ps, Temperature: 1600K – 1770K

T (K)	Band Gap (eV)	P_{ave} (Gpa)	Fermi (eV)	Tot. E_{ave} (kcal/mol)	Kin. E_{ave} (kcal/mol)
1600	1.577	-1.657	-4.2799488	-408836.381	2437.107
1610	1.637	-1.579	-4.8600984	-408803.925	2452.339
1620	1.491	-1.556	-4.5589594	-408772.691	2467.571
1630	1.401	-1.496	-4.3345576	-408738.605	2482.803
1640	1.414	-1.72	-3.6948405	-408706.256	2498.035
1650	1.417	-1.793	-4.1306633	-408675.329	2513.267
1660	1.245	-1.42	-4.2818376	-408641.609	2528.499
1670	1.493	-1.338	-4.4301323	-408609.405	2543.731
1680	1.458	-1.326	-4.1235379	-408575.576	2558.963
1690	1.171	-1.359	-4.1918042	-408545.403	2574.194
1700	1.216	-1.345	-4.3187107	-408511.052	2589.426
1710	0.927	-1.661	-4.1221953	-408481.035	2604.658

D. Evaluation of alternative Na-Si SCC-DFTB parameter sets

	NaSi (C2/c) structural details								
	Exp:	12.19		6.55		11.18		119	
Set #	a (Å)	%diff	b (Å)	%diff	c (Å)	%diff	β	%diff	ave (Diff)
1	11.99916	1.58	5.936151	9.83	11.527885	3.06	118.07814	0.78	3.81
2	11.96037	1.9	6.14586	6.37	11.481271	2.66	116.04106	2.52	3.36
3	11.88785	2.51	5.784499	12.41	10.999216	1.63	117.33325	1.41	4.49
4	11.89581	2.44	6.953014	5.97	11.594896	3.64	131.87778	10.27	5.58
5	11.9583	1.92	6.620871	1.08	10.910362	2.44	125.9332	5.66	2.78
6	**11.84698**	**2.85**	**6.752018**	**3.04**	**11.139217**	**0.37**	**117.24415**	**1.49**	1.94
7	11.51321	5.71	6.965595	6.15	10.908551	2.46	114.63131	3.74	4.52
8	11.50318	5.8	7.027037	7.03	11.056009	1.12	114.42008	3.92	4.47
9	11.12817	9.11	6.685971	2.05	11.342695	1.44	113.84303	4.43	4.26
10	11.26955	7.85	6.474088	1.17	10.210477	9.06	116.88467	1.79	4.97
11	11.33413	7.28	6.474375	1.16	10.314612	8.05	117.23962	1.49	4.50
12	11.39629	6.73	6.504515	0.7	10.392954	7.3	117.445	1.32	4.01
13	11.75254	3.65	6.652715	1.56	11.121307	0.53	123.17664	3.45	2.30
14	11.74035	3.76	6.431598	1.82	10.314139	8.06	124.23767	4.31	4.49
15	11.75052	3.67	6.371321	2.77	10.672265	4.65	129.46502	8.42	4.88
16	11.21761	8.31	6.411465	2.14	10.364063	7.57	125.64917	5.44	5.87
17	12.19568	0.05	5.639811	14.93	10.759755	3.83	123.12243	3.41	5.56
18	12.26395	0.6	5.637096	14.98	11.113617	0.6	127.56457	6.95	5.78
19	11.6498	4.53	7.726611	16.48	10.589124	5.43	130.57776	9.28	8.93
20	12.19032	0	6.474801	1.15	9.673287	14.45	120.31923	1.1	4.18
21	10.88559	11.31	8.034222	20.35	11.472384	2.58	127.32266	6.76	10.25
22	15.4171	23.38	5.81655	11.86	14.993363	29.14	141.39349	17.2	20.40
23	13.13061	7.43	7.555984	14.26	11.519487	2.99	137.40412	14.36	9.76
24	12.09162	0.81	9.848973	40.23	10.13857	9.77	131.78661	10.2	15.25
25	17.56942	36.15	6.319431	3.58	10.759752	3.83	126.97288	6.48	12.51
26	12.40213	1.73	8.66598	27.81	9.713111	14.04	132.51576	10.75	13.58
27	12.86738	5.41	10.160291	43.21	15.974249	35.31	143.66119	18.78	25.68
28	11.56901	5.23	7.261219	10.3	8.971266	21.92	120.61916	1.35	9.70
29	12.29312	0.84	9.254137	34.22	13.701829	20.27	140.25767	16.4	17.93
30	10.09143	18.84	9.220932	33.87	9.902791	12.12	113.40948	4.81	17.41
31	12.43448	1.99	6.290703	4.04	12.228702	8.96	135.90551	13.26	7.06
32	13.90995	13.18	5.880288	10.78	12.691193	12.66	137.00645	14.07	12.67
33	13.18288	7.83	6.410586	2.15	12.431665	10.6	138.00933	14.79	8.84
34	13.05171	6.83	6.456543	1.44	12.501542	11.16	138.07752	14.84	8.57
35	12.90786	5.72	7.305943	10.91	13.547286	19.15	141.40136	17.21	13.25
36	12.2024	0.1	6.860247	4.63	11.199179	0.17	94.09151	23.38	7.07
37	17.13069	33.7	6.976303	6.3	13.629102	19.74	79.05998	40.33	25.02
38	15.04583	20.97	6.303693	3.83	19.514177	54.3	112.61522	5.51	21.15
39	13.85555	12.79	13.036778	66.24	10.057864	10.57	120.03408	0.87	22.62
40	17.42063	35.33	10.304887	44.56	9.163917	19.82	83.56396	34.99	33.68
41	17.28236	34.56	10.250414	44.05	9.130619	20.18	84.53382	33.87	33.17
42	16.14918	27.94	11.736166	56.72	13.328394	17.53	125.38546	5.23	26.86
43	18.12701	39.17	9.334572	35.06	10.082661	10.32	95.68529	21.72	26.57

E. Evaluation of alternative Na-Si SCC-DFTB parameter sets continued

	NaSi (C2/c) lattice parameters								
	Exp:	12.19		6.55		11.18		119	
Set #	a	%diff	b	%diff	c	%diff	β	%diff	ave (Diff)
44	17.2141	34.17	10.497029	46.31	10.62715	5.07	80.59367	38.48	31.01
45	21.86947	56.84	6.73355	2.76	18.384233	48.74	126.27531	5.93	28.57
46	16.96381	32.75	9.285936	34.55	18.432157	48.98	141.68732	17.41	33.42
47	22.02867	57.5	5.434177	18.62	12.171074	8.49	122.37456	2.8	21.85
48	17.10088	33.53	7.821287	17.69	9.86123	12.54	116.34597	2.26	16.51
49	13.17118	7.74	8.300984	23.58	9.305239	18.3	121.71833	2.26	12.97
50	14.32819	16.13	4.684572	33.21	16.219753	36.79	124.92907	4.86	22.75
51	11.73773	3.78	5.560475	16.34	12.71993	12.89	133.85935	11.75	11.19
52	14.1696	15.02	7.962459	19.47	9.029977	21.28	127.36246	6.79	15.64
53	13.20395	7.99	9.683457	38.6	10.966925	1.92	143.99673	19.01	16.88
54	10.31696	16.64	10.316189	44.66	10.905226	2.49	148.20507	21.86	21.41
55	12.89562	5.63	12.349513	61.37	10.692536	4.46	162.69941	31.03	25.62
56	17.48869	35.71	9.903994	40.77	14.85438	28.23	168.68409	34.54	34.81
57	14.08926	14.45	10.316189	44.66	10.905226	2.49	148.20507	21.86	20.87
58	-	-	-	-	-	-	-	-	-
59	14.94576	20.31	10.546794	46.75	14.60274	26.55	173.39998	37.21	32.71
60	13.13952	7.5	14.575575	75.98	12.789814	13.43	178.52852	40.02	34.23
61	14.80103	19.35	9.877095	40.51	14.9288	28.72	172.47557	36.69	31.32
62	17.96585	38.31	8.400189	24.75	19.025945	51.95	169.25737	34.87	37.47
63	12.20194	0.1	8.648427	27.61	10.915073	2.4	116.48765	2.13	8.06
64	-	-	-	-	-	-	-	-	-

F. A list of the structures constituting the DFT ground state line in Figure 5-5, their compositions *x* and formation energies DHf

```
# x(1:k,1:nC) | DHf / atom [eV] | structure title             | cell formula |  space group
# ------------------------------------------------------------------------------
0.0000000000    1.0000000000          0.0000000000     ce2      Si             Fm-3m
0.2000000000    0.8000000000         -0.2413296000     ce57     LiSi4          I4/m
0.5000000000    0.5000000000         -0.4587730000     ce4      LiSi           P4/mmm
0.7500000000    0.2500000000         -0.3564132500     ce15     Li3Si          I4/mmm
0.8000000000    0.2000000000         -0.3333636000     ce54     Li4Si          I4/m
1.0000000000    0.0000000000          0.0000000000     ce1      Li             Fm-3m
```

G. A list of the structures constituting the DFT ground-state line in Figure 5-6, their compositions *x* and formation energies DHf.

```
# x(1:k,1:nC) | DHf / atom [eV] | structure title             | cell formula |  space group
# ------------------------------------------------------------------------------
0.0000000000    1.0000000000          0.0000000000     ce2      Si             Im-3m
0.2000000000    0.8000000000         -0.3092812000     ce51     LiSi4          C2/m
0.2500000000    0.7500000000         -0.3500592500     ce22     LiSi3          P2/m
0.3333333333    0.6666666667         -0.3926870000     ce9      LiSi2          P-3m1
0.4000000000    0.6000000000         -0.4020428000     ce47     Li2Si3         C2/m
0.6666666667    0.3333333333         -0.4061086667     ce6      Li2Si          P-3m1
0.8000000000    0.2000000000         -0.3263196000     ce33     Li4Si          R-3m
1.0000000000    0.0000000000          0.0000000000     ce1      Li             Im-3m
```

H. A list of the structures constituting the DFT ground-state line in Figure 5-16, their compositions x and formation energies DHf.

# x(1:k,1:nC)	DHf / atom [eV]	structure title		cell formula	space group
0.0000000000	1.0000000000	0.0000000000	ce2	Na	Fm-3m
0.2500000000	0.7500000000	-0.5285595000	ce25	Na3Si	I4/mmm
0.5000000000	0.5000000000	-0.4486487500	ce19	Na2Si2	P4/nmm
0.6666666667	0.3333333333	-0.3822516667	ce6	NaSi2	Immm
1.0000000000	0.0000000000	0.0000000000	ce1	Si	Fm-3m

I. A list of the structures constituting the DFT ground-state line in Figure 23, their compositions x and formation energies DHf.

# x(1:k,1:nC)	DHf / atom [eV]	structure title		cell formula	space group
0.0000000000	1.0000000000	0.0000000000	ce2	Mg	Fm-3m
0.2500000000	0.7500000000	-0.1553582500	ce29	Mg3Si	Pm-3m
0.5000000000	0.5000000000	-0.1746155000	ce4	MgSi	P4/mmm
0.6666666667	0.3333333333	-0.1603566667	ce6	MgSi2	Immm
0.7500000000	0.2500000000	-0.1290327500	ce12	MgSi3	Pmmm
1.0000000000	0.0000000000	0.0000000000	ce1	Si	Fm-3m